Compact Solar Thermal Energy Storage Systems Using Phase Change Materials

Maher Al-Maghalseh

PhD

2014

Compact Solar Thermal Energy Storage Systems Using Phase Change Materials

Maher Al-Maghalseh

A thesis submitted in partial fulfilment of the requirements of the University of Northumbria at Newcastle for the degree of Doctor of Philosophy

Research undertaken in the

School of Engineering and Environment

August 2014

Declaration

I declare that the work contained in this thesis has not been submitted for any other award and that is all my own work. I also confirm that this work fully acknowledges opinions, ideas and contributions from the work of others.

Name: Maher Al-Maghalseh

Signature:

Date: August 2014

Acknowledgements

I must be thanking the Almighty Allah for giving me the courage, determination and guidance in conducting this work.

Special and foremost, I would like to thank my supervisor Professor Khamid Mahkamov, for his invaluable guidance, encouragement and support over the duration of this work.

I would like to express my appreciation to my beloved parents for their continuous support and wisdom over the course of my academic journey. Furthermore, I would like to thank my brothers and sisters for their care and assistance throughout my years of education. Special thanks of course are due to my loving wife for her love, support, care and patience since the beginning of this work. Finally, thanks to my little son Mohammad who joined the family in the last stage of this work.

Moreover, I am indebted to my colleagues and friends in the UK and Palestine for providing an enjoyable and fun environment. Many thanks are due to the academic and technical staff at Northumbria University for their support and encouragement.

Abstract

The present research explores numerically and experimentally the process of melting and solidification of Phase Change Materials (PCM) in a latent heat thermal energy storage system (LHTESS). Further, the study will investigate various methods of intensification of heat transfer in such materials by means of metallic fins, filling particles or nanoparticles and by choosing the optimal system geometry for a rapid development of free convection flows during the melting process.

The study includes three main parts. First, 3D CFD modelling was performed for the melting performance of a shell-and-tube thermal storage system with *n-Octadecane* as a PCM. The predicted model was in very good agreement with experimental data published in open literature. A series of numerical calculations were then undertaken to investigate the effect of nanoparticles on the heat transfer process. Dimensionless heat transfer correlations were derived for the system with Pure PCM and PCM mixed with nano-particles.

In the second part of this study the experimental studies were carried out in order to investigate the performance of the laboratory thermal storage system with paraffin as the PCM. The thermal storage system was connected to evacuated tube solar collectors and its performance was evaluated in various conditions. 3D CFD model of the system was developed and numerical simulations were run for constant heat source conditions. Computational results were compared with experimental data obtained on the test rig at Northumbria University. Comparison revealed that the developed CFD model is capable to

describe process of heat transfer in the system with high accuracy and therefore can be used with high confidence for modelling further cases.

Finally, 3D CFD model was developed to predict the transient behaviour of a latent heat thermal energy storage system (LHTESS) in the form of a rectangular container with a central horizontal pipe surrounded by paraffin as PCM (melting temperature is 60 ^{o}C). Water was used as a heat transfer fluid (HTF). The enhancement of heat transfer in specific geometries by using external longitudinal fins on the tube and metallic porous matrix were numerically investigated. The influence of the number of fins and porosity of the matrix on the temperature distribution, melting process, melting time and natural convection phenomena were studied. Dimensionless heat transfer correlations were derived for calculation of the Nusselt number as function of Fourier, Stefan and Rayleigh numbers. These correlations to be used in the further designing process of similar thermal storage units at Northumbria University.

Table of Contents

List of Figures

List of Tables

Nomenclature

A	Area (m^2)
A_{Mush}	Mushy zone constant
Bi	Biot number
C	Constants
C_2	Inertia resistance factor
C_p	Specific heat (J/Kg^oC)
D	Diameter
E	Total energy
E_f	Total fluid energy
E_s	Total solid energy
F	Force
G	Gravitational acceleration
Gb	Generation of kinetic energy due to buoyancy
Gk	Generation of turbulent kinetic energy due to the mean velocity gradients
Gr	Grashof number
h	Sensible enthalpy (J)
H	Enthalpy
H	High
h_{ref}	Reference enthalpy
I	Unit tensor
K	Constant
k	Thermal conductivity (W/m^oC)

k_{eff}	Effective thermal conductivity
L	Latent heat (Kj/Kg)
L	Length
LMTD	Logarithmic mean temperature difference
m	Mass in each space (Kg)
$\dot{m}$	Mass flow rate
Nu	Nusselt number
P	Static pressure
Pr	Prandtl number
P_{rt}	Turbulent Prandtl number for energy
q	Heat transfer rate
r	Radial coordinate
Ra	Rayleigh number
Re	Reynolds number
S	Source term
S_h	Heat from any volumetric sources
S_m	Mass source
Ste	Stefan number
t	Time (s)
T	Temperature
To	Operation temperature
T_{ref}	Reference temperature
u	X velocity components (m/s)
v	Y velocity components (m/s)
v_n	Normal components of the velocity of the interface

v_r	Radial velocity component
v_x	Axial velocity component
w	Z velocity components (m/s)
W	Width
x	Axial coordinate
Y_M	Contribution of the fluctuating dilatation in compressible turbulence to The overall dissipation rate

Subscripts

L	Liquid
eff	Effective
f	Fluid
i	Inlet
m	Melting
np	Nano-particles
o	Outlet
s	Solid
T	Total
w	Wall

Greek symbols

ρ	Density (Kg/m^3)
$\bar{\bar{\tau}}$	Stress tensor (Pa)
μ_t	Turbulent viscosity (Pa s)
β	Coefficient of thermal expansion (1/K)
μ	Viscosity (Kg/ms)
$\dot{j}$	Diffusion flux
$(\tau_{ii})_{eff}$	Deviatoric stress tensor
β_t	Liquid fraction
ξ	Porosity of the media
α	Permeability
ϕ	Volumetric fraction

Acronyms

ANN	Artificial Neural Network
CENG	Compressed Expanded Natural Graphite
CF	Carbon Fiber
CFD	Computational fluid dynamics
CNFs	Carbon Nanfibers
DAQ	Data Acquisition System
DES	Detached Eddy Simulation
EG	Expanded Graphite
ETSS	Encapsulation Thermal Storage Systems
HTF	Heat Transfer Fluid
LES	Large Eddy Simulation
LHTESS	Latent Heat Thermal Energy Storage System
MEPCM	Microencapsulated Phase Change Material
MPCM	Multiple Phase Change Material
MVF	Molten Volume Fraction
MWCNTs	Multiwall Carbon Nanotubes

NEPCM	Nanoparticles Enhancement Phase Change Material
PCM	Phase Change Material
PCO	Phase Change Operation
RNG	Renormalization-Group
RSM	Reynolds Stress Model
SPCM	Single Phase Change Material
SST	Shear-Stress Transport
SWCNTs	Single Wall Carbon Nanotubes
TESS	Thermal Energy Storage Systems
TSS	Thermal Storage Systems
UDF	User Defined Function

Chapter 1 Introduction

The rapid utilization of fossil has fuels resulted in a considerable increase in the level of greenhouse gases. Carbon dioxide emissions amount to approximately 347 billion tons since 1751 [1]. Therefore, significant efforts are being made by scientists to reduce consumption of fossil fuels and to generate energy from natural renewable sources, such as wind, sunlight, geothermal as well as hydropower. Solar energy, given that it is abundant and freely available, is one of the most promising renewable energy resources. The International Energy Agency has estimated that solar power will produce 21% of the world's electricity by 2050 [2]. However, there are several problems associated with utilisation of the solar energy: the intensity of the solar radiation varies with the location and during the day and seasons and depends on the local weather conditions (clear or cloudy sky). Because of this, it is a sensible engineering solution for the solar energy to be stored in various forms including electrochemical storage and thermal energy storage systems (TESS) [3].

The thermal energy storage systems can be classified into several main groups, namely thermochemical storage, sensible heat storage and latent heat storage, or combination of these both [4]. Thermochemical heat storage involves chemical reactions to take place in the storage vessel. In the sensible storage systems, the heat is stored by increasing the temperature of a single phase storage medium, while the latent heat systems store the energy as a result of the phase transition of the materials at the constant or nearly constant temperature. It is highlighted in a number of works that the latent heat storage systems using a Phase Change Material (PCM) is perhaps the most effective heat storage technique because it provides a very high energy density during the melting and solidification processes

compared to the conventional sensible heat energy storage. This means that the latent heat storage system using a PCM requires a much smaller volume of materials to store a certain amount of energy. A detailed review of energy storage using PCMs has been performed in [5-8].

This research work focuses on numerical and experimental investigations of melting and solidification processes in PCMs of a latent heat thermal energy storage system (LHTESS). The study also looks at various methods of intensification of the heat transfer in such materials by means of deployment of metallic fins, filling particles or nanoparticles and selection of the optimal system geometry which creates conditions for a rapid development of free convection flows during the melting process.

1.1 Research objectives

The overall aim of this work is to propose the most efficient means of enhancement of heat transfer in the thermal storage systems with PCMs and derive dimensionless correlations for determination of heat transfer in such thermal storage systems as a function of process and design parameters. To achieve these numerical and experimental investigations were conducted to obtain information on the flow, heat transfer, the temperature distribution in PCMs and analyse the influence of metallic fins, filling particles or nano-particles on the heat transfer enhancement.

The main objectives of the study can be summarised as follows:

1. To carry out a comprehensive literature review related to the thermal energy storage technologies using PCMs, thermal storage systems design and configurations and on methods of heat transfer intensification.

2. To develop CFD models of the thermal storage systems to be experimentally investigated.
3. To study the influence of the geometry of the thermal storage systems, filling particles or nano-particles on the enhancement of the heat transfer in the PCM storage systems.
4. To experimentally investigate the performance of thermal storage system with the PCM, coupled with evacuated tube solar collectors.
5. To validate the developed CFD model using the obtained experimental information and to refine the model if necessary.
6. To use the refined model to investigate wider range of geometries and configurations of thermal storage systems with PCMs.
7. To derive dimensionless correlations for determination of heat transfer in various thermal storage systems as a function of process and design parameters.

1.2 Research methodology

The work will consist of both experimental and numerical investigations.

1.2.1 Experimental investigations

In order to design and build an optimal PCM storage unit the acquisition of experimental data on the performance of such systems is required. The main objectives of the experimental part in this study are:

1. To investigate the heat transfer in the thermal storage system this is in the form of the rectangular container with horizontal pipes surrounded by a phase change material.

2. To test the system using conditions typical for three different seasons in the North-East region of the UK.

3. To test the system operating at the steady state regime in order to validate the CFD model.

4. To study the effect of the inlet temperature of the heat transfer fluid (HTF).

5. To study the influence of the flow rate of the HTF.

1.2.2 Numerical investigations

CFD modelling has been used to simulate numerically the heat and mass transfer processes taking place during melting and solidification processes in PCM. The study has involved application of two and three dimensional CFD models using ANSYS/FLUENT software. Theoretical results have been validated using experimental data. In final stages of investigations, the numerical models have been used to study the transient behaviour of the heat storage units with different geometries.

1.2.3 Physical definitions of the dimensionless parameters

This section presents the physical definition of the dimensionless parameters which are used to estimate the heat transfer in the thermal storage systems.

Fourier number (Fo) is the ratio of the heat conduction rate to the rate of thermal energy storage in a solid. Fo is dimensionless time and can be calculated using the following equation:

$$Fo = \frac{\alpha t}{L^2} \tag{1.1}$$

Grashof number (Gr) is measure of the ratio of buoyancy forces to viscous forces. Gr is calculated using the following equation:

$$Gr = \frac{g\beta(T_s - T_\infty)L^3}{v^2} \tag{1.2}$$

Nusselt number (Nu) is the ratio of convection to pure conduction heat transfer. Nu is calculated using the following equation:

$$Nu = \frac{hL}{k_f} \tag{1.3}$$

Prandtl number (Pr) is the ratio of the momentum and thermal diffusivities. Pr is calculated using the following equation:

$$Pr = \frac{C_p \mu}{k} = \frac{v}{\alpha} \tag{1.4}$$

Reynolds number (Re) is the ratio of the inertia and viscous forces. Re is calculated using the following equation:

$$Re = \frac{VL}{v} \tag{1.5}$$

Stefan number (Ste) is the ratio of the sensible heat to latent heat. Ste is calculated using the following equation:

$$Ste = \frac{C_p \Delta T}{L} \tag{1.6}$$

1.3 Contribution to knowledge

Analysis of existing literature indicates that investigations on the heat transfer in thermal storage systems have been mainly concentrated on the encapsulated PCMs and on the shell-and-the-tube type PCM storage systems. It also reveals the relevance of the development of accurate and feasible CFD models and an importance of derivation of dimensionless heat transfer correlations.

In this work accurate 3D CFD models were developed to evaluate performance of the thermal storage systems with the metallic porous matrix, external fins and PCM mixtures with nano-particle fillings.

Dimensionless correlations for determination of heat transfer for investigated thermal storage systems were derived as a function of a wide range of process and design parameters. These correlations are for use in the designing process in the further development of similar thermal storage systems at Northumbria University.

1.4 Thesis structure

Chapter 1, Introduction: this chapter highlights the scope of the research, aims and research objectives and methodology. It also describes the contribution to knowledge and the thesis structure.

Chapter 2, Literature review: This chapter presents results of the comprehensive review of the most significant studies which are relevant to the current research topic. The review focuses on the techniques applied to enhance the performance of thermal storage systems and the methods used to analyse the heat transfer problems in the phase change materials. Also,

this chapter describes the published results and discussions on the heat transfer intensification methods including application of fins, filling materials, nano-fluids, nano-particles, microencapsulation and the thermal conductivity enhancement.

Chapter 3, Fundamentals of CFD modelling and data analysis: In this chapter the governing equations of the CFD modelling technique are presented which describe flow, heat transfer and solidification/melting of PCMs. Additionally, specifics of modelling heat transfer in the porous media and taking into account of nano-particles are discussed.

Chapter 4, CFD model validation: This chapter presents results of the 3-D CFD modelling of the PCM in shell-and-tube thermal storage system. Then, the numerical results obtained by the CFD are compared to experimental data published by Lacroix [9]. Finally, a detailed parametric study of heat transfer processes in the melting PCM with nano-particles was carried out and results were discussed.

Chapter 5, Experimental study of the thermal storage system with the PCM: This chapter describes the experimental set up to investigate the thermal characteristics of the PCM heat exchanger heated by the solar evacuated tube collectors. The test procedure and measurements taken are described together with the uncertainty analysis conducted. The system was tested under the steady state conditions in order to validate the developed CFD model.

Chapter 6, Numerical study of performance of a rectangular PCM storage unit: This chapter discusses the results obtained with application of the 3-D CFD modeling using ANSYS/FLUENT software. The model is used to analyze the heat transfer intensification methods in the Thermal Storage Systems (TSS), including the fins and porous medium. Simulations performed provide information on the flow and heat transfer in the storage and

solidification/melting processes dynamics. The chapter contains heat transfer correlations in the dimensional form, which were derived using the obtained numerical results.

Chapter 7, Conclusion and future recommendations: This chapter highlights the major findings and presents the main conclusion from the study conducted and recommendations for future investigations.

Chapter 2 Background and Literature Review

2.1 Introduction

This chapter presents results of the literature review on thermal energy storage technologies as well as the latent heat thermal energy storage (LHTES) using PCMs. The chapter discusses outcomes of previous studies on the design and configuration of thermal storage systems, methods of heat transfer intensification, and on the experimental testing and mathematical simulation of systems with PCMs.

2.2 Encapsulation and packed bed thermal storage systems

Recent developments in the field of thermal energy storage systems using PCMs have led to renewed interest in encapsulation thermal storage systems (ETSS) and packed bed storage systems. Such systems have the advantage of the higher storage density with the higher efficiency, and a large number of published papers describe relevant performance analyses. In these works the following aspects were investigated: storage system designs and their configurations, the PCM materials used; heat transfer enhancement methods deployed, and the flow and heat transfer processes during both the charging and discharging processes. A number of the published articles, which describe the heat transfer in the thermal storage systems using PCM capsules, have been summarised by Regin in [10]. A large amount of the

published literature also was discussed in the extensive review of the research carried out on the packed beds thermal storage systems [11].

Regin et al. [12] developed a numerical model to analyse and predict the thermal performance of the packed bed cylindrical latent heat thermal storage system. The storage container was filled with spherical capsules filled with paraffin wax. These were in the flow of the heat transfer fluid. Figure 2.1 presents the layout of this system.

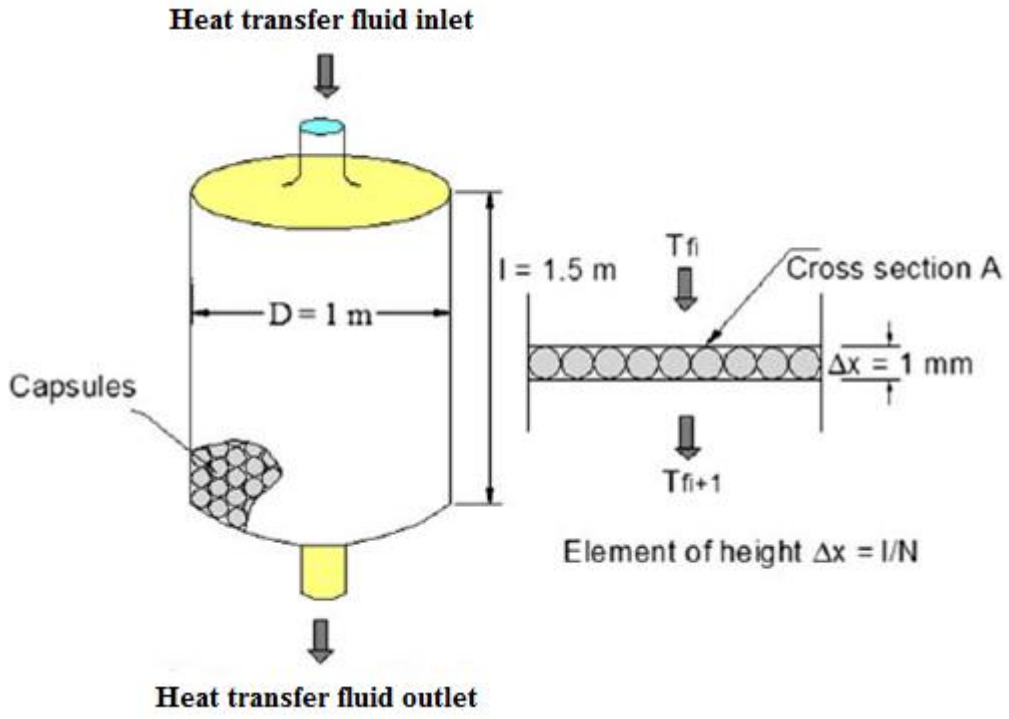

Figure 2.1: Layout of the storage system [12].

The inlet temperature of the heat transfer fluid, the phase change temperature range and capsule sizes were discussed by the author. The results of the study show that the solidification time was longer than the duration of the melting process. This was due to a very low value of heat transfer coefficient during the solidification process because of the high thermal resistance of the solidified layer which formed on the inner wall of the capsule. With the increase in the inlet heat transfer fluid temperature, the time to reach the melting point

and the charging time were reduced. Similarly, for higher mass flow rates of the heat transfer fluid, the time interval needed for complete charging was shorter. The second major finding was that the capsule size had a significant effect on the charging and discharging process. Smaller capsules provided higher storage rates, and a shorter time was needed to reach the melting point. These findings were consistent with those of Zeinab et al. [13], who numerically investigated the thermal performance of a cylindrical packed bed thermal storage unit filled with the PCM in spherical capsules.

Cho and Choi [14] experimentally investigated the thermal characteristics of the storage system with paraffin in spherical capsules during the freezing and melting process. The influence of two factors were investigated; namely, the Reynolds number and inlet temperature. The temperature distribution in the storage tank and inside the spherical capsules was measured during both processes. It was found that the temperature on the capsule surface was lower than that inside the capsule during the freezing and melting process due to the difference between the heat removal rate and solidification heat release rate. Moreover, the phase-change period during the freezing and melting process decreased as the Reynolds number increased, even with reduced inlet temperature. Another important finding was that the phase-change period for the capsule in the first layer was shorter than that for the capsule in the seventh layer, and the phase-change period in the centre of the capsule was longer than that in the capsule edge. The reason for this is that the porosity at the edge of the tank is greater than that at the centre. Bedecarrats et al. [15, 16] also experimentally investigated the thermal behaviour of the system with spherical PCM capsules filling up randomly the cylindrical storage tank. The obtained results were used to explain the temperature distribution and the duration of solidification and melting processes in spherical capsules.

The thermal characteristics of a packed bed thermal storage system with spherical capsules were also investigated numerically and experimentally by Ismail and Henríquez [17]. This study concentrated on the effect of the working fluid entry temperature and its mass flow rate as well as the capsule temperature during both the charging and discharging processes. Moreover, capsules made of different materials were also investigated, and the numerical results corroborated the findings of the experimental work. Singh et al. [18-21] developed a mathematical model to predict the thermal performance of packed bed storage systems using a computer code written in the C++ language. Different shapes and sizes of thermal storage systems were studied, and the computational model predicts the temperature distribution, thermal energy stored in the unit and the energy consumption.

Wang et al. [22] conducted the experimental study of the charging process in cylindrical heat storage capsules filled with multiple PCMs. Two cylindrical capsules made of three coaxial red copper tubes were horizontally immersed in the water tank. One of these was filled with three different PCMs: stearic acid, sliced paraffin and lauric acid. The other tube was filled with sliced paraffin only. The experiment results showed a significant enhancement of the charging process using the multiple PCM (MPCM) capsule compared to that using a single PCM (SPCM). Moreover, the complete melting time in the MPCM capsule was significantly decreased, namely by 37-42%. In addition, the melting process time in MPCM capsules was shorter by 15-25% in the charging process.

The isothermal phase change of the PCM encapsulated in a storage tank was analysed mathematically and experimentally by Zivkovic and Fujii [23]. A computational model was developed using the enthalpy method to simulate the transient performance of the isothermal phase change process. The reason for this was that such a method did not require an explicit treatment of the boundary conditions in the phase change system. Both cylindrical and rectangular containers were investigated. The volumes of the containers as well as the

convective heat transfer area for both types were selected to be equal. It was demonstrated that the melting time increased gradually with increasing volume for both types of containers. However, the melting time of the rectangular container was much shorter compared to that of the cylindrical container with the same volume and heat transfer area. The use of a rectangular container for the encapsulation of the PCM was recommended.

Tan et al. [24] experimentally investigated the buoyancy and natural convection phenomena during the melting process of the PCM inside a spherical capsule. These results were validated with a numerical solution obtained using CFD software FLUENT. The most interesting finding was that the conduction heat transfer dominated during the early stage, whereas, buoyancy-driven convection becomes more prominent as the liquid fraction volume is increased. However, the molten PCM ascends upwards to the upper regions of the sphere due to the natural convection. Consequently, the upper regions of the sphere melt first, followed by the other regions. Another interesting finding from the computational results was that the temperature distribution fluctuated chaotically at some points inside the sphere, due to the existence of the unstable fluid layer at these points. The findings of this study supported observations in the previous research by the same author [25, 26].

Koizumi [27] experimentally examined the heat transfer on an isothermally heated sphere placed in a uniform, downwardly directed flow using a micro-foil heat sensor (HFS). This study dealt with the opposing flow mixed convection, where the direction of the free flow was opposite to that of the forced flow. Two situations were analysed and discussed. In the first case, isothermal spheres were used, made of 3 mm thick copper with an outer diameter of 50 mm, while in the second case, solid PCM capsules were used, which were made of 1 mm thick glass and with an outer diameter of 50 mm. The spherical capsules were filled with *n-Octadecane* as a PCM. Figure 2.2 shows schematics of these two cases.

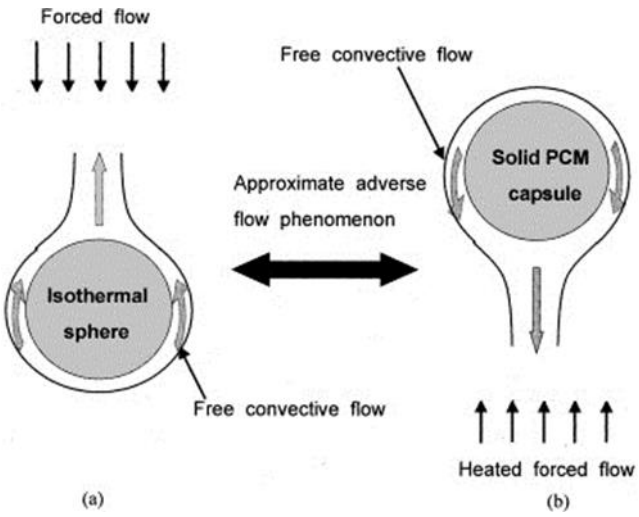

Figure 2.2: Schematic drawing of the opposing flow mixed convection. (a) Isothermal sphere and (b) solid PCM capsule [27].

In this study, three types of air flow patterns with a Grashof number (*Gr*) of 3.3×10^5 were investigated. These were chaotic flow at Reynolds number (*Re*) < 240, two-dimensional steady separated flow at $240 \leq Re \geq 500$, and three-dimensional unsteady separated flow at *Re* >500. The time average local Nusselt number (*Nu*) was obtained using the following formula:

$$\overline{Nu} = \frac{hd}{k} = \frac{qd}{\left(T_w - T_f\right)k} \tag{2.1}$$

The measurements of the Nusselt number for the three types of patterns are illustrated in Figure 2.3. The dashed line shows the experimental results for the pure forced convection found by Yuge [28].

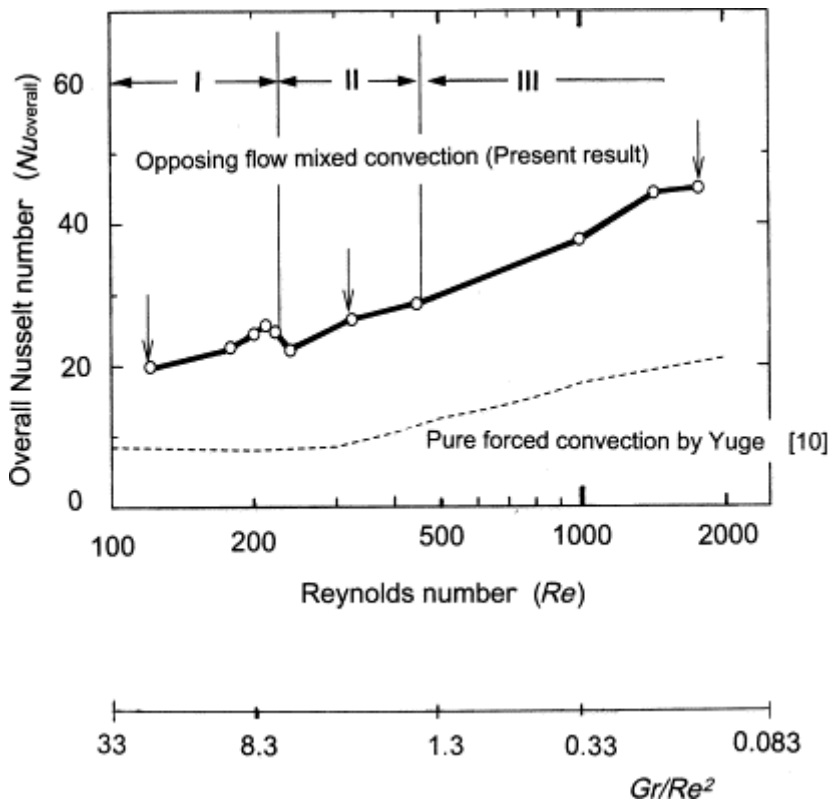

Figure 2.3: Nusselt Number vs Reynolds number [27].

The experimental results show that, in the case of the chaotic flow at $Re < 240$, the Nusselt number around the sphere is 10% higher than that for the pure forced convection, while it is greater by factor of two in the case of $Re \geq 500$. Moreover, the results were validated using the numerical results of Jia and Gogos [29], and very good agreement between the numerical and experimental results was obtained. Additionally, the experiments investigated the influence of copper plates inserted inside the solid PCM capsule. There was a significant improvement in the latent heat storage rate by the solid PCM when the copper plate was inserted inside the spherical capsule.

A study in [30] addressed the transient thermal response of a packed bed of spheres containing a PCM. The authors presented a computational model which analysed both isothermal and nonisothermal melting behaviour, axial thermal dispersion effects, and

intraparticle conditions (Biot number) effects. In order to validate the results, an experiment was conducted on a cylindrical bed filled with high-density polypropylene spheres. Data from the computational model was compared with the experimental results. The results showed good agreement for the temperature distribution and energy stored in the system. On the other hand, the study provided an opportunity to explain the heat transfer, isothermal melting and phase trajectory melting processes under a variety of conditions, such as the varying Reynolds number.

Khalil et al. [31] experimentally investigated the thermal performance of a packed bed thermal storage system containing spheres of different sizes. The study examined the effect of the Reynolds number and particle size on the heat transfer in the system. The results indicated that heat transfer improved significantly when the porous media were used, and it was also improved when the flow Reynolds number was increased. Correlations were proposed between the Nusselt and Reynolds numbers for the cases with and without the porous material. The Nusselt number in the case of using the porous material was

$$Nu_D = 17.30\left(\frac{D}{d}\right)^{-0.77} Re_D{}^{0.235}\left(\frac{D}{d}\right)^{0.3} \tag{2.2}$$

For $2167 \le Re_D \le 19400$ and $3.54 \le D/d \le 14.16$.

The Nusselt number as a function of the Reynolds number for the case without the porous material was

$$Nu_D = 0.042\, Re_D{}^{0.76} \tag{2.3}$$

For $2778 \le Re_D \le 19400$ and $1.5 \le P_r \le 3.4$.

Nsofor and Adebiyi [32] also experimentally investigated the heat transfer and natural convection phenomena in a packed bed thermal storage system at high temperature conditions. Heat transfer correlations were proposed as the Nusselt number as a function of the Prandtl and Reynolds numbers and comparisons were carried out with the existing correlations derived previously for the similar storage media. The heat transfer and pressure drop characteristics of a backed bed thermal storage system were experimentally investigated by Varun et al. [33]. The storage tank was filled with large cylindrical elements with various horizontal and vertical orientations. Significant correlations were derived to calculate the Nusselt number and friction factor as a function of the Reynolds number. Therefore, these correlations could be efficiently used in predicting the performance of solar thermal energy storage systems in the form of large cylindrical elements.

The efficiency of the effective thermal conductivity of latent heat storage capsules was evaluated numerically by Shiina and Inagaki [34]. The uniform and non-uniform heat transfer around the cylindrical surface was observed. In this study water, octadecane, Li_2CO_3 and NaCL were selected as PCMs, and copper, aluminium and carbon steel were used as the porous media. The PCM injected inside the capsule had the following dimensions: 6.6 mm of the outer diameter, 6 mm of the inner diameter, and 0.3 mm of the thickness. Acrylic resin and copper were used as the capsule walls. Moreover, air, helium and water were used as the HTF. Figure 2.4 shows results obtained on the melting time as a function of the effective thermal conductivity of two composite PCMs of octadecane and Li_2CO_3 at Re= 7500 and with helium as HTF.

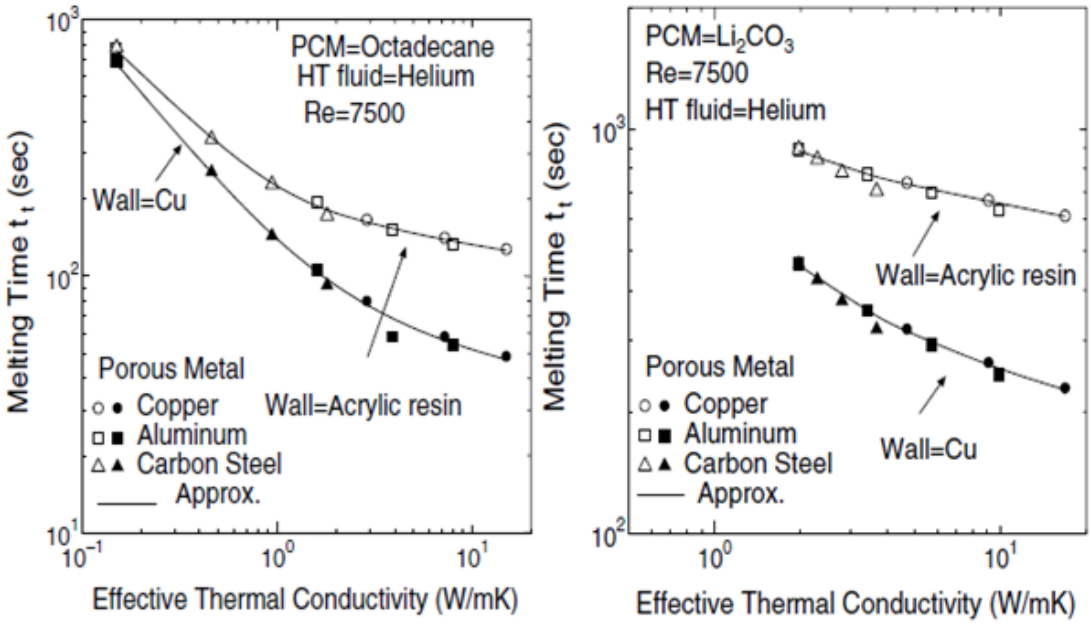

Figure 2.4: Melting time for composite PCMs of octadecane and Li_2CO_3 [34].

It can be seen that the melting time is reduced when the effective thermal conductivity is increased. Furthermore, the melting of the PCM in the case of the acrylic wall is much longer compared to the result for the copper wall. It can be seen that, unlike the PCM with the high thermal conductivity, the influence of the effective thermal conductivity on the melting time is greater for the PCM with the low thermal conductivity.

Hawlader et al. [35] conducted a numerical and experimental study of the thermal energy storage involving the encapsulated PCM. The study investigated the effect of the encapsulation ratio, hydrophilicity, and energy storage on the thermal performance of PCM capsules. It was concluded that using the PCM capsule increases both the thermal energy charging and discharging capacity. In addition, the capsule maintained its original geometrical profile and the energy storage capacity after 1000 thermal cycles. A large volume of published papers describe the role of heat transfer and phase change processes in packed bed thermal storage systems. Results of some of these studies are summarised in Table 2.1.

Table 2.1: Heat transfer and phase change process studies in packed bed thermal storage system.

No	Author	Geometry	Methods	PCM	HTF	Process	Parameters/range	Dimensions
1.	Regin et al. [12]	Cylindrical storage/ spherical capsule	Numerical Modelling	Paraffin wax	Water	Charging and discharging	Charging:$T_i = 50℃$, $70 < T_{HTF} < 82℃$, $0.0398 < \dot{m}_f < 0.1592\ Kg/s$. Discharging: $T_i = 70℃$, $50 < T_{HTF} < 35℃$, $0.0398 < \dot{m}_f < 0.1592\ Kg/s$.	Tank: D=1 m, L=1.5 m, Sphere, D=1 mm.
2.	Cho and Choi [14]	Acryl storage/ spherical capsule	Experimental	n-tetradecan ($C_{14}H_{30}$) n-hexadecane ($C_{16}H_{34}$)	Water	Charging and discharging	Re= 8,12 and 16. Charging,$T_{init} = -7, -4$ and $-1℃$, $T_{inlet} = 10℃$. Discharging, $T_{init} = 10℃$, $T_{inlet} = -7, -4$ and $-1℃$	Tank: D_i= 220 mm, thickness=10 mm, H=173 mm
3.	Chen [36, 37]	Cylindrical storage/ spherical capsule	Experimental and numerical	Water/ice	Alcohol	Charging process	$2 < \dot{m}_f < 5\ Ipm$, $-20 < T_i < -10℃$	Capsule: D=34 mm, porosity $0.365 < \varepsilon < 0.61$
4.	Silva et al. [38]	Rectangular	Experimental and numerical	Paraffin wax	Air	Charging and discharging	$\dot{m}_f$:0.005488kg/s , $T_{HTF} = 19.3℃$, heat flux (q):480W/m^2	Tank: H=813 mm, L=623 mm
5.	Zeinab et al. [13]	Cylindrical storage/ spherical capsule	Numerical Modelling	Paraffin wax	Water	Charging and discharging	Charging, $T_{init} = 50℃$, $70 < T_{HTF} < 82℃$, $0.0398 < \dot{m}_f < 0.16\ Kg/s$. Discharging,$T_{ini} = 70℃$, $50 < T_{HTF} < 35℃$, $0.0398 < \dot{m}_f < 0.16\ Kg/s$.	The porosity of the bed is 0.4

No	Author	Geometry	Methods	PCM	HTF	Process	Parameters/range	Dimensions
6.	Bedecarrats et al. [15, 16]	Cylindrical storage/spherical capsule	Experimental	Water/ice	Chilling fluid	Charging and discharging	Charging, $T_{HTF} = -6℃$, Flow rate = 1.3m^3/h. Discharging, $T_{HTF} = 5℃$, Flow rate = 1.1m^3/h	Tank: D=0.95 m, H=1.42m. Sphere: D_o=77 mm, thickness=2 mm
7.	Bilir and İlken [39]	Cylindrical spherical storage	Numerical Modelling	Water/ice	-	Discharging process	$0.01 < Ste < 0.5$, $1 < Bi < 50$.	
8.	Ismail and Henríquez [17]	Cylindrical/spherical capsule	Experimental and numerical	Water/ice	Ethylene glycol	Charging and discharging	$T_{initial} = 20℃$. $0.5 < \dot{m}_f < 1.5\ m^3/h$, $-15 < T_{inlet} < -3℃$,	Tank: D= 0.92 m, L = 1.54 m.
9.	Ismail and Henríquez [40]	spherical capsule	Numerical Modelling	Water/ice	Ethanol	Discharging process	$0.01 < Ste < 0.5$, $1 < Bi < 100$, $-25 < T_{HTF} < -5℃$, $5 < T_{init} < 35℃$,	Capsules: D= 20, 40, 100, 140, 200, 300 and 400 mm. thickness=0.1 m
10.	Ismail [41]	Cylindrical storage/spherical	Numerical Modelling	Stone/ steel	Water/air	Charging and discharging	$0.5 < \dot{m}_f < 1 kg/s$, $0.3 < \varepsilon < 0.5$,	particle D= 25-50 mm,
11.	Singh et al. [18-20]	Cylindrical	Numerical	-	Air	System performance	$T_{inlet} = 40℃$.	Tank: D=0.95 m, H=6 m.
12.	Farid and Husian [42]	Cylindrical	Experimental and numerical	Paraffin wax	Air	Charging and discharging	$0.007 < \dot{m}_f < 0.014\ Kg/h$, $28 < T_{init} < 70℃$, $T_{HTF} = 75℃$	Tank: (D= 31.8 mm, L = 335 mm)
13.	Kousksou et al. [43]	Cylindrical/spherical capsule	Experimental and numerical	Water/ice	Chilled glycol	Charging process	$T_i = 6℃$, $-8 < T_{HTF} < -3.5℃$, $1 < \dot{m}_f < 2.5\ m^3/h$.	Tank: D= 0.95 m, L=1.42 m. Sphere: D=77 mm,
14.	Wang et al. [22]	Cylindrical/ spherical capsule	Experimental	Stearic acid/ sliced paraffin/ lauric acid	Water	Charging process	$T_{inlet} = 70 - 72.5℃$, $\dot{m} = 1.5 m^3/h$	Tank volume 200 litres

No	Author	Geometry	Methods	PCM	HTF	Process	Parameters/range	Dimensions
15.	Eames et al.[44]	Spherical	Experimental	Water/ice	Chilled water	Charging and discharging	$-9.5 < T_{HTF} < -4.4℃$, $\dot{m}_f = 0.1\ m/s$.	Spheres: D=8.14, 7.00 and 6.27 cm
17.	Zivkovic and Fujii [23]	Cylindrical and rectangular/spherical capsule	Experimental and numerical	calcium chloride hexahydrate	Air	Charging process	$T_{inlet} = 60℃$, $T_{initial} = 15\ ℃$, Heat transfer (q)= 16 W/m^2K	Tank L=100 mm, W= 100 mm, H=20 mm.
18.	Hirata et al. [45]	Rectangular capsule	Experimental and numerical	Octadecane/ ice	-	Discharging process	$T_{init} = (T_{melting} - 2)\ ℃$, $0.0287 < Ste < 0.251$	
19.	Tan et al. [24]	Spherical capsule	Experimental and numerical	Paraffin wax *n-Octadecane*	-	Charging process	$T_{subcool} = 1℃$ $T_{surface} = 40℃$	Sphere D=101.66 mm, thickness=1.5 mm
20.	Tan and Chan [25]	spherical capsule	Experimental	n-hexadecane	Water	Discharging process	$T_{initial} = 8, 2$ and $0\ ℃$ $T_{surf} = 13, 8$ and $3\ ℃$	
21.	Tan [26]	Spherical capsule	Experimental	*n-Octadecane*	Water	Charging process	$T_{init} = 1\ ℃, 10\ ℃$ and $20\ ℃$ $T_{surfac} = 35\ ℃, 40\ ℃$ and $45\ ℃$	Sphere D=101.66 mm, thickness=1.5 mm
22.	Khodadadi and Zhang [46]	Spherical container	Numerical Modelling	Paraffin wax	-		$0.008 < Ste < 0.0533$ T_{init}: ambient	Sphere $20 < D < 100\ mm$
23.	Fomin and Saitoh [47]	Spherical capsule	Numerical Modelling	*n-octadecane*	-	Charging process	$0.1 < Ste < 0.5$	

No	Author	Geometry	Methods	PCM	HTF	Process	Parameters/range	Dimensions
24.	Koizumi [27]	Spherical capsule	Experimental	*n-Octadecane*	Air	Charging process	$T_{inlet} = 321℃$	Sphere D=55 mm, thickness=3 mm
25.	Saito et al. [48]	Cylindrical capsule	Experimental and numerical	Gelled sodium sulphate decahydrate	Water	Discharging process	$1500 < R_e < 1800$ $5 \times 10^{-4} < cooling\ rate < 1.6 \times 10^{-3}℃$, $0.00926 < Ste < 0.0926$, $26 < T_{initial} < 34℃$	Capsule: D=24.3 mm, L=1220 mm.
26.	Besley and Ramanarayanan [30]	Cylindrical storage/spherical capsule	Experimental and numerical	Paraffin wax	Air	Charging process	Re =260	Tank: D= 20.3 cm, H=30.5 cm. Sphere: D=2.1 cm.
27.	Khalil et al. [31]	Cylindrical storage/spherical capsule	Experimental	-	Water	Charging process	$2167 < R_e < 19400$	Tank: D= 42.5 mm, L=0.5 m, thickness=5.5 mm
28.	Yagi [49]	Spherical capsule	Experimental and numerical	AaCl, KNO_3	Nitrogen gas	Charging and discharging	$2.33 \times 10^{-3} < \dot{m}_f < 4.67 \times 10^{-3}\ m^3/s$, $300 < T_{HTF} < 900℃$,	Sphere: D= 40 mm.
29.	Nsofor and Akiyama [32]	Cylindrical storage and spherical capsule	Experimental	-	Gas	Charging process	$T = 400℃$ to $1000℃$ $100 < \dot{m}_f < 610\ kg/h$	Tank: D=0.61 m, L= 0.61 m. Pellet D=18.3 mm, L=18.3 mm.
30.	Benmansour et al.[50]	Cylindrical storage/ spherical capsule	Experimental and numerical	Paraffin wax	Air	Charging and discharging	$T_{inlet} = 70℃$ $560 < R_e < 1120$	Tank: D=0.2 m, thickness= 1 mm, H=0.6 m. Sphere: D=31.8 mm.

No	Author	Geometry	Methods	PCM	HTF	Process	Parameters/range	Dimensions
31.	Katayama et al. [51]	Cylindrical capsule	Experimental and numerical	Naphthalene	Water	Charging and discharging		Capsule :(D= 30 mm, L = 300 mm)
32.	Shiina and Inagaki [34]	Cylindrical capsule	Numerical Modelling	Water/O-ctadecane/ Li_2CO_3/NaCL	Air/helium/ water	Charging process	Re =300, 3000 and 7500, $T_{HTF} - T_{final} =$ 5 ℃ , $T_{init} - T_f = -5$ ℃	Capsule D= 6.6 mm, thickness= 0.3 mm
33.	Varun et al. [33]	Cylindrical storage/ Cylindrical capsule	Experimental	N/A	Air	Charging process	$700 < Re < 1300$	Tank: D=0.6 m, L=1.25 m. Cylindrical elements: D= 0.06 m , L=0.12 m
34.	Wei et al.[52]	Cylindrical storage/spherical capsule	Experimental and numerical	Paraffin wax	Water	Discharging process	$0.3 < \dot{m}_f < 1.2\ m^3/h$ $40 < T_{initial} < 105$℃	Tank: L=303 mm, W=103 mm, thickness=175 mm, Sphere: D=2-5 mm
35.	Arkar and Medved [53]	Cylindrical storage/spherical capsule	Numerical Modelling	Paraffin (RT20)	Air	Charging and discharging	For charging:$108 < \dot{m}_f < 215 m^3/h$. For dis charging: $76 < \dot{m}_f < 166 m^3/h$	Tank : (D= 340 mm, L = 1.52 m). Sphere D= 50 mm)
36.	Lacroix [54]	Parallelepedic capsule	Numerical Modelling	n-Octadecan	-	Discharging process	$0 < cooling\ rate < 5$, $0.00926 < Ste < 0.0926$	Tank: L=75 mm, $25 < W < 225$, H=30 mm
37.	Assis et al.[55]	Spherical shell	Experimental and numerical	Paraffin wax	Air	Charging process	$T_{initial}$: 23 ℃, wall temperature varies from 2 to 20 ℃ > T_m	Spheres D= 40, 60 and 80 mm

2.3 Cylindrical PCM container storage systems

Cylindrical PCM containers have been classified in three types [7]. In the first type the PCM fills the shell and the HTF flows through a single tube (Figure 2.5a), this is called a pipe model. The second type the PCM fills the tube and HTF flows parallel to the tube (Figure 2.5b); this is called the cylinder model. The third type is called a shell and tube model (Figure 2.5c). This contains several parallel tubes, and the HTF flows through the tubes while the PCM fills the space around them.

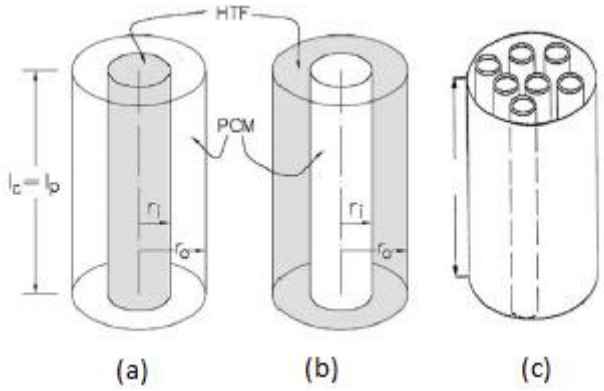

Figure 2.5: Cylindrical PCM containers [7].

2.3.1 Pipe model

Jian et al. [56] developed a numerical model to predict the transient thermal behaviour during charging and discharging processes of a latent thermal storage unit involving a triplex concentric tube with the PCM filling the middle channel. A simple numerical method, called the temperature and thermal resistance iterations, was used in the numerical calculation. The data from the numerical model was then compared with experimental results, and a good agreement was observed. Ho and Chen [57] also developed a numerical model for the

melting of ice around a horizontal isothermal cylinder. The model's results were compared with experimental data published by White in [58], and a good agreement was found. It was concluded that the melting process of ice is strongly affected by the changing recirculation occurring in the molten water. Another numerical model of melting around a horizontal pipe was developed by Rieger et al. [59]. The numerical solution was obtained for Rayleigh numbers (*Ra*) up to 1.5×10^5, Stefan numbers in the range of $0.005 \le Ste \le 0.08$, and for *Pr*=50. It was found that the natural convection is the dominant process in the heat transfer mechanism throughout almost the entire melting process.

Dimaano and Watanabe [60] studied the charging and discharging processes of a latent heat storage system with a capric and lauric acid mixture with a melting point of 18-19.5 ℃. A vertical cylindrical storage unit involving a copper tube filled with the PCM was employed in the study. The temperature distribution in both radial and axial directions was experimentally measured, as was the heat stored during the charging and released during the discharging process.

Bareiss and Beer [61] carried out an experimental and mathematical investigation of a horizontal cylindrical tube filled with PCM. A photographic technique was used to evaluate the melting and solidification fraction. They used both $C_{18}H_{38}$ *n-Octadecane* and C_9H_{10} p-xylene as PCM. The numerical and experimental results were compared and the excellent agreement between them was observed. However, the validity of the analytical model was limited to the following conditions:

$$Ste\,\rho^* \frac{Ra}{\mathrm{Pr}\,Ar} < 1.4 \tag{2.4}$$

Ismail and Abugderah [62] developed a fixed grid one-dimensional numerical model using the control volume finite difference method. The model predicts the transient behaviour of

the thermal storage system of a vertical tube type. The influence of several parameters were investigated, including Reynolds and Stefan numbers, phase change temperature range, system length, outer radius and time periods. It was noted that both Reynolds and Stefan numbers had a significant effect on the system performance whereas there was no considerable influence of the phase change temperature range. Another interesting finding was that the tube's outer radius and system length both noticeably affected the system performance.

Sari and Kaygusuz [63] experimentally evaluated the thermal behaviour of a eutectic mixture of lauric and stearic acid as a PCM in the system with two vertical concentric pipes. The key experimental parameters were the Reynolds and Stefan numbers. It was demonstrated that these two parameters had more effect on the total PCM melting time than on the total solidification time due to the convection phenomena occurring during the melting process which improved the melting rate, whilst the thermal resistance during the solidification process decreased the solidification rate. On the other hand, the Reynolds number had more effect on the heat transfer coefficient during the melting process rather than solidification, whilst the Stefan number had more effect on the solidification than melting.

The same authors then conducted a series of experimental studies [64-68] on a latent heat storage system involving a vertical double pipe. The phase change stability and the thermal characteristics of several PCMs during the solidification and melting processes were investigated. Stearic, palmitic, lauric, myristic and fatty acids were used as PCMs in the storage system, and the influence of the transition time, temperature range, the expansion of the solid-liquid interface and heat flow rate on the phase change stability were investigated. It was found that stearic, palmitic and myristic acids are all suitable for domestic solar water heating storage systems because they do not exhibit any subcooling, while lauric acid is suitable as an energy storage material for space heating and greenhouses applications.

Khillarkar et al. [69] carried out a numerical study to examine the free convection of the pure PCM during melting in tube geometries of two different configurations: a square external tube with a circular tube inside, and a circular tube with a square tube inside. The effects of heating the inside wall, the outside wall or both walls, as well as of the Raleigh number on the system performance were described. The results indicated that the rate of melting is lower at the bottom part compared to the top part due to the buoyancy force acting during the melting of the PCM. Furthermore, in both cases, the effect of heating the inside walls and outside walls was the same as heating both walls until an interaction occurred between the two zones.

2.3.2 Cylinder model

Shmueli et al. [70] performed a numerical investigation into melting PCM in vertical circular tubes. The effects of various parameters in the numerical model on the results were examined, including a detailed study of the effect of pressure-velocity coupling and pressure discretization schemes. PISO vs SIMPLE and PRESTO vs. Body-Force-Weighted schemes were examined, and no difference was found in the results using PISO and SIMPLE. On the other hand, there were considerable differences between results using the PRESTO and Body-Force-Weighted schemes. Also, the term describing the magnitude of the mushy zone in the momentum equation was analysed, and it was concluded that an optimum value of the specific constant C, should be used for this term.

Jones et al. [71] conducted an experimental and numerical study of the melting of the moderate-Prandtl-number material (n-eicosane) in a cylindrical enclosure heated from the sides. A multiblock finite volume method and enthalpy method for a range of values of the Stefan number were deployed in the numerical calculations, and numerical data was validated

against the experimental information. A good agreement was observed between both methods for the Stefan number value of up to 0.1807.

Regin et al. [72] conducted the theoretical study of the latent heat thermal storage using a horizontal cylindrical capsule filled with paraffin wax as a PCM. The effects of various parameters on the melting performance were considered. The numerical modelling was conducted using the finite difference approach and fixed approach based on the enthalpy method technique. The model was validated by comparison of theoretical results to experimental data, and an acceptable agreement was found between these two data sets.

The enthalpy-temperature relationship is presented below for the four regions during the melting processes (Figure 2.6): the solid phase, solid-solid phase change below the melting point, solid-liquid phase and liquid phase.

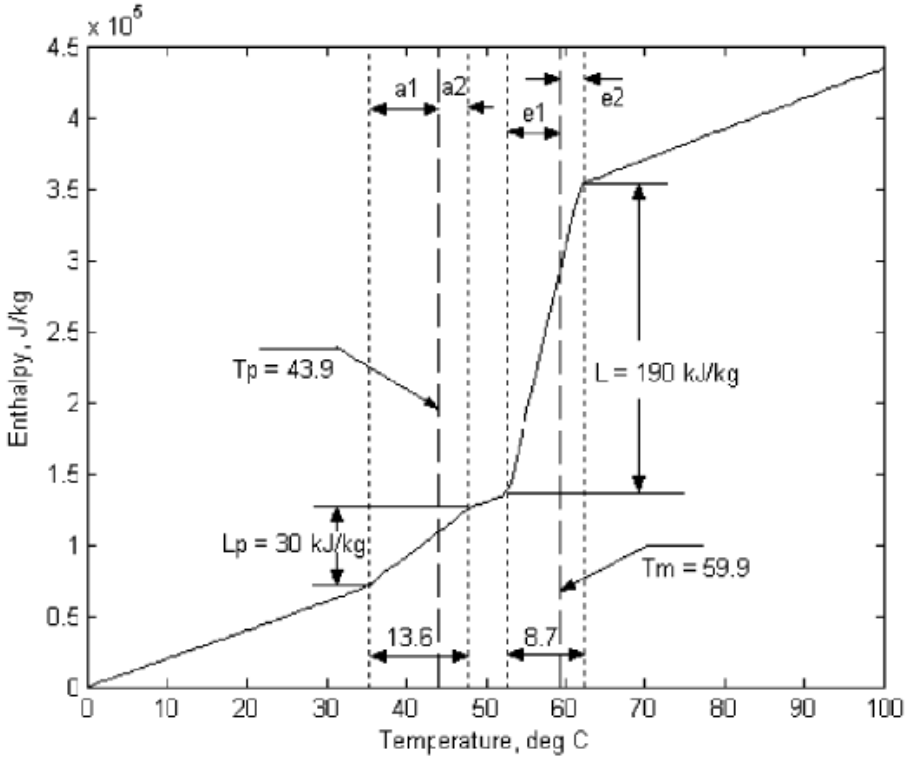

Figure 2.6: Enthalpy temperature relationship [72].

$$H = C_{ps}T + \frac{L_p}{(a1+a2)}\left(T - T_{(p-a1)}\right), \quad T_{(p-a1)} < T < T_{(p+a2)} \tag{2.5}$$

$$H = C_{ps}T + T_p, \quad T_{(p+a2)} \le T \le T_{(m-e1)} \tag{2.6}$$

$$H = C_{pl}T + L_p + \frac{L}{(e1+e2)}\left(T - T_{(m-e1)}\right), \quad T_{(m-e1)} < T < T_{(m+e2)} \tag{2.7}$$

$$H = C_{pl}T + L_p + L, \qquad T \ge T_{(m+e2)} \tag{2.8}$$

The PCM's thermal conductivity, *k*, in the interface phase was expressed as

$$k = k_s + \left(\frac{k_l - k_s}{(\Delta T)_m}\right)\left(T - \left(T_{m-e1}\right)\right), \qquad T_{(m-e1)} < T < T_{(m+e2)} \tag{2.9}$$

The stored energy in a unit volume of the PCM was expressed as:

$$E = \int_{T_o}^{T_{p-a1}} \rho_s C_{ps} dT + \int_{T_{p-a1}}^{T_{p+a2}} \rho_s C_{ps} dT + \rho_s L_p + \int_{T_{m-e1}}^{T_{m+e2}} \rho_l C_{pl} dT + \rho_l L + \int_{T_{m+e2}}^{T_f} \rho_l C_{pl} dT \tag{2.10}$$

The melting of particle-laden slurry in a cylinder was numerically and experimentally investigated by Sun et al. [73]. A particle-diffusive model and the enthalpy method were used in the numerical analysis. This study was later validated with results by Jones et al. [71]. It was found that the melting behaviour of the slurry with a lower particle loading ($\phi = 5\%$) was similar to the melting of pure wax. Indeed, a strong influence of the convection was observed in both cases. On the other hand, the natural convection was reduced as the particle loading increased and the melting process was then dominated by the conduction. Nevertheless, one major drawback of the diffusive flux model is that the model is not sufficiently adequate to describe the melting of slurries with various particle loadings.

The melting of the PCM in the latent heat thermal energy storage having a hollow cylinder form was studied semi-analytically by Zhang and Faghri [74] using the integral approximation method. The results were then validated using findings by the same authors in [75]. The structure of the thermal storage system in both above studies was similar but initially without external radial fins. It was demonstrated that the laminar forced convection heat transfer never reached the fully developed state, even with application of a very long tube.

Cabeza et al. [76] experimentally examined the PCM behaviour in cylinders at the top of the water tank. Several configurations with two, four and six PCM modules were investigated, see Figure 2.7. Commercial aluminium bottles filled with PCM were used as PCM modules. Several PCMs were investigated: paraffin, sodium acetate trihydrate and fatty acids. It was found that this technique provides long periods of the storage time as well as increasing the energy capacity and density.

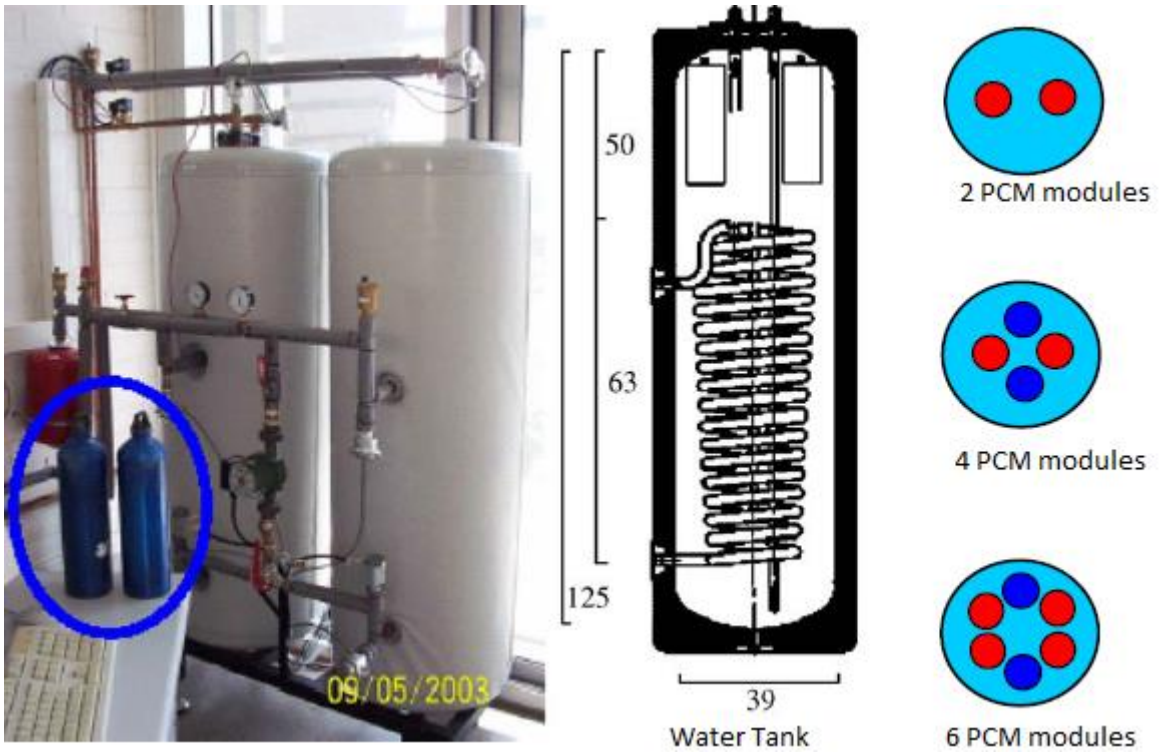

Figure 2.7: Water tank with PCM modules of different configurations [76].

Wu and Lacroix [77] analysed numerically the natural convection in the melting PCM in a vertical cylindrical capsule heated from below. The model was created using the finite-difference method. They compared their numerical predictions with the numerical and experimental results in [78-80], and reported that the heat transfer rate at the top surface was dominated by the conduction, but this decreased to zero as melting progressed and the natural convection developed fully. On the other hand, they also observed that the most intensive heat transfer was taking place at the bottom surface of the capsule.

Rieger and Beer [81] examined the effect of the natural convection flow on the heat transfer during the melting process of ice inside an isothermal horizontal cylinder. They predicted numerically the overall and local heat transfer coefficients, temperature fields, interface positions and flow pattern. They compared their numerical results with experimental data, and reported that the heat transfer was enhanced at the lower part of the ice body at wall temperatures less than 8℃ because of the density effect, whilst for the wall temperature exceeding 8^{o}C the ice body moved downwards. The same procedures have been applied by Rieger et al. [82] to investigate the heat transfer during melting *n-Octadecane* as a PCM inside a horizontal tube.

Tay et al. [83] carried out an experimental investigation of a tube-in-tank thermal storage unit during the freezing and melting process of salt hydrate as a PCM. The HTF circulated inside the tube and the PCM was contained in the cylindrical tank. Three different experiments with different configurations were carried out. The first was conducted in a tube which was 5.46m in length in a cylindrical tank (Figure 2.8a), whilst the second configuration used two tubes with lengths of 5.61 and 6.01m, respectively (Figure 2.8b). The third experiment was conducted on four tubes with lengths of 5.95, 6.05, 5.79 and 6.04 m (Figure 2.8c).

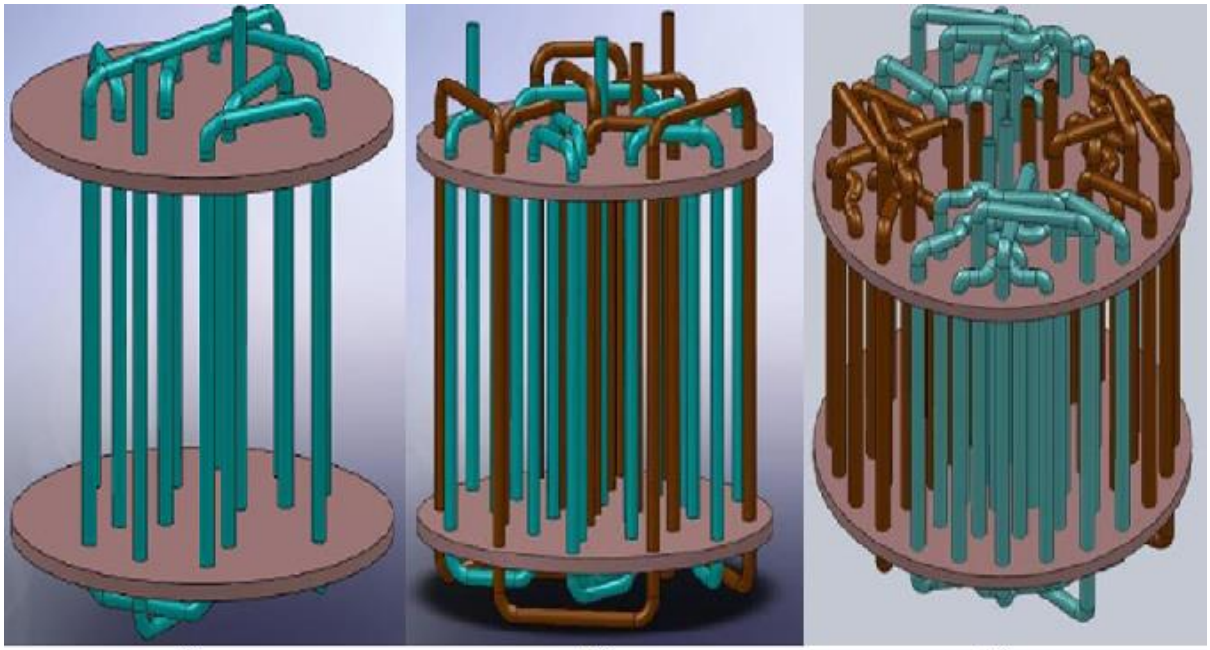

Figure 2.8: Schematic of the tube tank with different configurations [83].

Temperature distributions, average effectiveness and solidification and melting times were analysed. The experimental measurements were compared to numerical results by Tay et al. [84] with a good agreement demonstrated between the two sets of data. The numerical model was developed using ANSYS code, and a three-dimensional CFD model was created in order to analyse transient heat transfer during the melting and solidification process. It can be concluded from the results that the CFD model can accurately predict the performance of the thermal storage system, and it also can be used to optimize its design.

Saitoh and Hirose [85] numerically investigated the natural convection heat transfer inside a horizontal circulator cylinder capsule packed with a PCM during the melting and solidification process for high Rayleigh numbers. The model predicted the formation of the transient solid-liquid interface, solid-liquid temperature, streamlines, isotherms, and heat stored. The numerical results were validated through comparison with those of Pannu et al.

[86], and, in general, considerable quantitative and qualitative differences were found. It is interesting to note that the natural convection controlled the melting heat transfer inside the capsule, and also that thermal instability occurred at the bottom portion of the capsule.

Sparrow and Broadbent [87] experimentally examined the melting process in a phase change medium contained in a vertical tube. The experimental results were compared with a numerical solution and good agreement was observed. It was demonstrated that the rates of melting and heat transfer are significantly affected by the natural convection inducing the fluid flow in the liquid molten zone. The experimental measurements of the energy transferred and stored in the liquid molten zone were higher than those predicted by the numerical model.

2.3.3 Shell and tube model

Fukai et al. [88-90] carried out an experimental and numerical investigation of the effect of a carbon-fibre brush on the thermal conductivity in a thermal energy storage system. Several techniques for the thermal conductivity enhancement using carbon-fibre brushes were investigated. These include: randomly oriented carbon fibres packed in a cylindrical capsule (Figure 2.9a); a carbon fibre brush packed in a cylindrical capsule (Figure 2.9b) [88], carbon fibre brush/PCM composite inserted around tubes (Figure 2.9c) [89]; and carbon fibre on the shell side [90]. The findings of such studies indicated that the type of the brush had a significant effect on the thermal conductivity enhancement. The randomly oriented fibres had little effect on the magnitude of the thermal conductivity. In addition, the transient thermal response in the brush/PCM composite is improved as the diameter of the brush increased. However, the response did not improve when the diameter of the brush was greater than the distance between the tubes, due to the increased thermal resistance near the tube wall. The

heat exchange rate during both charging and discharging processes was significantly improved when brushes inserted around the tube were used.

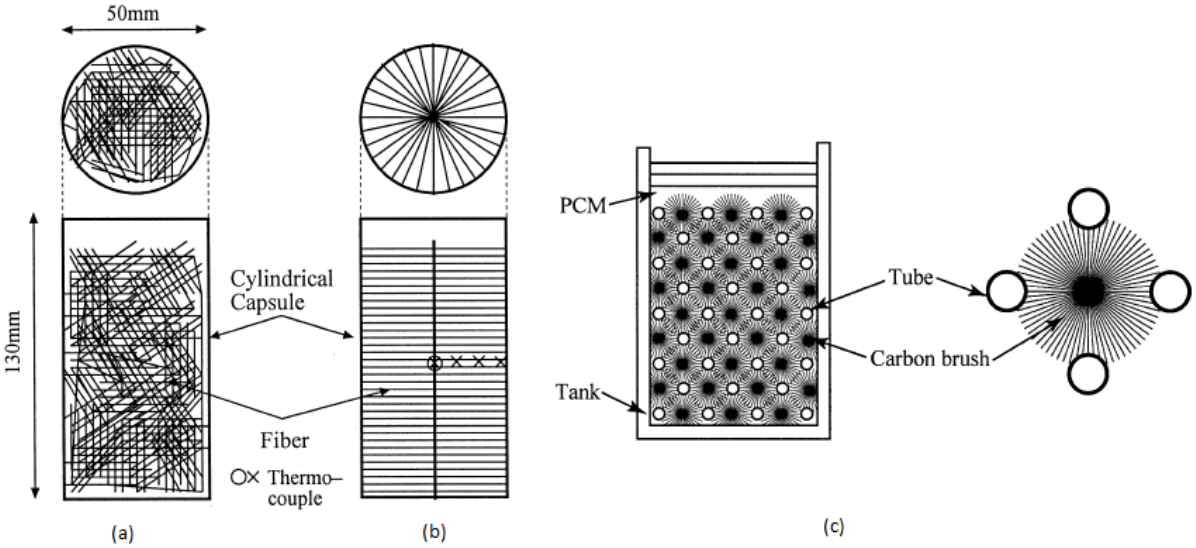

Figure 2.9: Configurations of the carbon fibres [88-90].

Hamada et al. [91] also experimentally and numerically studied two heat transfer enhancement mechanisms using carbon-fibre chips and carbon brushes packed into a shell-and-tube thermal storage system. For the experimental investigations, four steel tubes were vertically placed in a cylindrical container made of acrylic resin and insulated using glass wool. Carbon-fibre chips with a diameter of 10μm and length of 5mm were packed in the container. The PCM *n-Octadecane*, with a thermal conductivity of 0.34 W/m K, was used to fill the container. Figure 2.10 illustrates the experimental apparatus.

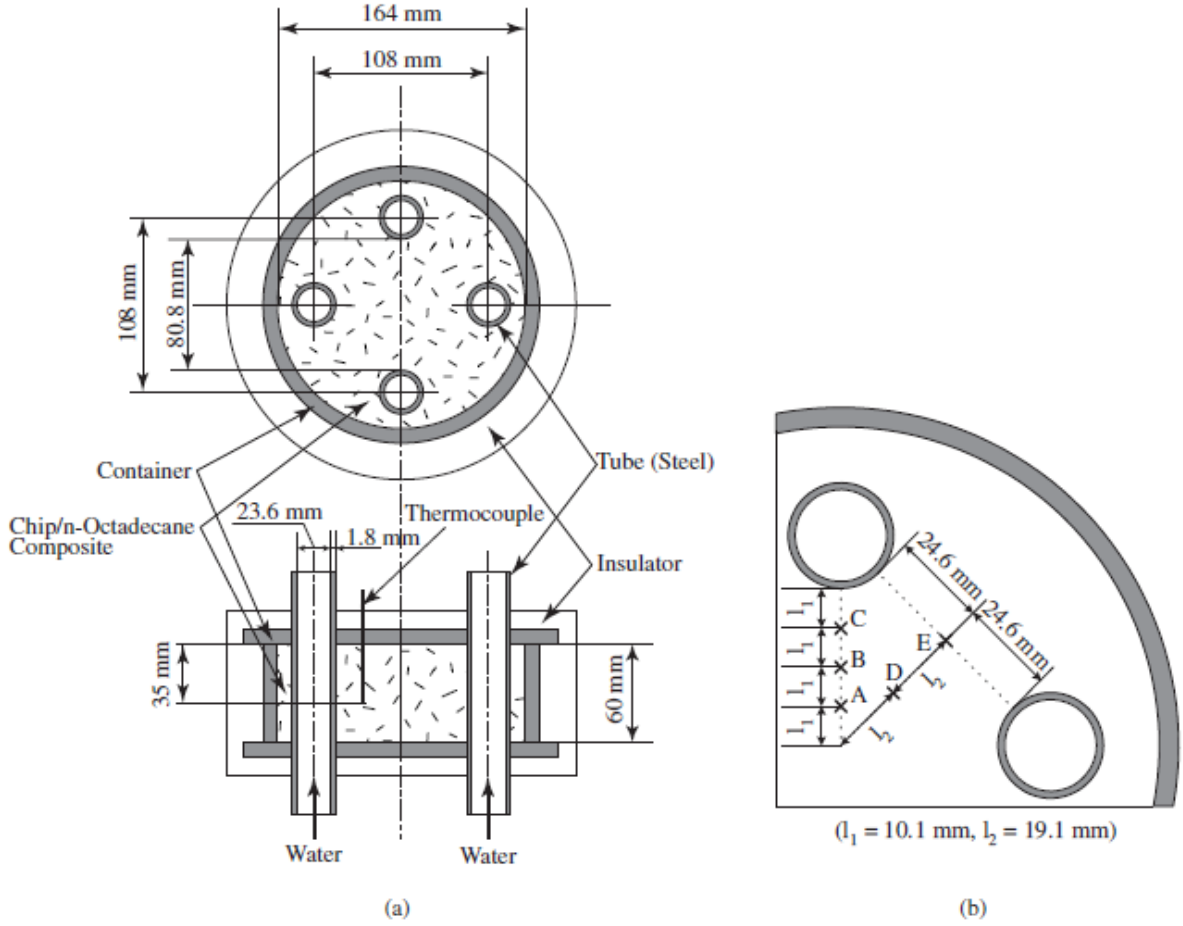

Figure 2.10: Experimental apparatus [91].

Three types of the fibre were used, namely those with low, medium, and high levels of the thermal conductivity (k_f = 5, 190 and 500 W/m K, respectively). The control volume method was used in the numerical model, and the computational domain is illustrated in Figure 2.11. The mathematical and experimental data were then compared, and it was found that the carbon-fibre chips significantly improved the heat transfer rate in the PCMs. However, taking into account the effect of the thermal resistance near the heat transfer surface, the overall heat transfer for the carbon brushes was higher than that for the carbon-fibre chips.

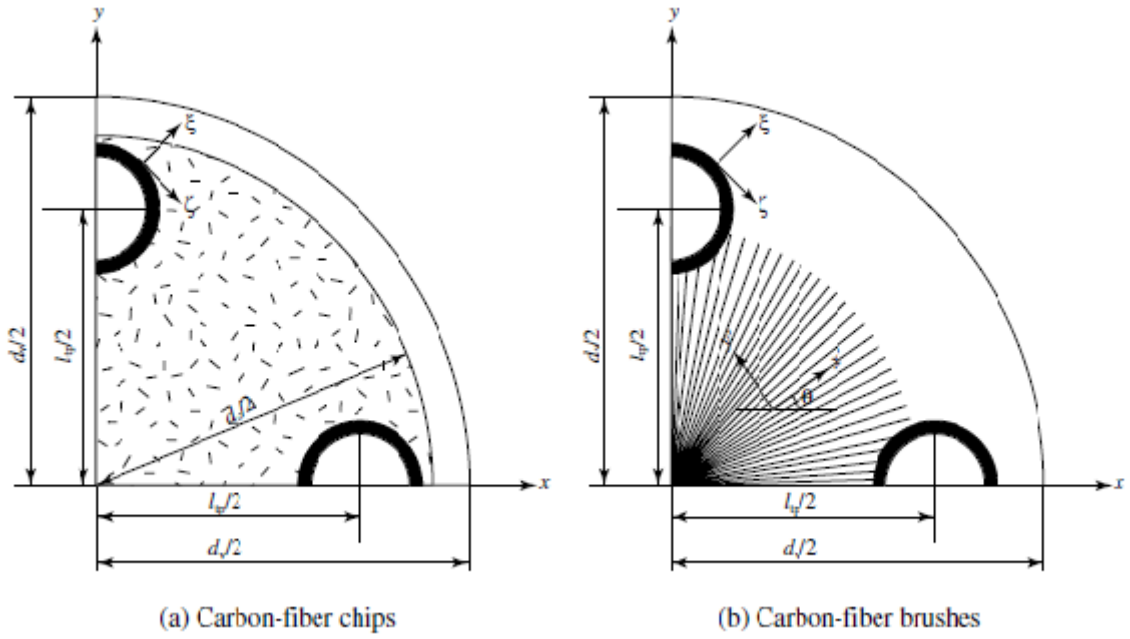

Figure 2.11: Computational domain [91].

Trp studied the transient heat transfer in the shell-and-tube thermal storage system in an experimental and numerical study [92, 93]. He developed a mathematical model based on the non-isothermal phase transition, and it was implemented as a FORTRAN computer code. The numerical results were validated with experimented data, and it was concluded that heat transfer from the HTF to the PCM was low due to the large Prandtl numbers of the HTF. Therefore, a large amount of heat was carried downstream with the HTF, whilst a small amount of heat was transferred to the PCM upstream. The same author [94] numerically investigated the effects of several geometrical parameters and different HTF operational conditions on heat transfer during both melting and solidification processes by measuring the transient temperature distribution of the HTF, PCM and tube wall.

Lacroix [9] developed a numerical model using an enthalpy-based method. The model predicted the transient behaviour of a shell-and-tube storage unit with circulating HTF inside the pipe with PCM on the shell side. The model was validated by comparison with

experimental data and the effects of several thermal and geometric parameters on heat transfer were investigated. It was found that the shell radius, mass flow rate and inlet temperature must be selected carefully in order to optimize the storage unit performance.

Morcos [95] experimentally analysed both the charging and discharging processes in the thermal energy storage involving a shell-and-tube unit. Two types of the PCM were investigated, namely paraffin wax and asphalt. Experimental measurements of the temperature distribution, heat stored during charging and the heat released during discharging were compared for these different storage substances. Ezan et al. [96] experimentally investigated the effect of natural convection and several design/flow parameters on charging and discharging processes for ice in a shell-and-tube design. It was found that the natural convection dominated the heat transfer mechanism after a short period in which the conduction was main mode of the heat transfer. Furthermore, the flow rate, inlet temperature, shell diameter, and thermal conductivity of the tube material had considerable effects on charging and discharging processes.

Akgün et al. [97, 98] carried out an experimental investigation on charging and discharging processes of paraffin as a PCM. They used a novel tube-and-shell configuration which was oriented vertically. The key experimental parameters investigated were the HTF inlet temperature and Reynolds number. It was concluded that increasing the inlet temperature results in a decrease in the total melting time, whilst the Reynolds number had no significant influence. The PCM started to melt in the lower region close to the inner wall, and the molten PCM ascended radially outwards to form a conical shape of the molten region as a result of the natural convection currents. A large number of studies considered the enhancement of heat transfer using fin configurations. A summary of some of these studies are presented in Table 2.2.

Table 2.2: Results of studies on the shell and tube thermal storage systems with PCMs.

No	Author	Geometry	Methods	PCM	HTF	Process	Parameters/range	Dimensions
1.	Jian [56]	Pipe model	Experimental and numerical	n-Hexacosane	Water	Charging and discharging	Charging process: $T_{HTF} = 58℃$	$300 < L < 3100\ mm$ $15 < Di < 90\ mm$ $17 < Do < 94\ mm$
2.	Ho and Chen[57]	Pipe model	Numerical	Ice	-	Charging process	$T_i = 4, 6, 8, 9, 10℃$	Cylinder: D_i=25.4 mm
3.	Rieger et al. [59]	Pipe model	Numerical	Ice	-	Charging process	$Ra = 1.5 \times 10^5$, $0.005 \leq Ste \leq 0.08$, Pr=50	-
4.	Dimaano and Watanabe [60]	Pipe model	Experimental	capric and lauric acid	Water	Charging and discharging	Charging: $\dot{m} = 1.67 \times 10^{-5}\ m^3/s$ $30 < Ti < 39.8℃$ Discharging: $\dot{m} = 2.51 \times 10^{-5} m^3/s$, $Ti = 2.1℃$	Tube: D=30 mm, thickness= 0.1 mm, L=420 mm) Cylinder: (D=56 mm, thickness=10 mm, L=345 mm)
5.	Bareiss and Beer [61]	Pipe model	Experimental and numerical	*n-Octadecane* and p-xylene		Charging and discharging		Tube: (D=60 mm, thickness= 1 mm, L=40 mm)
6.	Sarı and Kaygusuz [63-68]	Pipe model	Experimental	Stearic, palmitic, lauric, myristi and fatty acids	Water	Charging and discharging	Investigate the effect of flow operation conditions	Tube: : (D=50 mm, L=350 mm) Cylinder: (D=120 mm, L=200 mm)
7.	Khillarkar et al. [69]	Pipe model	Numerical	octadecane		Charging process	$0.0432 < F_o < 0.432$, $2.844 \times 10^6 < Ra < 2.844 \times 10^7$	-
8.	Lu et al.[99]	Pipe model	Numerical	Molten salt	-	Charging and discharging	T_s=300K, Inlet velocity=1 m/s, T_o=453K	Pipe (D_i=0.008 m, D_o=0.01 m, L=2 m)
9.	Ismail and Abugderah [62]	Vertical tube type	Numerical			Charging and discharging	$100 < Re < 2200$, $0.1 < Ste < 0.6$, $0.75 < Do < 2.5$	-

No	Author	Geometry	Methods	PCM	HTF	Process	Parameters/range	Dimensions
10.	Shmueli et al [70]	Cylinder model	Experimental and numerical	Rubitherm GmbH	-	Charging process	-	Cylinder: (D=30 and 40 mm)
11.	Jones et al [71]	Cylinder model	Experimental and numerical	n-Eicosane	Water	Charging process	$T_{wall} = 45, 55$ and 70℃,$T_s =$ 32℃,$Re = 5.45 \times 10^6, 1.31 \times 10^7$ and 2.72×10^7,$Ste =$ 0.1807, 0.3265 and 0.0836	Cylinder: (D=31.9 mm, thickness=5.97 mm, L=59.8 mm)
12.	Regin et al. [72]	Cylinder model	Experimental and numerical	Paraffin wax	Water	Charging process	$0.04 < Ste < 0.24$ $T_{HTF} = 75$ ℃	Cylinder: D_i=76 mm, thickness=2 mm, L=100 mm)
13.	Sun et al. [73]	Cylinder model	Experimental and numerical	n-Eicosane	Water	Charging process	$T_{HTF} = 70$ ℃ Ti = 35.5 ℃	Cylinder: D_i=63.8 mm, D_o=69.5 mm, L=59.8 mm
14.	Zhang and Faghri [74]	Cylinder model	Numerical modelling	*n-Octadecane*	Water	Charging process	$0.25 < Fo < 4$	
15.	Cabeza et al [76]	Cylinder model	Experimental	Paraffin, sodium acetate trihydrate and fatty acids	Water	Charging process		Cylinder module : (D= 8.8 cm, H=31.5 cm) Tank : (D= 39 cm, H=125 cm)
16.	Wu and Lacroix [77]	Cylinder model	Numerical modelling	-	-	Charging process	Ste = 0.1 Ra = 10^5 and 10^6	-
17.	Rieger [81, 82]	Cylinder model	Experimental and numerical	Ice/ *n-Octadecane*	-	Charging process	$10^5 < Ra < 10^6$	Cylinder tube: D_i=32 mm, thickness=1 mm, L=40 mm
18.	Tay et al. [83, 84]	Cylinder model	Experimental and numerical	Salt hydrate	Nano-fluid	Charging and discharging	$\dot{m} = 0.013, 0.019, 0.024$ and 0.026 kg/s	Cylinder tank: D= 290 mm, H=330 mm
19.	Saitoh and Hirose [85]	Cylinder model	Numerical modelling	Paraffin, Ice/ *n-Octadecane*	-	Charging and discharging	P_r = 54.6, R_a = 15800, 426400, 3411000, and 2914000 ΔT =7K and 13K	Cylinder capsule: D= 0.01, 0.02, 0.03, 0.0448 and 0.06 m

No	Author	Geometry	Methods	PCM	HTF	Process	Parameters/range	Dimensions
20.	Sparrow and Broadbent [87]	Cylinder model	Experimental and numerical	Paraffin		Charging process	Ste= 0.0387, 0.0971, and 0.248	Cylinder: D_i=5.08 cm, thickness=0.152 cm, L=39.4 cm
21.	Hasan [100]	Cylinder model	Experimental	Palmitic acid	Water	Charging and discharging	$Ti = 40$ ℃, $\dot{m} = 0, 1, 2, 3.2,$ and 5.1 kg/min, $T_{HTF} = 40.65.71.$ and 75 ℃	Cylinder tube: D_i=40 mm, thickness=1.5 mm, L=550 mm
22.	Yang and Tao [101]	Cylinder model	Numerical modelling	-	-	Charging process	$R_a = 10^3$-10^6	Slot width=0-0.5, r_0/r_i=2.6
23.	Fukai et al [88-90]	Shell-and-tube	Experimental and numerical	Paraffin wax	Water	Charging and discharging	Charging: $55 < T_{HTF} < 60$ ℃ Discharging: $-35 < T_{HTF} < -38$ ℃ HTF velocity= 0.015, 0.03 and 0.08m/s	Cylindrical: D=50 mm, H=130 mm. Brush: D=10 μm, L= 5 and 200 mm. Tube D_i= 8 mm, D_o=9.5 mm
24.	Hamada et al. [91]	Shell-and-tube	Experimental and numerical	*n-Octadecane*	Water	Charging process	$Ti = 18$℃ HTF velocity= 0.35 m/s $T_{HTF} = 23$ ℃	Tube: D_i=23.6 mm, D_o=25.4 mm.Shell: D=164 mm, L=60 mm
25.	Trp [92-94]	Shell-and-tube	Experimental and numerical	RUBITHERM RT30	Water	Charging process	$\dot{m} = 0.017$ kg/s $13 < T_{inlet} < 45$ ℃	Inside tube: (D_i=0.033m, D_o=0.035m, L=1m) Outside tube: : (D_i=0.128m, D_o=0.133m, L=1m)
26.	Lacroix [9]	Shell-and-tube	Experimental and numerical	*n-Octadecane*	Water	Charging process	$0.03 < \dot{m} < 0.07\ kg/s$ $32 < T_{inlet} < 47$℃ $Ti = 9.5$℃	Inside tube: D_i=0.0127m, D_o=0.0158m, L=1m Outside tube: D_i=0.0258m, L=1m
27.	Morcos [95]	Shell-and-tube	Experimental	Paraffin wax and Asphalt	Water	Charging and discharging	$10 < \dot{m} < 55\ kg/h$ $62 < T_{inlet} < 95$℃ $Ti = 25$℃	Inside tube: D_i=026.64mm, D_o=33.4mm, L=1m) Outside tube: D_i=52.5mm,D_o=60.33 mm, L=1m)

No	Author	Geometry	Methods	PCM	HTF	Process	Parameters/range	Dimensions
28.	Ezan et al. [96]	Shell-and-tube	Experimental	Ice	Water, Ethylene, and Glycol	Charging process	Tube material: s. steel and copper. $\dot{m} = 2{,}4$ and 8 l/min Ti $= -5, -7.5, -10,$ and -15℃	D_i=15mm, D_o=25mm, L=0.4m
29.	Akgün [97, 98]	Shell-and-tube	Experimental	Paraffin P24-44 Paraffin P46-48 Paraffin P56-58	Water	Charging and discharging	Charging process: T_{HTF}= 60, 65, 70 and 75 ℃ $\dot{m} = 2, 6$ and 8 kg/s Charging process: T_{HTF}= 20 ℃ $\dot{m} = 2, 6$ and 8 kg/s	Tube diameter = 28mm Cylindrical Storage (D =94.67mm, L=465mm) Storage geometry with a shell angle: (upper D = 133.4mm, lower D=56mm)
30.	Hendra et al[102]	Shell-and-tube	Experimental and numerical	Mikro	Water	Charging and discharging	Ti=300K	Tube diameter: 0.015m Container diameter: 0.2625m
31.	Ismail and Gonçalves [103]	Shell-and-tube	Numerical modelling	n-Eicosane	Water	Discharging process	$0 < Bi < 50$, $1 <$ R* < 6 $10 <$ T_{inlet} < 35℃	
32.	Castell et al [104]	Shell-and-tube	Experimental	Hydrate salt	-	Charging process		Pipe: (Di= 0.008m, L=5.46m) Tank: (Di=0.29m, H=0.35m)

2.4 Methods used for the heat transfer intensification

The low values of the thermal conductivity in PCMs resulted in a big number of studies on the enhancement of heat transfer during solidification and melting of PCMs. various techniques were tested to enhance the heat transfer performance and melting and solidification processes in PCM latent heat thermal storage systems. This section presents a review of these methods and provides information on their advantages and disadvantages.

2.4.1 Intensification using fins

Fins or extended surfaces can be used to provide an additional heat transfer surface in the thermal system and thus to increase the heat transfer rate. A range of fin geometries were extensively studied by a number of researchers. Liu et al. [105] experimentally studied the enhancement of the PCM thermal conductivity by using copper fins with a spirally twisted configuration. The experimental results showed that the fin design had a profound effect on both the conductive and natural convective heat transfer. It was also observed that finer fins are more effective than large fins in enhancing the melting process if an equal amount of fin material is used. It was concluded that changing the fin width could lead to a more significant enhancement of the PCM's thermal conductivity.

Stitih [106] investigated the heat transfer enhancement in a thermal storage unit with a finned surface during both solidification and melting processes. The storage unit was made as a rectangular box with an inlet and outlet, while water was used as the HTF. The other part of the system was a heat exchanger with 32 rectangular fins. The exchanger was filled with RUBITHERM RT paraffin as a PCM. The heat transfer and natural convection phenomena

were investigated and compared with those of the storage unit without fins. Experimental correlations were presented for the fin effectiveness as a function of Stefan (*Ste*) and Fourier numbers (*Fo*) and the Nusselt number (*Nu*) as a function of Rayleigh number (*Ra*):

$$\eta_f = 1\times10^7 * (Ste.Fo)^2 - 1719.4 * (Ste.Fo) + 0.7813 \tag{2.11}$$

$$Nu = 8\times10^{-12} Ra^{1.0392} \tag{2.12}$$

It was found that, for the low Fourier number, the fin effectiveness was less than 1. The reason for this was that the natural convection, which was dominant in the process of melting, was suppressed due to the presence of the fins. In the solidification process the fin effectiveness varied from 0.4 to 3.06 depending on the Stefan and Fourier numbers.

An experimental study with numerical modelling of the solidification process of the PCM inside a cylindrical vertical tube and using internal longitudinal fins was performed by Velraj et al. [107]. The experimental results showed that the surface heat flux increased significantly with an increase in the number of fins. The effect of the radius of the tube on the surface heat flux was also investigated. It was found that for tube of small radius the surface heat flux initially increased but after a certain period of time this heat flux became lower than for the corresponding case with tube of large radius. The reason for this is that in the smaller tube the thickness of the solidification layer is greater. Therefore the conductive resistance of the solidification layer becomes higher than in the case in which the tube radius is smaller. The solidification process for cases with and without fins was also compared. It was found that the complete solidification time for the tube with fins was approximately 1/n-th (n is a number of fins) of the case of the tube without fins. A numerical model was developed to investigate the effect on heat transfer of different tube wall and fin thicknesses. The calculations were conducted for a tube with a radius of 0.03 m, and it was demonstrated that

there was no reduction in the heat transfer until the tube wall and fin thicknesses were reduced to 0.0015m.

The same authors [108] studied different heat enhancement techniques for thermal storage units, shown in Figure 2.12, namely internal longitudinal fins inside a plain cylindrical storage tube filled with paraffin; the same tube filled with Lessing rings of 1cm in the diameter with a small amount of water in the tube, which was then evacuated using a vacuum pump after adding the molten paraffin. The vacuum was maintained such that the saturation temperature of the water inside the tube was nearly equal to the melting temperature of paraffin. It was found that the total solidification time was significantly reduced to the one-quarter value by using fin configurations compared with the plain tube and to one-ninth when Lessing rings were used.

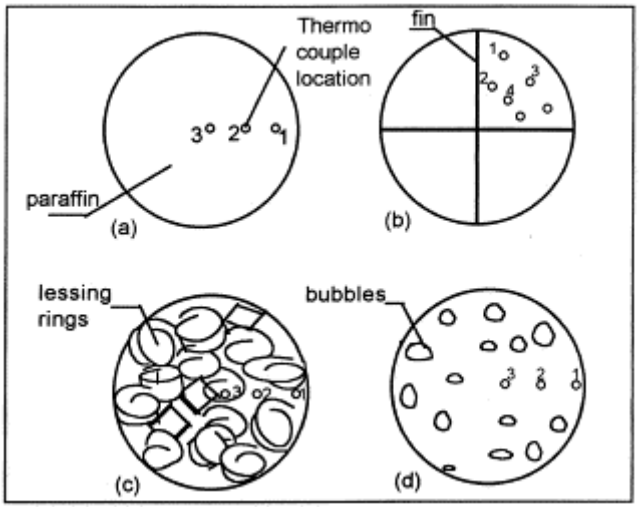

Figure 2.12: The cross section of tube storage units with different configurations: (a) plain tube (b) with internal longitudinal fins (c) Lessing rings (d) bubbles [108].

Kayansayan and Acar [109] conducted a numerical and experimental study of the solidification of ice in a cold thermal storage system with a horizontal finned tube. The effects of the HTF inlet temperature, flow rate, fin density, and fin size were investigated.

The numerical model was validated with comparison to experimental data and the numerical model was also tested against the results of Lacroix in [110], who developed his own mathematical model for the melting process with the same geometrical and flow parameters. Kayansayan and Acar used water as HTF and *n-Octadecane* (n-$C_{18}H_{38}$) as the PCM, while the later study used ethyl-alcohol as the HTF and ice as PCM. The comparison was carried out for a tube with 12 fins and the working fluid having the same Peclet numbers of 75.4, 754, and 7540 respectively. Figure 2.13 shows the effect of the flow rate on the molten fraction and HTF exit temperature. In general, a good agreement was observed, and the results demonstrated that increases in the flow rate, HTF inlet temperature and the number of fins led to an increase in the heat transfer rate and the amount of energy stored in the system.

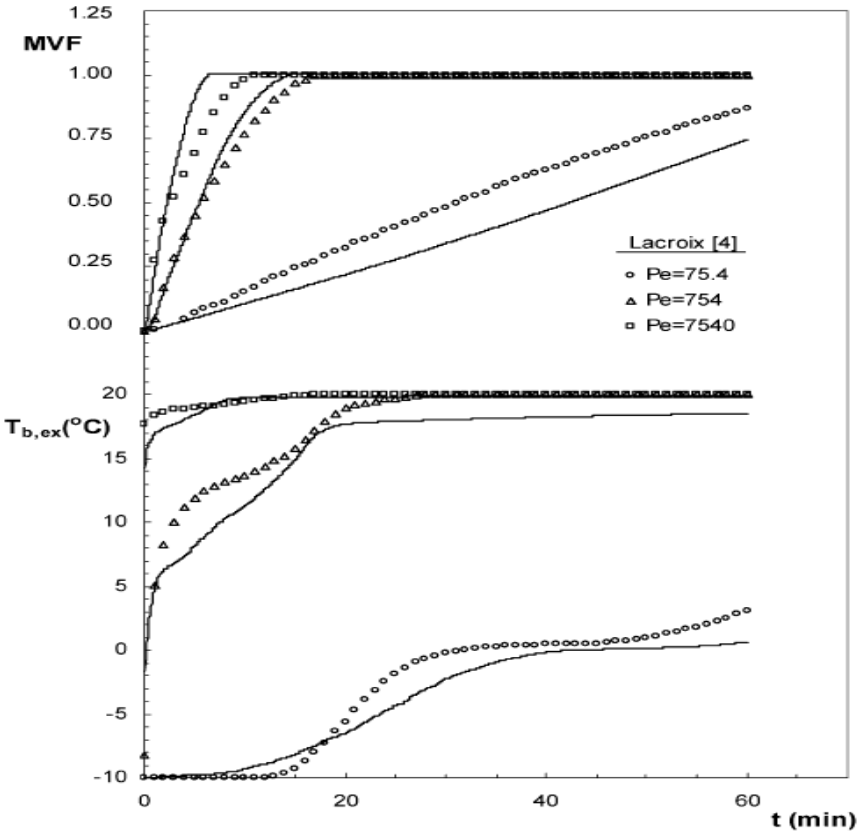

Figure 2.13: The comparison of numerical results on the effect on the HTF exit temperature and molten fraction in [109] and [110].

Ismael et al. [111] presented a numerical model of the solidification process around a vertically axially finned tube immersed in a PCM. The model results were compared with experimental data. The study was designed to determine the effect of the fin length, thickness and number, the aspect ratio of the annular space, and the temperature difference between phase change temperature and the wall temperature of the tube. The numerical results were supported by the findings in the experimental work, and these indicated that, as the fin length increases, the complete solidification and the solidified mass fraction are reduced significantly. An increase in fin thickness as well as the number of fins resulted in an increase in the solidified mass fraction and a reduction in the solidification time. The results also demonstrated that an increase in the aspect ratio of the annular space resulted in the increase in both solidification time and the solidified mass fraction, whilst an increase in the temperature difference resulted in the reduction in the solidification time and solidified mass fraction.

Zhang and Faghri [75, 112] developed theoretical methods to study the heat transfer enhancement in the latent heat thermal energy storage unit using tubes with internal longitudinal fins (Figure 2.14a) and external radial finned tubes (Figure 2.14b). The most interesting finding was that the use of internal fins provides stronger effect of enhancing melting heat transfer for transfer fluids at low Reynolds numbers. Another important finding for the externally finned case was that tube wall temperature and Nusselt number were increased significantly when the thickness of the wall increased, but the latter had no significant effect on the molten liquid volume. On the other hand, the fin height had a significant impact on the molten volume fraction (MVF).

Castell et al. [113] experimentally investigated the natural convection phenomena for a cylindrical model of the system with external vertical fins. The model consisted of a PCM

placed in the middle upper part of a cylindrical water tank. Experimental correlations between Nusselt number and Rayleigh number were proposed.

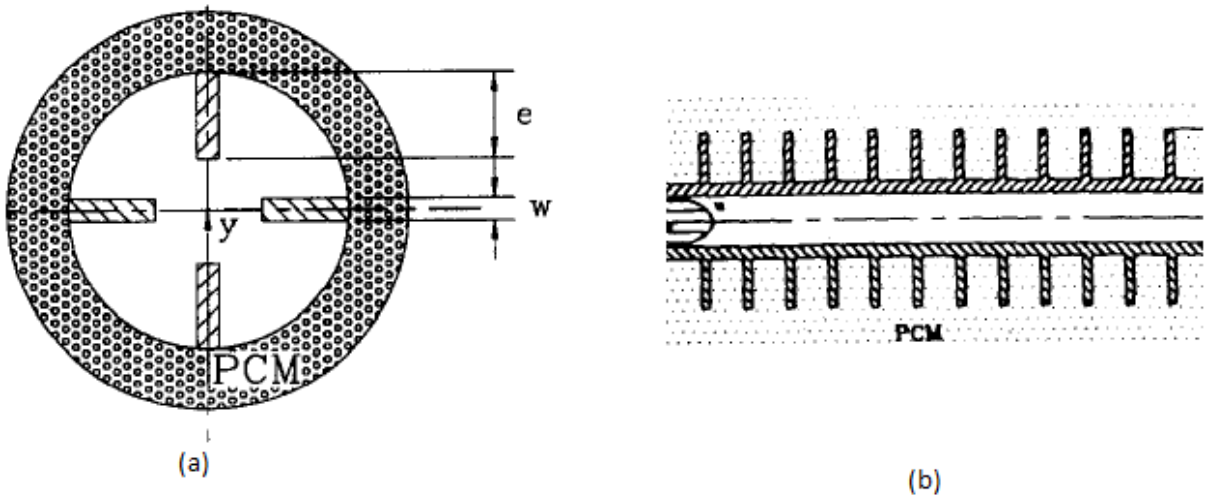

Figure 2.14: Schematic of internally and externally finned tubes deployed in [75] and [112] .

Agyenim et al. [114] studied different aspects of the enhancement of the heat transfer in a medium temperature thermal storage system using both circular and longitudinal fins. It was reported that longitudinal fins achieved a sufficient enhancement of the heat transfer, and that the average temperature was higher than in the control and circular finned systems. The circular fins did not provide a noticeable improvement of heat transfer during sensible heat absorption even though they increased the heat transfer area.

Shatikian et al. [115, 116] conducted a numerical study of the melting of the PCM in a heat storage system with internal fins and a horizontal base. He reported that the melting process and heat flux were affected by changes in the geometry of the system and the boundary conditions. It was found that the Nusselt number and melting fraction depended on a

combination of dimensionless numbers, such as the Fourier (*Fo*), Stefan (*Ste*) and Rayleigh (*Ra*) numbers:

$$Nu = 5 + \frac{4}{\left(Fo * Ste * Ra_{lf}^{-1/4} Ra_{lb}^{1/6}\right) + 0.015} \tag{2.13}$$

Sparrow et al. [117] experimentally examined the enhancement of the conduction and convection heat transfer during the solidification process in a thermal storage unit with a vertical tube with external fins. It was found that the conduction enhancement for fins is less than the area ratio of the finned and unfinned tubes, whilst the enhancement in the natural convection was very nearly equal to the area ratio. On the other hand, the degradation in the heat transfer due to the natural convection increased with time and this degradation was greater for lower values of the temperature difference across the frozen PCM layer.

Using an artificial neural network (ANN), Ermis et al. [118] analysed the heat transfer in a latent heat thermal storage system with a finned tube. ANN modelling was used to predict the amount of heat transfer through the PCM around the finned tube. The four network input parameters considered (Figure 2.15) were the heat transfer area, Reynolds number, HTF inlet temperature and time, whereas the output parameter was the total thermal energy stored. The hidden node was modified to minimize the errors in the output values, and the ANN was validated by comparison with experimental data. Very good agreement was achieved for both laminar and turbulent flows.

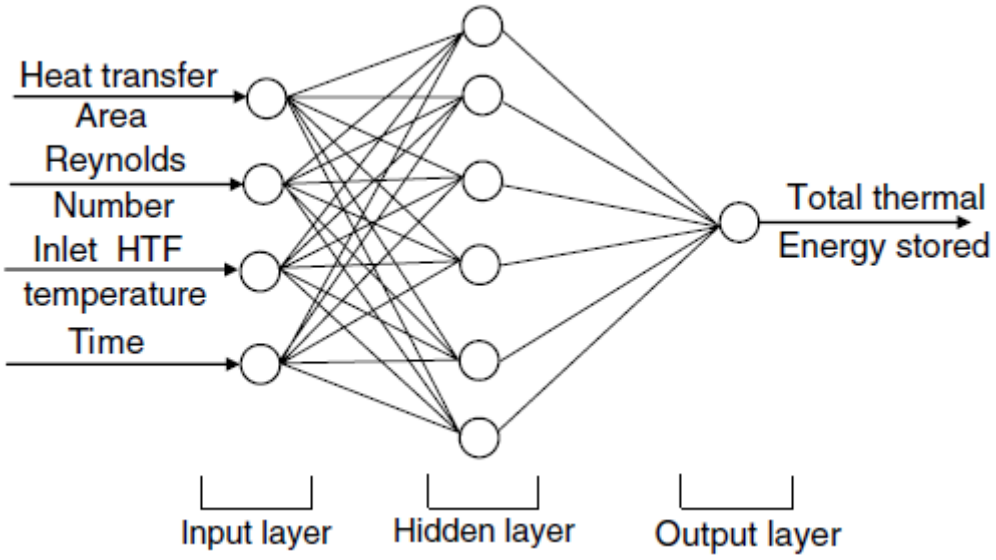

Figure 2.15: A three layer feed-forward back propagation neural network for heat transfer analysis [118].

Eftekhar et al. [119] experimentally studied the enhancement in the heat transfer in a thermal storage system with a heated and cooled horizontal finned-tube. The heat transfer and natural convection effect at the liquid-solid interface were investigated, and correlations were obtained from the experimental data for the Nusselt number and the volumetric rate of liquid produced. These correlations were validated with results in [120] and agreement between the two sets of data was found to be satisfactory. These correlations are presented below:

$$\overline{Nu} = 0.0270\, f_s^{-1} \left(Ra / Ste \right)^{1/3} \tag{2.14}$$

where

$$\overline{Nu} = f_c^{2/3} \left(\frac{\overline{h}_e L_c}{k} \right) \tag{2.15}$$

$$f_s = \frac{S}{\left(S_f + S_p \right)} \tag{2.16}$$

$$f_c = \frac{\left(\overline{T_w} - \overline{T_u}\right)}{\left(\overline{T_w} - T_m\right)} \tag{2.17}$$

The following heat transfer correlation equation was derived by Bathelt and Viskanta in [120]:

$$\overline{Nu} = 0.0178\left(Ra / Ste\right)^{1/3} \tag{2.18}$$

The volumetric rate of liquid produced can be described as

$$\frac{dV}{dt} = 0.0270\, f_c^{-2/3}\left(\frac{Ra}{L_c^3 Ste}\right)^{1/3}\left(\frac{k}{\rho L}\right)\left(S_f + S_p\right)\left(\overline{T_w} - T_m\right) \tag{2.19}$$

where S_f is the area of vertical fins, S_p is the area of heated bottom plate, T_w is the mean wall temperature, T_m is the melting temperature and S is the area of solid liquid interface.

A theoretical model was derived by Padmanabhan and Murthy [121] to study the phase change occurring in a cylindrical annulus with axial fins on the inner tube. The theoretical model was based on the finite-difference method. It was concluded that the melt/frozen fraction could be estimated using the following formula, which was recommended for engineering design purposes:

$$VF = 1.1275\left(Fo * Ste * T_f\right)^{0.624}\left(N\right)^{0.028}\left(L\right)^{-1.385}\left(W\right)^{-0.049} \tag{2.20}$$

where N is the number of fins, L is the fin length and W is the fin thickness

Tan et al. [122] studied both experimentally and numerically the impact of the configuration of spiral aluminium fillers on the PCM's melting performance in a fin type latent heat storage system. A two-dimensional simulation domain was designed using Fluent 6.3 software for both fin type and fine-spiral fillers slab (Figure 2.16). The numerical results were validated

with experimental data, and good agreement between results was observed. It was also found that the aluminium spiral fillers have a strong influence on the PCM's melting behaviour. The heat conduction increased due to the rise in the induction area as a result of adding the spiral fillers, whilst the natural convection was reduced.

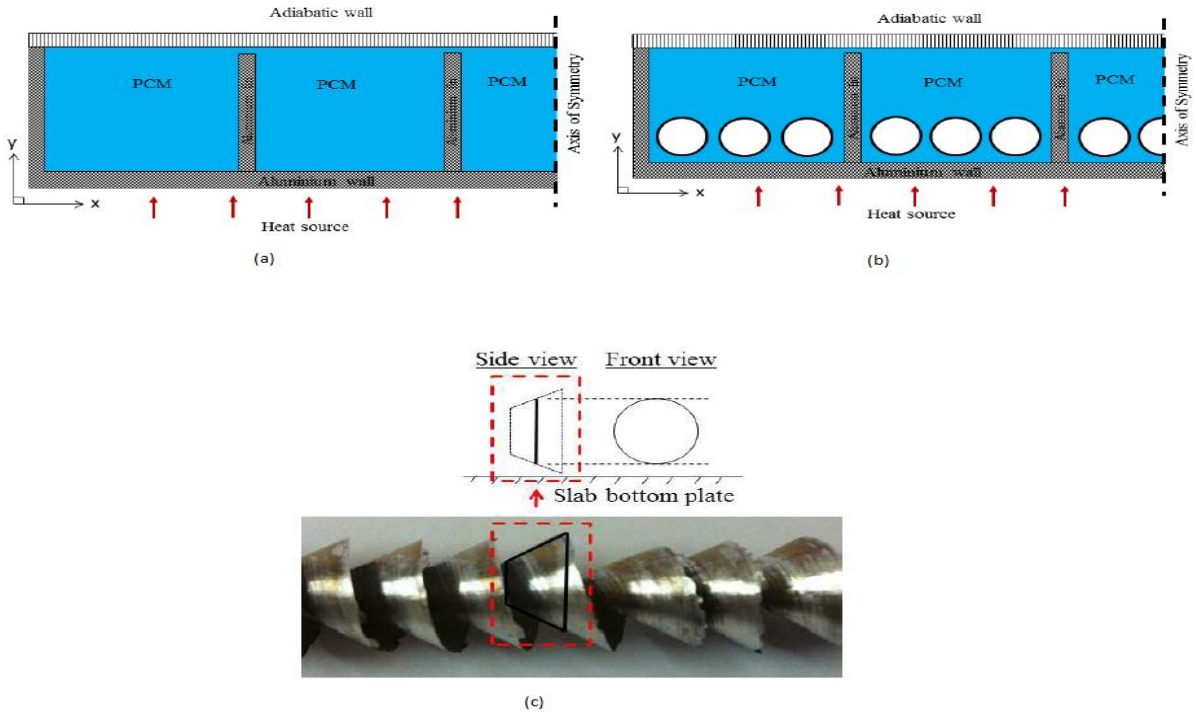

Figure 2.16: Two-dimensional simulation domain [122].

Agyenim et al. [123] experimentally studied the melting and solidification processes in a shell-and-tube design with longitudinal fins used to power a LiBr/H_2O absorption cooling system (Figure 2.17). The experiments were carried out for different values of the charging mass flow rate and inlet HTF temperatures. The temperature gradients in the axial, radial and angular directions during charging were recorded. The results demonstrated that the optimal parameters for charging the LiBr/H_2O absorption system were as follows: the mass flow rate of 30 kg/min and the inlet temperature of 140^{o}C.

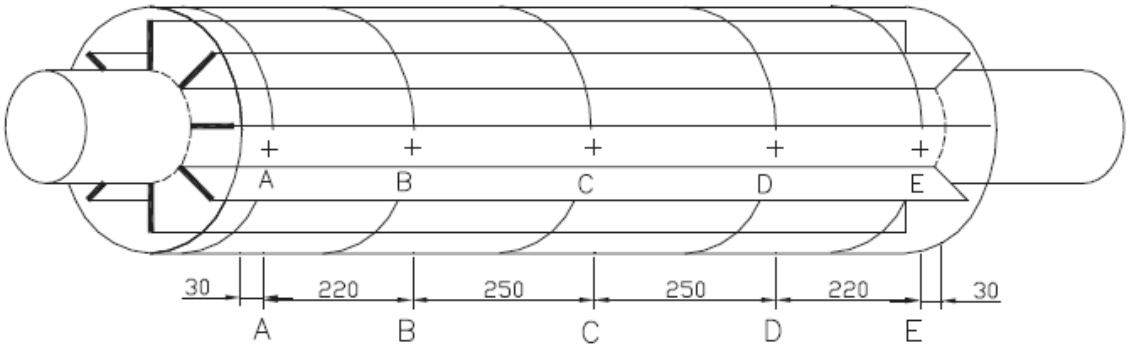

Figure 2.17: Schematic diagram of shell and tube system [123].

Choi and Kim [124] experimentally investigated the heat transfer characteristics of magnesium chloride hexahydrate ($MgCl_2.6H_2O$) in circular finned and unfinned systems. It was found that the molten fraction in a 5-finn tube was 25% greater than that in the unfinned tube. However, the molten fraction in the 10-finned tube was similar to that in the 5-finned tube which meant that the additional surface in the 10-finned tube did not have the desirable effect on the molten fraction. Heat transfer correlations were obtained for the amount of energy storage in terms of Fourier, Stefan and Reynolds numbers:

For the unfinned-tube systems,

$$\frac{Q}{Q_{\max}} = 7.42\times10^{-4} Fo^{0.96} Ste^{1.07} Re^{0.48}, \quad Re \le 8000 \tag{2.21}$$

For the 5-finned-tube systems,

$$\frac{Q}{Q_{\max}} = 10.10\times10^{-4} Fo^{0.92} Ste^{0.94} Re^{0.45}, \quad Re \le 8000 \tag{2.22}$$

For the 10-finned-tube systems,

$$\frac{Q}{Q_{\max}} = 24.90\times10^{-4} Fo^{0.85} Ste^{1.07} Re^{0.40}, \quad Re \le 8000 \tag{2.23}$$

Table 2.3: Heat intensification using fins.

No	Author	Fin geometry	Fin material	Methods	PCM	HTF	Process	Parameters investigated	Dimensions
1.	Liu et al. [105]	Rectangular fins	Copper	Experimental	Stearic acid	-	Charging process	Effect of fin size and pitch on the heat transfer	Tube: D_i=46mm, L=550mm
2.	Stritih [106]	Rectangular	Steel	Experimental and numerical	Paraffin	Water	Charging and discharging	Effects of fins on heat transfer enhancement	Fins: H=0.5m, L=0.12m, thickness 1mm. Rectangular Storage: H=0.5m, L=0.12m, W=0.65m.
3.	Velraj et al. [107]	Rectangular internal longitudinal fins	Aluminium	Experimental	Paraffin RT60	-	Discharging process	Effect of fin number and tube radius on heat flux and solidification fraction	Rectangular fins: H=27mm, L=300mm, thickness 1.5mm. Cylindrical tube: D_i=54mm, L=600mm, D_o=60mm.
4.	Kayansayan and Acar [109]	Annular fins	Copper	Experimental and numerical	Ice	Ethyl-alcohol	Discharging process	Effect of HTF inlet temperature, flow rate, fin density, and fin size	Horizontal section: (L=57cm, W=50cm, H= 42cm) Tube: (D_i=20mm, L=492mm, D_o=30mm)
5.	Lacroix [110]	Annular fins	Copper	Theoretical model	*N-Octadecane*	Water	Charging process	Effect of shell radius, mass flow rate, inlet temperature.	Inner tube: D_i=12.7mm, L=1m, D_o=15.8mm. Outer Tube: D_i=25.8mm, L=1m. Annular fins: Do=25.6mm.

No	Author	Fin geometry	Fin material	Methods	PCM	HTF	Process	Parameters investigated	Dimensions
6.	Ismail et al. [111]	Vertical axially finned	-	Experimental and numerical modelling	Paraffin	Water	Discharging process	Effect of fin length, thickness and, number, aspect ratio of the annular space and the temperature difference between phase change temperature and the wall temperature of the tube	Fins length: 0.087, 0.196, 0.348mm. Aspect ratio: 2.481 Fins number: 2, 3, 4 and 5 The angular half-width of the fin: 0.55, 0.45 and 0.36
7.	Zhang and Faghri [112]	Internal fins	-	Numerical modelling	-	-	Charging process	Effect of internal longitudinal fins on heat transfer	Fins thickness W=0.05
8.	Zhang and Faghri [75]	External radial finned	-	Numerical modelling	-	-	Charging) process	Effect of external radial fins on the heat transfer	
9.	Castell et al.[113]	External vertical fins		Experimenta	Sodium acetate trihydrate	Water	Natural convection phenomena during solidification process	Effect of fins on natural convection phenomena	Cylindrical Tank: D=440mm, H=450mm. Cylindrical model: D=88mm, H=315mm. Fins: H=310mm, L=20 and 40mm.
10.	Agyenim et al [114]	Circular and longitudinal fins	Copper	Experimental	Erythritol	Silicon oil	Charging and discharging	Effect of circular and longitudinal fins on the heat transfer of medium temperature thermal storage system	Fins number: 8 Fin thickness: 0.001m Fin pitch: 0.04m Circular fin diameter: 0.134m Longitudinal fin length: 0.95m

No	Author	Fin geometry	Fin material	Methods	PCM	HTF	Process	Parameters investigated	Dimensions
11.	Shatikian et al [115, 116]	Internal longitudinal fins	Aluminium	Numerical	Paraffin wax	-	Charging process	Effect of fins on the melting process and heat flux	0.15 < Fins thickness <1.2 mm, 5 < fins high < 10mm, 0.5<PCM store between fins<4mm
12.	Sparrow et al [117]	External vertical fins	Styrofoam	Experimental	Paraffin (n-eicosane)	-	Discharging process	Effect of fins on natural and conduction heat transfer	Storage unit: D=15.2cm and H=11.5cm.
13.	Ermis et al [118]	Internal fins	Bronze	Experimental and numerical modelling	Water/ice	Ethyl-alcohol	Charging and discharging	Effect of fins and flow parameters on the phase change process using artificial neural network	Fin: L= 440mm, thickness=3mm. Tube: D_i=10mm, D_o=15mm, L=570mm. Tank: W=420mm, L= 570mm, H=500mm.
14.	Eftekhar et al [119]	Vertical fins		Experimental	P116 paraffin wax	Water	Charging process	Effect of fins on the enhancement of heat transfer and natural convection	Storage unit: H= 53.5mm, L= 61.5mm and W=56mm.
15.	Padmanabhan and Murthy [121]	Axial fins	Copper	Numerical	N-Eicosane	Water	Charging and discharging	Phase change process of specific storage unit	Dimensionless fin thickness= 0.1 Dimensionless fin length= 1.5
16.	Tan et al. [122]	Fins and Spiral Fillers	Aluminium	Experimental and numerical	Paraffin wax	-	Charging process	Effect of spiral fillers on melting performance	Spiral fillers diameter = 12mm

No	Author	Fin geometry	Fin material	Methods	PCM	HTF	Process	Parameters investigated	Dimensions
17.	Ismail and Lino [125]	Radial rectangular fins	Copper	Experimental	Water	Ethanol	Discharging process	Effect of radial fins and turbulence promoters on heat transfer	Tank: 700×500×500, thickness=10mm. Tube: D_i=12.25mm, D_o=18.35mm, L=1m.
18.	Saha and Dutta [126]	Plate fins		Numerical	N-Eicosane	-	Charging process	Effect of aspect ratio and applied heat flux on the thermal performance of the heat sinks	Heat sink: (L=20mm, H=2mm) Fin thickness= 0.2, 2.2, 4.2, 6.2, 8.2, 9.2, and 9.9mm. Fin height= 2.7, 3.1, 5, 10, 20, 25, 30, 35, and 40mm.
19.	Agyenim et al. [123]	Longitudinal fins	Copper	Experimental	Erythritol	Silicon oil and water	Both charging and discharging	Effect of mass flow rate and inlet temperature of HTF on the thermal behaviour of PCM system	Shell, D_o=154mm Tube, D_o=54mm
20.	Choi and Kim [124]	Circular fins	Stainless steel	Experimental	Magnesium chloride hexahydrate	Air	Charging (melting) process	Effect of circular fins on heat transfer characteristics	Shell; D_i=55mm, H=140mm and thickness= 2.5mm

2.4.2 Intensification of the heat transfer using filling materials

Another technique widely used to increase the heat transfer surface in the thermal system is incorporate filling materials, such as graphite materials and porous media (metal foams and matrix materials).

2.4.2.1 Graphite materials

Pincemin et al. [127] experimented with graphite flakes combined with salts or eutectics as PCMs at melting temperatures of 200-300^{o}C. Graphite was added to improve the thermal conductivity of the PCM and storage capacity. Three different types of graphite have been used: natural graphite flakes (Figure 2.18a); expanded natural graphite (Figure 2.18b); and ground expanded natural graphite (Figure 2.18c). A significant enhancement of the thermal conductivity was found to be up to a factor of 14 with the effective conductivity of 9 W/m K and a factor of 10 for with the effective conductivity of 6 W/m K. Also, no significant changes were found in the phase change temperature, but a reduction in the phase change temperature variation was observed.

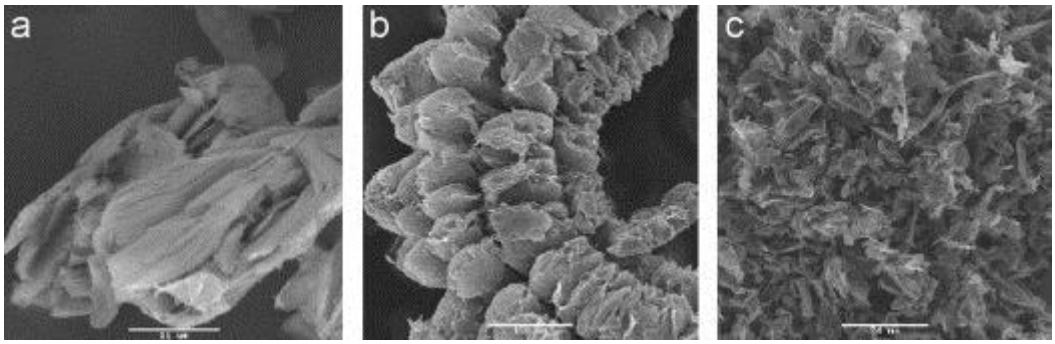

Figure 2.18:- Tested graphite [127].

Zhao and Wu [128] studied experimentally the intensification of heat transfer in a high temperature thermal storage system using metal foams and expanded graphite filled with the PCM. It was found that application of both metal foams and expanded graphite significantly enhanced the heat transfer during both charging and discharging processes; the complete freezing and melting times were reduced and the effect of metal foams was greater than that of expanded graphite. Another interesting finding was that the heat transfer was significantly enhanced in the solid regions due to increase in the conduction heat when using metal foams and expanded graphite, but these materials suppressed the natural convection effect in the liquid region.

Py et al. [129] studied theoretically and experimentally the performance of a composite PCM made of paraffin saturated with compressed expanded natural graphite (CENG). They concluded that the composite thermal conductivity can be improved up to 70 W/mK depending on the CENG density and shape. CENG also significantly suppressed the natural convection in the melted PCM region.

Zhang and Fang [130] studied the behavior of a paraffin/expanded graphite composite PCM. Expanded graphite with an average particle size of 300μm and an expansion ratio of 200ml/g was used in the study. The thermal performance of the composite was compared with that of paraffin, and the results showed that the phase change temperature and latent heat remained the same for these both materials. On the other hand, the time needed to reach the required temperature during the melting process was reduced by 27.4% for the composite PCM compared to paraffin. It also can be seen in Figure 2.19 that the total solidification time for the composite PCM was reduced by 56.4% compared to paraffin. The heat transfer rate in the composite PCM was higher than that of paraffin due to the improved thermal conductivity.

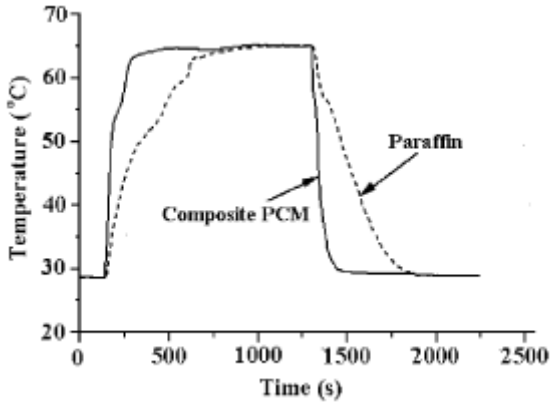

Figure 2.19: Temperature variation during the melting and solidification process [130].

The same method of enhancing the thermal conductivity was adopted by Xiao et al. [131] for paraffin using a thermoplastic elastomer poly composite. The thermal storage performance of the composite was compared with that of paraffin, and it was reported that the heat transfer rate in the composite increased significantly with the rise of the mass of expanded graphite during the solidification process. This was due to the increase in the thermal conductivity of the composite. In the case of melting, the heat transfer rate was reduced due to the weaker natural convection, which plays a significant role during melting. The most interesting finding was that the composite PCM with paraffin content of 80% had the same phase transition as pure paraffin.

Sarı and Karaipekli [132] obtained similar results from the experimental study of the melting process in the composite PCM made of paraffin (n-docosane) with expanded graphite (EG). The effect of the mass fraction of EG on the thermal storage characteristics was investigated. The results indicated a strong relationship between the mass the fraction of EG and thermal conductivity. The continuous introduction of EG resulted in an increase in the thermal conductivity, thereby reducing the complete melting time. On the other hand, for all EG mass fractions, the latent heat capacities were roughly the same and very close to that of paraffin.

The composite PCM made of 10% EG and 90% of paraffin was recommended for LHTES applications due to its stable properties.

In an effort to improve the thermal conductivity of static acid, Karaipekli et al. [133] have used expanded graphite (EG) and carbon fibre (CF) and compared the results with those of authors in [88, 131, 134-137]. They discovered a linear relationship between the thermal conductivity and the mass fractions of EG and CF additions:

$$k = 0.0841M_f + 0.2194 \qquad (\textit{for Expanded Graphite}) \tag{2.24}$$

$$k = 0.0659M_f + 0.2831 \qquad (\textit{for Carbon Fiber}) \tag{2.25}$$

Zhang et al. [138] also studied the influence of graphite powders on the thermal conductivity of mixed shape-stabilized PCMs. It was reported that the thermal conductivity of the composite PCM could be increased up to 20 times. Beyond this value the mechanical robustness of the composite deteriorated. Furthermore, the authors developed a correlation for the effective thermal conductivity as a function of the graphite mass fraction and this correlation showed a good agreement with experimental data:

$$k = -333.3X^4 + 213.3X^3 - 31.97X^2 + 2.187X + 0.15 \qquad (0 \le X \le 0.2) \tag{2.26}$$

Mills et al. [139] used a graphite matrix to form a paraffin/graphite composite. The graphite matrix was made of flake graphite which can be obtained from stacked sheets of carbon. The thermo physical properties of the composite were investigated, and their experimental results were compared with correlations published by other authors in [129, 140, 141] with a good agreement. It was found that the PCM mass fraction was decreased for higher bulk densities, while the thermal conductivity of the composite PCM increasing anisotropically for the higher bulk densities.

2.4.2.2 Intensification of heat transfer using porous media, metal foams and matrix materials

Mesalhy et al. [142] numerically investigated the influence of a porous matrix with different values of the thermal conductivity and porosity filled with the PCM in two concentric cylinders. The finite element approach was used, and in order to validate the numerical model the free convection during the melting process of pure PCM was investigated. The numerical results were compared to those by Khillarkar et al. [69] and found to be in a good agreement. The results demonstrated that a decrease in the porosity resulted in an increase in the melting rate as well as in the convection flow of liquid PCM fractions due to the reduction in the matrix permeability. Also, decreasing the porosity reduced the storage capacity of the PCM due to reduction in the PCM quantity. On the other hand, using a solid matrix with the high thermal conductivity and porosity resulted in the significant heat transfer enhancement in the PCM storage. Also, Hoogendoorn and Bart [143] developed a mathematical model to study the effects of metal matrix structure on the temperature transition range of melting/solidification in paraffinic materials. It was demonstrated that the mathematical model provided a good agreement with the experimental results.

Phanikumar and Mahajan [144] carried out both experimental and numerical analysis of the natural convection inside the high porosity metal foams heated from below. The numerical model was validated with experimental data and with the results of Beckermann et al. [145]. The effect of several metal foams (aluminium, carbon and nickel) on the heat transfer enhancement was examined, and it was found that using metal foams led to significant enhancement in heat transfer. On the other hand, the effect of Darcy and Rayleigh numbers on the heat transfer was also reported, and it was demonstrated that local thermal non-equilibrium effects became significant at high Darcy and Rayleigh numbers. Sasaguchi et al.

[146] proposed a numerical model for the solidification of pure water in the porous media placed around a single cylinder and two cylinders. The model was used to study the effect of the natural convection on the solidification process for the system with and without porous media. Also, the effects of the initial water temperature as well as the number of cylinders on solidification were studied. The model was validated with experimental results and excellent agreement was found. It was concluded that both the initial temperature of water and the number of cylinders had considerable effects on the solidification process. Their next paper [147] examined the effect of the position of the cylinder on the solidification process. The results demonstrated that the position of the cylinder had a significant influence on temperature distribution, average Nusselt number over the cylinder surface, and the cooling rate of the water.

Bhattacharya et al. [148] conducted both analytical and experimental analysis of the physical properties of high porosity metal foams. The effect of the thermal conductivity, permeability, and internal coefficient of high porosity were investigated, and the theoretical model was validated with experimental data which demonstrated the excellent agreement. A metal fibre was used (Figure 2.20), and it was concluded that the thermal conductivity depended on the porosity and the ratio of the cross-section of the fibre to the intersection area. The permeability increased with the increase of pore diameters and the porosity of the medium.

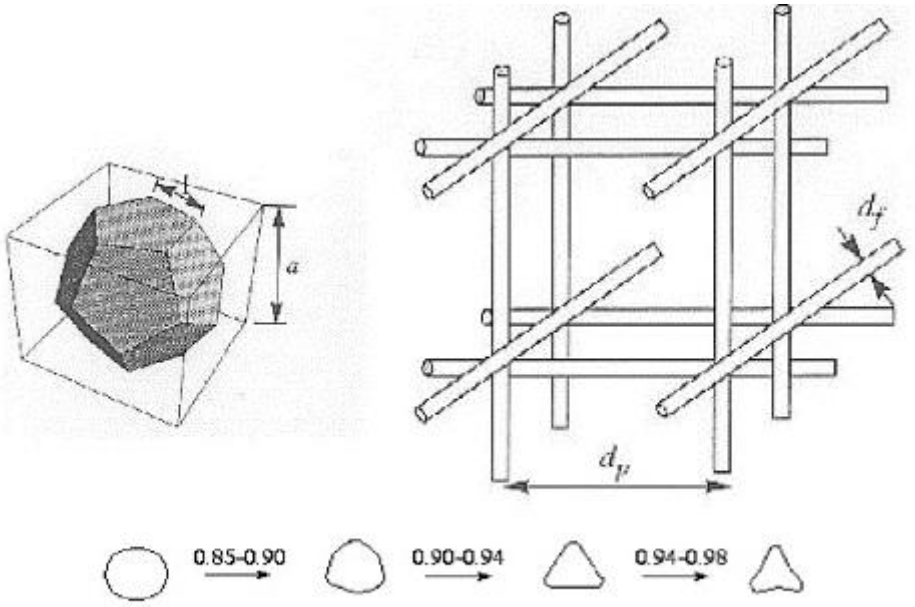

Figure 2.20: Open cell representation of the metal foam and schematic of the fibre cross-sections at different porosities [148].

Boomsma and Poulikakos [149] developed a three dimensional numerical model to evaluate the effective thermal conductivity of the fluid saturated metal foam. The foam structure was represented as cylindrical ligaments attached to cubic nods at their centres as shown in Figure 2.21. The aluminium foam with a porosity of 95% was used as the foam metal, whilst air and water were used as fluids. The model was validated with the experimental data by Calmidi and Mahajan [150] and good agreement was observed. It was concluded that changing the fluid conductivity slightly increased the effective thermal conductivity which demonstrated that the heat conductivity of the solid phase determined the overall effective thermal conductivity.

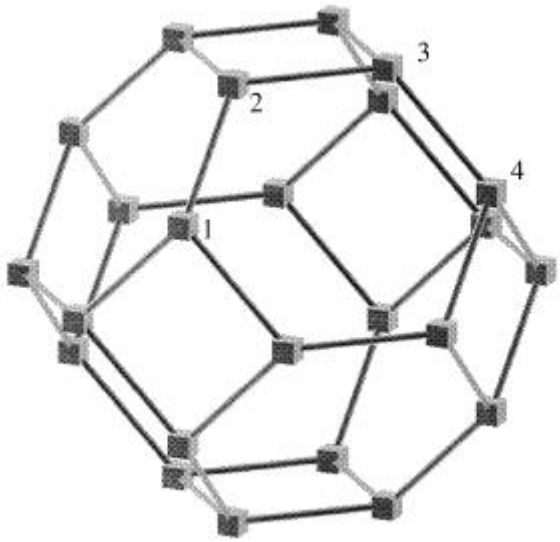

Figure 2.21: Foam structure [149].

Calmidi and Mahajan [150, 151] numerically modelled and experimented with the forced convection in high porosity metal foams. Experiments were carried out with the aluminium metal foam saturated with air and water as the fluid medium. The numerical results were compared to experimental data by Hunt and Tien [152], and it was demonstrated that the enhancement effect of the thermal dispersion was very small for the foam-air compound due to the high conductivity of the solid matrix, whilst for the foam-water the thermal dispersion was very large.

Erk and Duduković [153] numerically modelled and experimentally analysed the heat storage in a phase change regenerator consisting of *n-Octadecane* retained by capillary force in a porous silica support. CO_2 was used as the HTF in the phase change regenerator. The experiment measured the outlet temperature and compared it with the predicted value, and the results indicated the presence of a significant amount of heat losses. As much as 50% of the energy stored in the experimental unit could be lost to the surroundings via the end plates.

Also, predictions of the net front movement were compared quantitatively with the experimental data, showing a reasonable agreement in 60% of the volume of the bed.

Weaver and Viskanta [154] experimentally investigated the freezing of distilled water in the saturated porous media. Spherical glass balls with the diameter of 1.59 and 6 mm were used as the porous media, and their permeabilities were calculated to be 1.6×10^{-9} and 2.85×10^{-8} m^2 respectively. It was concluded that the porous media had a significant effect on the natural convection during the solidification process inhibiting the fluid motion.

Beckermann and Viskanta [155] carried out both experimental and numerical analysis of the phase change of a fluid inside a vertical rectangular enclosure filled with glass beads as a porous matrix. Numerical results were compared to experimental data to demonstrate a good agreement. It was concluded that the porous media had a considerable effect on the natural convection in the melt as well as on the conduction in the solid fraction.

Zhao and Lu [156, 157] produced a general model for heat transfer performance in metal foam filled pipes. Detailed information on the velocity and temperature distributions were obtained using the Brinkman-extended Darcy momentum model and a two-equation heat transfer model. The results indicated that the metal foam significantly increased the heat transfer by a factor of forty. Also, the metal foam with a small porosity and pore density resulted in the better heat transfer performance, but with the increased pressure drop. In their later papers [158-161] they examined the influence of the metal foam on the phase change process during the solidification and melting of paraffin. It was found that the additive metal foam significantly increased the heat transfer rate during both solidification and melting. The degree of the heat transfer enhancement depended on the metal foam structure and material used. Some results described in this section are summarised in Table 2.4.

Table 2.4**:** Heat transfer intensification using filling materials.

No	Authors	Methods	PCM	Filling material	Process	Validation
1.	Pincemin et al. [127]	Experimental	Slat and eutectics	Graphite	Charging process	Yes [162, 163]
2.	Zhao and Wu [128]	Experimental	Sodium nitrate $nano_3$	Metal foams and graphite	Charging and discharging	No
3.	Py et al. [129]	Experimental and numerical	Paraffin	Expanded natural graphite	Charging and discharging	No
4.	Zhang and Fang [130]	Experimental	Paraffin	Expanded graphite	Charging and discharging	No
5.	Xiao [131]	Experimental	Paraffin	Thermoplastic elastomer poly graphite	Charging and discharging	No
6.	Sarı and Karaipekli [132]	Experimental	Paraffin (n-docosane)	Expanded graphite	Charging and discharging	No
7.	Karaipekli [133]	Experimental	Static acid	Expanded graphite and carbon fibre	Charging process	Yes [88, 131, 134-137]
8.	Zhang et al. [138]	Experimental and numerical		Graphite	Charging process	Yes
9.	Mills et al. [139]	Experimental	Paraffin wax	Graphite matrix	Charging and discharging	Yes[129, 140, 141]
10.	Haillot et al. [164]	Numerical	Paraffin, stearic and other acids	Expanded natural graphite	Charging and discharging	No
11.	Yin et al. [165]	Experimental	Paraffin	Expanded graphite	Charging and discharging	No
12.	Mesalhy [142]	Numerical modelling	*N-Octadecane*	Metal matrix	Charging process	Yes [69]
13.	Hoogendoorn and Bart [143]	Experimental and numerical	Paraffinic materials	Metal matrix	Charging and discharging	Yes
14.	Phanikumar and Mahajan [144]	Experimental and numerical	-	Metal matrix (aluminium, carbon and nickel)	-	Yes[145]
15	Sasaguchi et al. [146, 147]	Experimental and numerical	Pure water	Porous media	Discharging process	Yes
16.	Bhattacharya et al. [148]	Experimental and numerical	Water	Metal foams	-	Yes
17.	Boomsma and Poulikakos [149]	Experimental and numerical	Water	Metal foam	-	Yes [150]
18.	Calmidi and Mahajan [150, 151]	Experimental and numerical	-	Metal foam	-	Yes [152]

No	Authors	Methods	PCM	Filling material	Process	Validation
19.	Erk and Duduković [153]	Experimental and numerical	*N-octadecane*	Porous silica support	Charging process	Yes
20.	Weaver and Viskanta [154]	Experimental	Water	Porous (spherical glass balls)	Discharging process	No
21.	Beckermann and Viskanta [155]	Experimental and numerical	Gallium	Porous (spherical glass balls)	Charging and discharging	Yes
22.	Siahpush [166]	Experimental	Eicosane	Copper porous foam	Charging and discharging	Yes
23.	Zhao and Lu [156, 157]	Analytical model	-	Metal foam	Charging process	Yes [167]
24.	Zhao and Lu[158]	Experimental	Paraffin RT58	Metal foam	Charging and discharging	Yes
25.	Krishnan [168, 169]	Numerical	-	Metal foam	Charging and discharging	Yes [155]
26.	Tong [170]	Numerical	Water	Metal matrix	Charging and discharging	Yes [171-173]
27.	Ettouney et al. [174]	Experimental	Paraffin wax	Metal screens and metal spheres	Charging process	No

2.4.3 Heat transfer intensification using nano-fluid, nano-particles and microencapsulation

2.4.3.1 Nano-particles

Ho and Gao [175] experimentally evaluated the effect of alumina (AL_2O_3) nano-particles on the thermo physical properties of paraffin (*n-Octadecane*) during melting/freezing processes. From the results obtained, adding AL_2O_3 nanoparticles in paraffin had a small effect on the melting/freezing behaviour of paraffin. A similar result was obtained for the thermal conductivity enhancement using nano-particles. The thermal conductivity of nanoparticles in paraffin becomes considerable higher with the rise of its temperature due to intensification of the Brownian motion. Furthermore, the measured dynamic viscosity and density of pure paraffin was compared with those found in [176] and excellent agreement was observed. The results also revealed that the dynamic viscosity increased significantly as the amount of AL_2O_3 nanoparticles increased. Wu et al. [177] carried out similar work on paraffin saturated with nanoparticles. Cu, AL, and C/Cu nanoparticles were used to improve the heat transfer rate during both freezing and melting processes. It was concluded that the paraffin with nano-particles has the significantly enhanced heat transfer rate compared with pure paraffin, and also that the nano-particles had a little influence on the melting/freezing temperatures. The analysis conducted indicated that Cu nanoparticles provided the strongest enhancement compared to Al and C/Cu nanoparticles.

Zeng et al. [178] experimentally investigated the influence of Ag nano-particles on the thermal conductivity of the PCM. Tetradecanol (TD) was used as the PCM, and the experiment was carried out using several types of thermal analysis: differential scanning calorimetry (DSC), thermogravimetry (TG), power X-ray diffraction (XRD), and

transmission electron microscopy (TEM). It was found from the results that the thermal conductivity of the composite material increased with the rise of amount of Ag nano-particles.

A numerical simulation using FLUENT software was carried out by Arasu et al. [179] to investigate the effect of AL_2O_3 nanoparticles on the paraffin wax in a concentric double pipe heat exchanger. The computed thermo-physical properties of paraffin saturated with AL_2O_3 nano-particles were compared with Ho and Gao's measurements in [175] and a good agreement was observed between these two data sets. The results demonstrated that the AL_2O_3 nano-particles in paraffin wax have a significant effect on the charging-discharging rates of the thermal energy compared to the case with pure paraffin. A similar enhancement in the thermal conductivity of the composite materials and in the heat transfer rate was found. Furthermore, the viscosity of the composite materials increased as the volumetric farction of AL_2O_3 nano-particles rose, thus improving the natural convection heat transfer effectiveness. Their study in [180] repeated this investigation for a square enclosure heated from below and from the vertical side. The results indicated that paraffin wax saturated with nano-particles exhibited increased thermo-physical properties compared to pure paraffin. In [181] the effect of the volume fraction was studied for both AL_2O_3 and CuO nano-particles on the solidification and melting processes of paraffin wax. The Authors found that the enhancement in the thermal performance of paraffin wax was greater when AL_2O_3 nano-particles were used compared to the application of CuO nano-particles.

Khodadadi and Fan [182] analytically solved the one-dimensional Stefan problem for the freezing process of nano-particle-enhanced PCM (NEPCM) in a finite slab. Combinations of both water and cyclohexane as a PCM with additions of four types of nanoparticles (alumina, copper, copper oxide and titanium) were selected for investigations. The physical model for this investigation is illustrated in Figure 2.22. In their next paper [183], the authors

investigated the model experimentally. They demonstrated that freezing process depended only on the volume fraction of nano-particles and was not related to the type of nano-particles. The experimental results indicated that the freezing rate for NEPCM containing 5% of nano-particles was considerably increased. With the volume fraction of nano-particles of 1% and 2% the freezing process was not affected.

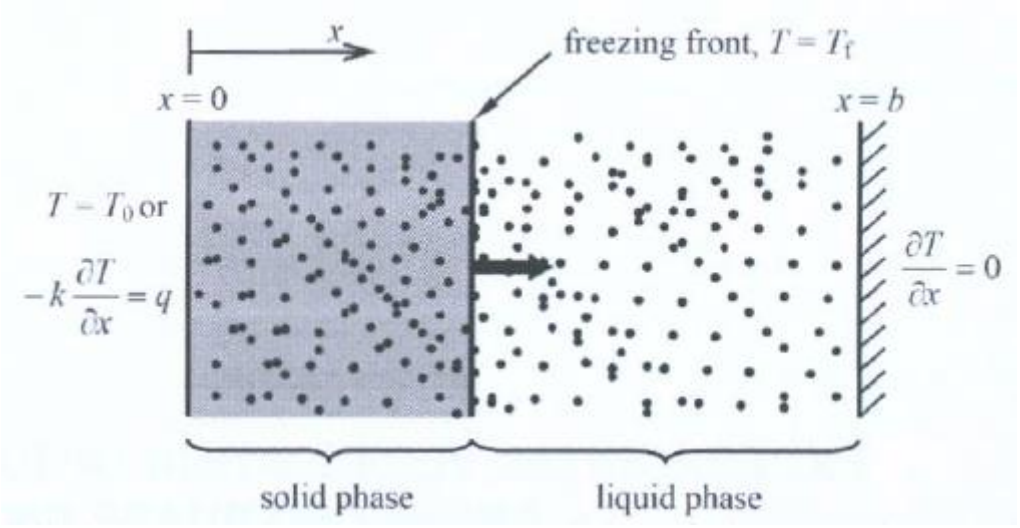

Figure 2.22: Schematic diagram for 1-D modelling of the PCM freezing in a finite slab [182, 183].

Khodadadi and Hosseinizadeh [184] also carried out analytical investigations of the effect of nano-copper particles on natural convection and PCM thermal conductivity in a square storage model. They applied the Boussinesq approximation model in FLUENT to simulate the buoyancy force and density variation. The results obtained from this model were compared with the results by other authors in [185-188]. In general, there was a good agreement between data sets. It was pointed out that the latent heat of the PCM decreased as the addition of nano-particles increased. The results indicated that the solidification fraction

increased rapidly as the mass fraction of suspended particles rose. This is because of the enhanced thermal conductivity and smaller value of their latent heat. Ranjbar et al. [189] obtained similar results from the numerical study of the solidification process in a 3-D rectangular enclosure filled with PCM with addition of nanoparticles. It was pointed out that the addition of nano-particles suppressed the natural convection, and therefore the heat conduction dominated heat transfer in both solid and liquid phrases.

Kim and Drzal [190] experimentally investigated the behaviour of exfoliated graphite nano-platelets (xGnP) filled with paraffin wax. The effects of xGnP on the thermal conductivity, melting time, melting temperature, and the latent heat capacity of paraffin were investigated. Their findings indicated that the thermal conductivity increased with the xGnP content. On the other hand, the use of xGnP did not lead to a decrease in the latent heat of paraffin/xGnP composite PCMs. Therefore, its latent heat storage was not reduced. Liu et al. [191] carried out experimental work on the solidification/melting of $BaCl_2$ filled with TiO_2 nano-particles. They found that the thermal conductivity and heat transfer were significantly enhanced by adding nano-particles, which also reduced the supercooling of the suspension. Wang et al. [192] used the fractal theory to model the effective thermal conductivity of the liquid with nano-particles. The effects of the particle size and surface adsorption were examined, and when the model results were compared to experimental results [193] a good agreement was observed for the particle content less than 0.5%.

Seeniraj et al. [194] proposed the theoretical expression for the energy storage and heat flux for cases with and without dispersed particles in the PCM and identified the optimum fraction of dispersed particles to maximise the energy storage and heat flux. The schematic arrangement used in this study is shown in Figure 2.23. It was reported that the cumulative energy storage capacity was decreased as the particle fraction was increased, due to the particles reducing the volume occupied with the PCM. However, the addition of particles

increased the instantaneous surface heat flux and hence accelerated the energy storage process. The results also revealed that the optimum fraction of dispersed particles to maximise the stored energy depends on the thermal conductivity of the dispersed fraction. Siegel [195] conducted a similar analysis for planer solidification process.

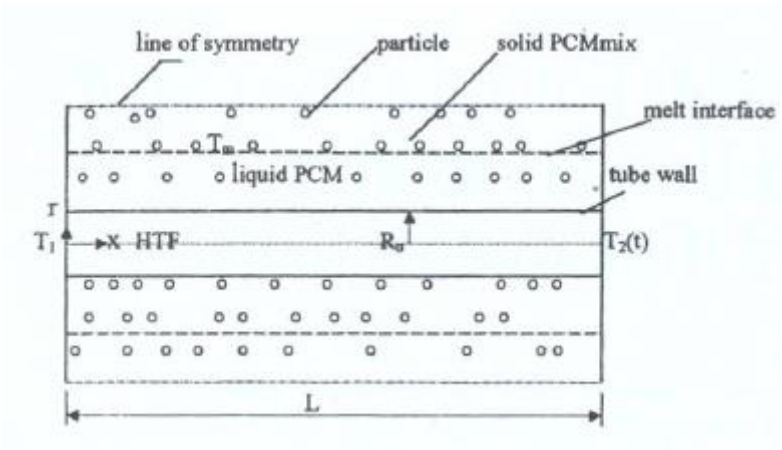

Figure 2.23: Schematic of the storage unit containing dispersed particles [194].

Wang and Choi [196] experimentally evaluated the thermal conductivity of the nano-particle-fluid mixture. They used Al_2O_3 and CuO nano-particles with diameters of 28 nm and 23 nm respectively. Several fluids, such as distilled water, ethylene glycol, engine oil, and vacuum pump fluid were dispersed with the two types of nano-particles and examined. The effect of the mixture preparation technique on its thermal conductivity was also investigated. The three different techniques, namely mechanical blending, coating particles with polymers and filtration, were tested and the measured thermal conductivity was compared with the predictions of various theoretical methods [197-202] shown in Table 2.5. It was reported that the measured thermal conductivity differed from data reported in the literature, due to the different particle sizes used in the study. The results further indicated that the thermal

conductivity of the mixture increased with decreasing particle size and also depended on the dispersion technique used.

Table 2.5**:** Effective thermal conductivity of a mixture [196].

Author	Theoretical expressions	Remarks
Maxwell [197]	$\frac{k_e}{k_f}=1+\frac{3(\alpha-1)\varnothing}{(\alpha+2)-(\alpha-1)\varnothing}$	Applicable $\varnothing \ll 1 or \lvert\alpha-1\rvert \ll 1$
Jeffrey [198]	$\frac{k_e}{k_f}=1+3\beta\varnothing+\varnothing^2\left(3\beta^2+\frac{3\beta^2}{4}+\frac{9\beta^3}{16}\frac{\alpha+2}{2\alpha+3}+\frac{3\beta^4}{2^6}+..\right)$	Accurate to order $\emptyset^2$
Davis [199]	$\frac{k_e}{k_f}=1+\frac{3(\alpha-1)}{(\alpha+2)-(\alpha-1)\varnothing}\left[\varnothing+f(\alpha)\varnothing^2+0(\varnothing^3)\right]$	Accurate to order $\emptyset^2$ $f(\alpha)=2.5\ for\ \alpha=10$ $f(\alpha)=0.5\ for\ \alpha=\infty$
Lu et al. [200]	$\frac{k_e}{k_f}=1+a.\varnothing+b.\varnothing^2$	For spherical particles a=2.25, b=2.27. For $\alpha=10$; a=3, b=4.51 for $\alpha=\infty$

Shaikh et al. [203] carried out an experimental and numerical study of the latent energy storage with a PCM containing dispersed single wall carbon nanotubes (SWCNTs), multiwall CNTs (MWCNTs) and carbon nano-fibers (CNFs). The numerical model results were compared to experimental results and a good agreement between them was found. Figure 2.24 illustrates the physical model and the 2-D arrangement of carbon nanotubes (CNTs) used in the theoretical model. From the experimental results, the maximum value of the latent heat enhancement was found to be in the wax/SWCNTs composite followed by that of the wax/MWCNTs composite, whilst the minimum enhancement was found in wax/CNFs composite. The theoretical model also examined the effect of nanoparticle mass fraction, size and type on the intermolecular attraction within the mixture. It was concluded that the

molecular density of the SWCNTs was higher compared to those of the MWCNTs and CNFs, resulting in the enhanced latent energy. A considerable number works were published on the heat transfer enhancement in PCMs using nanoparticles, as summarised in Table 2.8.

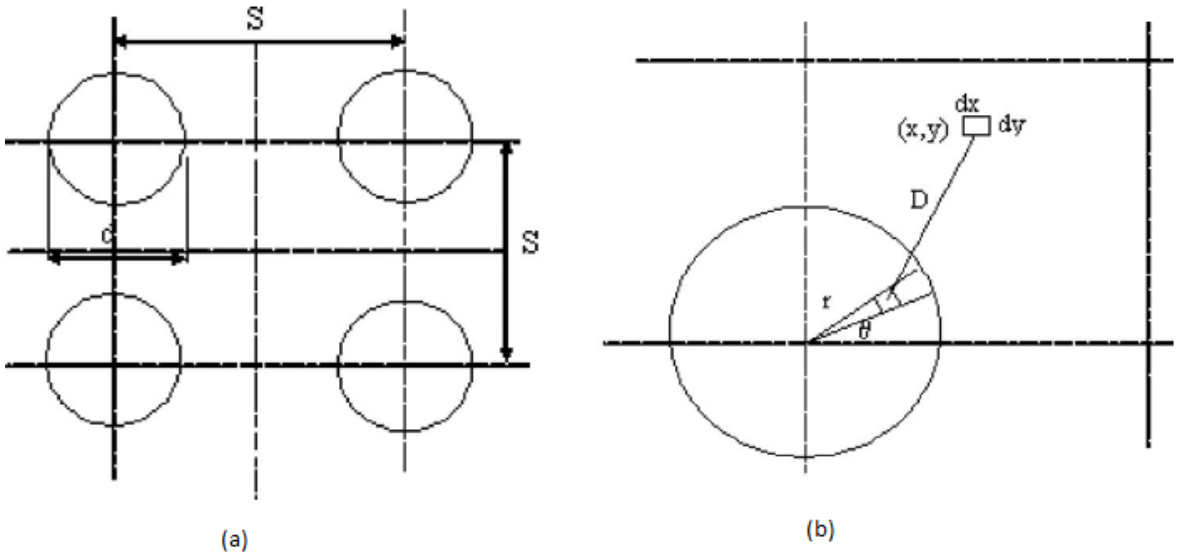

Figure 2.24: Physical model (a) and CNT arrangement (b) [203].

2.4.3.2 Nano-fluids

Nanofluids are dilute liquid suspensions of solid nanoparticles or nanofibres with sizes of 1-100 nm [204]. Recent developments in the field of heat transfer have led to a renewed interest in nanofluids because of their enhanced thermo physical properties and heat transfer. Ding et al. [204] reviewed the relevant literature which covered heat conduction using nanofluids, convection heat transfer for both natural and forced flow conditions, and boiling heat transfer in the nucleate regime. In an extensive study, Godson et al. [205] summarised the results of experimental and theoretical studies on the enhancement of heat transfer using nanofluids,

improvements in thermal conductivity, Brownian motion, and free convection in heat transfer. Recent developments in the enhancement of heat transfer using nanofluids have been reviewed by Trisaksri and Wongwises [206].

Ho et al. [207] numerically examined different models of the effect of the dynamic viscosity and thermal conductivity of nanofluids in natural convection heat transfer. Numerical 2D modelling was carried out for a vertical square enclosure (Figure 2.25), with a water-alumina (AL_2O_3) mixture chosen as the working nanofluid. Results indicated that the heat transfer across the enclosure was improved with respect to the base fluid. Vajjha et al. [208] experimentally measured the density of three different nanofluids containing aluminium oxide (AL_2O_3), antimony-tin oxide (Sb_2O_5:SnO_2), and zinc oxide (ZnO) nanoparticles in a fluid mixture consisting of 60% ethylene glycol and 40% water. The experimental results for density compared favourably with the theoretical results of Pak and Cho [209] and it was concluded that there was an excellent agreement between them, demonstrating that the density was increased with rise of nanoparticles content.

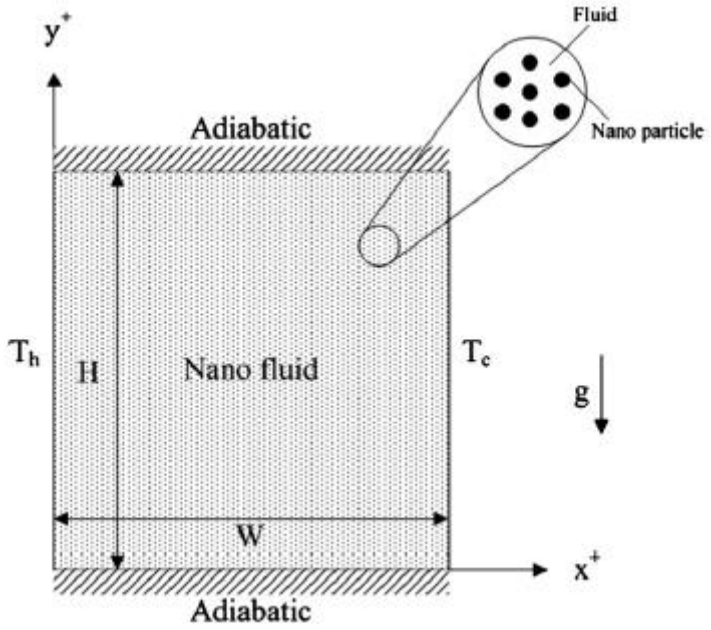

Figure 2.25: Schematic of a vertical enclosure system [207].

In another major study, Vajjha and Das [210] experimentally developed a correlation for the thermal conductivity of three nanofluids over a temperature range of 298-363K, taking into account the effect of Brownian motion on the thermal conductivity as a function of temperature. They compared their experimental results with those of several existing models [211-219] and found a good agreement. The results indicated that the thermal conductivity of nanofluids increased with the volume fraction of nanoparticles as well as with the increase in the temperature. A subsequent paper [220] examined the impact on heat transfer of nanofluid circulating within the flat tubes of an automobile radiator. Using the thermo physical properties of nanofluids derived in their previous work [208, 210], the problem was solved using the control volume method in FLUENT software. They demonstrated that the average heat transfer coefficient significantly increased as the particle volumetric concentration increased. Nevertheless, increasing nanoparticles resulted in an increase in the local skin friction, which caused a large pressure drop across the flat tube.

Khanafer et al. [185] performed numerical simulation to analyse the heat transfer behaviour of the nanofluid inside a two-dimensional enclosure for a range of Grashof numbers and volume fractions. The findings seemed to be consistent with those of other researchers [221-224]. The study found that the addition of nanoparticles considerably increased the heat transfer rate for any given Grashof number. Furthermore, heat transfer increased with the nanoparticle volume fraction. A correlation was proposed for the average Nusselt number as a function of the Grashof number $(10^3 \ll Gr \leq 10^5)$ and the nanoparticle volume fraction $(0 \leq \varnothing \leq 0.25)$. Li and Xuan [225] also established a new convective heat transfer correlation for Cu-water nanofluid under single-phase fluid model. These correlations are presented below:

$$\overline{Nu} = 0.5163\left(0.4436 + \varnothing^{1.0809}\right) Gr^{0.3123} \qquad [185] \qquad (2.27)$$

$$\overline{Nu_{nf}} = 0.4328(1+11.285\phi^{0.754}Pe_d^{0.218})Re_{nf}^{0.333}Pr_{nf}^{0.4} \quad \text{(for laminar Flow) [225]} \quad (2.28)$$

$$\overline{Nu_{nf}} = 0.0059\left(1+7.6286\varnothing^{0.6886}Pe_d^{0.001}\right)Re_{nf}^{0.9238}Pr_{nf}^{0.4} \quad \left(\text{For turbulent flow}\right) \text{[225]} \quad (2.29)$$

Abdulhassan et al. [226] experimentally studied the heat transfer performance of nanofluids circulating through a horizontal tube. Experimental measurements of the nanofluids thermo physical properties were compared with results of several studies [196, 209, 212, 227-230] with deviation not exceeding 3.5%. The results indicated that the presence of nano-particles significantly increased the heat transfer rate as well as the thermo physical properties of the nanofluid. The most interesting finding was that circulating nanofluids through the tube did not result in a large drop in pressure, because nanoparticles did not affect the flow behaviour. Gavtash et al. [231] obtained similar results from a numerical study of the nanofluid in a cylindrical heat pipe. A 2-D model of the heat pipe was created using FLUENT software. They found that the nanofluid improved the heat transfer rate in the heat pipe and reduced its thermal resistance. A preliminary work on heat transfer enhancement was undertaken by Xuan and Roetzel [230]. Two methods were presented to analyse the convection heat transfer with nanofluids. The first considers the nanofluid as a single phase fluid, while the other considering nanofluid as a multiphase fluid made of the nanofluid and the particles.

Maïga et al. [232] have also reported that nanoparticles substantially increase the heat transfer compared to base fluid. They attempted to provide correlations for the Nusselt numbers of nanofluids in terms of Reynolds and Prandtl numbers. Syam Sundar et al. [233] numerically investigated the laminar flow and heat transfer characteristics with three different nanofluids, namely AL_2O_3, CuO, and TiO_2, in a circulating tube using FLUENT software. Particle concentrations were in the range from 0.3 to 2%, and the results revealed that the heat transfer coefficient increased with the particle concentration. In addition, the highest heat transfer coefficient was provided by AL_2O_3 nanoparticles, followed by CuO, with the lowest

for TiO_2. Sasmito et al. [234] also studied the laminar flow heat transfer problem in square cross-section tubes with two different nanofluids, namely AL_2O_3 and CuO in water. The heat transfer was improved with nanofluids and AL_2O_3 provided a better performance than CuO. According to Wen and Ding [235], particle migration is the reason for the enhancement of the convection heat transfer and results in a non-uniform distribution of the thermal conductivity and the viscosity field as well as a reduction in the thermal boundary layer thickness.

Two-dimensional turbulent flow and heat transfer with three different nanofluids (AL_2O_3, CuO and SiO_2 in water) circulating through a circular tube under constant heat flux was numerically investigated by Namburu et al. [236]. They developed a new correlation for Nusselt number and viscosity for nanofluids with up to 10% volume fraction of nanoparticles. They compared their model's results with the correlation presented by Gnielinski [237] and found a good agreement. Based on their results, they stated that the heat transfer coefficient of nanofluids increased with volume fraction of nanoparticles and Reynolds number. The analysis indicated that CuO nanofluid had a higher heat transfer performance than AL_2O_3 and SiO_2. Figure 2.26 shows the computational grid used in this study. Several methods were used to calculate the dynamic viscosity and thermal conductivity of the nanofluid, as summarised in Table 2.6 and Table 2.7, respectively.

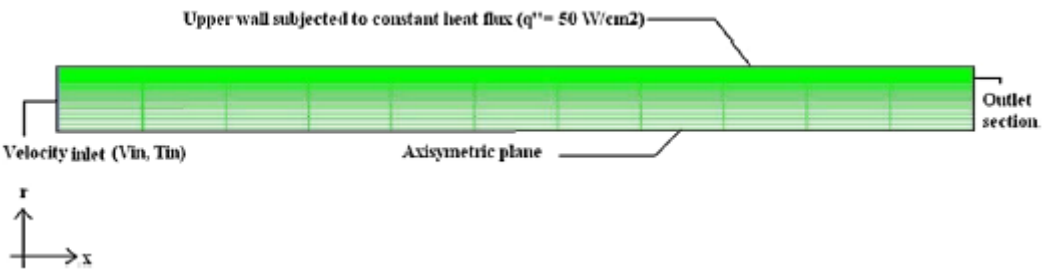

Figure 2.26: Computational grid used in [236].

Table 2.6: List of methods used to determine the nanofluid dynamic viscosity.

NO	Model	Dynamic viscosity	Remark
1.	Brinkman [238]	$\mu_{nf} = \mu_f (1 - \varnothing)^{-2.5}$	∅ is nanoparticle volume fraction
2.	Maïga et al. [232]	$\mu_{nf} = \mu_f (1 + 7.3\varnothing + 123\varnothing^2)$	∅ is nanoparticle volume fraction
3.	Vajjha [208]	$\mu_{nf} = \mu_f A_2 e^{(C_2\varnothing)}$	$293K \le T \le 363K$ $0.01 \le \varnothing \le 0.1$
4.	Ashrae [239]	$\mu_{nf} = \mu_f A_4 e^{\left(\frac{B_4}{T}\right)}$	$293K \le T \le 363K$ B_4=2664
5.	Namburu et al. [240]	$\log \mu_{nf} = Ae^{-BT}$	A and B are cubic polynomial functions of the particles volumetric concentration $T \le 50℃$
6.	Sahoo et al. [241]	$\mu_{nf} = A_1 e^{\left(\frac{B_1}{T} + C_1\varnothing\right)}$	$T \ge 90℃$

Table 2.7: A list of methods used to determine the nanofluid effective thermal conductivity.

No	Model	Thermal conductivity	Remarks
1.	Maxwell [197]	$\frac{K_{nf}}{K_L}=\frac{K_s+2K_L+2(K_s-K_L)\varnothing_s}{K_s+2K_L-(K_s-K_L)\varnothing_s}$	$\emptyset_s$: solid volume fraction
2.	Charunyakorn et al. [242]	$K_e=K_m\left(1+b\varnothing Pe_p^{\varnothing}\right)$	
3.	Hamilton and Crosser [228]	$\frac{K_{nf}}{K_L}=\frac{K_s+(n-1)K_L-(n-1)\varnothing_s(K_L-K_s)}{K_s+(n-1)K_f+\varnothing_s(K_L-K_s)}$	n dependent on particle shape and K_s/K_L, $n=3/\psi$
4.	Jeffrey [198]	$\frac{K_n f}{K_L}=1+3\phi_s\left(\frac{K_s/K_L-1}{K_s/K_L+2}\right)+3\phi_s^2\left(\frac{K_s/K_L-1}{K_s/K_L+2}\right).[1+\frac{1}{4}\left(\frac{K_s/K_L-1}{K_s/K_L+2}\right)+$ $\frac{3}{16}\left(\frac{K_s/K_L-1}{K_s/K_L+2}\right)\left(\frac{K_s/K_L-2}{K_s/K_L+3}\right)+..]$	
5.	Davis [199]	$\frac{K_{nf}}{K_L}=1+\frac{3(K_s/K_L-1).\left[\varnothing_s+f.\varnothing_s^{\,2}+O\left(\varnothing_s^{\,3}\right)\right]}{(K_s/K_L+2)-(K_s/K_L-1)\varnothing_s}$ $f(\alpha)=2.5\ for\ \alpha=10,\ f(\alpha)=0.5\ for\ \alpha=\infty$	Accurate to order $\varnothing^2$
6.	Bruggeman [211]	$\frac{K_{nf}}{K_L}=\left[(3\varnothing_s-1)\frac{K_s}{K_f}+(2-3\varnothing_s)+\sqrt{\Delta}\right]/4$ $\Delta=(3\varnothing_s-1)^2(K_s/K_L)^2+(2-3\varnothing_s)^2+2\left(2+9\varnothing_s-9\varnothing_s^{\,2}\right)(K_s/K_L)$	Spherical particles

No	Model	Thermal conductivity	Remarks
7.	Yu and Choi [212]	$K_{pe}=\frac{\left[2(1-\gamma)+(1+\chi)^3(1+2\gamma)\right]\gamma}{-(1-\gamma)+(1+\chi)^3(1+2\gamma)}K_s$ $\frac{K_{nf}}{K_L}=\frac{K_{pe}+2K_L+2(K_{pe}-K_L)(1+\chi)^3\varnothing_s}{K_{pe}+2K_L-(K_{pe}-K_L)(1+\chi)^3\varnothing_s}$ $\gamma=K_{layer}/K_s,\ \chi=h/r,\ 10K_L<K_{layer}<100K_L$	h is nano-layer thickness K_{layer} is nanolayer thermal conductivity r is particles radius
8.	Xuan et al. [213]	$\frac{K_{nf}}{K_L}=\frac{K_s+2K_L+2(K_s-K_L)\varnothing_s}{K_s+2K_L-(K_s-K_L)\varnothing_s}+\frac{\rho_s\varnothing Cp_s}{2}\sqrt{\frac{KT}{3\pi\mu_L r_c}}$	r_c is the mean radius of gyration of cluster
9.	Koo and Kleinstreuer [214, 215]	$\frac{K_{nf}}{K_L}=\frac{K_s+2K_L+2(K_s-K_L)\varnothing_s}{K_s+2K_L-(K_s-K_L)\varnothing_s}+5\times10^4\beta\varnothing\rho_L Cp_L\sqrt{\frac{KT}{\rho_s d_s}}f(T,\varnothing,etc.)$	β is fraction of liquid volume
10.	Xue and Xu [216]	$\left(1-\frac{\varnothing}{\omega}\right)\times\frac{K_{nf}-K_L}{2K_{nf}+K_L}+\frac{\varnothing}{\omega}\frac{(K_{nf}-K_2)(2K_2+K_s)-\omega(K_s-K_2)(2K_2+K_{nf})}{(2K_{nf}+K_2)(2K_2+K_s)+2\omega(K_s-K_2)(K_2-K_{nf})}=0$ $\omega=\left[\frac{r_s}{r_s+t}\right]^3$	K_2: is thermal conductivity of the interfacial shell. T: is the thickness of interfacial shell
11.	Chon et al. [217]	$\frac{K_{nf}}{K_L}=1+64.7\varnothing^{0.7460}\left(\frac{d_L}{d_s}\right)^{0.3690}\left(\frac{K_s}{K_L}\right)^{0.7476}Pr^{0.9955}Re^{1.2321}$ $Pr=\frac{Cp_L\mu_L}{K_L},\quad Re=\frac{\rho_L KT}{3\pi\mu_L^2 l_L}$	l_L is mean-free path for the fluid

No	Model	Thermal conductivity	Remarks
12.	Prasher et al. [218]	$\frac{K_{nf}}{K_L}=\left(1+ARe^{m}Pr^{0.333}\varnothing\right)\left(\frac{\left[K_s\left(1+2\alpha\right)+2K_m\right]+2\varnothing\left[K_s\left(1-\alpha\right)-K_m\right]}{\left[K_s\left(1+2\alpha\right)+2K_m\right]-\varnothing\left[K_s\left(1-\alpha\right)-K_m\right]}\right)$ $Re=\frac{1}{\nu}\sqrt{\frac{18KT}{\pi\rho_s d_s}},\ K_m=K_L\left[1+\left(1/4\right)Re.Pr\right],\ \alpha=2R_bK_m/D_s$	$A=4\times10^4$ R_b is the interfacial thermal resistance between nanoparticles and fluid
13.	Jang and Choi [219]	$\frac{K_{nf}}{K_L}=\left(1-\varnothing\right)+\beta_1K_p\varnothing+C_1\frac{d_L}{d_s}K_LRe_{dp}^2Pr\varnothing$ $Re_{dp}=\frac{\bar{C}_{R.M}d_s}{\nu},\ \bar{C}_{R.M}=\frac{KT}{3\pi\mu_Ld_sl_L}$	$C_1=18\times10^6$
14.	Vajjha and Das [210]	$\frac{K_{nf}}{K_L}=\frac{K_s+2K_L+2\left(K_s-K_L\right)\varnothing_s}{K_s+2K_L-\left(K_s-K_L\right)\varnothing_s}+5\times10^4\beta\varnothing\rho_LCp_L\sqrt{\frac{KT}{\rho_sd_s}}f\left(T,\varnothing\right)$ $f\left(T,\varnothing\right)=\left(2.8217\times10^{-2}+3.917\times10^{-3}\right)\left(\frac{T}{T_0}\right)+\left(-3.0669\times10^{-2}\varnothing-3.91123\times10^{-3}\right)$ for AL_2O_3particles, $\beta=8.4407\left(100\varnothing\right)^{-1.07304},0.01\le\varnothing\le0.1$ for Zno particles, $\beta=8.4407\left(100\varnothing\right)^{-1.07304},0.01\le\varnothing\le0.07$ for CuO particles, $\beta=9.881\left(100\varnothing\right)^{-0.9446},0.01\le\varnothing\le0.06$	Temperature range $298\le T\le363K$

No	Model	Thermal conductivity	Remarks
15.	Wang et al. [192]	$\frac{K_{nf}}{K_L}=\frac{(1-\varnothing)+3\varnothing\int_0^{\infty}\frac{K_s(r)n(r)}{K_s n(r)+2K_L}dr}{(1-\varnothing)+3\varnothing\int_0^{\infty}\frac{K_s n(r)}{K_s(r)+2K_L}dr}$	$n(r)$ is the radius distribution function
16.	Keblinski et al. [243]	$\frac{K_{nf}}{K_L}=(1-\varnothing)+K_s\varnothing+3C\frac{d_1}{d_s}K_L Re_d^2 Pr\varnothing$ $Re_{dp}=\frac{\bar{C}_{R.M}d_s}{\nu}$	$\bar{C}_{R.M}$ is the random motion velocity of nanoparticles

2.4.3.3 Microencapsulation

A microencapsulated phase change material (MEPCM) is obtained by placing a micro-size solid/liquid PCM core within a solid structure (shell/wall) [244]. A wide range of materials can be used to make the shell, including natural and synthetic polymers [245]. MEPCM can be prepared by two methods, namely complex coacervation and spray drying, details of which can be found in [245-249]. Figure 2.27 shows an SEM image of MEPCM prepared in [247].

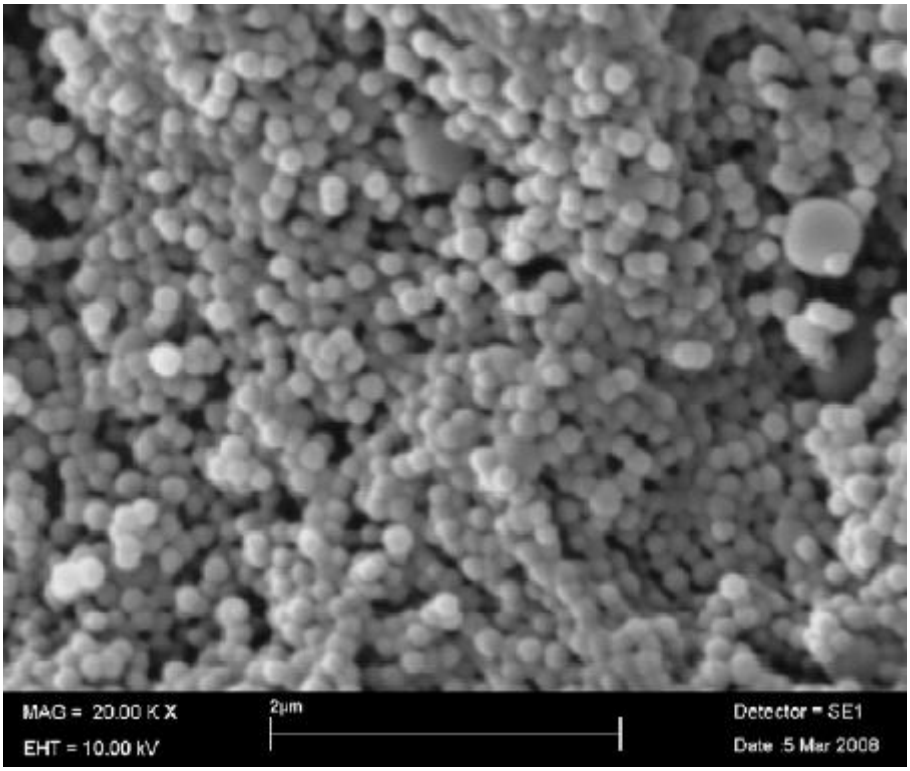

Figure 2.27**:** SEM image of microencapsulated PCM [247].

Xuan et al. [250] investigated experimentally the effect of microencapsulated PCM components on the specific heat capacity and thermal conductivity of an MEPCM suspension. The MEPCM core was paraffin while the shell was made of melamine urea

formed from aldehyde resin and iron particles. It was reported that the specific heat of the MEPMC depends on the temperature inside the MEPCM and the volume fraction of the MEPCM particles. In addition, the specific heat capacity of the suspension in the solid region was smaller than that in the liquid region for the same volume of MEPCM. On the other hand, the thermal conductivity increased linearly with the volume fraction of the MEPCM and it also increased with increasing iron nanoparticles inside the MEPCM.

Salaün et al. [251] used microcapsules filled with paraffin and nanoparticles of polyvinyl alcohol/hydrated salt to decrease the thermal conductivity of PCM. They also found that polymer nanoparticles did not affect the latent heat, but that the phase change took place over a wide range of temperatures compared to pure paraffin. Hu and Zhang [252] carried out a numerical investigation of the enhancement of convective heat transfer in microencapsulated PCM. The model analysed the effect of various factors on the heat transfer enhancement in a laminar flow in a circular tube with the constant wall temperature. This numerical simulations compared favourably with the results of the experimental investigation in [253]. In [254] authors conducted similar analysis for a circular tube with the constant heat flux, using the effective specific heat capacity model. The numerical simulation results were supported by findings of Alisetti and Roy in [255]. Namely that the Stefan number, the mass flow rate of HTF, and the volumetric concentration of microcapsules can improve the heat transfer rate.

Alvarado et al. [256] experimentally studied the enhancement of heat transfer in microencapsulated PCM under constant heat flux and turbulence conditions. The results indicated that microencapsulated PCM substantially increased heat transfer even with a low mass fraction. The analysis of results further indicated that the material's melting point was affected by a slurry velocity more than heat flux. Su et al. [257] investigated the influence of the core/shell ratio of microPCMs, their average diameter and the thermal conductivity on the phase change behaviour. They found that shell thickness did not have a strong effect.

However, higher volume fractions of microPCMs and smaller enhanced the thermal conductivity of the composite.

Özonur et al. [258] used a microencapsulated natural coco fatty acid mixture as a PCM for a thermal storage system. The transition temperature and the stability of the thermal energy storage of the PCMs were investigated during both charging and discharging processes. It was demonstrated that the thermal properties of the microencapsulated PCM were stable after 50 cycles. Rao et al. [259] experimentally investigated enhancement of the convective heat transfer in microencapsulated PCM-water additives flowing through rectangular minichannels. It was found that an increase in the mass flow rate and MEPCM volume substantially increased the heat transfer rate. The analysis also indicated that the thermal performance of the suspensions with a higher mass concentration was less effective at high mass flow rates due to the shorter residence time of the MEPCM additives.

The effect of several microencapsulated products on the heat transfer in gas-fluidized beds has been examined by Brown et al. [260]. Paraffin and octadecane were used as MEPCM cores while the shells were made of polymethylene-urea, cross-linked nylon, and gelatine. The results revealed that the octadecane/gelatine MEPCM exhibited better heat transfer performance. The heat transfer was enhanced by 85% during the phase transition compared to that of the single phase.

Table 2.8: Literature on PCM heat transfer intensification using filling materials.

No	Author	Methods	PCM	Enhancement method	Process	Validation
1.	Ho and Gao [175]	Experimental	*N-octadecane*	Nanoparticles	Charging and discharging	Yes [176]
2.	Wu et al. [177]	Experimental	Paraffin wax	Nanoparticles	Charging and discharging	Yes [175, 261-265]
3.	Zeng et al. [178]	Experimental	Tetradecanol (TD)	Nanoparticles	Charging process	No
4.	Arasu [179-181]	Numerical	Paraffin wax	Nanoparticles	Charging and discharging	Yes [175, 184]
5.	Khodadadi and Fan [182]	Numerical	Cyclohexane and water	Nanoparticles	Discharging process	Yes
6.	Fan and Khodadadi [183]	Experimental	Cyclohexane and water	Nanoparticles	Discharging process	Yes
7.	Khodadadi and Hosseiniza deh [184]	Numerical	Water	Nanoparticles	Discharging process	Yes [185-188]
8.	Putnam et al. [266]	Numerical	Polymethylme thacrylate	Nanoparticles	-	No
9.	Ranjbar et al. [189]	Numerical	-	Nanoparticles	Discharging process	Yes [23, 184-186]
10.	Kim and Drzal [190]	Experimental	Paraffin	Nanoplatelets of exfoliated graphite (xgnp)	Charging process	No [193]
11.	Liu et al. [191]	Experimental	$Bacl_2$	Nanoparticles	Charging and discharging	No
12.	Wang [192]	Numerical modelling	Water	Nanoparticles	Charging (melting) process	Yes
13.	Seeniraj [194]	Numerical	*N-Octadecane*	Dispersed particles	Charging process	No
14.	Siegel [195]	Numerical	*N-Octadecane*	Dispersed particles	Discharging process	No
15.	Wang and Choi [196]	Experimental and Numerical	Distilled water, ethylene glycol, engine oil, and vacuum pump fluid	Nanoparticles		Yes [197-202]
16.	Shaikh [203]	Experimental and Numerical	Paraffin wax	Nanoparticles	Charging process	Yes
17.	Halte et al. [267]	Experimental	-	Nanoparticles	-	No
18.	Elgafy and Lafdi [268]	Experimental and Numerical	Paraffin wax	Nanoparticles	Discharging process	Yes
19.	Zeng et al. [269]	Experimental	Nitric acid	Nanoparticles	Charging process	No

No	Author	Methods	PCM	Enhancement method	Process	Validation
20.	Zeng et al. [270]	Experimental	Tetradecanol	Nanoparticles	Charging process	No
21.	Wu et al. [271]	Experimental	Water	Nanoparticles	Discharging process	Yes [272, 273]
22.	Ho [207]	Numerical	Water	Nanofluids	Charging process	Yes [223, 224]
23.	Vajjha [208]	Experimental	Ethylene glycol and water	Nanofluid	Charging process	Yes [209]
24.	Vajjha and Das [210, 220]	Experimental and Numerical	Ethylene glycol and water	Nanofluid	Charging process	Yes models [211-219]
25.	Khanafer [185]	Numerical	-	Nanofluid	Charging process	Yes [221-224]
26.	Abdulhassan [226]	Experimental	Water	Nanofluid	Charging process	Yes [196, 209, 212, 227-230]
27.	Gavtash et al. [231]	Numerical	Water	Nanofluid	Charging process	No
28.	Maïga et al. [232]	Numerical	Water and ethylene glycol	Nanofluid	Charging process	Yes [274]
29.	Syam Sundar et al. [233]	Numerical	Water	Nanofluid	Charging process	Yes [275]
30.	Sasmito [234]	Numerical	Water	Nanofluid	Discharging process	Yes [276]
31.	Wen and Ding [235]	Experimental	Water	Nanofluid	Charging process	Yes [275]
32.	Namburu et al. [236]	Numerical	Water	Nanofluid	Charging process	Yes [237]
33.	Xuan and Roetzel [230]	Numerical	Water	Nanofluid	Charging process	Yes
34.	Li and Xuan [225]	Experimental	Water	Nanofluid	Charging process	Yes
35.	Keblinski et al. [243]	Numerical	-	Nanofluid	Charging process	No
36.	Wang [277]	Experimental	Water	Nanofluid	Charging process	No
37.	Bönneman n et al. [278]	Experimental	Water	Nanofluid	Charging process	No
38.	Gao et al. [279]	Experimental	Water	Nanofluid	Charging and discharging process	No
39.	Chein and Huang [280]	Numerical	Water	Nanofluid	Discharging process	Yes [281]
40.	Xuan [250]	Experimental	Paraffin	Microcapsules	Charging process	No
41.	Salaün et al. [251]	Experimental	Paraffin	Microcapsules	Charging process	No

No	Author	Methods	PCM	Enhancement method	Process	Validation
42.	Hu and Zhang [252]	Numerical	Water	Microcapsules	Charging process	Yes [253]
43.	Zhang [254]	Numerical	Water	Microcapsules	Charging process	Yes [255]
44.	Alvarado et al. [256]	Experimental	Water	Microcapsules	Charging and discharging	No
45.	Su et al. [257]	Experimental	Paraffin	Microcapsules	Charging process	No
46.	Özonur et al. [258]	Experimental	Natural coco a fatty acid mixture	Microcapsules	Charging and discharging	No
47.	Rao et al. [259]	Experimental	*N-Octadecane*	Microcapsules	Charging and discharging	No
48.	Brown [260]	Experimental	Octadecane and paraffin	Microcapsules	Charging process	No

2.5 Conclusions

This chapter presents an extensive review of significant studies relevant to the topic of this PhD research. The techniques deployed to enhance the energy performance of thermal storage systems and the methods used for to improve heat transfer in phase change materials were analysed.

From the review it can be seen that encapsulation and packed beds technologies have been analytically and experimentally well investigated with a large volume of published papers. Storage system designs and their configurations, PCM materials used, heat transfer enhancement methods, the parameters which affect the performance of the system were considered in detail. However, a limited number of studies have been devoted to assessing the pressure drops observed in packed bed thermal storage systems with determination of the friction factor as a function of the size, shape, and geometry of the packed bed system.

Different geometries and configurations of fins or other types of extended surfaces, porous media, metal foams, matrix materials and graphite materials have been extensively studied to enhance the heat transfer process in thermal storage systems by increasing the effective thermal conductivity in the mixture of phase change materials and additive components. The key disadvantage with the above methods is that it is necessary to increase the system volume in order to provide the same amount stored energy.

A considerable number of studies have been devoted to investigating the effect of nano-fluid, nano-particles, and microencapsulation on the thermal performance of LHTS.

The outcome of the literature review is that the natural convection plays an important role during the PCM solidification and melting processes. The natural convection flows are extremely sensitive to the geometry and size of the enclosures and depend on the density, viscosity and thermal conductivity of the phase change materials used. Therefore, the detailed study of natural convection inside the storage system with the liquid PCM is very important for the designing process.

The main aim of this study is formulated as a result of the conducted literature review. This is to select the most efficient means of the enhancement of heat transfer in thermal storage systems with PCMs and to derive dimensionless correlations for determination of heat transfer in such thermal storage systems as a function of process and design parameters.

The objective of this study is to develop accurate theoretical methods for predicting the heat transfer in the PCMs storage systems and determine the most efficient heat transfer enhancement methods to improve the system’s performance.

Chapter 3 Fundamentals of CFD Modelling and Data Analysis

3.1 Introduction

Computational fluid dynamic (CFD) is a powerful computer-aided engineering (CAE) tool for the analysis of physical systems involving fluid flow and associated phenomena such as chemical reactions by means of computer-based simulation. The technique has been extended to a wide range of industrial and non-industrial applications, for instance, aerodynamics, combustion in IC engines and gas turbines, mixing and separation, polymer moulding, and turbomachinery [282]. In this chapter the governing equations of the CFD modelling are described, including those used to describe solidification/melting of PCMs, modelling heat transfer through porous media, and modelling nano-particles effect using user-defined functions (UDFs).

3.2 Governing differential equations of fluid flow and heat transfer

The governing equations of the fluid flow represent mathematical statements of the conservation laws of physics [282, 283], concerning:

- The mass of fluid;
- the momentum;
- the energy;

This section is concerned with the fundamental governing equations of the fluid flow and heat transfer, which are the continuity, momentum and energy equations.

3.2.1 Continuity equation

FLUENT solves conservation equations for mass for all flows. The equation describing the continuity or mass in the computational domain is written as follows [284]:

$$\frac{d\rho}{dt} + \nabla.\left(\rho\vec{V}\right) = S_m \tag{3.1}$$

Nabla ∇ is an expression for the three-dimensional Cartesian coordinate system, i.e., the x-y-z coordinates.

Equation (3.1) is considered to be the main general equation which can be applied to both compressible and incompressible flows. Following the dispersed second phase, S_{m} is the mass source which can be added to the continuous phase, and in such case its value is zero. In additional cases involving user-defined sources its value is also zero due to the vaporization of fluid droplets [284]. The equation can then be rearranged as in Equation (3.2), which suggests that the total mass flow out of a control volume is equal to the time rate of change in density.

$$\frac{\partial\rho}{\partial t} = -\nabla.\left(\rho\vec{V}\right) \tag{3.2}$$

For 2D axisymmetric geometries, the continuity equation is given by [284]:

$$\frac{\partial\rho}{\partial t} + \frac{d}{dx}\left(\rho v_x\right) + \frac{d}{dr}\left(\rho v_r\right) + \frac{\rho v_r}{r} = S_m \tag{3.3}$$

where x is the axial coordinate; r is the radial coordinate; v_x is the axial velocity component; v_r is the radial velocity component.

3.2.2 Momentum conservation equation

The conservation of momentum equation is formulated from the fundamental physical principle (Newton's 2nd law), namely

$$\bar{F} = m\bar{a} \tag{3.4}$$

While in non-accelerating reference frame the calculation of conservation momentum can be calculated via Equation (3.5) [284]:

$$\frac{d}{dt}(\rho\vec{v}) + \nabla.(\rho\vec{v}\vec{v}) = -\nabla p + \nabla.\left(\bar{\bar{\tau}}\right) + \rho\vec{g} + \vec{F} \tag{3.5}$$

where, p is the static pressure, $\bar{\bar{\tau}}$ is the stress tensor, $\rho\vec{g}$ and $\vec{F}$ are the gravitational body force and external body force respectively (for example arising from the interface with the dispersed phase), respectively. $\vec{F}$ additionally encompasses other model-dependent source terms, such as user-defined porous-media sources.

This conservation of momentum equation is directly detected from the fundamental physical principle being applied to an infinitesimal fluid element. Equation (3.5) is in a non-conservation form due to the fluid elements affecting the flow movement; it is called the *Navier-Stokes* equation as it is a vector equation. The *Navier-Stokes* equation form is as follows [283]:

$$\frac{\partial(\rho u)}{\partial t} + \nabla.\left(\rho u\vec{V}\right) = -\frac{dp}{dx} + \frac{d\tau_{xx}}{dx} + \frac{d\tau_{yx}}{dy} + \frac{d\tau_{zx}}{dz} + \rho f_x \tag{3.6}$$

$$\frac{\partial(\rho v)}{\partial t} + \nabla.\left(\rho v\vec{V}\right) = -\frac{dp}{dy} + \frac{d\tau_{xy}}{dx} + \frac{d\tau_{yy}}{dy} + \frac{d\tau_{zy}}{dz} + \rho f_y \tag{3.7}$$

$$\frac{\partial(\rho w)}{\partial t} + \nabla.\left(\rho w\vec{V}\right) = -\frac{dp}{dz} + \frac{d\tau_{xz}}{dx} + \frac{d\tau_{yz}}{dy} + \frac{d\tau_{zz}}{dz} + \rho f_z \tag{3.8}$$

where *u*, *v*, and *w* are the velocity components (m/s) for the *x*, *y*, and *z* axe respectively; τ_{xx}, τ_{yy}, τ_{zz} are the components of normal stress for each direction; and τ_{ij} are the components of the shear stress acting on each direction.

The stress tensor $\overline{\overline{\tau}}$ is expressed by [284]:

$$\overline{\overline{\tau}} = \mu\left[\left(\nabla\vec{v} + \nabla\vec{v}^{T}\right) - \frac{2}{3}\nabla.\vec{v}\,I\right] \tag{3.9}$$

where μ is the molecular viscosity; *I* is the unit tensor; and the second term on the right-hand side is the effect of volume dilation.

For 2D axisymmetric geometries, the axial and radial momentum conservation equation are given by [284]:

$$\begin{aligned}&\frac{\partial}{\partial t}\left(\rho v_x\right) + \frac{1}{r}\frac{\partial}{\partial x}\left(r\rho v_x v_x\right) + \frac{1}{r}\frac{\partial}{\partial r}\left(r\rho v_r v_x\right) = -\frac{\partial p}{\partial x} + \frac{1}{r}\frac{\partial}{\partial x}\left[r\mu\left(2\frac{\partial v_x}{\partial x} - \frac{2}{3}\left(\nabla.\vec{v}\right)\right)\right] \\ &+ \frac{1}{r}\frac{\partial}{\partial r}\left[r\mu\left(\frac{\partial v_x}{\partial r} + \frac{\partial v_r}{\partial x}\right)\right] + F_x\end{aligned} \tag{3.10}$$

$$\begin{aligned}&\frac{\partial}{\partial t}\left(\rho v_r\right) + \frac{1}{r}\frac{\partial}{\partial x}\left(r\rho v_x v_r\right) + \frac{1}{r}\frac{\partial}{\partial r}\left(r\rho v_r v_r\right) = -\frac{\partial p}{\partial r} + \frac{1}{r}\frac{\partial}{\partial x}\left[r\mu\left(\frac{\partial v_r}{\partial x} + \frac{\partial v_x}{\partial r}\right)\right] \\ &+ \frac{1}{r}\frac{\partial}{\partial r}\left[r\mu\left(2\frac{\partial v_r}{\partial r} - \frac{2}{3}\left(\nabla.\vec{v}\right)\right)\right] - 2\mu\frac{v_r}{r^2} + \frac{2}{3}\frac{\mu}{r}\left(\nabla.\vec{v}\right) + \rho\frac{v_z^2}{r} + F_r\end{aligned} \tag{3.11}$$

where

$$\nabla.\vec{v} = \frac{\partial v_x}{\partial x} + \frac{\partial v_r}{\partial r} + \frac{v_r}{r} \tag{3.12}$$

and v_z is the swirl velocity.

3.2.3 Turbulence models

Fluctuating velocity fields is one of the characteristics of turbulent flows, the fluctuations have a mixture of transported quantities as momentum, energy, and species concentration resulting in the fluctuation of transported quantities. These fluctuations are characterized by small scales with high frequencies; which makes them computationally expensive to be simulated in practical engineering calculations. The governing equation, in the other hand, is time-averaged and it can eliminate small scale calculations by manipulation. Consequently, there is an increase in unknown variables in the modified equations which demands turbulence models to determine these variables in terms of known quantities [284]. In the present study, in the computational model it was assumed that the flow of the molten PCM was laminar, whilst the flow in the pipe depends on the mass flow input of the HTF. Therefore, the flow of the HTF in some cases was laminar and in others was turbulent.

The following options for turbulent models are available in ANSYS FLUENT [284]:

- Spalart-Almaras model;
- k-ε model:
    - Standard k-ε model;
    - Renormalization-group (RNG) k-ε model;
    - Realizable k-ε model;
- K-ω model:
    - Standard k-ω model;
    - Shear-stress transport (SST) k-ω model;

- Reynolds stress model (RSM);
    - Linear pressure-strain RSM;
    - Quadratic pressure strain RSM;
    - Low-Re stress-omega RSM l;
- Detached eddy simulation (DES) model; which includes one of the following RANS models:
    - Spalart-Almaras RANS model;
    - Realized k-ε RANS model;
    - Shear-stress transport k-ω model;
- Large eddy simulation (LES) model, which includes one of the following sub-scale models:
    - Smagorinsky-Lilly subgrid-scale model;
    - WALE subgrid-scale model;
    - Dynamic Smagorinsky model;
    - Kinetic-energy transport subgrid model.

3.2.3.1 The k-ε model

The simplest turbulence models are two-equation models such as the k-ε model. As mentioned above, there are three available k-ε models in the 13th version of ANSYS FLUENT: the standard k-ε model, the renormalization-group (RNG) k-ε model, and the

realizable *k*-*ε* model. All three models have a similar formula, with transport equations for *k* and *ε*. The major differences between the models are as follows [284]:

- The method of calculating turbulent viscosity;
- The turbulent Prandtl numbers governing the turbulent diffusion of *k* and *ε*;
- The generation and destruction terms in the *ε* equation

3.2.3.2 The standard *k*-*ε* model

The standard *k*-*ε* model is a semi-empirical model based on model transport equations for the turbulence kinetic energy, *k*, and its dissipation rate *ε*. The standard *k*-*ε* is valid only for fully turbulent flows and the effect of molecular viscosity is negligible. The transport equations for the standard *k*-*ε* model are given below [284]:

$$\frac{\partial}{\partial t}(\rho k)+\frac{\partial}{\partial x_i}(\rho k u_i)=\frac{\partial}{\partial x_j}\left[\left(\mu+\frac{\mu_t}{\sigma_k}\right)\frac{\partial k}{\partial x_j}\right]+G_k+G_b+\mathrm{P}\varepsilon-Y_M+S_K \tag{3.13}$$

and

$$\frac{\partial}{\partial t}(\rho \varepsilon)+\frac{\partial}{\partial x_i}(\rho \varepsilon u_i)=\frac{\partial}{\partial x_j}\left[\left(\mu+\frac{\mu_t}{\sigma_\varepsilon}\right)\frac{\partial \varepsilon}{\partial x_j}\right]+G_{1\varepsilon}\frac{\varepsilon}{k}(G_K+G_{3\varepsilon}G_b)-C_{2\varepsilon}\rho\frac{\varepsilon^2}{k}+S_\varepsilon \tag{3.14}$$

where G_k is the generation of turbulent kinetic energy due to the mean velocity gradients; G_b is the generation of kinetic energy due to buoyancy; Y_M represents the contribution of the fluctuating dilatation in compressible turbulence to the overall dissipation rate; $G_{1\varepsilon}$, $G_{2\varepsilon}$, and $G_{3\varepsilon}$ are constants; σ_ε and σ_k are the turbulent Prandtl numbers for *k* and *ε* respectively; $\mathrm{S_K}$ and S_ε are user-defined source terms.

The turbulent viscosity, μ_t, is computed by combining k and ε as follows [284]:

$$\mu_t = \rho C_\mu \frac{k^2}{\varepsilon} \tag{3.15}$$

The model constants $G_{1\varepsilon}$, $G_{2\varepsilon}$, σ_k, σ_ε, and C_μ have the following default values in FLUENT [284]:

$G_{1\varepsilon} = 1.44, G_{2\varepsilon} = 1.92, C_\mu = 0.09, \sigma_k = 1, \text{and } \sigma_\varepsilon = 1.3$

3.2.3.3 Effects of buoyancy on turbulence in the *k*-*ε* model

In ANSYS FLUENT using the *k*-*ε* models where non-zero gravity field and temperature gradient are present, both would account for the generation of k due to buoyancy (G_b in Equation (3.13)), and thus contributes to the calculation of ε in Equation (3.14) [284].

The generation of the turbulence due to buoyancy is given by [284]:

$$G_b = \beta g_i \frac{\mu_t}{\mathrm{Pr}_t} \frac{\partial T}{\partial x_i} \tag{3.16}$$

where Pr_t is the turbulent Prandtl number for energy and g_i is the component of the gravitational vector in the ith direction. For the standard and realizable *k*-*ε* models, the default value of Pr_t is 0.85. In the case of RNG *k*-*ε* model, $Pr_t = 1/\alpha$, where α is given by [284]:

$$\left|\frac{\alpha - 1.3929}{\alpha_0 - 1.3929}\right|^{0.6321} \left|\frac{\alpha + 2.3929}{\alpha_0 + 2.3929}\right|^{0.3679} = \frac{\mu_{mol}}{\mu_{eff}} \tag{3.17}$$

where $\alpha_0 = 1/Pr = k/\mu c_p$. In the high Reynolds number limit ($\frac{\mu_{mol}}{\mu_{eff}} \ll 1$), and ($\alpha_k = \alpha_z \approx 1.393$). The coefficient of thermal expansion, β, is expressed as:

$$\beta = -\frac{1}{\rho}\left(\frac{\partial \rho}{\partial T}\right)_P \tag{3.18}$$

For ideal gases, Equation (3.16) reduced to:

$$G_b = -g_i \frac{\mu_t}{\rho \mathrm{Pr}_t} \frac{\partial p}{\partial x_i} \tag{3.19}$$

In ANSYS FLUENT, if both non-zero gravity field and non-zero temperature (or density) gradient are present then the effects of buoyancy on the generation of *k* must be included. The buoyancy effects on ε are neglected by setting G_b to zero in the transport equation of ε (Equation (3.14)). If the effects of buoyancy on ε are to be included the value of G_b determined by Equation (3.19) is to be used in the transport equation for ε (Equation (3.14)) [284].

The degree to which ε is affected by buoyancy is calculated by [284]:

$$C_{3\varepsilon} = \tanh\left|\frac{v}{u}\right| \tag{3.20}$$

where *v* is the component of the flow velocity parallel to the gravitational vector and *u* is the component of the flow velocity perpendicular to the gravitational vector. In this way, $C_{3\varepsilon}$ will become 1 for buoyant shear layers for which the main flow direction is aligned with the direction of gravity. For buoyant shear layers perpendicular to the gravitational vector, $C_{3\varepsilon}$ will become zero [284].

3.2.4 Energy conservation equation

To predict the conduction and convection heat transfer, FLUENT uses the following energy conservation term [284]:

$$\frac{\delta}{\delta t}(\rho E)+\nabla.\left(\vec{u}\left(\rho E+p\right)\right)=-\nabla.\left(k_{eff}\nabla T-\sum_{j}h_{j}\vec{J}_{j}+\left(\bar{\bar{\tau}}_{eff}.\vec{u}\right)\right)+S_{h} \tag{3.21}$$

where k_{eff} is the effective thermal conductivity, which includes turbulent thermal conductivity defined by the selected turbulent model; $\vec{j}_j$ is the diffusion flux of spices j and S_h included heat in the reaction and any other volumetric heat sources defined by the user. The first three terms on the right-hand side represent conduction heat, species diffusion and viscous dissipation respectively.

$$E=h-\frac{p}{\rho}-\frac{u^2}{2} \tag{3.22}$$

where sensible enthalpy is defined for ideal gases as:

$$h=\sum_{j}Y_{j}h_{j} \tag{3.23}$$

And for incompressible flow as:

$$h=\sum_{j}Y_{j}h_{j}+\frac{p}{\rho} \tag{3.24}$$

In Equations (3.23) and (3.24), Y_j is the mass fraction of species j and:

$$h_{j}=\int_{T_{ref}}^{T}C_{p},jdT \tag{3.25}$$

where T_{ref} is 298.15K.

Natural convection can be modelled using two methods in FLUENT. These are the Boussinesq model and the Prewsise model. For the Prewsise model the user inputs the change in density experienced in the fluid as a function of temperature, whether it be a polynomial or a set of data points which describes the variation in density. The Boussinesq model treats the

density as a constant value in all solver equations, except for the buoyancy term in the momentum equation [284]:

$$(\rho - \rho_o) g \approx -\rho_o \beta (T - T_o) g \tag{3.26}$$

where ρ_o is the (constant) density of the flow, T_o is the operating temperature, and β is the thermal expansion coefficient. Equation (3.26) is obtained by using the Boussinesq approximation ($\rho = \rho_o (1 - \beta T_o)$) to eliminate ρ from the buoyancy term. This approximation is accurate as long as changes in actual density are small; specifically, the Boussinesq approximation is valid when $\beta (T - T_o) \ll 1$.

3.2.5 Convection heat and mass transfer modelling in the *k-ε* model

In ANSYS FLUENT, Reynolds' analogy concept is adapted to model turbulent heat transport for turbulent momentum transfer. The modelled energy equation is expressed in[284]:

$$\frac{\partial}{\partial t}(\rho \mathrm{E}) + \frac{\partial}{\partial x_i}\left[u_i(\rho \mathrm{E} + p)\right] = \frac{\partial}{\partial x_j}\left(k_{eff} \frac{\partial T}{\partial x_j} + u_i (\tau_{ii})_{eff} \right) + S_h \tag{3.27}$$

where E is the total energy, k_{eff} is the effective thermal conductivity, and $(\tau_{ii})_{eff}$ is the deviatoric stress tensor, defined as [284]:

$$(\tau_{ij})_{eff} = \mu_{eff} \left(\frac{\partial u_j}{\partial x_i} + \frac{\partial u_i}{\partial x_j} \right) - \frac{2}{3} \mu_{eff} \frac{\partial u_k}{\partial x_k} \delta_{ij} \tag{3.28}$$

To represent viscous heating, the term $(\tau_{ij})_{eff}$ is used, where it is computed in the density-based solver. It can be represented it in the Viscous Model Dialog Box, if it is not calculated in the pressure-based solver [284].

For the standard and realized *k-ε* models, effective thermal conductivity is given by [284]:

$$k_{eff} = k + \frac{c_p \mu_t}{\mathrm{Pr}_t} \tag{3.29}$$

where *k*, is the thermal conductivity and the default value of the turbulent Prandtl number is 0.85.

3.2.6 Numerical solution for PCMs

The mathematical formulations for solving PCM related problems have been categorized [285] as fixed grid, variable grid, front-fixing, adaptive grid generation, and enthalpy methods. Two methods are used to analyse the heat transfer in solid-liquid PCMs. These are the temperature-based and enthalpy-based methods. In the former, temperature is considered to be a single dependent variable. The energy equations for both solid and liquid are formulated separately; and thus the solid-liquid interface positions can be tracked easily to achieve an accurate solution for the problem [286].

$$\frac{\partial T_s}{\partial n} k_s = \frac{\partial T_l}{\partial n} k_l + \rho L v_n \tag{3.30}$$

where T_s denotes the temperature in the solid phase; T_l is the temperature in the liquid phase. k_s, and k_l are the thermal conductivity of the solid phase and liquid phase respectively; *n* is the unit normal vector to the interface; *L* is the latent heat of the freezing; and v_n is the normal component of the velocity of the interface, as shown in Figure 3.1.

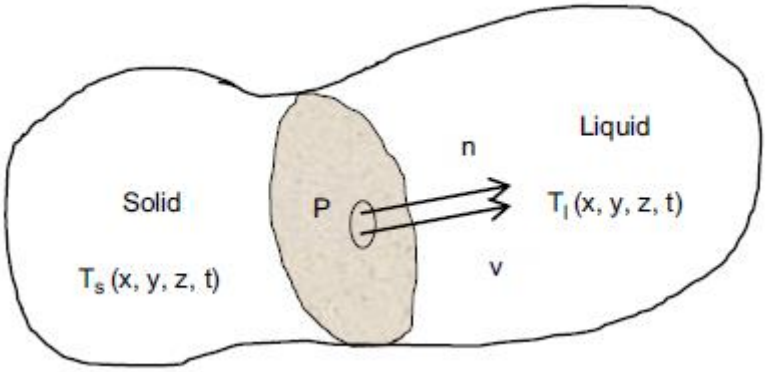

Figure 3.1: Solid-liquid interface for a multidimensional situation [285].

However, in the enthalpy-based method, the solid-liquid interface position does not need to be tracked. There are several advantages of using this method [287]:

1. The governing equations are similar to those for the single-phase.
2. No explicit conditions need to be satisfied at the solid-liquid interface.
3. The enthalpy formulation involves the solution within a mushy zone, involving both solid and liquid materials, between the two standard phases.
4. The phase change problem can be solved more easily.

In the enthalpy-based method

$$\frac{\partial(\rho H)}{\partial t} + \nabla.(\rho \bar{v} H) = \nabla.(k \Delta T) + S \tag{3.31}$$

where T denotes the temperature, k is the thermal conductivity, ρ is the density of the PCM, $\bar{v}$ is the fluid velocity, H is the enthalpy, and S is the source term.

Several software suites can be used to solve the PCM melting and solidification processes, including COMSOL Multiphysics and Star-CMM. Also, some researchers have developed

programs using the computational languages C++, Fortran, and Matlab in order to study the heat transfer in PCMs [286]. Some software has a specific model which can simulate the phase change which occurs at a single temperature (pure metals) or over a range of temperature (alloys, mixtures) [284].

3.2.6.1 Modelling solidification and melting

An enthalpy-porosity method is used for modelling the solidification/melting process [284]. This technique is described in detail by Voller and Prakash [288].

The energy conservation equation for this case is written as:

$$\frac{\partial}{\partial t}(\rho H)+\nabla.(\rho \vec{v} H)=\nabla .(k\nabla T)+S \tag{3.32}$$

where *H,* is the enthalpy, ρ is the density, $\vec{v}$ is fluid velocity and *S* is the source term.

The enthalpy of the material is calculated as the sum of the sensible heat, *h*, and latent heat, ΔH:

$$H = h + \Delta H \tag{3.33}$$

The sensible heat is calculated as:

$$h = h_{ref} + \int_{T_{ref}}^{T} c_p dT \tag{3.34}$$

where, h_{ref} is the reference enthalpy, T_{ref} is the reference temperature and c_p is the specific heat at constant temperature.

The latent heat is also calculated as:

$$\Delta H = \beta_l L \tag{3.35}$$

The liquid fraction, β_l, can be calculated as:

$$\begin{aligned} &\beta_l = 0, when T < T_{solid} \\ &\beta_l = 1, when T > T_{solid} \\ &\beta_l = \frac{T - T_{solid}}{T_{liquid} - T_{solid}} \ if\ T_{solid} < T < T_{liquid} \end{aligned} \tag{3.36}$$

The solid and liquid temperatures are also calculated as

$$T_{solid} = T_{melt} + \sum_{solutes} K_i m_i Y_i \tag{3.37}$$

$$T_{liquid} = T_{melt} + \sum_{solutes} m_i Y_i \tag{3.38}$$

where, K_i is the partition coefficient of solute *i*, which is the ratio of the concentration solid to that in the liquid at the interface; Y_i is the mass fraction of solute *i*, and m_i is the slope of the liquid surface with respect to Y_i [284].

The source term in the momentum equation can be written as [284]:

$$S = \frac{(1-\beta)}{(\beta_l^3 + \epsilon)} A_{mush} (\vec{v} - \vec{v}_p) \tag{3.39}$$

Due to the Darcy's law damping terms as a source term are added to the momentum equation because of the effect of phase change on convection, whereas ϵ is a small constant number (0.001) used to prevent division by zero, and A_{mush} is the mushy zone constant. Values between 10^4 and 10^7 are recommended for most computations [284]. In the present study, the mushy zone was set to 10^5. $\vec{v}_p$ is the solid velocity due to pulling solidification materials out

of the domain; and in the present study, pull velocities are not included in the solution and so $\vec{v}_p$ is set to zero.

The liquid velocity can be calculated by the following equation [284]:

$$\vec{v}_{liq} = \frac{\left(\vec{v} - \vec{v}_p\left(1-\beta_l\right)\right)}{\beta_l} \tag{3.40}$$

3.2.6.2 Modelling heat transfer through porous media

In porous media regions the ANSYS FLUENT standard energy transport equation resorts to modify conduction flux and transient terms only. In the conduction flux; where conductivity and the transient terms include the thermal inertia of the solid region on the medium as shown below [284]:

$$\begin{aligned} &\frac{\partial}{\partial t}\left(\gamma\rho_f E_f + \left(1-\xi\right)\rho_s E_s\right) + \nabla.\left(\vec{v}\left(\rho_f E_f + p\right)\right) = \\ &\nabla.\left[k_{eff}\nabla T - \left(\sum_i h_i J_i\right) + \left(\bar{\bar{\tau}}.\vec{v}\right)\right] + S_f^h \end{aligned} \tag{3.41}$$

where E_f is the total fluid energy; E_s is the total solid energy, ξ is the porosity of the medium, and S_f^h is the fluid enthalpy source term.

The effective thermal conductivity (k_{eff}) of the medium is calculated by ANSYS FLUENT the volume average of the fluid and the solid conductivity [284]:

$$k_{eff} = \xi k_f + \left(1-\xi\right)k_s \tag{3.42}$$

where k_f is the fluid thermal conductivity (including the turbulent contribution, k_t);and k_s is the solid medium thermal conductivity.

In terms of the momentum equation for the porous media, an additional source term is added to the standard flow equations. The source term is composed of two parts: a viscous loss term (Darcy, the first term on the right-hand side of Equation (3.43)), and an inertial loss term (the second term on the right-hand side of Equation (3.43)) [284]:

$$S_i = -\left(\sum_{j=1}^{3} D_{ij} \mu \upsilon_j + \sum_{j=1}^{3} C_{ij} \frac{1}{2} \rho |\upsilon| \upsilon_j \right) \tag{3.43}$$

where S_i is the source term for the *ith* (*x, y, or z*) momentum equation, $|v|$ is the magnitude of the velocity, and *D* and *C* are prescribed materials. In the porous cell, the pressure gradient is effected by momentum sink, leading a pressure drop proportional to the fluid velocity (or velocity squared) in the cell.

For simple homogeneous media:

$$S_i = -\left(\frac{\mu}{\alpha} \upsilon_i + C_2 \frac{1}{2} \rho |\upsilon| \upsilon_i \right) \tag{3.44}$$

where α is permeability and C_2 is an inertial resistance factor.

In laminar flows through porous media, the pressure drop is normally proportional to the velocity, and the constant C_2 can be considered to be zero. However, ANSYS FLUENT calculates the pressure drop in each of the three (*x*,*y*,*z*) coordinate directions as follows [284]:

$$\Delta p_x = \sum_{j=1}^{3} \frac{\mu}{\alpha_{xj}} \upsilon_j \Delta n_x \tag{3.45}$$

$$\Delta p_y = \sum_{j=1}^{3} \frac{\mu}{\alpha_{yj}} \upsilon_j \Delta n_y \tag{3.46}$$

$$\Delta p_z = \sum_{j=1}^{3} \frac{\mu}{\alpha_{zj}} \upsilon_j \Delta n_z \tag{3.47}$$

where $1/\alpha_{ij}$ are the entries in the matrix D in Equation (3.43), v_i are the velocity components in the *x, y,* and *z* directions, and Δn_x, Δn_y, and Δn_z are the thicknesses of the medium in the *x, y,* and *z* directions.

3.2.6.3 Modelling nano-particles using a user-defined function (UDF)

In order to investigate the effect of nanoparticles in small volumetric fractions on the heat transfer rate, UDF is written in the C++ language to define the temperature-dependence of the thermo-physical properties of the PCM with or without nanoparticles.

The thermo-physical properties of PCMs, such as density and viscosity, are temperature-dependent and can be determined by the following correlations [286, 289, 290]:

$$\rho_{pcm} = \frac{\rho_l}{\left(\beta\left(T - T_m\right) + 1\right)} \tag{3.48}$$

$$\mu_{pcm} = \beta \times exp\left(A + B/T\right) \tag{3.49}$$

where ρ_l is the density of the PCM at the melting temperature T_m, β is the PCM thermal expansion coefficient, *A*= -4.25, and B=1790 as suggested by Reid et al. [291].

The density and specific heat capacity of the composite of nanoparticles with PCM is defined as [184, 234]:

$$\rho_{npcm} = \varnothing_{np}\rho_{np} + \left(1 - \varnothing_{np}\right)\rho_{pcm} \tag{3.50}$$

$$Cp_{npcm} = \frac{\varnothing_{np}\rho_{np}Cp_{np} + \left(1 - \varnothing_{np}\right)\rho_{pcm}Cp_{pcm}}{\rho_{npcm}} \tag{3.51}$$

where ϕ_{np} and ρ_{np} are the volumetric fraction and density of nanoparticles respectively.

The effective thermal conductivity of the nano-PCM, which includes the effects of particle size, particle volume fraction and temperature dependence as well as the properties of the base PCM and particles subject to Brownian motion, is given by [220]:

$$k_{npcm} = \left[\frac{k_{np} + 2k_{pcm} - 2\left(k_{pcm} - k_{np}\right)\varnothing_{np}}{k_{np} + 2k_{pcm} + \left(k_{pcm} - k_{np}\right)\varnothing_{np}} \right] k_{pcm} + \left[\beta_l k_1 \varsigma \phi_{np} \rho_{pcm} Cp_{pcm} \sqrt{\frac{BT}{\rho_{np} d_{np}}} \right] f_{T,\phi} \quad (3.52)$$

The first part of Equation (3.52) is obtained from the Maxwell model while the second part accounts for Brownian motion, which causes the effective thermal conductivity to be temperature-dependent.

In Equation (3.52) d_{np} is the nanoparticle diameter, B is the Boltzmann constant $1.381\times10^{-23} J/K$, k_1 is the Brownian motion, 5×10^4, and β_l is the Brownian motion term for the liquid fraction, with its value as defined in Equation (3.36).

The empirical relationship is used to account for the Brownian motion, given by [220]:

$$\varsigma = \varsigma_1 \left(100\varnothing_{np}\right)^{\varsigma_2} \quad (3.53)$$

$$\mathrm{f}_{\mathrm{T},\phi} = \left(\mathrm{C}_1\varnothing_{\mathrm{np}} + \mathrm{C}_2\right)\left(\frac{\mathrm{T}}{\mathrm{T}_{\mathrm{ref}}}\right) + \left(\mathrm{C}_3\varnothing_{\mathrm{np}} + \mathrm{C}_4\right) \quad (3.54)$$

where C_1, C_2, C_3 and C_4 are constants.

The dynamic viscosity of the composite of nanoparticles with PCM is then defined as [220]:

$$\mu_{npcm} = C_1 \exp\left(C_2\varnothing_{np}\right)\mu_{pcm} \quad (3.55)$$

3.2.6.4 Choosing the solver

In Fluent there are two main solvers: the density-based solver and the pressure-based solver. The problem of PCM solidification and melting can only be solved by the pressure-based solver. Fluent is equipped with two pressure solver algorithms; a segregated algorithm and a coupled algorithm, see Figure3.2 [284, 286]. Using transient simulations, the flow inside the pipe is being analysed with the *k-epsilon* turbulence and the solidification/melting model was enabled to investigate the phase change phenomena in paraffin wax.

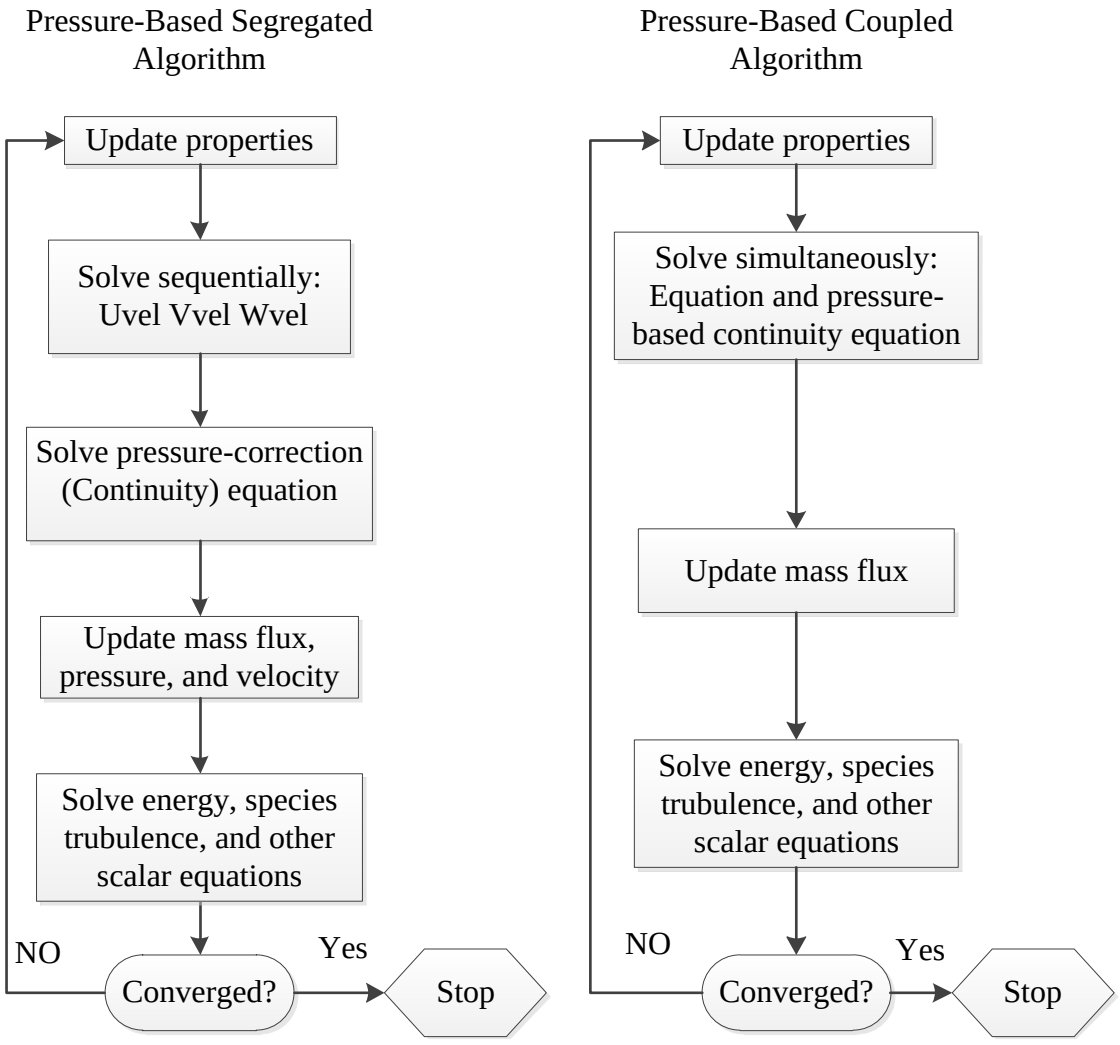

Figure 3.2: Overview of the pressure-based solution methods [284].

3.3 Data analysis

3.3.1 Average heat transfer coefficient

The local heat transfer coefficient could not be estimated accurately for the present thermal storage system as there is a temperature difference between the outer surface of the HTF pipe and the PCM along both axial and radial directions. Consequently, the average heat transfer coefficient for the melting process is calculated instead using the following equations [292] for the temporal heat transfer coefficient

$$h_p = \frac{q}{A \times \Delta T\left(LMTD\right)} \tag{3.56}$$

where, the surface area of HTFP is calculated using the following equation:

$$A = \pi D_o l \tag{3.57}$$

The heat transfer rate (q) in the thermal storage can be calculated through the HTF's enthalpy reduction rate in the HTF [293]. This enthalpy reduction can be calculated through the following equation:

$$q = \dot{m} c_p \left(T_i - T_o\right) \tag{3.58}$$

where, $\dot{m}$ is the HTF mass flow, T_i and T_o are the HTF's inlet and outlet temperatures respectively.

The average heat transfer coefficient is:

$$\overline{h_p} = \frac{Q_{total}}{A \times \Delta T\left(LMTD\right) t_n} \tag{3.59}$$

where Q_{total} is the total heat transfer in the PCM from the time when the test started and until the instance when the full melting is achieved, and t_n is the corresponding elapsed time.

3.3.2 Dimensional analysis

Different cases were analysed with various system's geometrical and thermo-physical parameters. To generalise results it is vital to characterise them in the dimensionless form. The dimensional parameters used in this work are:

Reynolds number (*Re*) -

$$Re = \frac{\rho_f u_m D}{\mu_f} \tag{3.60}$$

$$u_m = \frac{\dot{m}}{\rho_f A_c} \tag{3.61}$$

$$A_c = \frac{\pi D^2}{4} \tag{3.62}$$

$$Re = \frac{4\dot{m}}{\pi D \mu_f} \tag{3.63}$$

where u_m is the mean fluid velocity in the flow cross section, D is the pipe diameter, μ_f is the fluid's dynamic viscosity, ρ_f is the fluid's density, $\dot{m}$ is the fluid's mass flow, and A_c is the cross-sectional area of the pipe.

In the current study, the storage unit is considered as a container with a central circular pipe surrounded by the PCM, a working fluid flows inside the pipe, and the heat by conduction is transferred through the pipe walls to the PCM. The heat conduction results in a liquid layer formed between the HTF's pipe outer surface and the solid PCM. As the heat is transferred to

the PCM, the liquid/solid interface expands gradually both in the axial and radial directions. The natural convection heat transfer starts to dominate in the liquid region of the PCM. The buoyancy force induces a fluid current and the molten PCM ascends upwards and after cooling flows downwards to complete the natural convection circle. The density difference is attributed to the thermal expansion coefficient β, which is calculated using Equation (3.64)

$$\beta = -\frac{1}{\rho}\left(\frac{d\rho}{dT}\right)_p \approx -\frac{1}{\rho}\left(\frac{\rho_\infty - \rho}{T_\infty - T}\right) = -\frac{1}{\rho}\left(\frac{\Delta\rho}{\Delta T}\right) \tag{3.64}$$

where ρ is the density and T is the temperature.

Free convection flows can be quantified using the Grashof number (*Gr)*, which is the ratio between the buoyancy and the PCM's acting viscous force, and Prandtl number (*Pr*) which is the ratio between viscous diffusion rate and the thermal diffusion rate.

$$Gr = \frac{g\beta\Delta T_H r_{eq}^3}{v_{pcm}^2} \tag{3.65}$$

$$v_{pcm} = \frac{\mu_{pcm}}{\rho_{pcm}} \tag{3.66}$$

$$r_{eq} = \frac{D_H - D_o}{2} \tag{3.67}$$

$$\begin{aligned} D_H &= \frac{2Wh}{Wh} \qquad (\text{for regtangular storage unit}) \\ D_H &= \mathrm{D}_{sell} \qquad (\text{for cylinderical storage unit}) \end{aligned} \tag{3.68}$$

$$P_r = \frac{k_{pcm}}{\rho_{pcm} Cp_{pcm}} \tag{3.69}$$

where g is the gravitational acceleration, β is the thermal expansion coefficient, v_{pcm} is kinematic viscosity of PCM, μ_{pcm} is PCM dynamic viscosity, ρ_{pcm} is PCM density, ΔT_H is

the temperature difference between the HTF and the PCM melting temperature, k_{pcm} is the PCM thermal conductivity and $C_{P\,pcm}$ is the PCM specific heat capacity, D_H is the hydraulic diameter, D_o is the pipe outer diameter, D_{sell} is the outer diameter of the cylindrical storage unit, *W* is the rectangular storage width, and *h* is the storage height.

Usually, Grashof number and Prandtle number are combined to define a new dimensional parameter, which is the Rayleigh number (*Ra*) The Rayleigh number indicates transition from laminar to turbulence flow in the boundary layer flow in the natural convection. Rayleigh number is defined using the following equations:

$$R_a = G_r \times P_r \tag{3.70}$$

$$Ra = \frac{g\beta Cp_{pcm}\rho_{pcm}\Delta T_H r_{eq}^3}{\mu_{pcm}k_{pcm}} \tag{3.71}$$

Additionally, the Fourier number (*Fo)* is often used in presentation of results which is the time's dimensional measure for melting or solidification. *Fo* is calculated using the following equation:

$$Fo = \frac{\left(\alpha_{pcm}t_m\right)}{\left(r_{eq}\right)^2} \tag{3.72}$$

where α_{pcm} is the PCM's thermal diffusivity.

Also the Stefan number (*Ste)* is used which indicates the difference between the HTF's inlet temperature and the PCM's melting temperature. *Ste* is calculated using the following equation:

$$Ste = \frac{Cp_{pcm}\Delta T_H}{\lambda_{pcm}} \tag{3.73}$$

where λ_{pcm} is the PCM's latent heat.

Finally, the temporal Nusselt number (*Nu*) is used to quantify heat transfer and this can be calculated using the following equation:

$$Nu = \frac{h_p r_{eq}}{k_{pcm}} \tag{3.74}$$

The time-average Nusselt number, $\overline{Nu}$ is defined as

$$\overline{Nu} = \frac{\overline{h_p} r_{eq}}{k_{pcm}} \tag{3.75}$$

Chapter 4 CFD Model Validation

This chapter validates the capability of CFD modelling technique to accurately describe processes in the thermal storage system with the PCM. CFD modelling using FLUENT ANSYS was conducted for the experimental case described by Lacroix [9] and numerical results obtained in this study were compared to his published experimental results for the CFD model validation purposes. The comparison between experimental and numerical results was carried out in terms of the temperature distributions, average volume of the PCM liquid fraction, and the HTF outlet temperature. Additionally, the detailed parametric study of the storage system with the PCM and nano-particles was performed and results obtained were discussed with dimensional correlations being proposed to be used in the designing process.

4.1 The experimental case study by Lacroix

Lacroix experimentally studied the transient melting of the PCM in the shell-and-tube storage unit with the PCM on the shell side, and the HTF flowing inside the tube. Additionally, he conducted a series of experiments to study the effect of different thermal and geometric parameters of the heat transfer process.

4.1.1 The physical model

The system's physical model is presented in Figure 4.1. The PCM fills the shell with the diameter of D_e, whereas the HTF flows through the tube with diameter of Di. The PCM is

commercially available material *n-Octadecane*. The thermo-physical properties of the *n-Octadecane* are presented in Table 4.1.

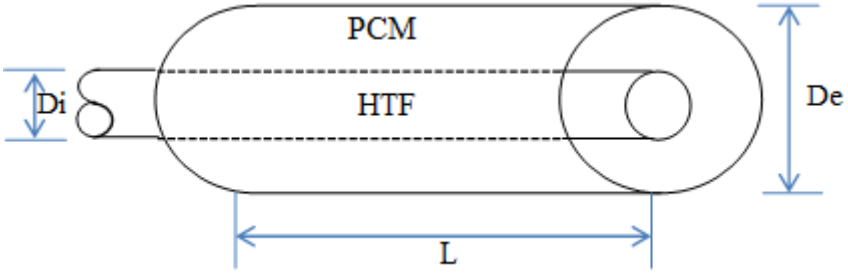

Figure 4.1**:** Schematic representation of the test unit.

Table 4.1**:** Thermo-physical properties of the *n-Octadecane* [294-296].

Properties	**Value**
Liquid density, ρ_l	814 kg/m^3
Solid density, ρ_s	814 kg/m^3
Liquid Thermal conductivity, k_l	0.148 W/(m^{o}C)
Solid Thermal conductivity, k_s	0.358 W/(m^{o}C)
Liquid specific heat, Cp_l	2200 J/Kg ^{o}C
Solid specific heat, Cp_s	1900 J/Kg ^{o}C
Latent heat, L	243.5 KJ/Kg
Viscosity, μ	3.878×10^{-3} Pa s
Thermal expansion coefficient, β	0.00091 1/K
Melting Temperature, T_m	300.7 K

For modelling of the phase change region, the enthalpy-based method [296, 297] was used. In addition, the following assumptions were made [9]:

- The PCM and the HTF thermo-physical properties are temperature independent;

- The PCM is homogenous and isotropic;
- Heat conduction is axisymmetric inside the tube;
- The tube's thermal resistance is negligible;
- The local convection heat transfer coefficient for the working fluid may vary along the tube.

Therefore, the conservation equations used for the PCM (4.1) and HTF (4.2) are:

$$\frac{\partial h}{\partial t} = \frac{1}{r}\frac{\partial}{\partial r}\left(\alpha r \frac{\partial h}{\partial r}\right) + \frac{\partial}{\partial z}\left(\alpha \frac{\partial h}{\partial z}\right) - \rho \Delta h_f \frac{\partial f}{\partial t} \tag{4.1}$$

$$\rho_c C_c \pi R_i^2 \frac{\partial T_c}{\partial t} = 2\pi R_i U (T - T_c) - \dot{m} C_c \frac{\partial T_c}{\partial z} \tag{4.2}$$

where $\alpha = k / \rho C$ is the thermal diffusivity; k is thermal conductivity; U is the convective heat transfer coefficient, T_c is the temperature of HTF, ρ is density; C is the specific heat [9].

During the melting, the effect of the convection heat transfer is calculated using the effective thermal conductivity for the liquid as a function of Rayleigh number based on melt layer thickness [42].

$$\frac{k_e}{k_l} = cRa^n \tag{4.3}$$

$$Ra = \frac{g\beta C_l (T_w - T_m) L^3}{\mu k_l} \tag{4.4}$$

However, the values for the constant c and n in Equation (4.3) are estimated experimentally and were found to be 0.099 and 0.25, respectively [9].

Consequently, the total enthalpy is calculated using the following equation:

$$H(T) = h(T) + \rho_s f \Delta h_f \tag{4.5}$$

where

$$h(T) = \int_{T_m}^{T} \rho_k C_k \, dT \tag{4.6}$$

Here ρ_k is the phase density; C_k is the phase specific heat; T_m is the phase change temperature; f is the liquid fraction.

Lacroix also produced numerical results using the finite difference method to solve the above equations. In the beginning of his simulations, the same temperature was set for both PCM and HTF. Then the working fluid was assigned the certain inlet temperature $(T)_{in}$ and mass flow rate $\dot{m}$. Further details concerning the numerical model by Lacroix can be found in [9, 296].

4.1.2 Experimental setup

The test unit scheme is shown in Figure 4.2. It consists of two concentric tubes. The inside tube (D_i=12.7 mm, D_o=15.8 mm, and L=1 m) is made of copper, and outside tube (D_i=25.8 mm, and L=1 m) is made of Plexiglas. The outside tube is well insulated using thick pipe insulation (Rubates Armstrong Armflex II). *n-Octadecane* is used as the PCM and it fills the annular space between the two tubes. In order to maintain the inlet temperature of the HTF, an electrical heater is used. The water flows through the copper tube with the mass flow ranging from 0.03 to 0.07 kg/s. To monitor the temperature of the PCM, three thermocouples are used at various locations with two additional thermocouples being used to monitor both the inlet and outlet temperature of the HTF (Figure 4.2). Thermocouple signals are recorded

in a PC using a data acquisition unit. To minimize the effect of natural convection, the apparatus is positioned vertically.

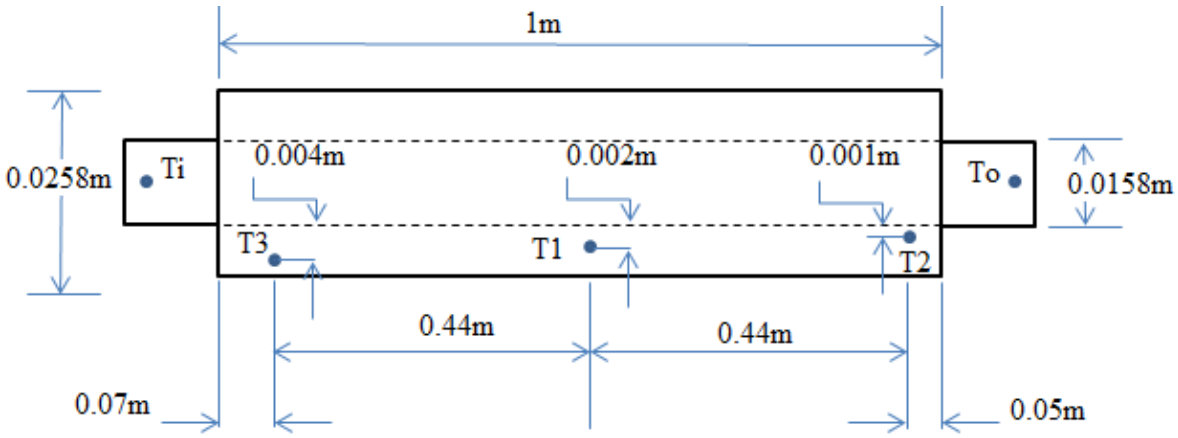

Figure 4.2**:** Experimental test unit.

4.1.3 Validation of the FLUENT model

Lacroix's experiments were recreated numerically using the ANSYS FLUENT 13.0 software. Different grid sizes and time steps were carefully examined in preliminary simulations to obtain computational grid convergence. Since the case is symmetric then only a half of the physical domain was used for 3D numerical simulations, see Figure 4.3. The computational grid was constructed using 282504 hexahedral elements and boundary layers were used surrounding the pipe.

Transient simulations were run using the *k-epsilon* turbulence model because of relatively high mass flow rate of HTF inside the pipe. The time step used in calculations was set to 0.1s. The solidification/melting model was enabled to describe the phase change phenomena in *n-Octadecane*. The first-order upwind spatial discretization and the pressure solver with the

PRESTO algorithm for pressure-velocity coupling were selected to obtain converged solution. Convergence criteria were established by setting the absolute residual values to 10^{-6} for energy and 10^{-3} for all other variables. Zero heat flux boundary conditions were set on all sides of the shell. The mass flow rate and temperature of the HTF were specified at the inlet of the copper pipe.

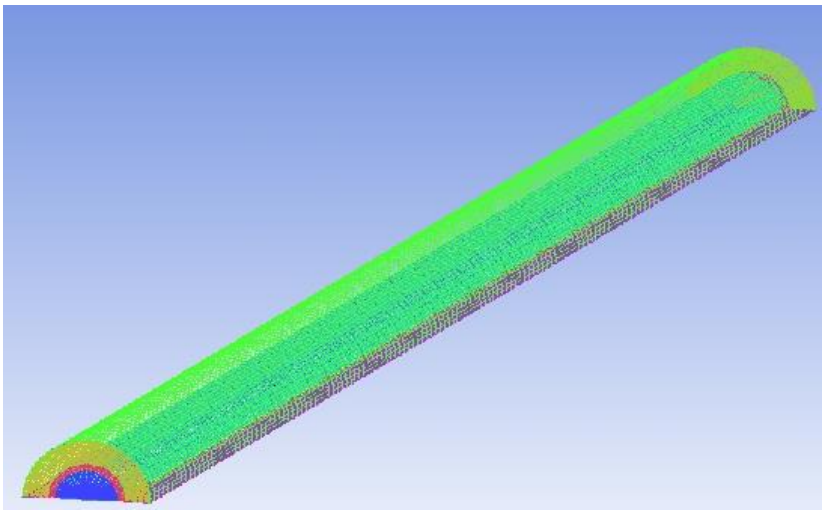

Figure 4.3**:** The computational grid.

The validation of the computational model was carried out by comparing numerical results from ANSYS FLUENT to experimental data obtained by Lacroix [9]. The melting of PCM is studied experimentally for three different HTF inlet temperatures above the melting temperature of *n-Octadecane* by 5, 10 and 20 K. The HTF mass flow rate was maintained at a constant value of 0.0315 Kg/s. Figures 4.4-4.6 show the temporal temperature variations in the experiment and FLUENT ANSYS simulations at locations T1 (h=0.51 m, r =0.002 m) and T2 (h=0.95 m, r =0.001 m) inside the PCM.

It can be seen that the numerically predicated temperature follows experimental trend in [9]. The main discrepancies between the numerical and experimental results can be attributed to

the measurements uncertainties and the difference in the PCM physical properties in the solid and liquid phase.

Additionally, CFD numerical results on the evolution of the liquid fraction in the PCM were compared with calculations of Lacroix [9]. Figures 4.7-4.9 show the variation of molten volume fraction of the PCM in a shell-and-tube storage unit as a function of time. The outer diameter (D_e) of the storage unit is 22 mm, the inside tube diameter (Di) is 12.7 mm, and the storage length (L) is 1 m. The HTF mass flow rate in simulations ranges from $1.5\times10^{-4}\, to 1.5\times10^{-2}$ and the HTF inlet temperature was 20K above the PCM melting temperature. As it can be seen in Figures 4.7-4.9, the current FLUENT model results are in a very good agreement with calculations of Lacroix [9].

In general comparison of CFD results with results presented in [9] demonstrate that the developed CFD model accurately describes processes taking place in the experimental test rig and therefore can be used with confidence for further transient heat transfer simulations in the shell-and-tube latent thermal storage unit.

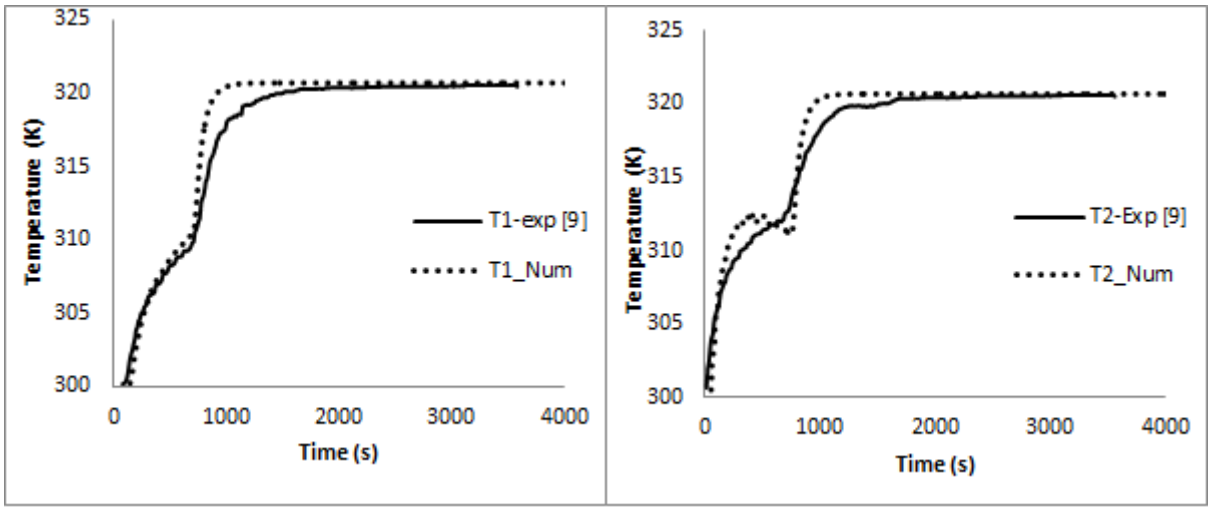

Figure 4.4: The variation of the predicted and experimental temperature at locations T1 and T2 ($T_{in} = T_{PCM\ Melting} + 20K$).

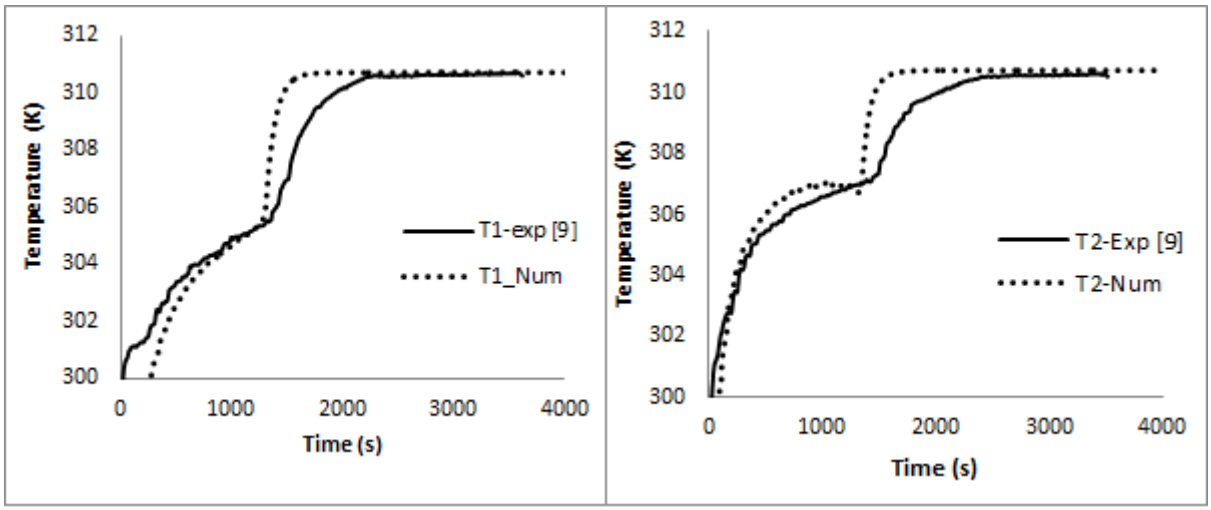

Figure 4.5: The variation of the predicted and experimental temperature at locations T1 and T2 ($T_{in} = T_{PCM\ Melting} + 10K$).

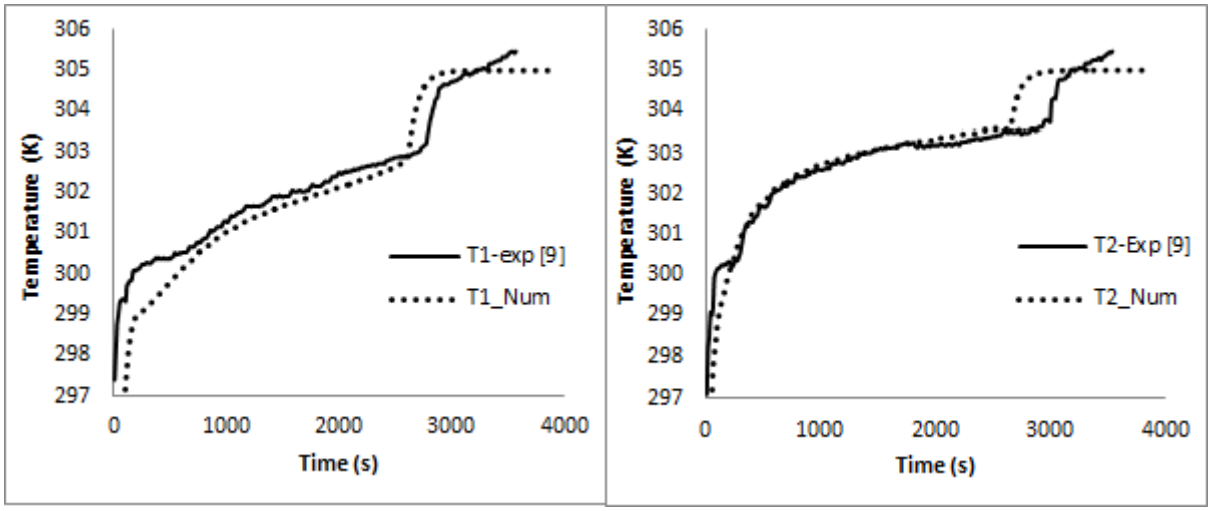

Figure 4.6: The variation of the predicted and experimental temperature at locations T1 and T2 ($T_{in} = T_{PCM\ Melting} + 5K$).

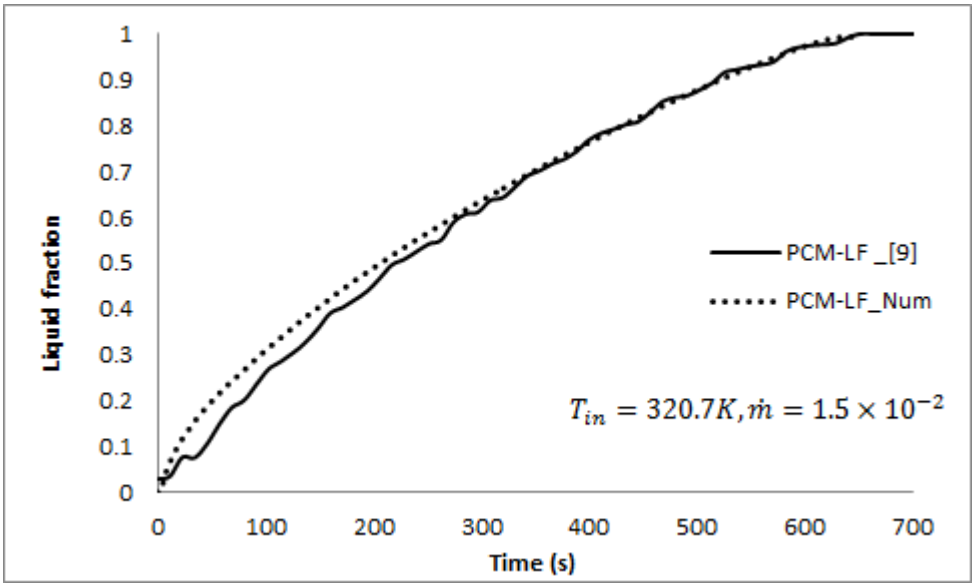

Figure 4.7: The liquid fraction variation in time (numerical from [9]),

$T_{in} = 320.7K,\ \dot{m} = 1.5 \times 10^{-2}$.

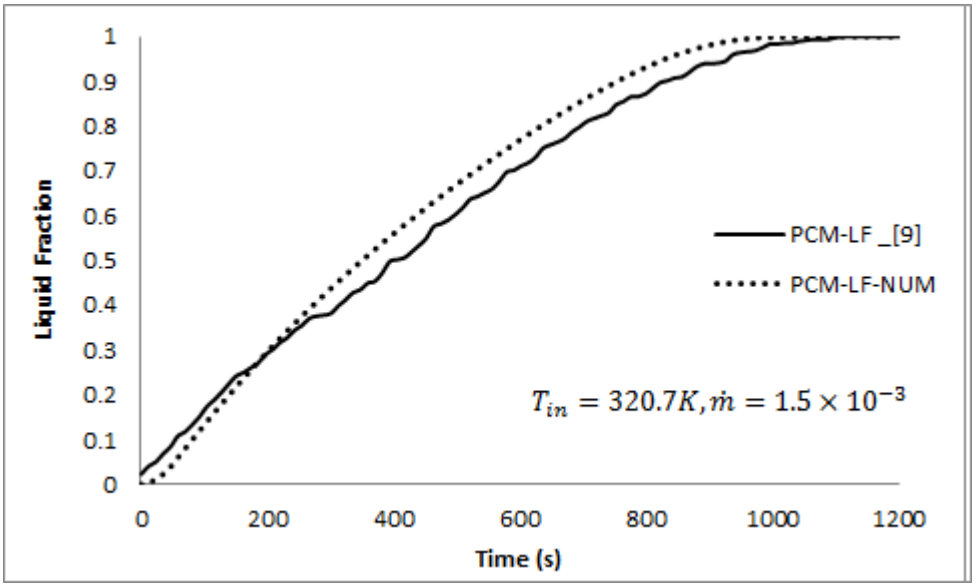

Figure 4.8 The liquid fraction variation in time (numerical from[9]),

$T_{in} = 320.7K,\ \dot{m} = 1.5 \times 10^{-3}$.

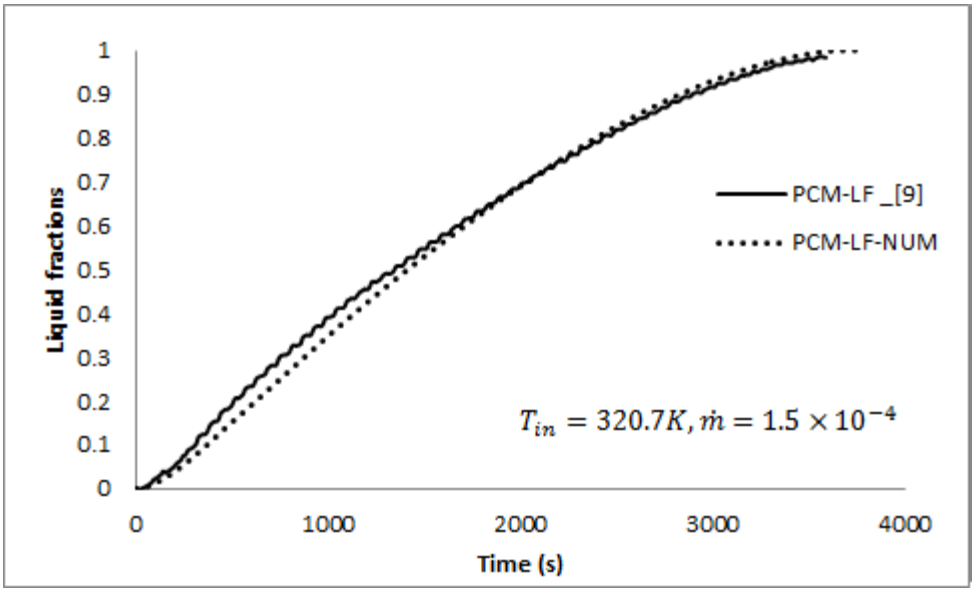

Figure 4.9: The liquid fraction variation in time (numerical from [9]),

$T_{in} = 320.7K,\ \dot{m} = 1.5 \times 10^{-4}$.

4.2 Heat transfer performance

Further numerical CFD modelling was performed to examine the performance of the shell-and-tube storage unit in the melting operation mode. Figure 4.10 shows samples of temperature and liquid fraction distribution in the computational domain along its axis for the instance when the elapsed time is 350 seconds (the inlet temperature of the HTF is 320K, the mass flow rate is 0.0315 Kg/s).

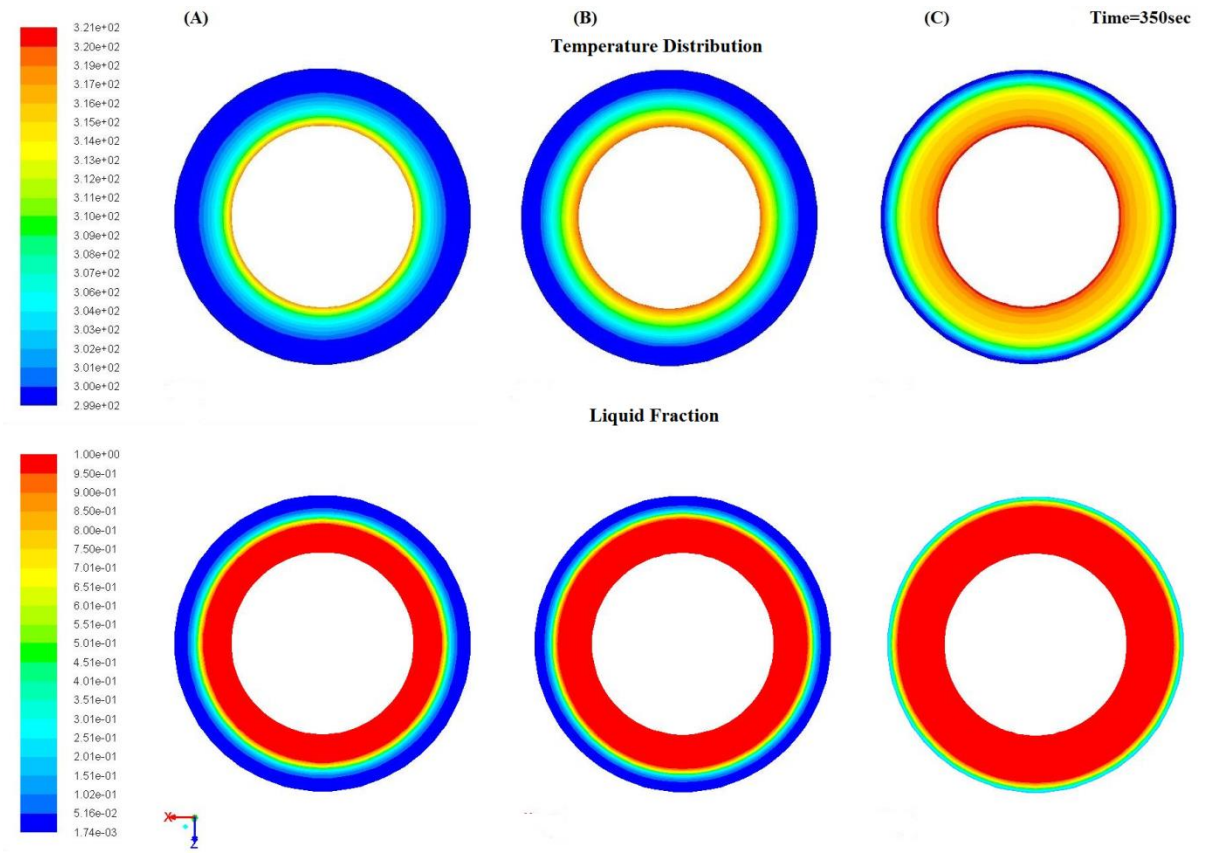

Figure 4.10: Temperature distribution in the PCM for (A) Bottom section plane, (B) Middle section plane, and (C) Top section plane ($T_i = 320$ K, $\dot{m} = 0.0315$ Kg / s , Elapsed time is 350 sec).

It can be seen that the temperature gradually rises in the regions close to the pipe walls and highest temperatures can be observed at the domain's top region close to the inlet of the HTF. As a result, the top part of the domain turns into liquid first and later on, melting expands to lower regions on the domain.

Figure 4.11, presents the temperature variation in the PCM for three different radial positions. As expected, the higher temperatures are observed in the regions close to the surface of the wall with the HTF, where the melting process takes place first. The temperature variations along the axis at the outer surface of the HTF tube are shown in Figure 4.12. It can be seen that higher temperatures exist at the domain's top. This is mainly because the HTF flows

from the top to the bottom and thus the temperature rises faster at the vicinity of the tube walls close to the inlet. At this period of time the effect of the natural convection is not profound yet.

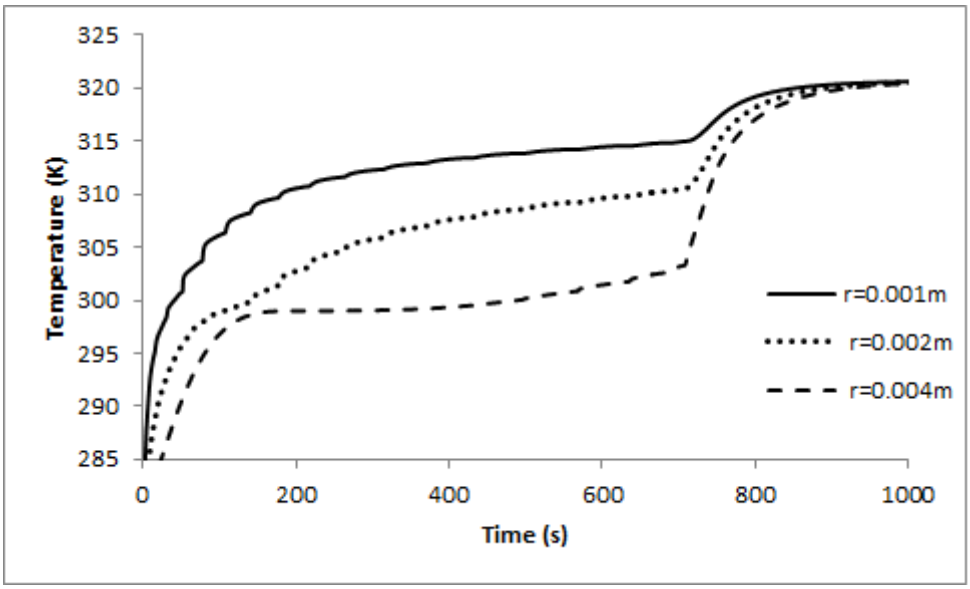

Figure 4.11: PCM temperature versus time at the different radial positions: r = 0.001, 0.002, and 0.004 m from the axis of the computational domain at y= 0.5 m ($T_{inlet} = 320\ K,\ \dot{m} = 0.0315\ Kg/s$).

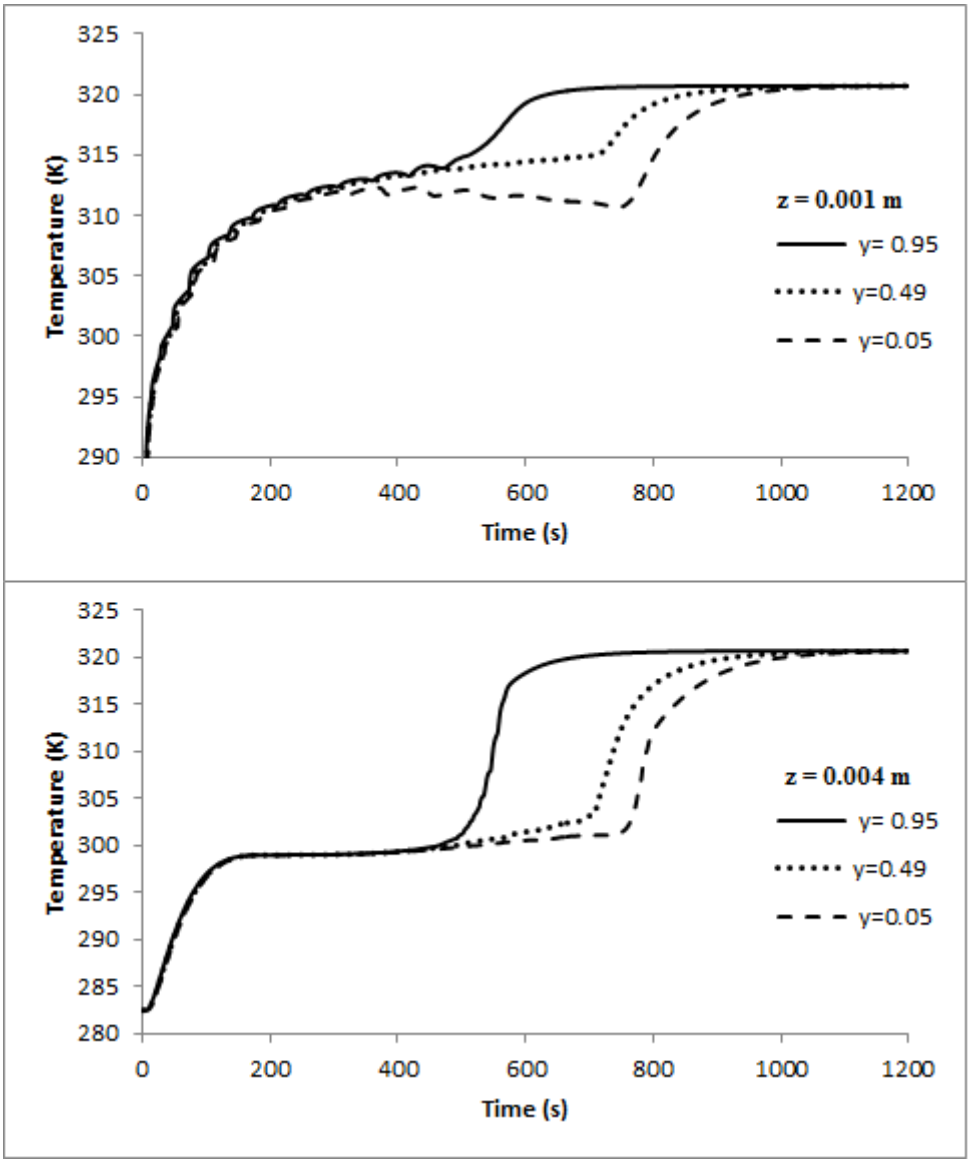

Figure 4.12: PCM temperature versus time along the axis (y = 0.05, 0.49, and 0.95 m) for the radial distances z = 0.001 and 0.004 m ($T_{inlet} = 320$ K, $\dot{m} = 0.0315$ Kg / s).

The effect of HTF inlet temperature on the melting process is examined in Figure 4.13. It can be seen that the inlet temperature of the HTF significantly affects the rate of the melting and the PCM temperature distribution. The increase in the inlet temperature of the HTF leads to rise in the temperature difference between the tube walls and the bulk of the PCM and thus intensifies the heat transfer rate. It results in faster rise of the liquid fraction and decreases the total melting time. Figure 4.14 shows that the time for completion of melting for the HTF

inlet temperature of 305 K is 2974s, for 310 K this time is reduced to 1617s and finally, for 320 K, the time of melting is only 963 s. Therefore, the total melting time is reduced approximately by 68% when the inlet temperature is increased from 305 to 320 K and by 45.6% when the inlet temperature is increased from 305 to 310 K.

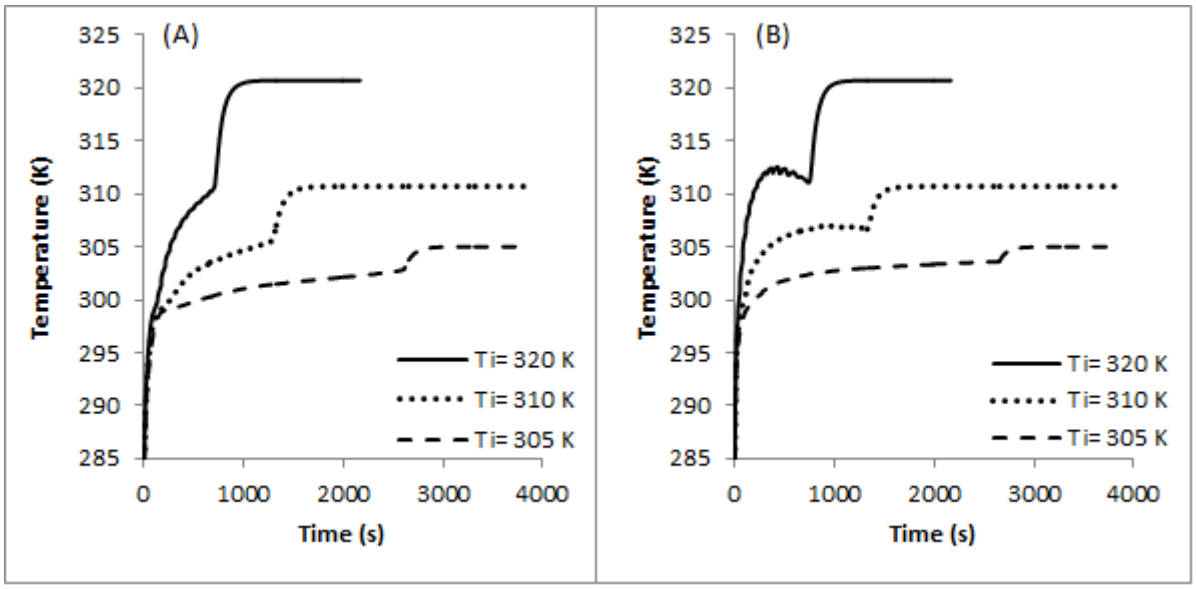

Figure 4.13: Effect of the HTF inlet temperature on the melting process: (A) Location T1 (h=0.51 m, r =0.002 m) and (B) Location T2 (h=0.95 m, r =0.001 m),

$T_{intial} = 282.5$ K, $\dot{m} = 0.0315$ Kg / s .

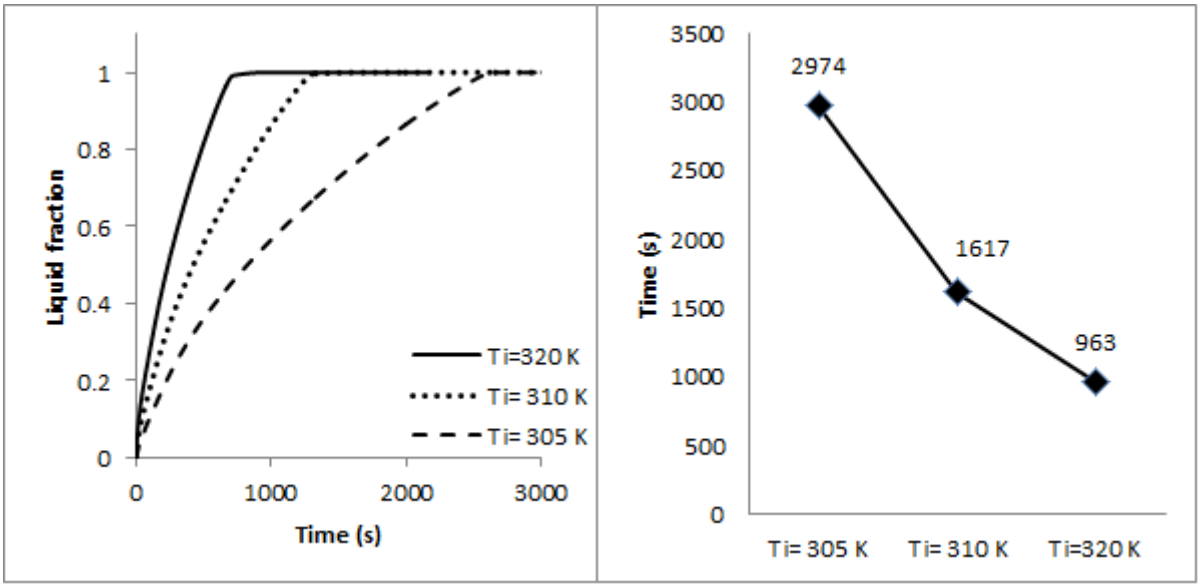

Figure 4.14: The effect of the inlet temperature of the HTF on the formation of the liquid fraction of the PCM and on the melting time. $T_{intial} = 282.5$ K, $\dot{m} = 0.0315$ Kg / s.

Figure 4.15 demonstrates the effect of the HTF flow rate on the meting process. It can be seen that the flow rate accelerates the melting process due to the increased heat transfer rate. It can be seen from Figure 4.16 that when the flow rate increases from 0.000315 to 0.00315 kg/s, the PCM melting time is reduced from 2781 to 1173 s (reduction by 57%). Also, the melting time is reduced by 17.8% when the mass flow rate increases from 0.00315 to 0.0315 kg/s. The effect of the HTF mass flow rate rise is less profound when compared with effect of rise in the HTF inlet temperature. This is demonstrated in Figure 4.17 using temperature distribution counters and the PCM fluid fraction evolution diagrams.

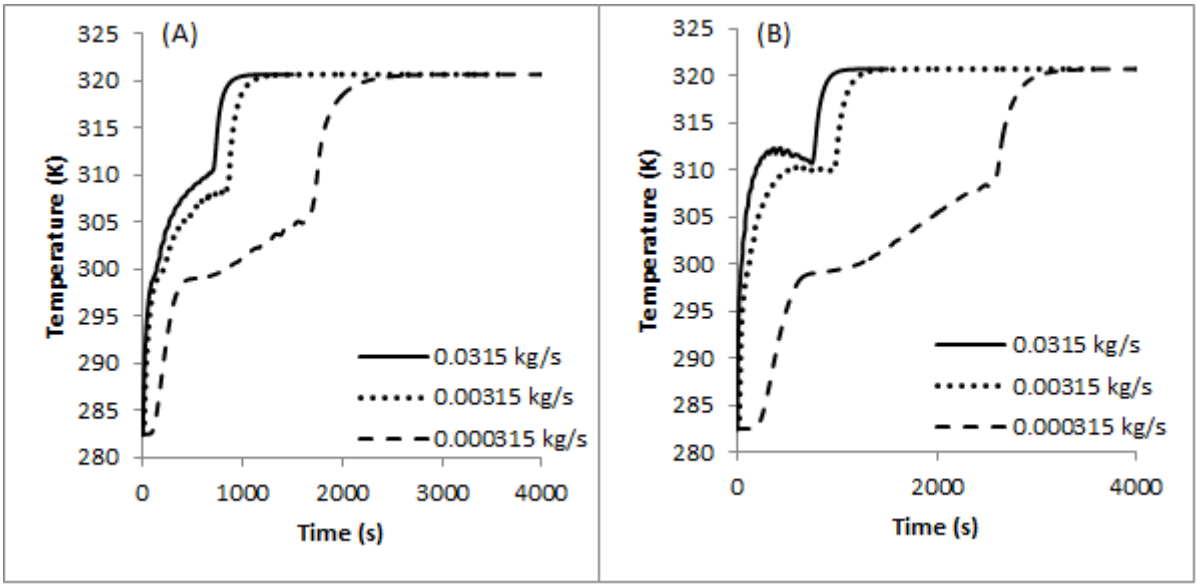

Figure 4.15: Effect of the HTF flow rate on the melting process. The PCM temperature at locations (A) T1 (h=0.51 m, r =0.002m) and (B) T2 (h=0.95 m, r =0.001m).

$T_{intial} = 282.5\ K,\ T_{inlet} = 320\ K$.

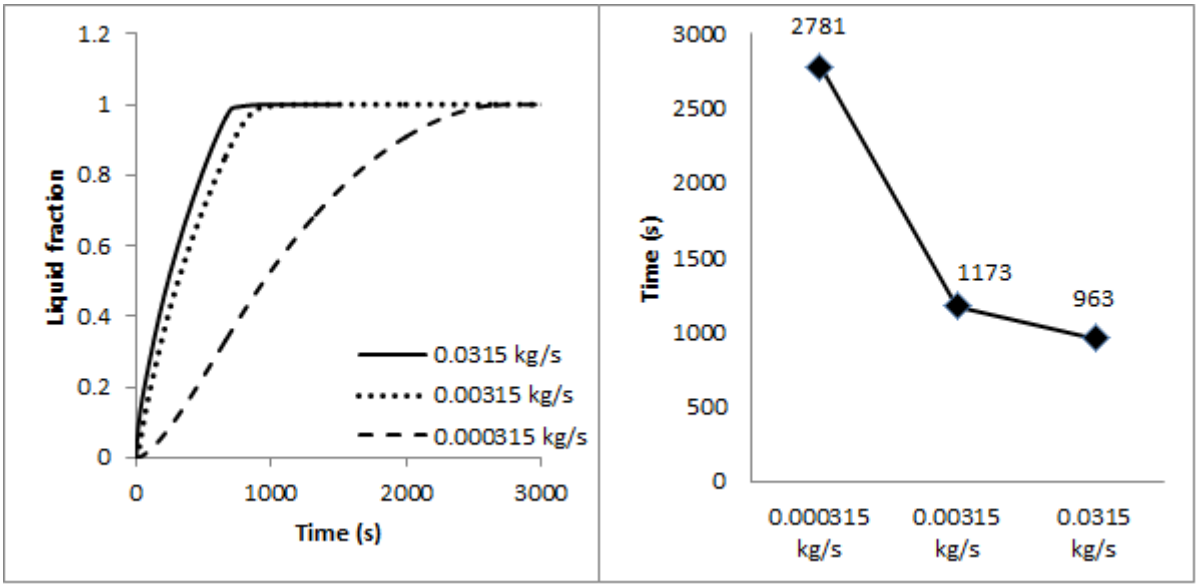

Figure 4.16: The effect of the HTF flow rate on the liquid fraction formation and the melting time. $T_{intial} = 282.5\ K,\ T_{inlet} = 320\ K$.

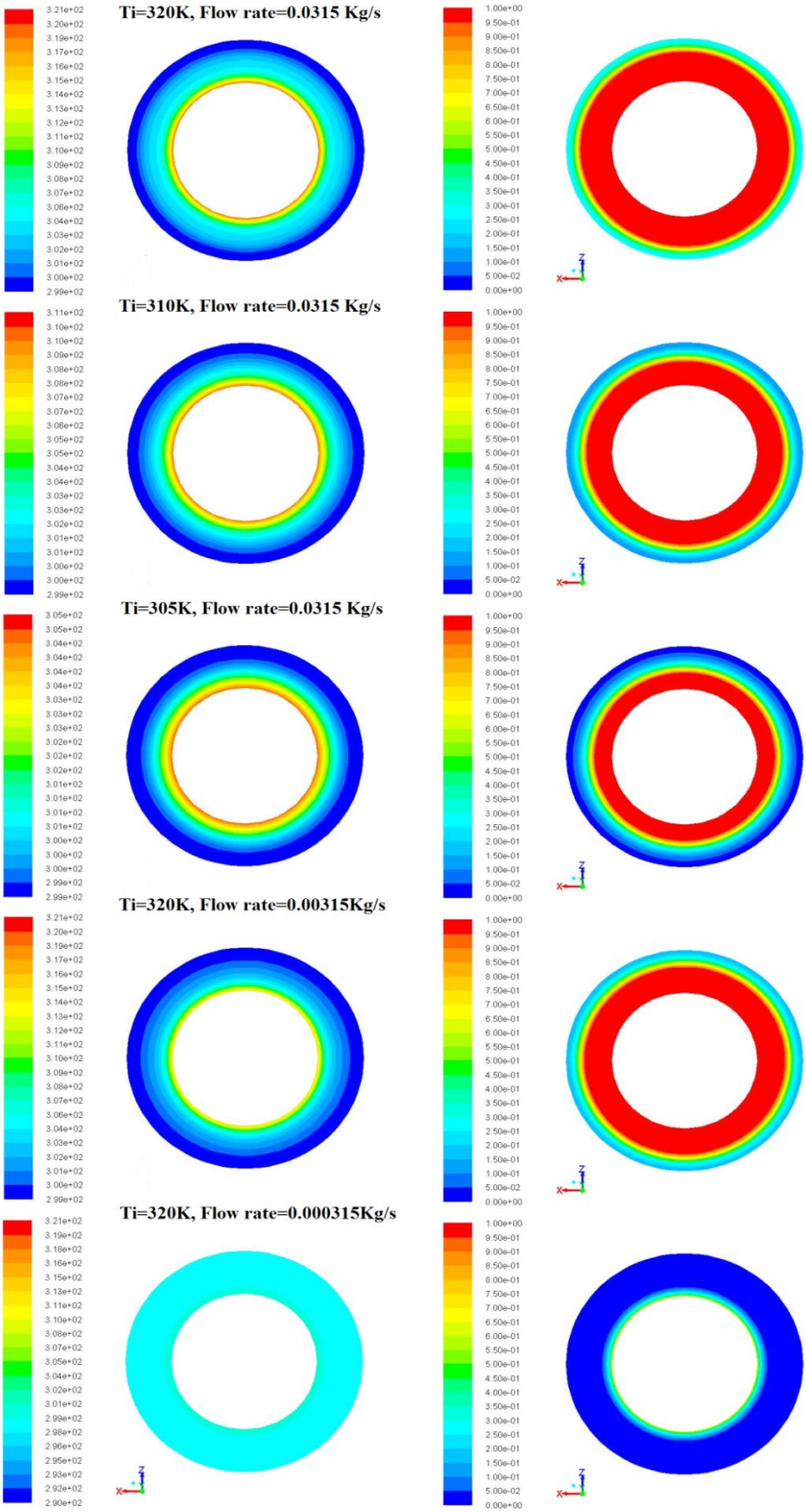

Figure 4.17: Temperature distribution and melting process at the bottom of the computational domain for the different HTF mass flow rates and inlet temperatures (Elapsed time is 850 s).

4.3 Heat transfer enhancement using nano-particles

The purpose of this section is to study performance of the thermal storage system with the PCM and dispersed nano-particles. The effect of nano-particles volume fraction on the melting process of *n-Octadecane* is analysed for Al_2O_3, CuO, and ZnO nano-particles. The geometry for the system used is the same used by Lacroix [9]. *n-Octadecane and n-Octadecane* with Alumina (Al_2O_3), copper oxide (CuO) and zinc oxide (ZnO) with different volume fractions are used as PCMs and water is used as the HTF in these investigations.

4.3.1 Thermo-physical properties of the PCM with nano-Particles

In order to study in detail the melting process of PCMs with nano-particles using FLUENT, the UDF was prepared using C++ language to define values of the temperature-dependent thermo-physical properties of the PCM with and without nanoparticles. The thermo-physical properties of nano-particles are listed in Table 4.2 and are used in the current numerical study.

Table 4.2: Thermo-physical properties of nano-particles used in this study [210].

Type of nano-particles	**Density (Kg/m^3)**	**Thermal conductivity (W/m K)**	**Specific heat (J/Kg K)**
Al_2O_3	3600	36	765
ZnO	5600	13	502.5
CuO	6500	17.65	540

The thermo-physical properties of *n-Octadecane* containing 0%, 1%, 3% and 6% of CuO nano-particles by volume are presented as a function of temperature and volumetric concentration in Figure 4.18. It can be seen that the nano PCM's specific heat is lower than

the base PCM, thus, nano PCM has the lower energy storage capacity but there is a higher heat transfer rate compared to the base PCM.

Figure 4.18 B shows the nano PCM's density depending on the volumetric concentration from 0% to 6% of CuO nano-particles. The density increases with an increase in the nano-particles volume concentration. The nano PCM's density increases by 32% when the volume concentration changes from 1% to 6% at the temperature of 290 K (compared to the base PCM). Additionally, the dynamic viscosity of nano PCM increases with the rise in the volumetric concentration of nano-particles, see Figure 4.18 D. The enhancement in the dynamic viscosity of the nano PCM plays significant role during the natural convection making it dominating phenomena during the melting process. Similar results were obtained for the PCM with Al_2O_3 and ZnO nano-particles.

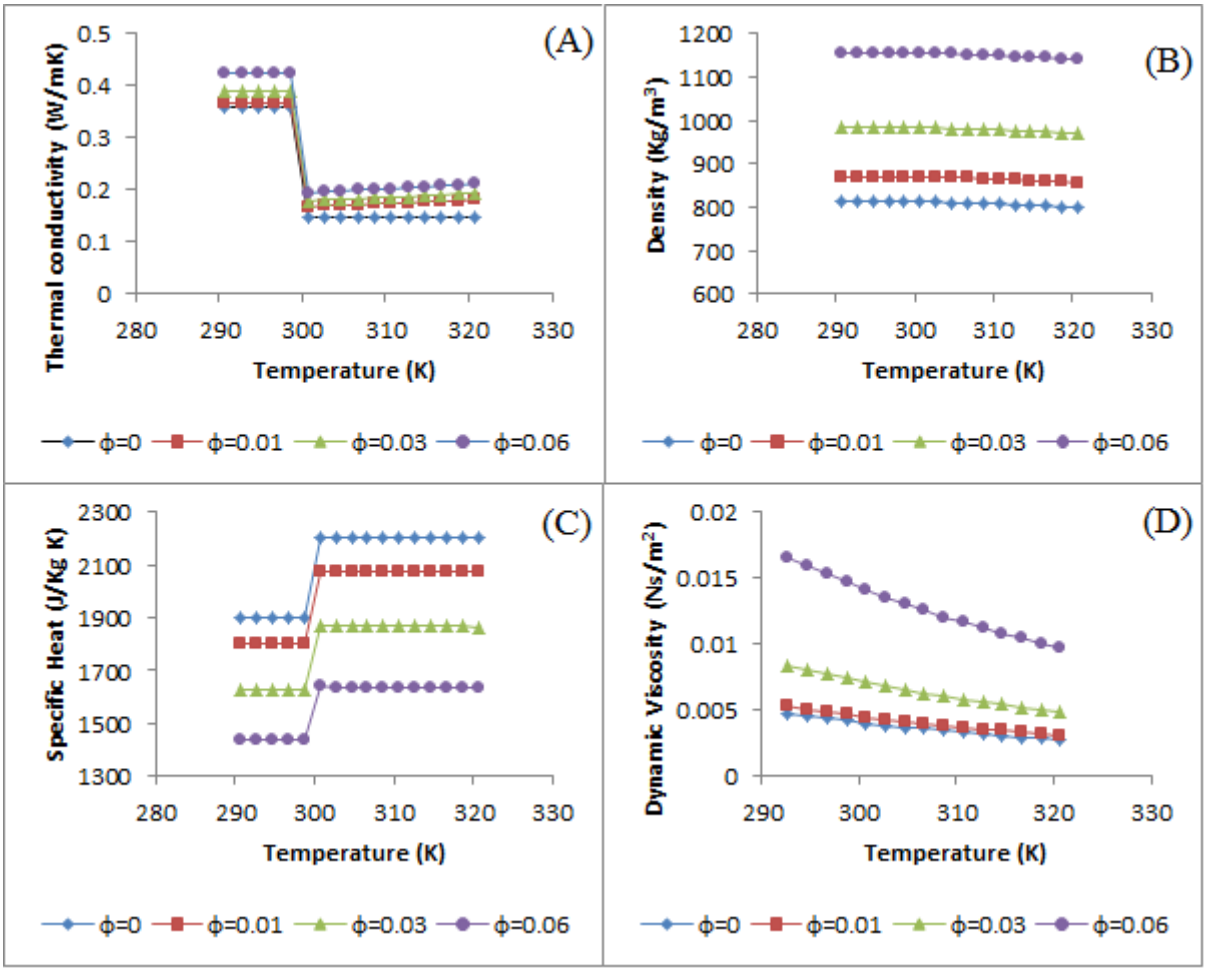

Figure 4.18**:** Thermo-physical properties of the nano PCM containing *n-Octadecane* and CuO. (A) Thermal conductivity, (B) Density, (C) Specific heat, (D) Dynamic viscosity.

It can be seen in Figure 4.19 that the nano PCM's relative thermal conductivity (compared to the pure PCM) increases with the rise in the temperature and nano-particles volumetric concentration. For instance, for a 3% volumetric concentration of nano particles, the relative thermal conductivity increases from 1.21 to 1.4 (15.91% increase) for temperatures between 300.7 and 320.7K. For the 6% volumetric concentration of nano particles the relative thermal conductivity increases by 54.43% at the temperature of 338.7 K. It can be assumed that the relative thermal conductivity increases linearly with nano particle volumetric concentration and temperature. These results are in agreement with results in [175, 210].

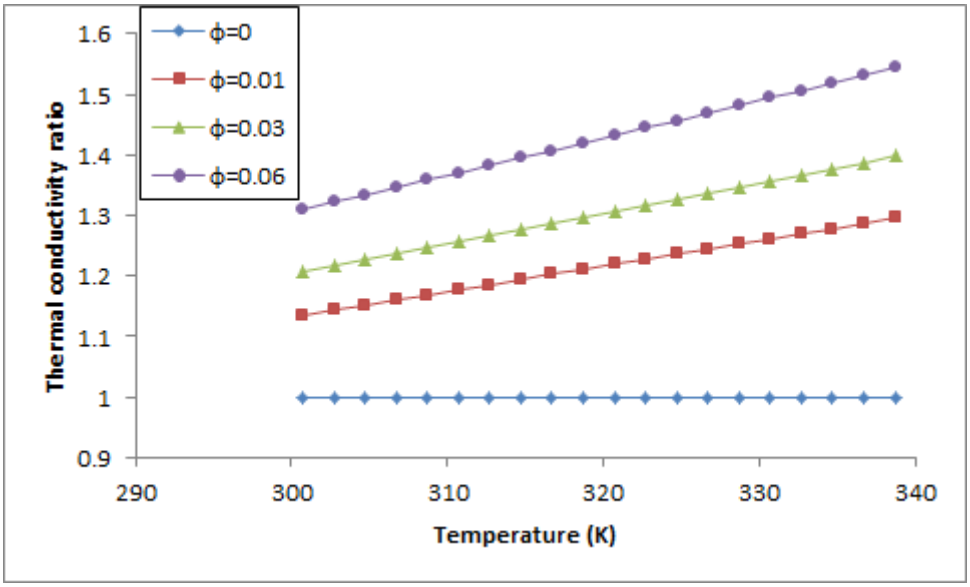

Figure 4.19: The relative thermal conductivity as a function of temperature for different volumetric concentrations of CuO nano-particles in *n-Octadecane*.

Figure 4.20 presents results on the dependence of thermo-physical properties of Al_2O_3, CuO, and ZnO nano PCMs with 6% volumetric concentration on the temperature. It can be seen that the nano PCM's thermo-physical properties are defined by the nano-particle material properties. The density of the nano PCM with CuO and ZnO nano-particles is greater compared to the PCM with Al_2O_3 and this due to the high density of CuO and ZnO nano-particles compared to that of Al_2O_3 (Figure 4.20 B). Similarly, the decrease in the nano-PCMs specific heat is greater with both CuO and ZnO nano-particles compared to Al_2O_3 nanoparticles in *n-Octadecane*, because the specific heat for Al_2O_3 nano-particles is greater than for CuO and ZnO nano-particles (Figure 4.20 C). The increase in the dynamic viscosity is greater for the CuO nano PCM compared to that with ZnO or Al_2O_3 nano-particles.

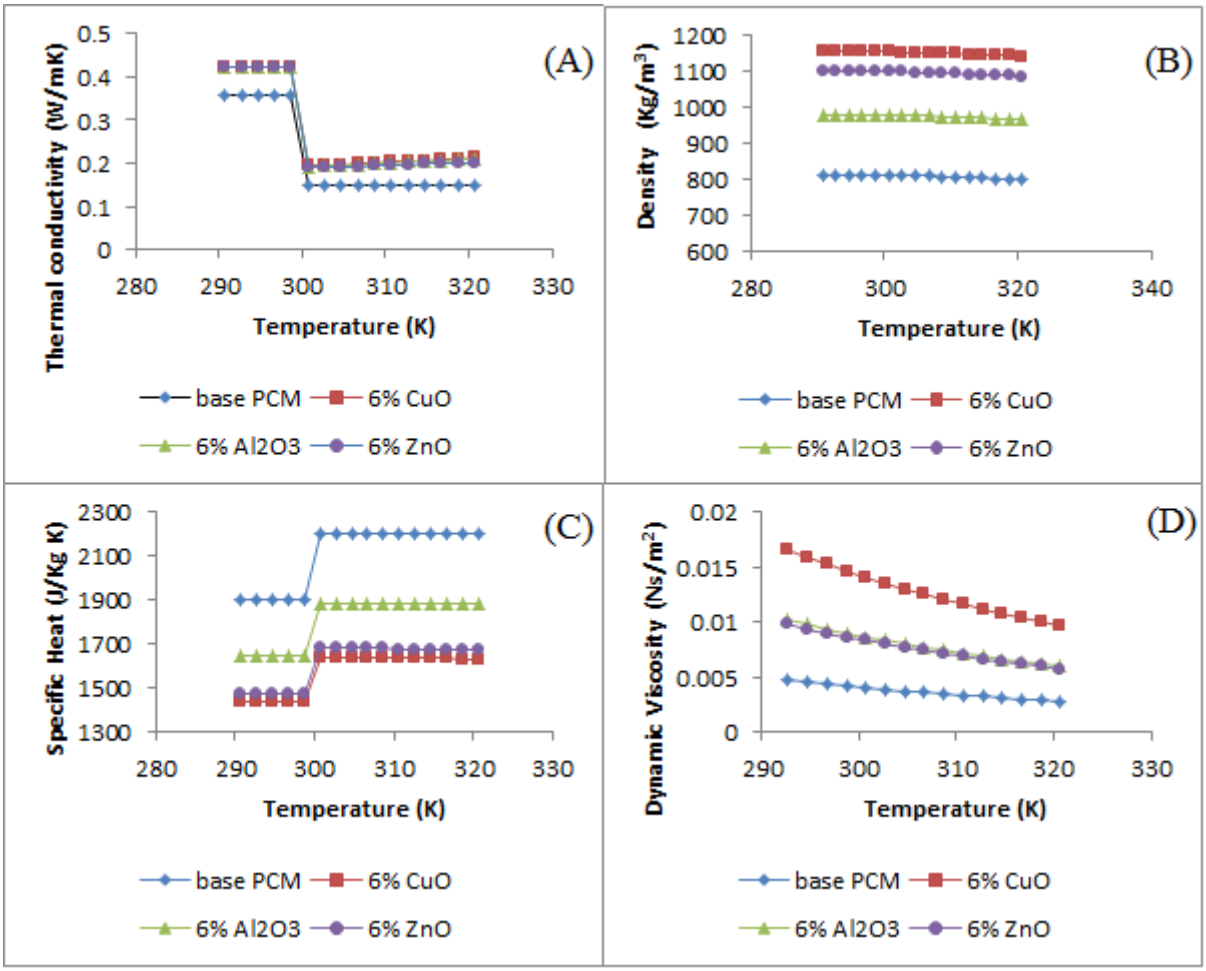

Figure 4.20: Thermo-physical properties of the nano PCM with 6% volumetric concentration of Al_2O_3, CuO, and ZnO nano-particles. (A) thermal conductivity, (B) density, (C) specific heat, (D) dynamic viscosity.

Figure 4.21 shows the nano PCM's relative thermal conductivity as a function of temperature for a 6% volumetric concentration of Al_2O_3, CuO, and ZnO nano-particles. The relative thermal conductivity linearly increases with an increase in temperature as well as the volumetric concentration of nano-particles. The relative thermal conductivity is higher for CuO nano-particles compared to Al_2O_3 or ZnO nano-particles in *n-Octadecane*. The increase in the relative thermal conductivity of the PCM with 6% volumetric concentration of CuO is 17.89% when temperature changes from 300 to 339K. For the same conditions and

volumetric concentration the relative thermal conductivity increases by 16.43% and 13.45% for Al_2O_3 and ZnO nano-particles, respectively.

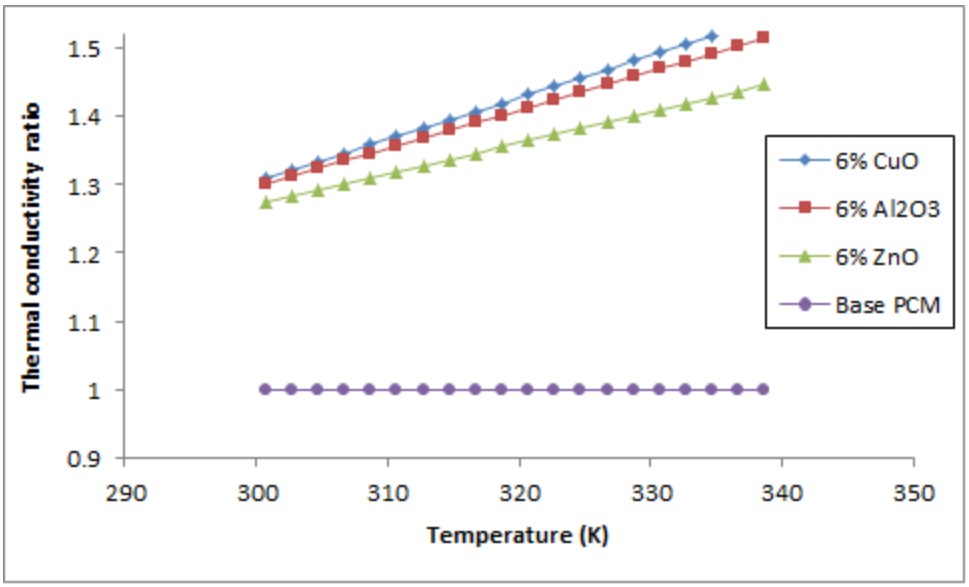

Figure 4.21: The relative thermal conductivity ratio vs temperature for the nano PCM with 6% of volumetric concentration for Al_2O_3, CuO and ZnO nano-particles.

4.3.2 Effect of nano-particles concentration on heat transfer

It is expected that nano-particles dispersed in the base PCM *(n-Octadecane)* would improve the melting process. This phenomena was studied numerically in this work using CDF modelling. Figures 4.22-4.27 summarize some of the obtained results and demonstrate the effect of the nano-particles concentration on the temperature variations at the same locations in the storage system indicated in Figure 4.2, namely T1 (h=0.51 m, r =0.002m) and T2 (h=0.95 m, r =0.001m). Simulations were carried out for the case in which the inlet temperature of the HTF is 320.7 K and its mass flow rate is 0.0315 kg/s. It can be concluded from the above figures that the rise in the nano-particle volumetric concentration strongly affects the temperature distribution in the PCM and enhances the overall heat transfer. The

overall heat transfer between the HTF and the PCM (via pipe) is directly proportional to the difference between the HTF and PCM temperatures. For the same initial temperature and flow rate conditions, the overall heat transfer from the HTF to the PCM is approximately constant. Since the initial temperature and flow rate conditions remain the same in all numerical experiments varied out, the heat transfer magnitude is determined by the nano-particles volumetric concentration.

Figure 4.22 demonstrates that the base PCM temperature at location T1 (h=0.51 m, r =0.002m) reaches the final temperature of 320.7 K in about 1111 s after the start of the numerical experiment. For the PCM with the 3% and 6% volumetric concentration of CuO, this time is reduced to 990 and 916 s, respectively, which are 11.2% and 17.8% reduction in the melting time. Similar results are obtained at location T2, see Figure 4.23. The time of melting is also reduced when using nano PCM with the increasing volumetric ratio of Al_2O_3 and ZnO nanoparticles (Figures 4.24 – 4.27). The typical values of these reductions at location T1 are as follows: for 3% of AL_2O_3 and ZnO the time is reduced by 11.8% and 10.3%, respectively. For the 6% volumetric concentration the time is reduced by 18.3% and 16.6% for AL_2O_3 and ZnO, respectively. Similar numbers are obtained for the location T2. These results indicate the higher heat transfer rates in PCMs with nano-particles due to the PCM's increased thermal conductivity. There was a very little difference in the reduction of melting time and in the temperature distribution for the same volumetric concentrations of CuO, Al_2O_3 and ZnO nano-particles, see Figure 4.28.

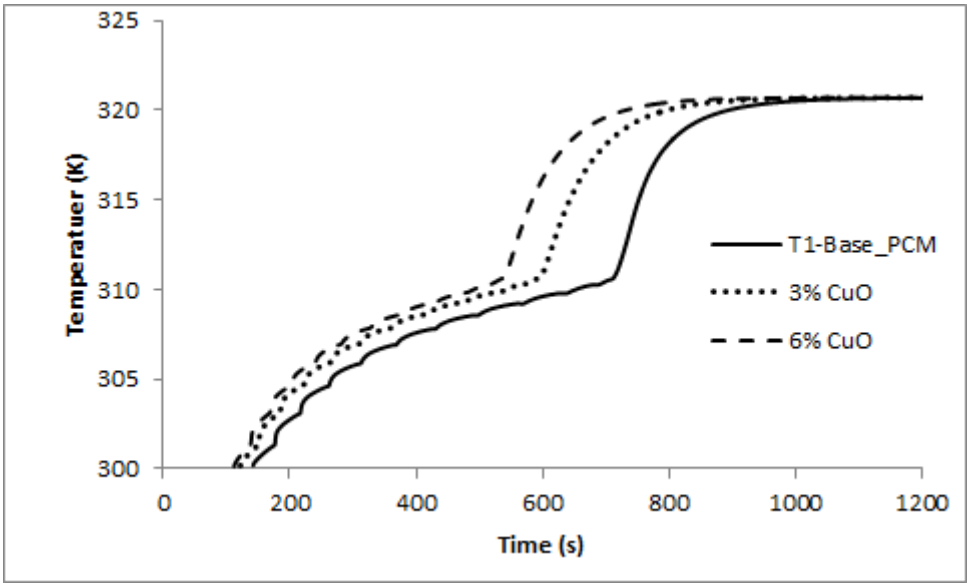

Figure 4.22: Temperature recordings during melting process of PCM at location T1 (h=0.51 m, r =0.002 m) with or without CuO nano-particles.

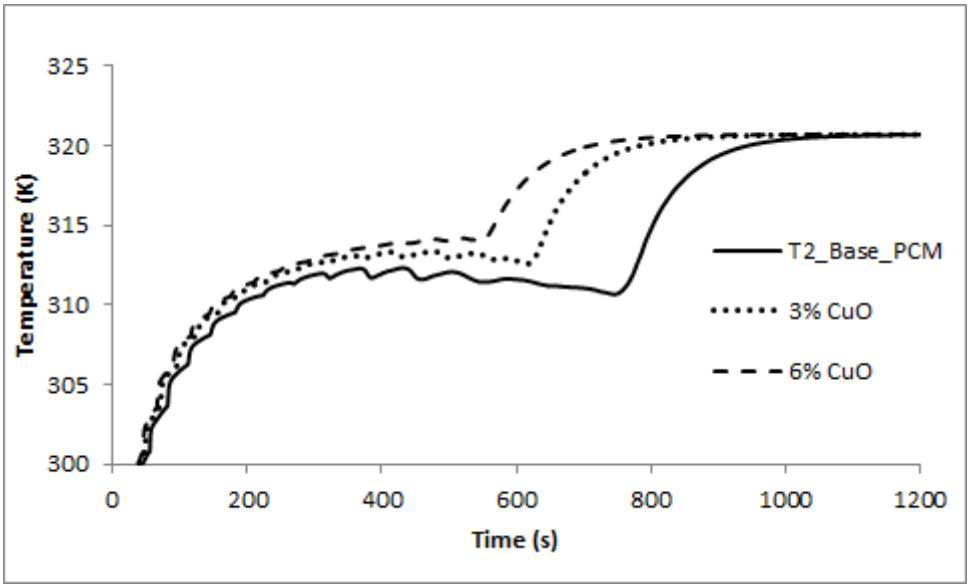

Figure 4.23: Temperature recordings during melting process of PCM at location T2 (h=0.95 m, r =0.001 m) with or without CuO nano-particles.

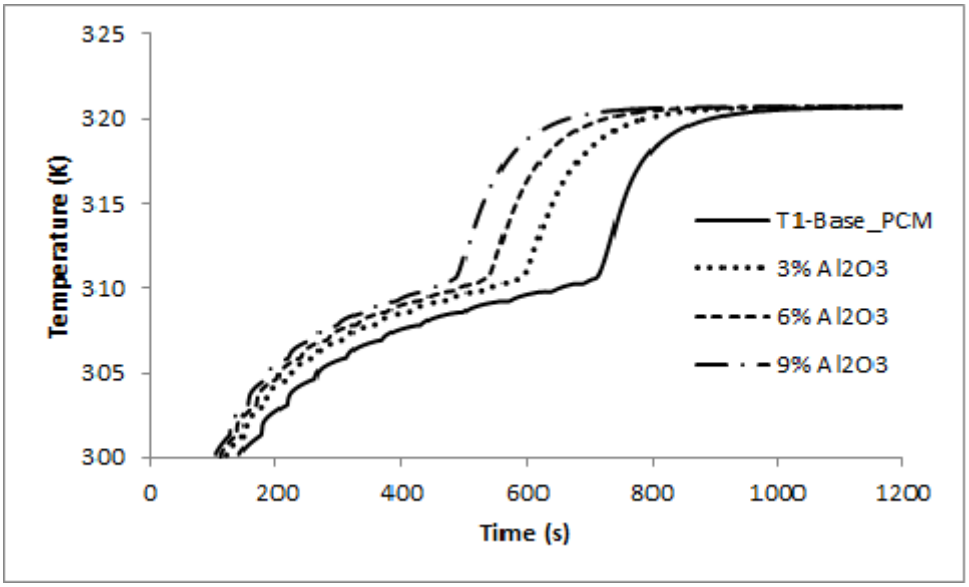

Figure 4.24: Temperature recordings during melting process of PCM at location T1 (h=0.51 m, r =0.002 m) with or without Al_2O_3 nano-particles.

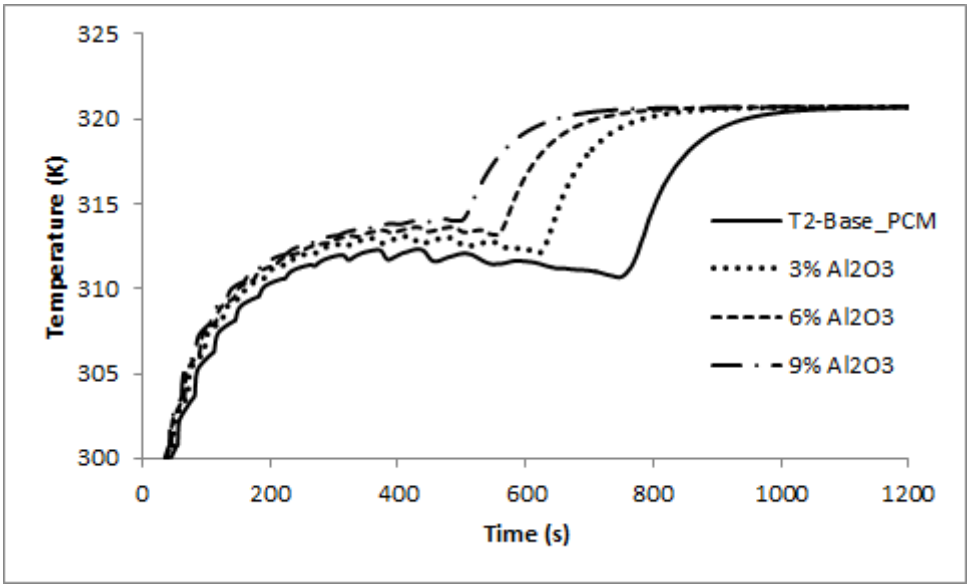

Figure 4.25: Temperature recordings during melting process of PCM at location T2 (h=0.95 m, r =0.001 m) with or without Al_2O_3 nano-particles.

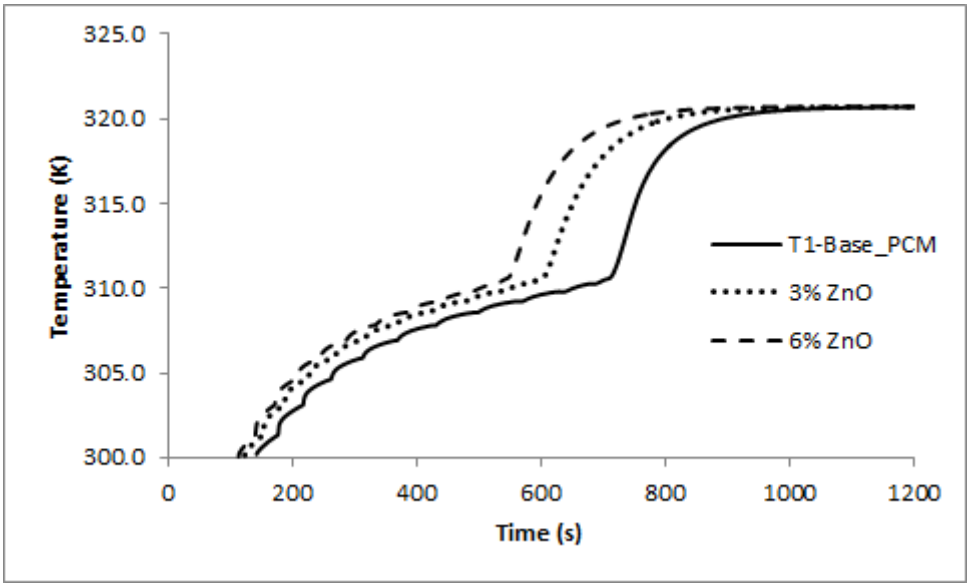

Figure 4.26: Temperature recordings during melting process of PCM at location T1 (h=0.51 m, r =0.002 m) with or without ZnO nano-particles.

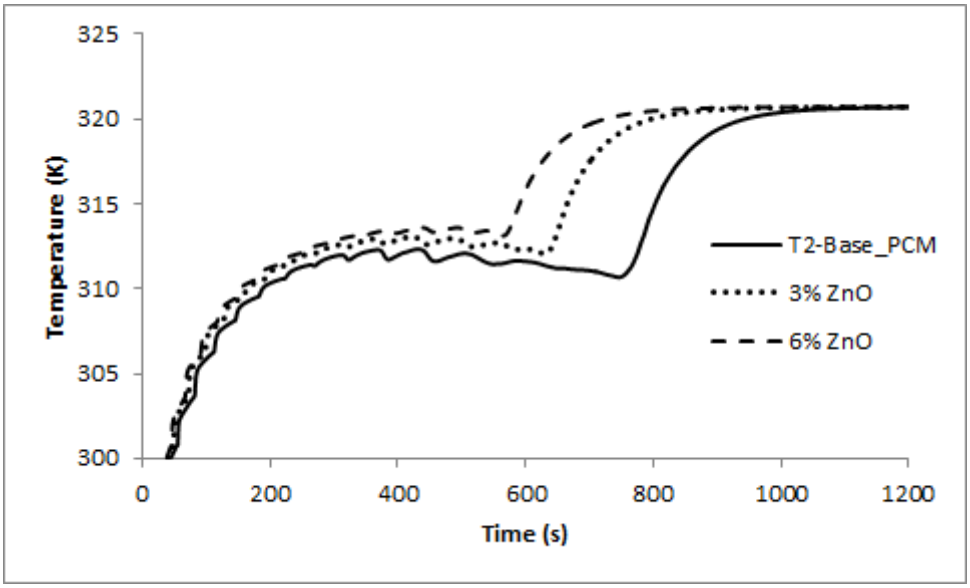

Figure 4.27: Temperature recordings during melting process of PCM at location T2 (h=0.95 m, r =0.001 m) with or without ZnO nano-particles.

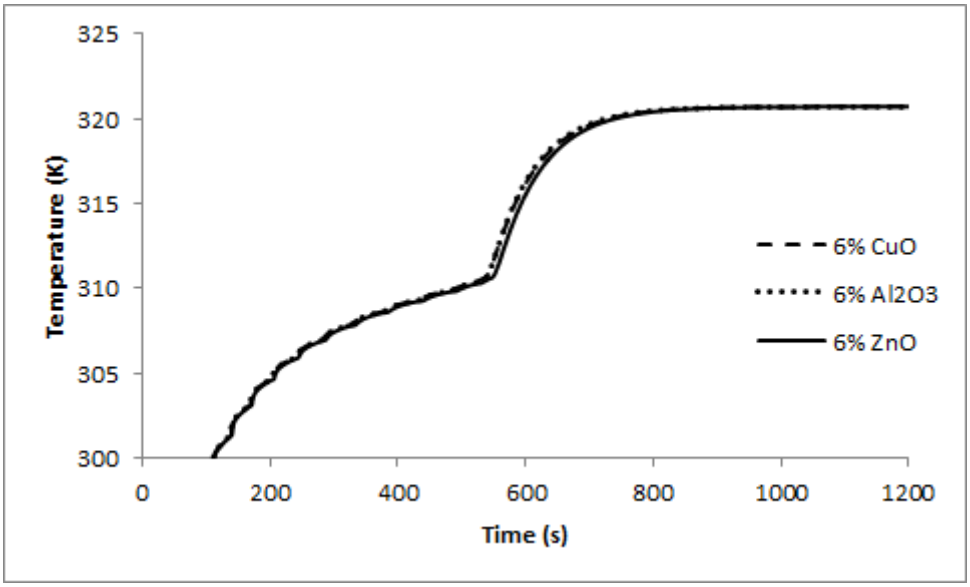

Figure 4.28: Temperature recordings during melting process of PCM at location T1 (h=0.51 m, r =0.002 m) with 6% volumetric concentration of CuO, Al2O3 and ZnO nano-particles.

The variations in time of the radial temperatures along the axis of the system are shown in Figure 4.29 for the base PCM, PCM with the 6% volumetric concentration of CuO, PCM with the 6% volumetric concentration of Al_2O_3 and PCM with the 6% volumetric concentration of ZnO nano-particles. Results show that the temperature difference between the radial temperatures is reduced with time and the temperatures in the PCM rises more rapidly with the increase in nano-particles volumetric concentration. These outcomes also confirm that nano-particles in the PCM enhance the heat transfer process and accelerate the melting of PCM.

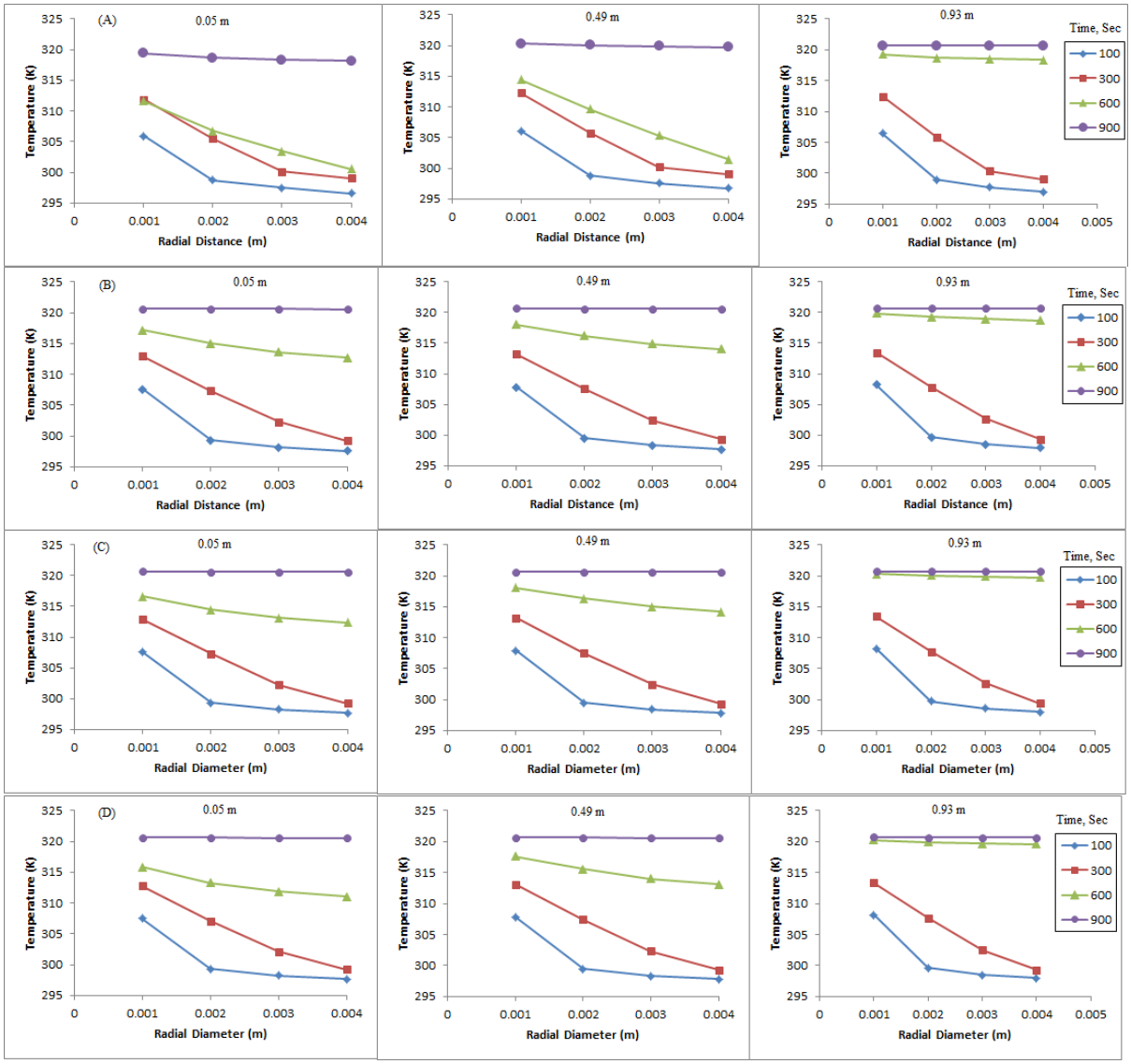

Figure 4.29: Variation in time of the radial temperature along the axis of the system. (A) base PCM, (B) PCM with the 6% volumetric concentration of CuO nano-particles, (C) PCM with the 6% volumetric concentration of Al_2O_3 nano-particles, (D) PCM with the 6% volumetric concentration of ZnO nano-particles.

Figure 4.30 represents the temperature distribution in the PCM with and without CuO nano-particles for the elapsed time of 750 s. It can be seen that the temperature rises faster in case of the PCM with the increased volumetric concentration of nano-particles.

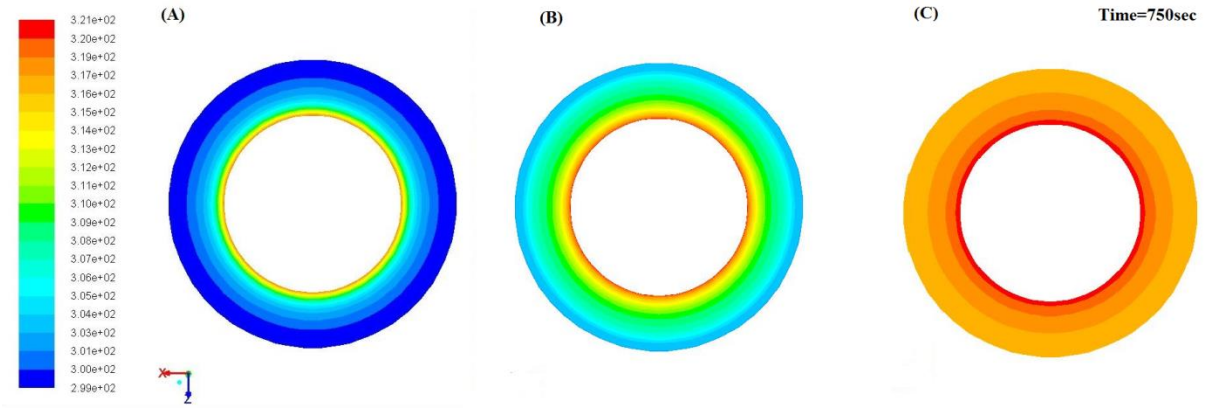

Figure 4.30: Temperature distribution at the bottom of the storage unit. (A) base PCM, (B) PCM with a 3% of CuO, (C) PCM with a 6% of CuO.

Enhancement of evolution of the liquid fraction formation using nano-particles is examined for volumetric concentrations of 3% and 6% for CuO, Al_2O_3 and ZnO nanoparticles. These results are presented for *n-Octadecane* without and with nano-particles in Figures 4.31-4.33. It can be seen that the liquid fractions formation is intensified with the increase in the nanoparticle volume concentrations due to the enhancement of the heat transfer phenomena. These results are also demonstrated in Figure 4.34.

The magnitudes of the total melting time for *n-Octadecane* with and without nano-particles are presented in Figure 4.35. It can be seen that the total melting time is reduced as the nano-particles volumetric concentration is increased. However, there is a reduction in the fusion's latent heat which in its turn reduces the thermal energy accumulated per mass unit of the nano PCM. The time for completion of melting of pure PCM (*n-Octadecane*) in the storage system is 931s, for a 3% volumetric concentration of CuO the time is reduced to 750 s and for the 6% volumetric concentration the melting time is 636 s (19.4% and 31.7% reductions). A similar conclusion can be drawn for the PCM with Al_2O_3 and ZnO nano-particles. The total melting time is reduced by 18.5% and 28.6% when the volumetric concentration of Al_2O_3 is

3% and a 6%. The reduction in the time of melting is 17.2% and 27.2% when the volumetric concentration of ZnO is 3% and a 6%, respectively.

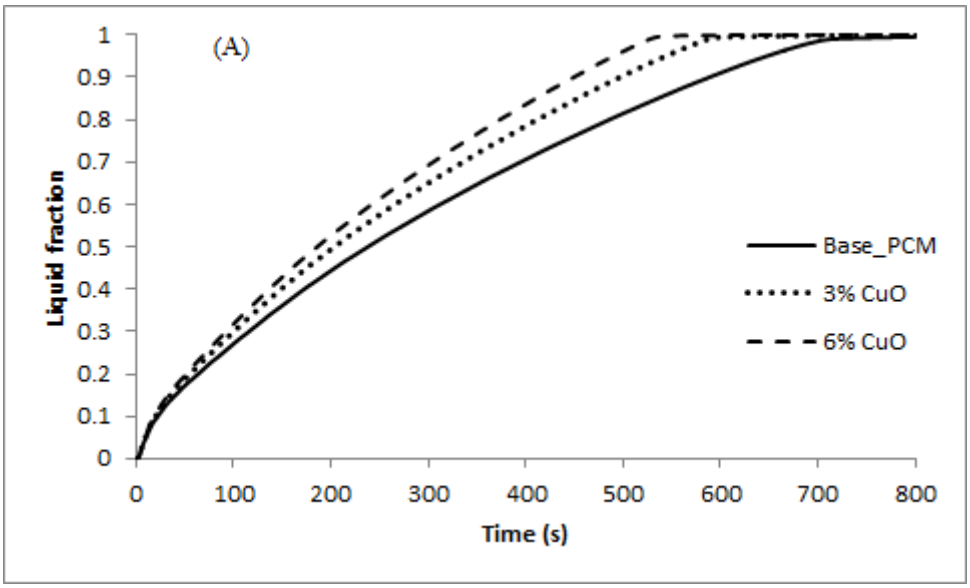

Figure 4.31: Evolution of the liquid fraction in the pure PCM and PCM with 3% and 6% volumetric concentration of CuO nano-particles.

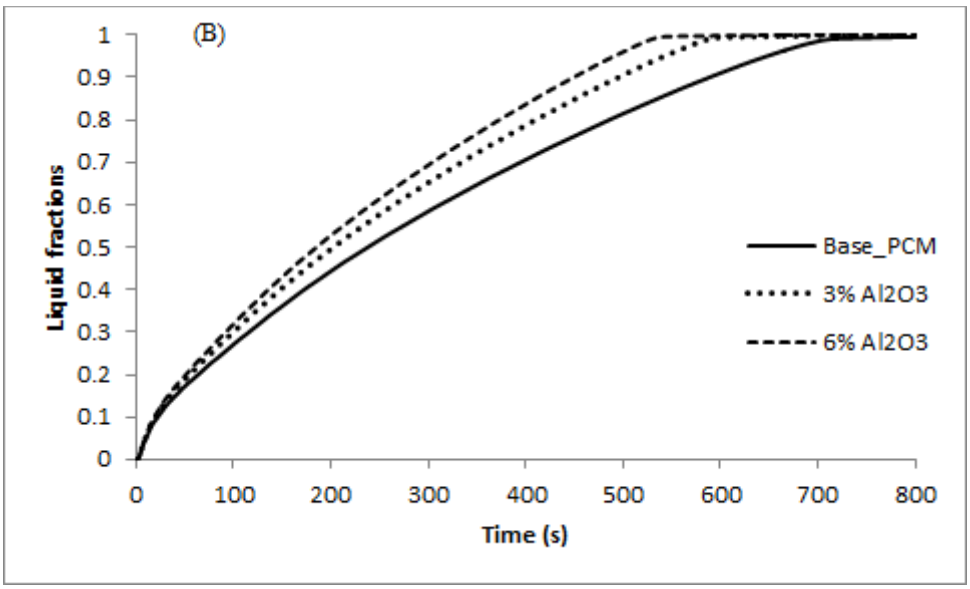

Figure 4.32: Evolution of the liquid fraction in the pure PCM and PCM with 3% and 6% volumetric concentration of Al_2O_3 nano-particles.

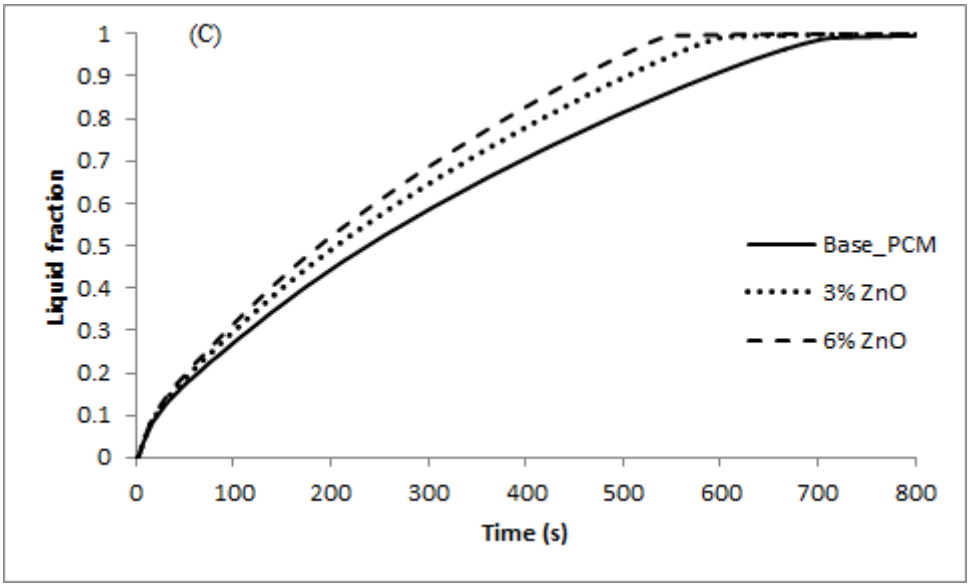

Figure 4.33: Evolution of the liquid fraction in the pure PCM and PCM with 3% and 6% volumetric concentration of ZnO nano-particles.

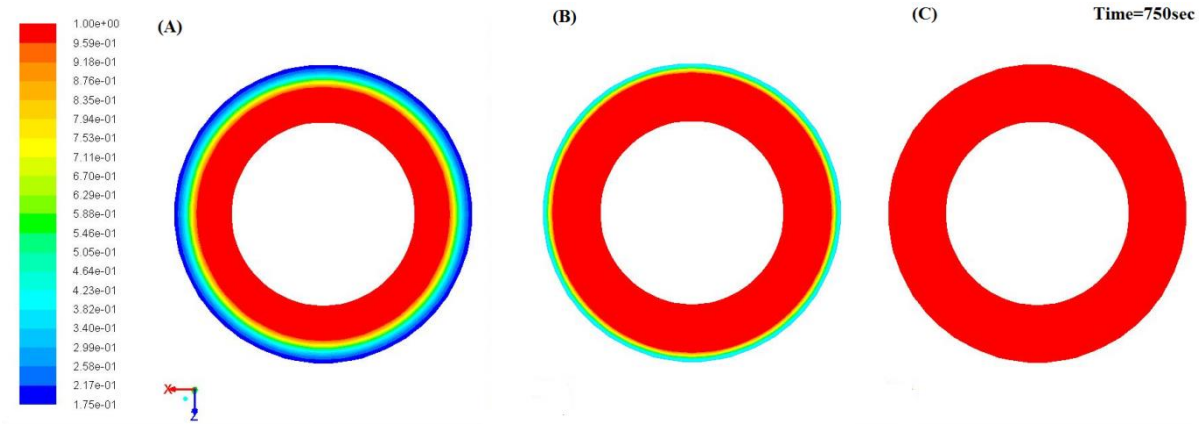

Figure 4.34: Liquid fraction of the PCM at the bottom of the storage unit. (A) Pure PCM, (B) PCM with 3% of CuO, (C) PCM with 6% of CuO.

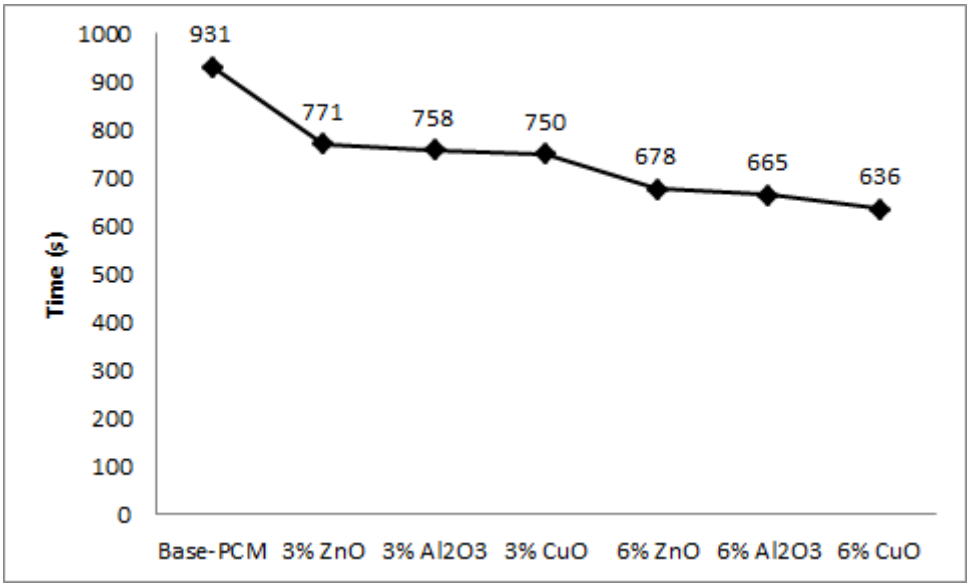

Figure 4.35: Total melting time for pure PCM and PCM with 3% and 6% volumetric concentration of CuO, Al2O3 and ZnO nano-particles.

The total amount of heat stored in the PCM when its temperature is risen from the initial (T_{in}) to final level (T_f) during the melting process can be calculated using the following equations

$$Q = \rho_{pcm} V_{liquid\ pcm} \left[L_{hpcm} + C_{pcm} \left(T_m - T_{in} \right) + C_{pcm} \left(T_f - T_m \right) \right] \tag{4.7}$$

$$V_{liquid\ pcm} = \left[liquid\ fraction \right] \times V_{pcm} \tag{4.8}$$

where ρ_{pcm}, $V_{liquid\ pcm}$, L_{hpcm}, T_{in}, T_m and T_f are the density, the volume of the liquid PCM, the latent heat, the initial, melting and the final temperature, respectively.

Figure 4.36 shows the heat storage rate as a function of time for the system with various volumetric concentrations of CuO, Al_2O_3 and ZnO nano-particles. It can be seen that the maximum amount of energy which can be stored using the nano PCM will be insignificantly decreased with the rise in the nano-particles volumetric concentration. This is due to the reduction in the volume occupied by the pure PCM, and lower specific and latent heat of the

nano PCM. However, *n-Octadecane* with nanoparticles not only exhibits rapid melting performance but also retains the high energy storage capacity for a given storage size.

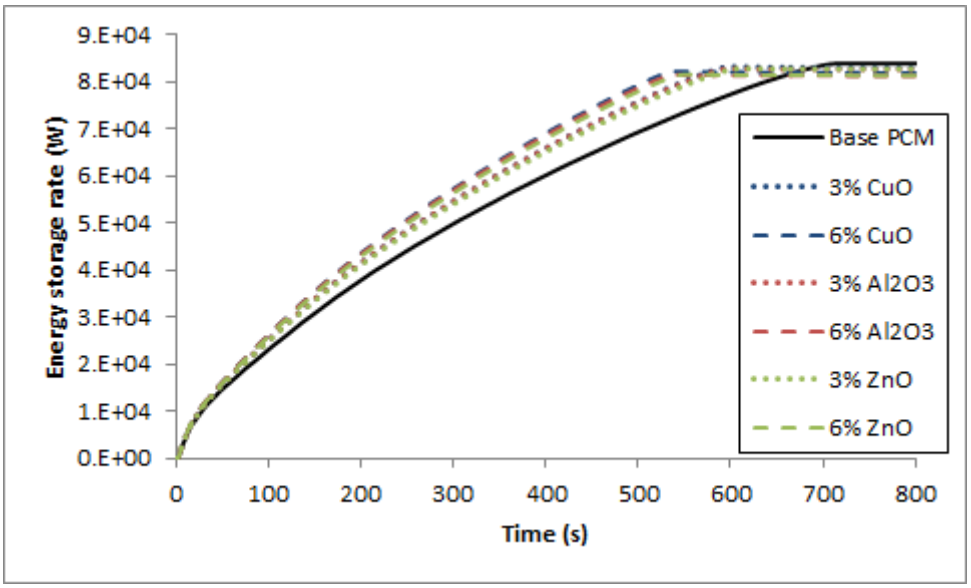

Figure 4.36: Energy storage rate as a function of time.

4.3.3 Effect of nano-particles on natural convection

In order to scale up the natural convection, the system needs to be installed in the horizontal position. A number of points were created inside the computational domain to monitor the variation of the temperature inside the PCM during numerical CFD modelling. These monitoring points are placed in planes, which are perpendicular to the axis of the system and located at distances of 0.07, 0.51 and 0.95 m from the front of the system. Figure 4.37 indicates the locations of monitoring points in the plane at the distance of 0.07 m from the front of the system.

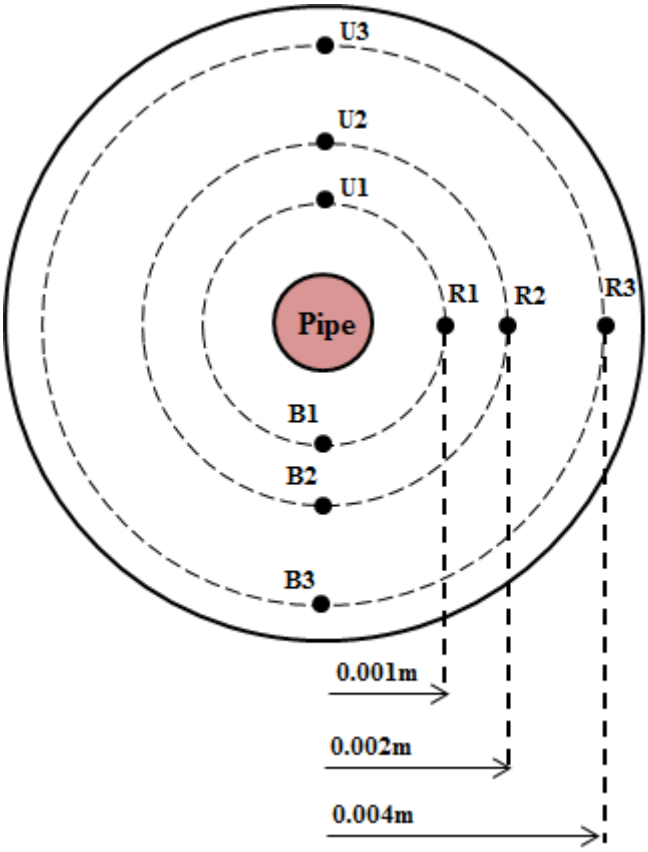

Figure 4.37: Locations of the monitoring points around the pipe.

Figure 4.38 shows the temperature variation at some of monitoring points at the front plane of the system with the pure PCM (without nanoparticles) for the case when the inlet temperature of the HTF is 320.7 K and the mass flow rate is 0.0315 kg/s. It can be seen that initially the temperature increases rapidly from 280 to 299 K due to the heat transfer from the pipe walls to the solid PCM by conduction. The temperatures at monitoring points u1, r1, and b1 rise more rapidly due to their proximity to the pipe. Temperatures in monitoring points u3, r3, and b3 rise considerable slower since these points are located on the edge of the storage unit.

During the melting process the temperature increases from 299 to 300.7K and equalise at all monitoring points. Initially during the melting process a thin liquid layer is formed between the pipe and the solid PCM. Gradually, the solid-liquid interface expands in the axial and radial directions and the melting then is dominated by natural convection in the PCM's liquid

regions. The melting process is intensified in the upper regions of the container, resulting in higher temperature recordings at the top of the computational domain (point u1).

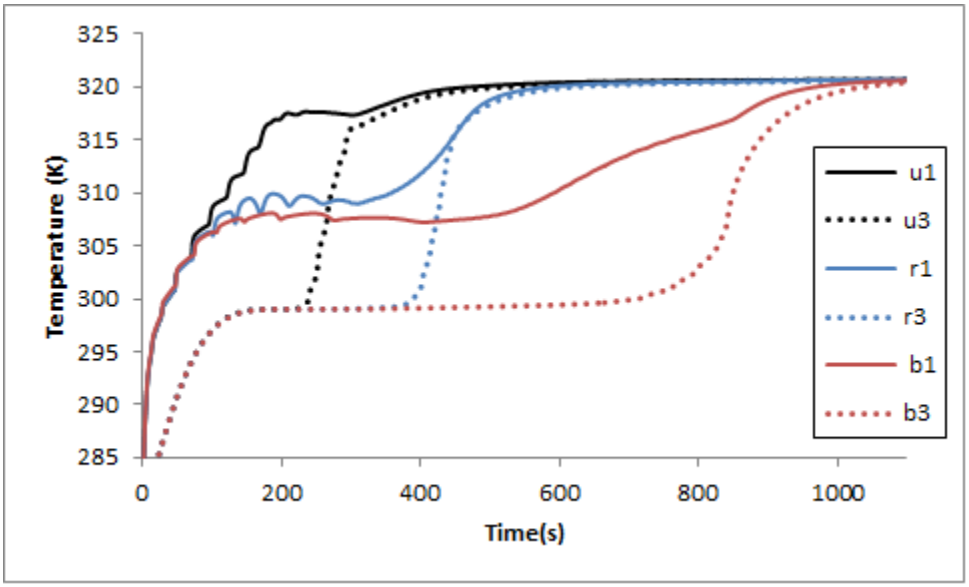

Figure 4.38: Variation of the Base PCM temperature as function of time.

Similar observations can be made in the system with the PCM with nanoparticles. Figure 4.39 presents results on the temperature variation in the PCM with 6% volumetric concentration of Al_2O_3 nano-particles for the case when the inlet temperature of the HTF is 320.7 K and the mass flow rate is 0.0315 kg/s. The figure demonstrates that higher temperatures are recorded in regions close to the pipes walls and this is due to the enhanced conduction and at the top layer of the PCM, which can be explained by dominant effect of natural convection in the molten PCM.

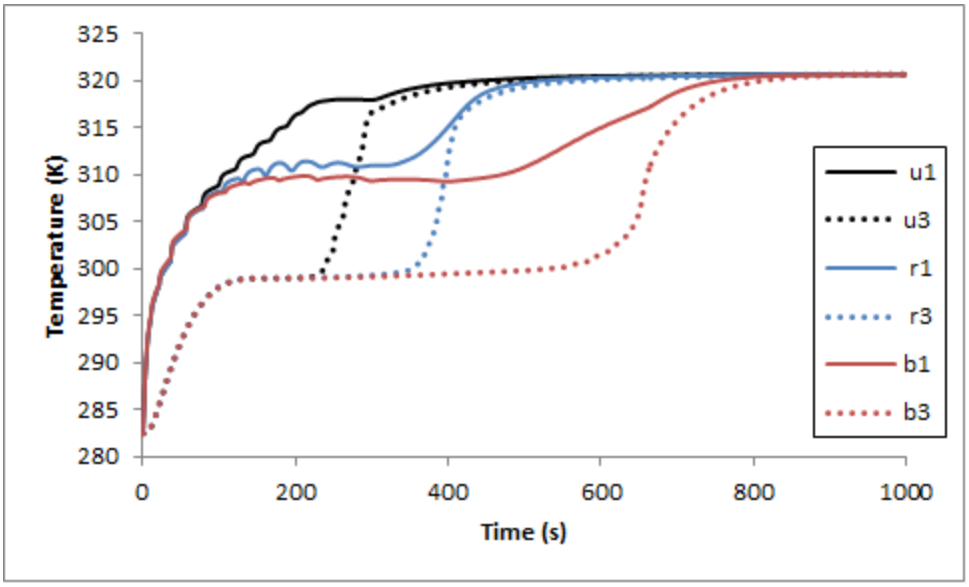

Figure 4.39: Temperature variations in the PCM with 6% volumetric concentration of Al_2O_3 nano-particles as a function of time.

To analyse the effect of nanoparticles on the natural convection and the heat transfer in the system, results on the temperature distribution at the top, bottom and side regions of the PCM storage system along its axis were produced. It can be seen in Figure 4.40 that the temperature rise in the PCM with or without nanoparticles at the top layers is almost identical which indicates that adding nanoparticles to the PCM does not have significant effect on the buoyancy force and natural convection phenomena during the PCM's melting process. Figure 4.41 shows the temperature rise in the nano PCM at the side region and at the centre of the storage unit (monitoring points r1 and r3). This information demonstrates that the nano PCM temperature rise is more rapid than that of the pure PCM (*n-Octadecane*). Figure 4.42 indicates that nano PCM's temperature variation also takes place at higher rate than that in the pure PCM at the bottom of the unit (monitoring points b1 and b3). These results can be explained by heat transfer to the bottom and side regions by conduction. Adding nano-particles to the PCM enhances the thermal conductivity which accelerates the temperature rise.

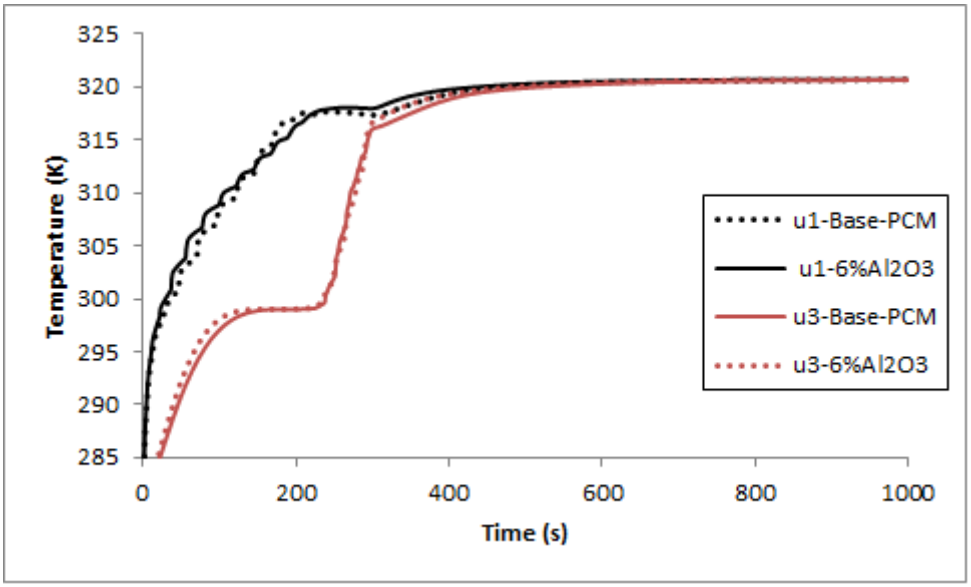

Figure 4.40: Temperature variation in the PCM with 6% volumetric concentration of Al_2O_3 nano-particles at the top of the unit.

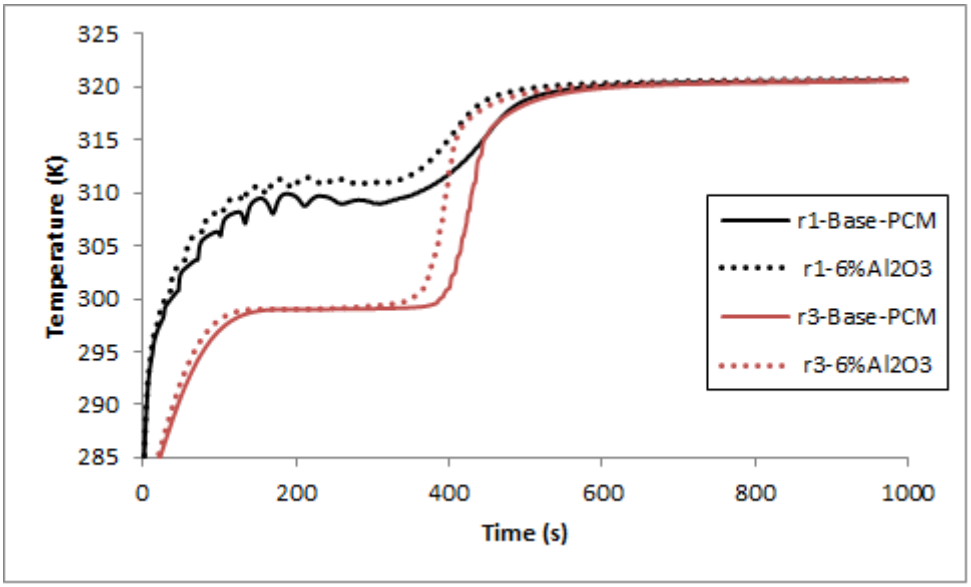

Figure 4.41: Temperature variation in the PCM with 6% volumetric concentration of Al_2O_3 nano-particles at the side region of the unit.

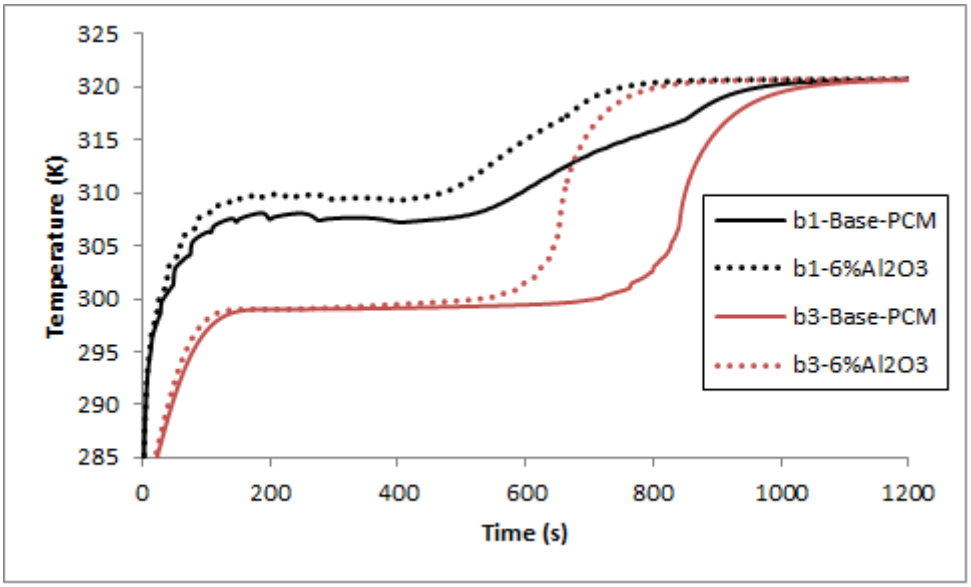

Figure 4.42: Temperature variation in the PCM with 6% volumetric concentration of Al_2O_3 nano-particles at the bottom of the unit.

Figure 4.43 shows the temperature distribution and liquid fractions of the pure PCM and PCM with 6% volumetric concentration of Al_2O_3 nano-particles. The temperatures are higher in the nano PCM which is a result of nano-particles accelerating the melting process in the PCM.

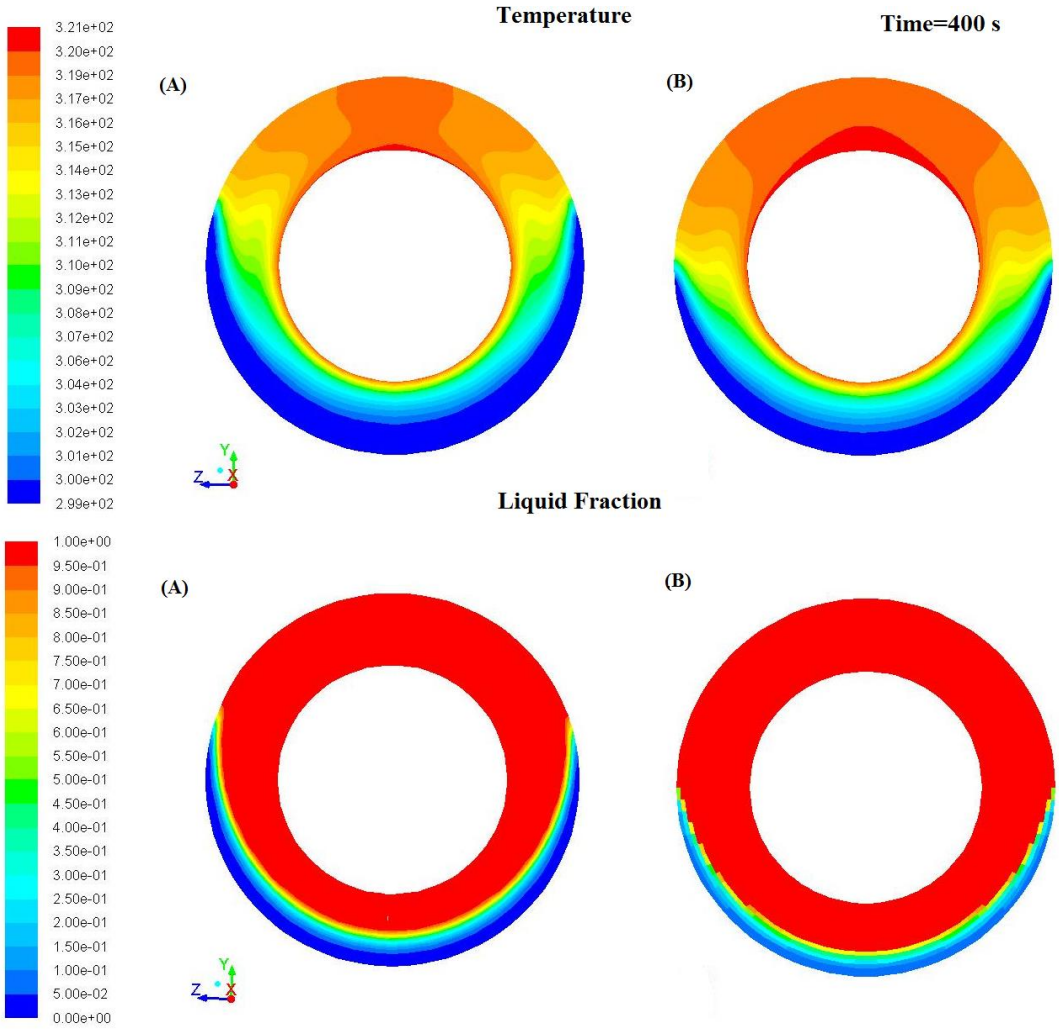

Figure 4.43: The temperature distribution and liquid fraction in (A) pure PCM; (B) PCM with 6% volumetric concentration of Al_2O_3 nano-particles. Elapsed time is 400 s.

The velocity vectors in the liquid pure PCM and PCM with 6% volumetric concentration of Al_2O_3 nano-particles are shown in Figure 4.44 for the elapsed time of 300, 400 and 550 s. It can be seen that the molten PCM ascends upwards from the top regions at the centre of the unit and then after cooling flows downwards to complete the natural convection circle. The convection is intensified as the liquid fraction volume increases. The velocity magnitude gradually decreases in time due to reduction in the temperature difference in the molten PCM. These results are in good agreement with results of a number of experimental and numerical investigations [177, 191, 298].

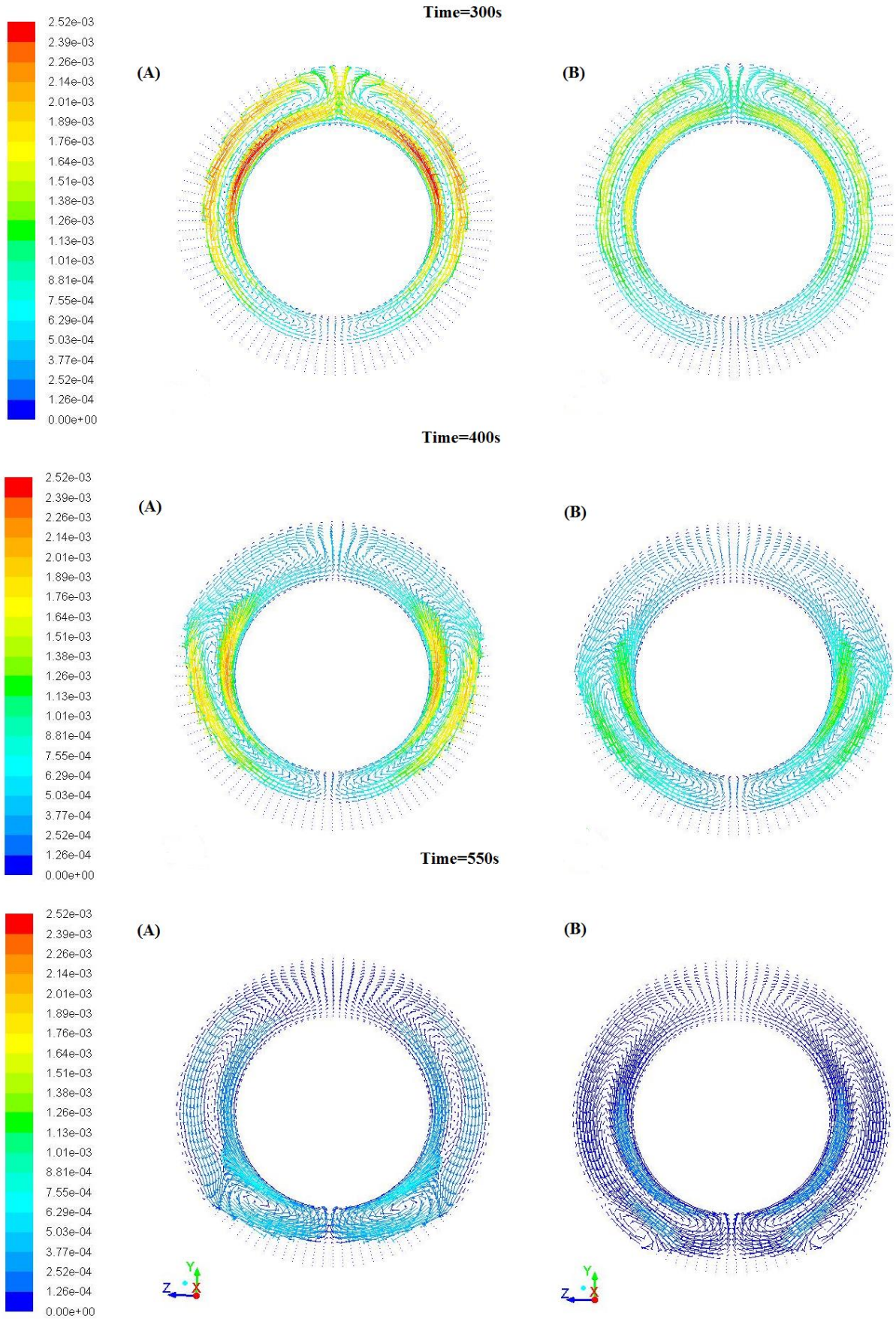

Figure 4.44: Velocity vectors in (A) pure PCM (B) PCM with 6% volumetric concentration of Al_2O_3 nano-particles.

The heat transfer coefficient values were calculated for the top, side and bottom regions of the storage unit for the case when the inlet temperature of the HTF is 320.7 K and the mass flow rate is 0.0315 kg/s. Figures 4.45-4.47 present results on the heat transfer coefficient changing as a function of time for the pure PCM and PCM with 6% volumetric concentration of CuO nano-particles. It can be seen that the heat transfer coefficients for both top and side regions increase with time. This agrees well with the initial solid PCM's temperature rise followed by the melting process. The higher heat transfer coefficient values can be observed at the top regions of the system. This can be attributed to the effect of natural convection. For the longer elapsed times, the heat transfer value stabilises. This is because the temperature distribution becomes more established within the PCM body when the system reaches the steady state operation. At this stage, the majority of the PCM is melted and a very small part of it, which is close to the bottom regions of the unit, may be in the solid state.

The analysis of results also indicates that the heat transfer coefficient in the pure PCM at the top regions is greater than that in the PCM with 6% volumetric concentration of CuO nano-particles. This is due to the effect of the natural convection which is the most intensive at the top regions of the unit. Adding nano-particles to *n-Octadecane* increases the density and suppresses the effect of natural convection in the PCM with nanoparticles. The heat transfer coefficient for PCM with nanoparticles at the bottom regions is higher than that of *n*-Octadecane. This is because of intensification of heat transfer at the bottom region by conduction. Adding nanoparticles to the PCM, enhances the thermal conductivity of nano PCM in comparison to that of *n-Octadecane*.

The average heat transfer coefficients at the top, side, and bottom regions for the pure PCM (*n-Octadecane*) are 299, 205 and 116 W/m^2K, respectively. For the PCM with 6% volumetric concentration of CuO nano-particles, the average heat transfer coefficient at the top, side, and bottom regions are 277, 207, and 150 W/m^2K, respectively. The average heat

transfer coefficient value at the top region is reduced by 7.4%, and increased by 29.3% for the bottom region when using 6 % volumetric concentration of CuO nano-particles.

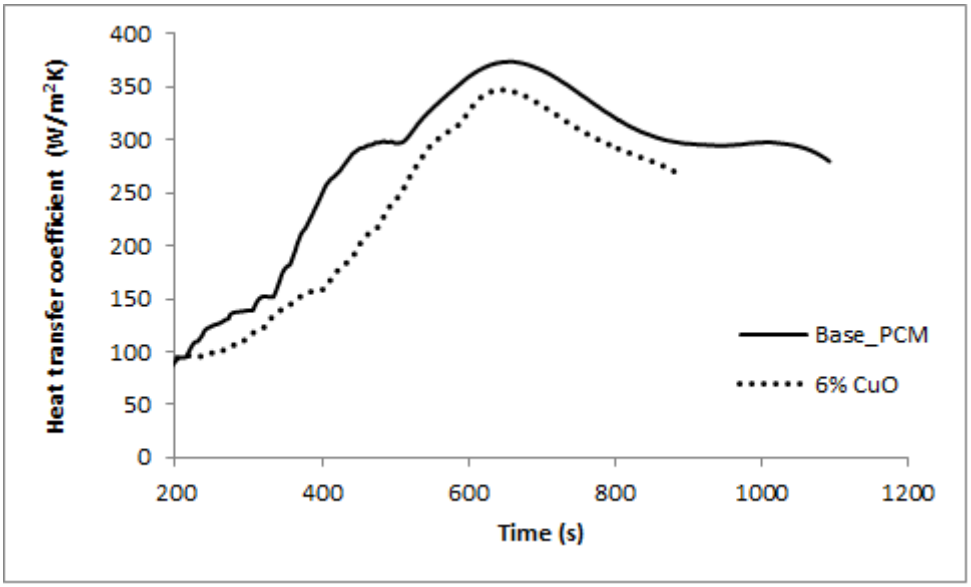

Figure 4.45: The heat transfer coefficient variation at the top regions of the system.

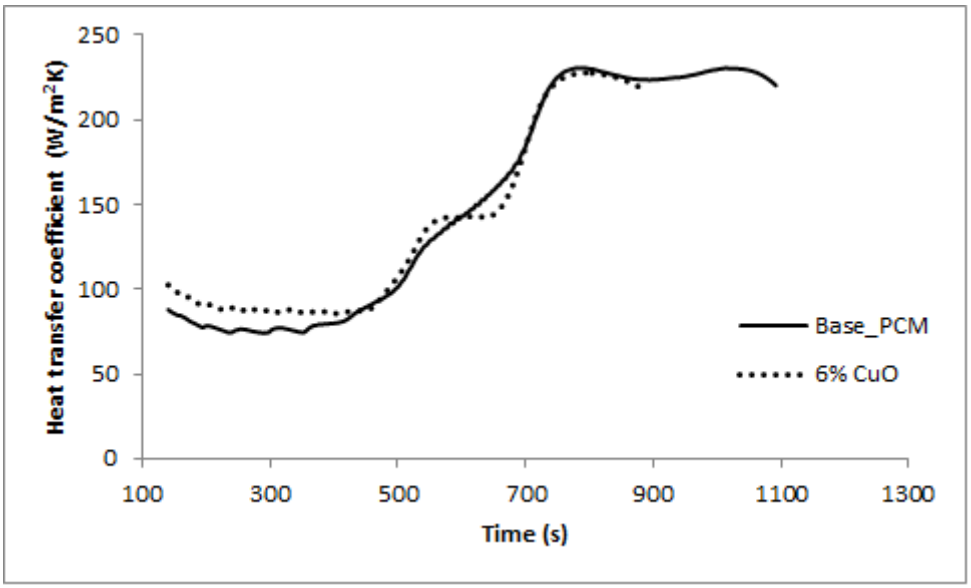

Figure 4.46: The heat transfer coefficient variation at the side regions of the system.

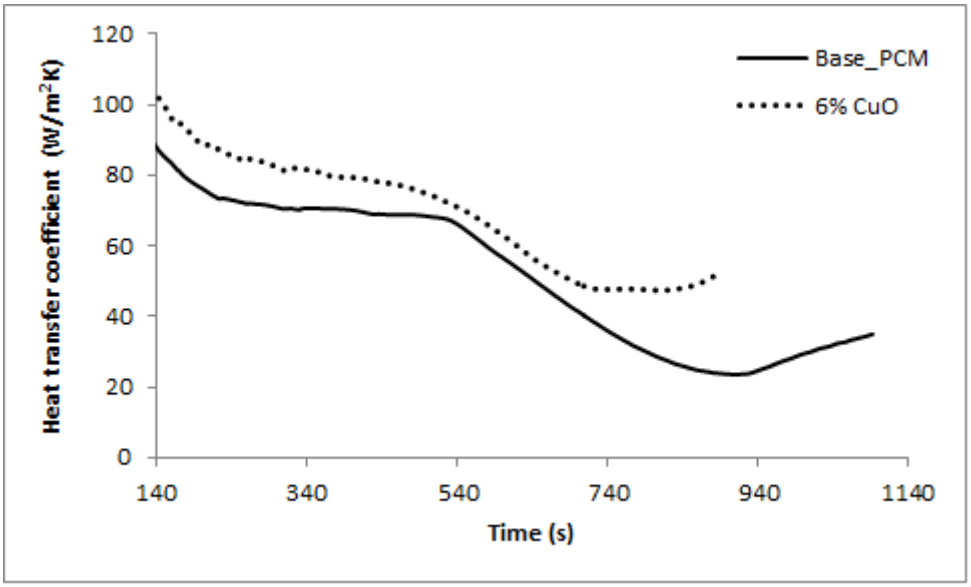

Figure 4.47: The heat transfer coefficient variation at the bottom regions of the system.

.

The average heat transfer coefficient values for various HTF inlet temperature and flow rates were obtained and used to calculate the Nusselt number for the two cases, namely the pure PCM and PCM with 6% volumetric concentration of CuO nano-particles. The flow rates of the HTF considered were 0.000315, 0.00315, 0.005, and 0.0063 Kg/s. The HTF inlet temperatures used in the modelling are 305, 310, and 320 K. In order to derive generic heat transfer correlations, the Nusselt numbers were calculated at the top, side and bottom regions of the storage unit. Thereafter, the average Nusselt number value for all regions is calculated. Figures 4.48-4.59 show results of these CFD modelling.

As it can be seen in Figures 4.48-4.51, the Nusselt number increases with the rise in the Stefan number which is proportional to the difference between the inlet temperature of the HTF and the melting temperature of the PCM (the increase in the inlet temperature of HTF increases the Stefan number). Similar observations can be made with regard to the Rayleigh number, see Figures 4.52-4.55. The Rayleigh number is also proportional to the difference between the inlet temperature of the HTF and the melting temperature of the PCM.

Figures 4.56-4.59 show that the Nusselt number decreases with the rise in the Fourier number. The Fourier number is proportional to the melting time. However, an increase in the inlet temperature and flow rate of the HTF will lead to decrease the total melting time, and thus, reduce the Fourier number.

Figures 4.48 and 4.49 illustrate the change in the Nusselt number for the system with the pure PCM and PCM with 6% volumetric concentration of CuO nano-particles at the top and side regions of the storage unit. It can be seen that Nusselt number is higher when pure PCM compared to the case when the PCM with 6% volumetric concentration of CuO nano-particles is deployed. The effect of natural convection becomes smaller for PCMs with nano-particles and the reduction in the Nusselt number after adding nano-particles is caused by the higher density.

It can be seen in Figures 4.52-4.56 that the Rayleigh number is decreased when the nano-particles are added. This is because of a reduction in the specific heat of the PCM. Also, nanoparticles increase the viscosity and thermal conductivity of the PCM which also leads to reduction of the Rayleigh number.

The change in the Nusselt number for the pure PCM and PCM with 6% volumetric concentration of CuO nano-particles at the bottom regions of the storage unit is presented in Figures 4.50, 4.54, and 4.58. As expected, the Nusselt number for PCM with 6% volumetric concentration of CuO nano-particles is higher than in the case when pure PCM is used. This is because of more intensive heat transfer in the bottom regions by conduction and adding nano-particles to the PCM enhances the thermal conductivity of PCMs.

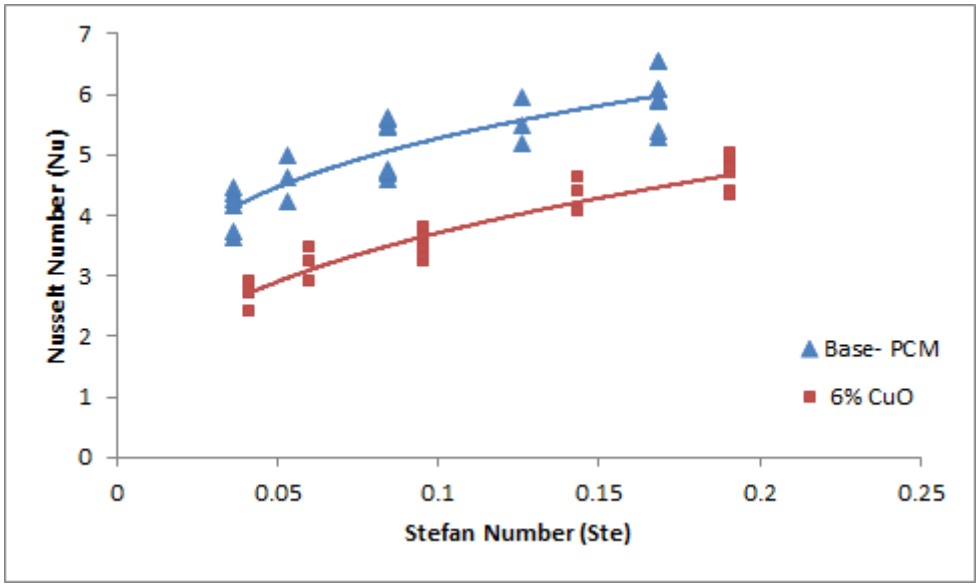

Figure 4.48: Variation in the Nusselt number as a function of Stefan number for upper regions.

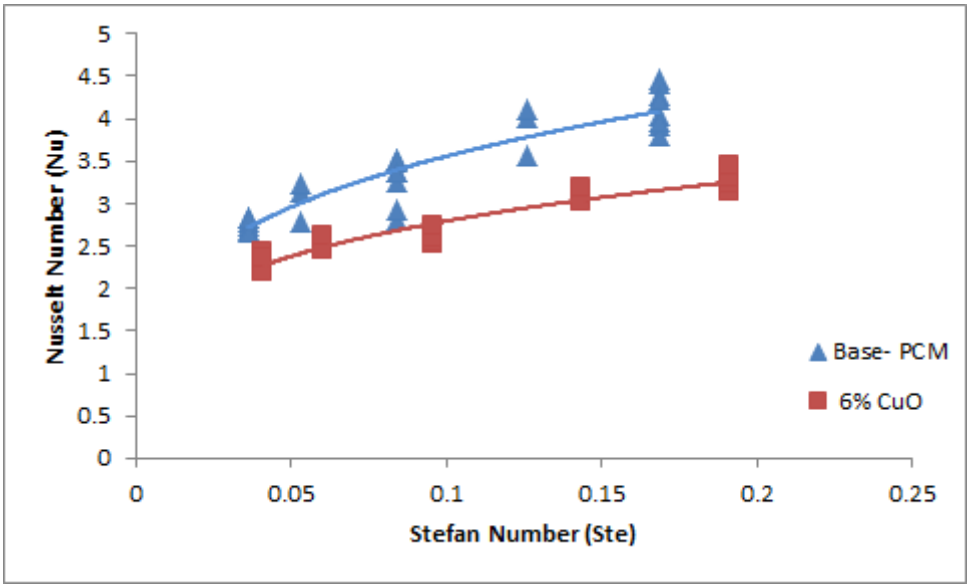

Figure 4.49: Variation in Nusselt number as a function of Stefan number for side regions.

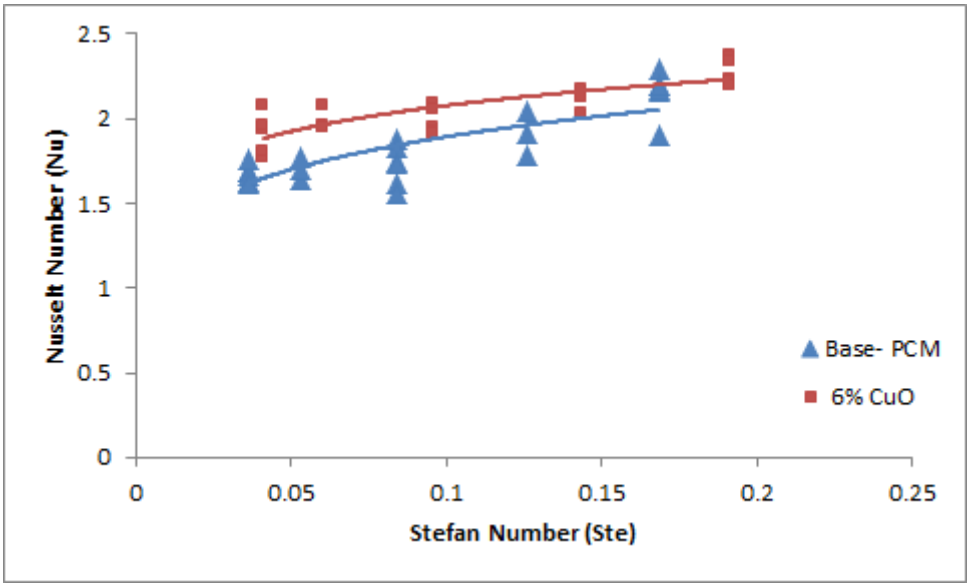

Figure 4.50: Variation in Nusselt number as a function of Stefan number for bottom regions.

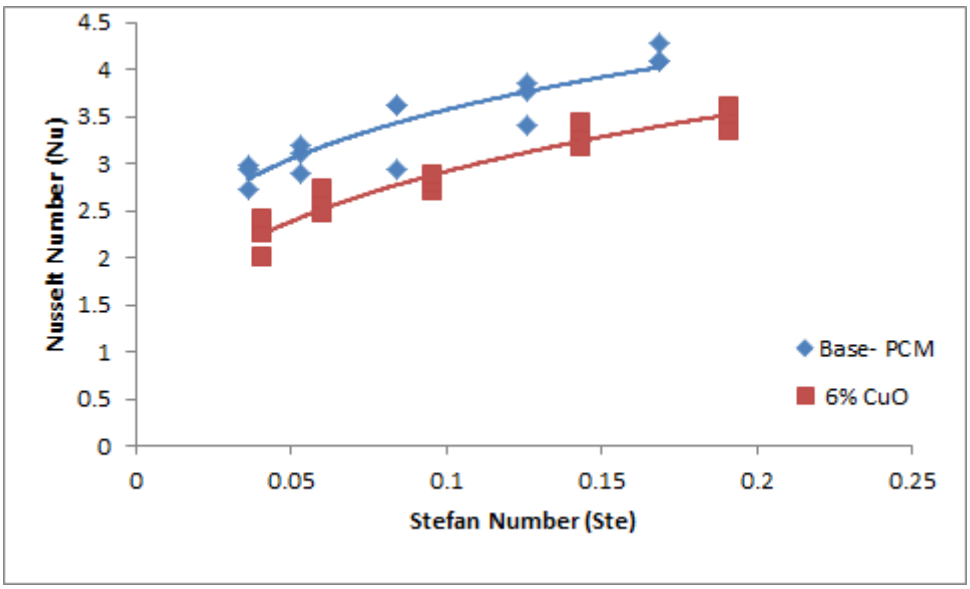

Figure 4.51: The variation in the average Nusselt number (in the system) as a function of Stefan number

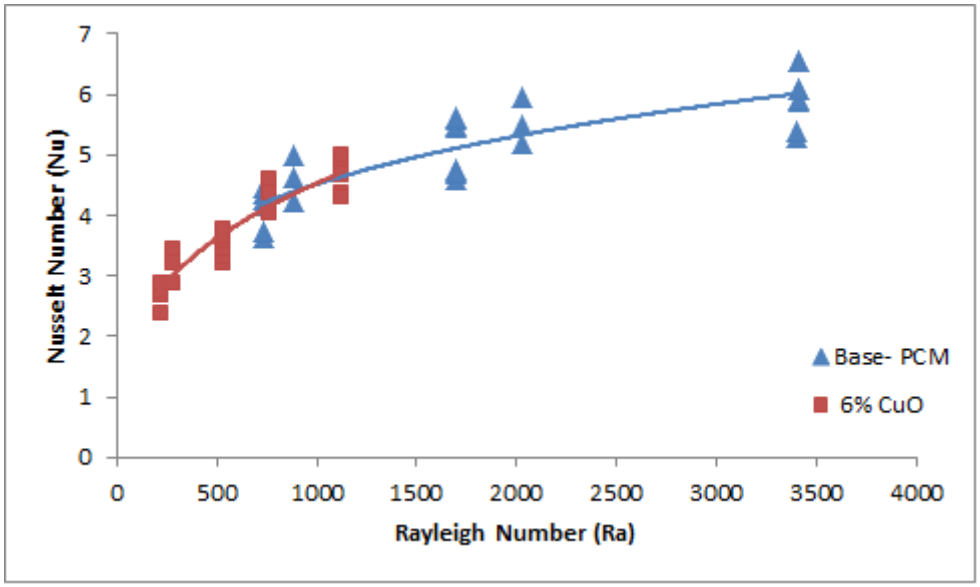

Figure 4.52: Variation in the Nusselt number as a function of Rayleigh number in upper regions.

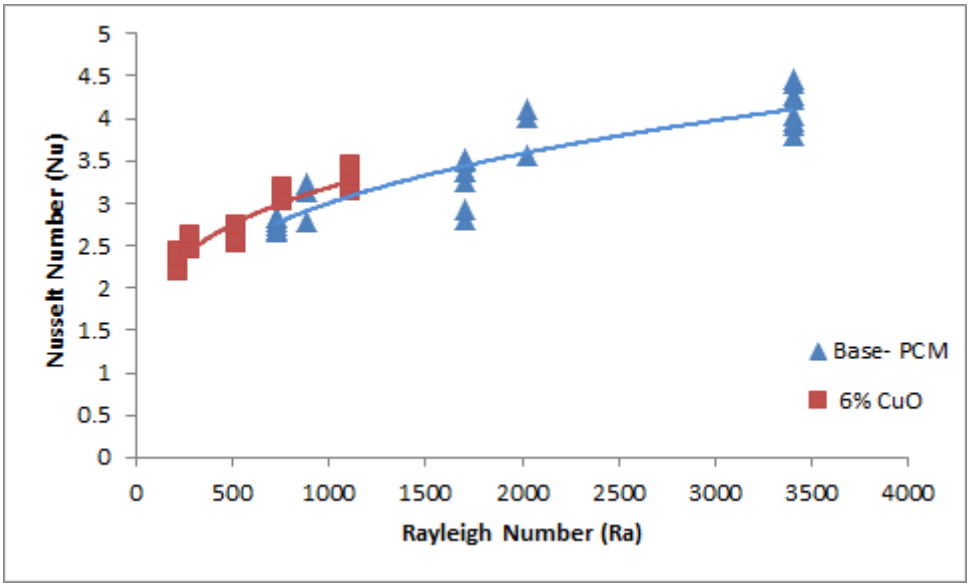

Figure 4.53: Variation in the Nusselt number as a function of Rayleigh number in side regions.

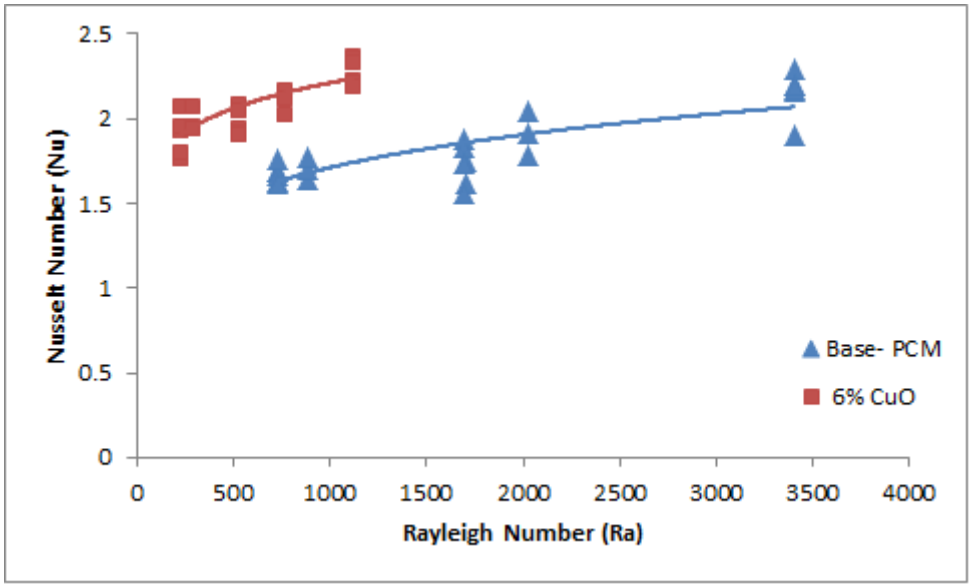

Figure 4.54: Variation in Nusselt number as a function of Rayleigh number in bottom regions.

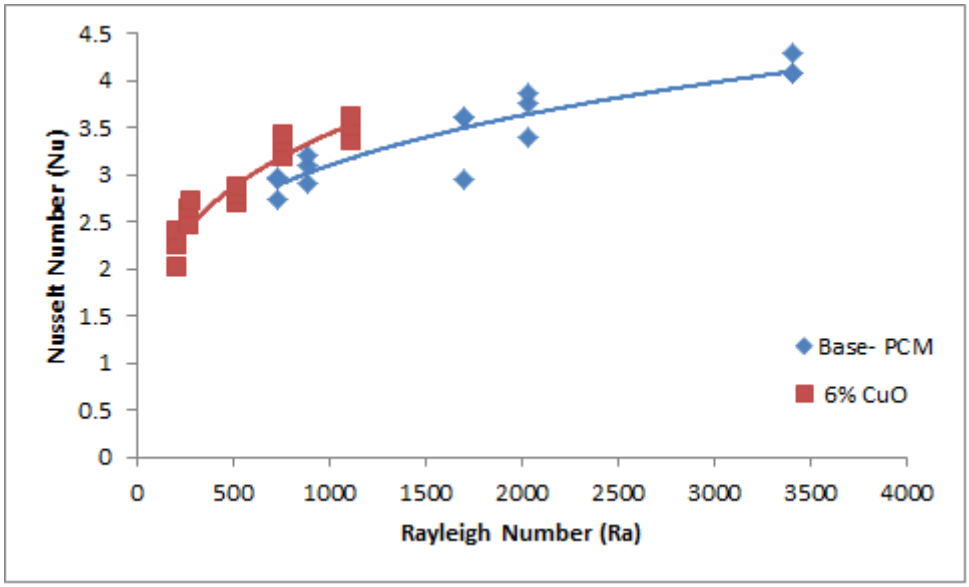

Figure 4.55: The variation in the average Nusselt number (in the system) as a function of Rayleigh number.

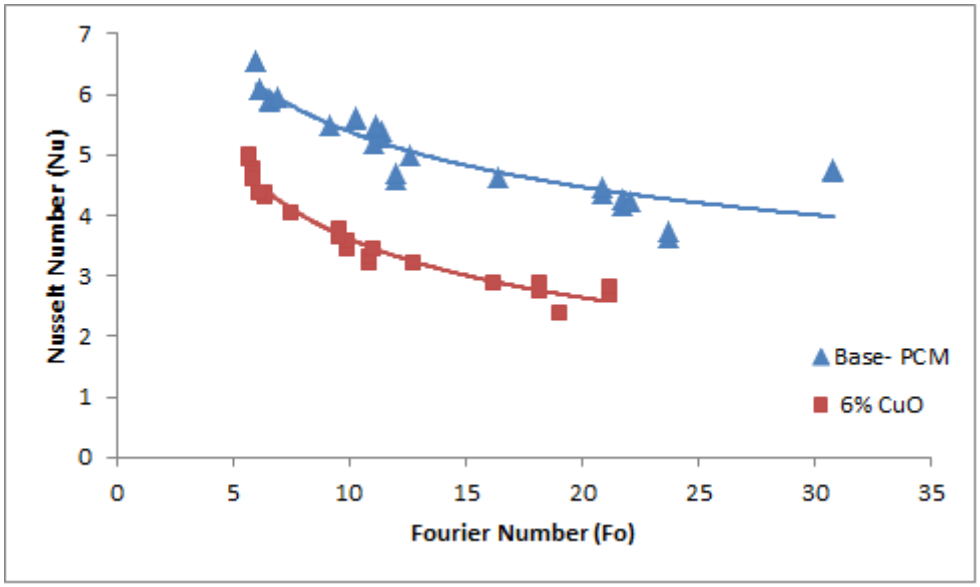

Figure 4.56: Variation in the Nusselt number as a function of Fourier number in upper regions.

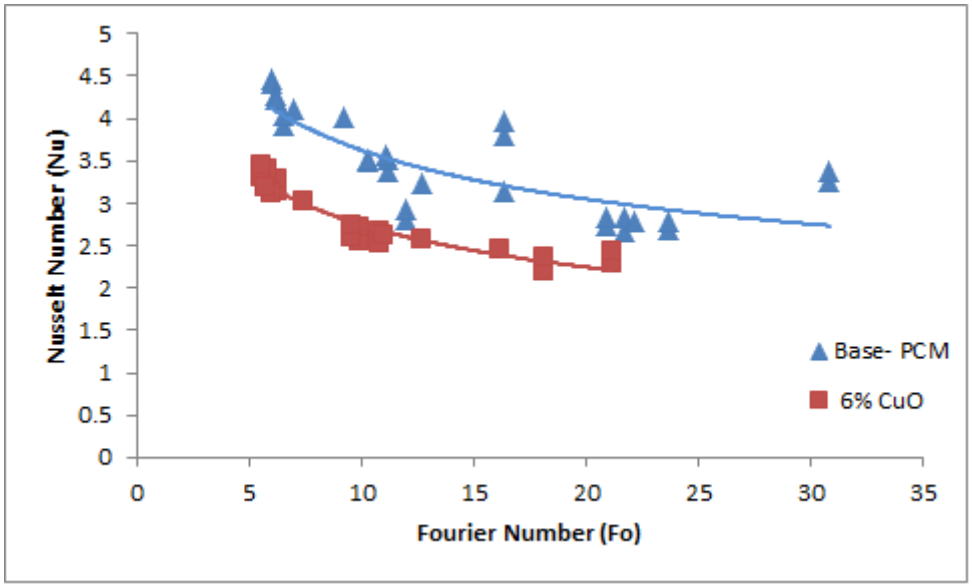

Figure 4.57: Variation in the Nusselt number as a function of Fourier number in side regions.

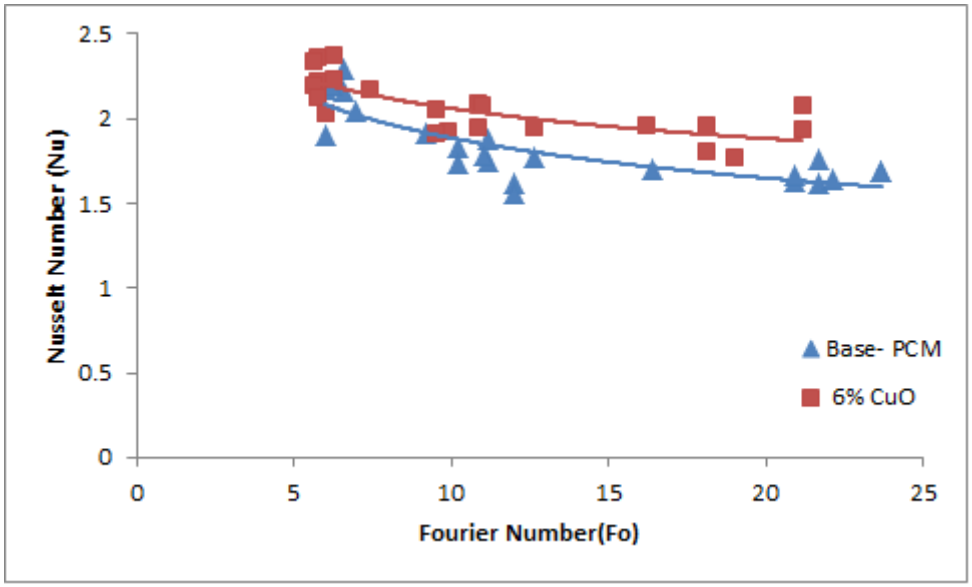

Figure 4.58: Variation in the Nusselt number as a function of Fourier number in bottom regions.

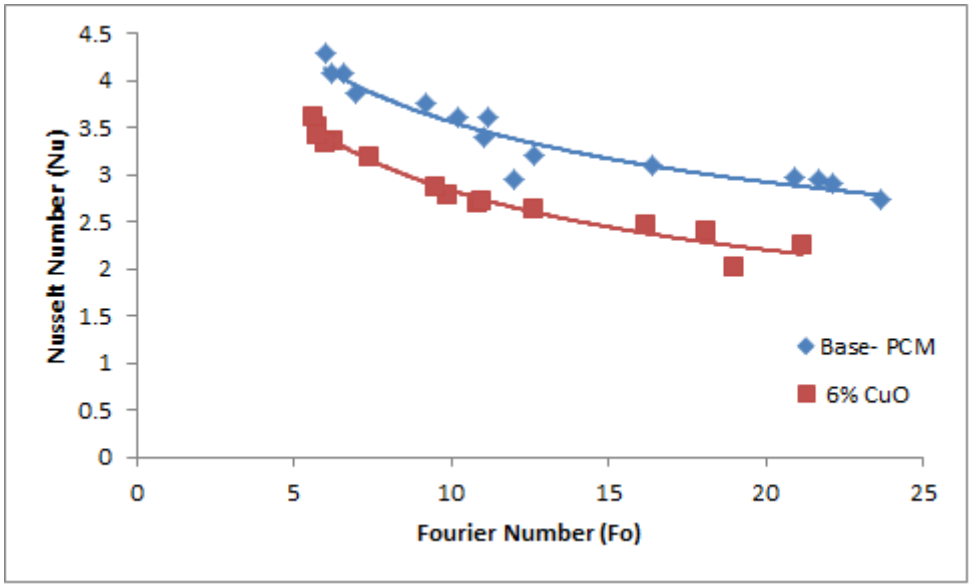

Figure 4.59: The variation in the average Nusselt number (in the system) as a function of Fourier number.

The average Nusselt numbers in the system are presented in Figures 4.51, 4.55, and 4.59. This data was used to derive the Nusselt number correlations for the pure PCM and PCM

with 6% volumetric concentration of CuO nano-particles. The correlations are derived as a function of the Stefan, Fourier, and Rayleigh numbers.

The Nusselt number for the pure PCM is ($R^2 = 0.8524$)

$$Nu = 2.9883(Ste)^{0.0758}(Fo)^{-0.095}(Ra)^{0.0759} \tag{4.9}$$

Nusselt number for the PCM with 6% volumetric concentration of the CuO nano-particles is ($R^2 = 0.9407$)

$$Nu = 2.7597(Ste)^{0.0968}(Fo)^{-0.121}(Ra)^{0.0873} \tag{4.10}$$

The correlations between numerically obtained and calculated using Equations (4.9) and (4.10) are shown in Figures 4.60 and 4.61. It can be seen that the Nusselt number varies between 2 and 4.3 for the system under investigations. The lower Nusselt numbers are for the low HTF inlet temperature, and the high Nusselt numbers values are obtained at the high HTF inlet temperatures.

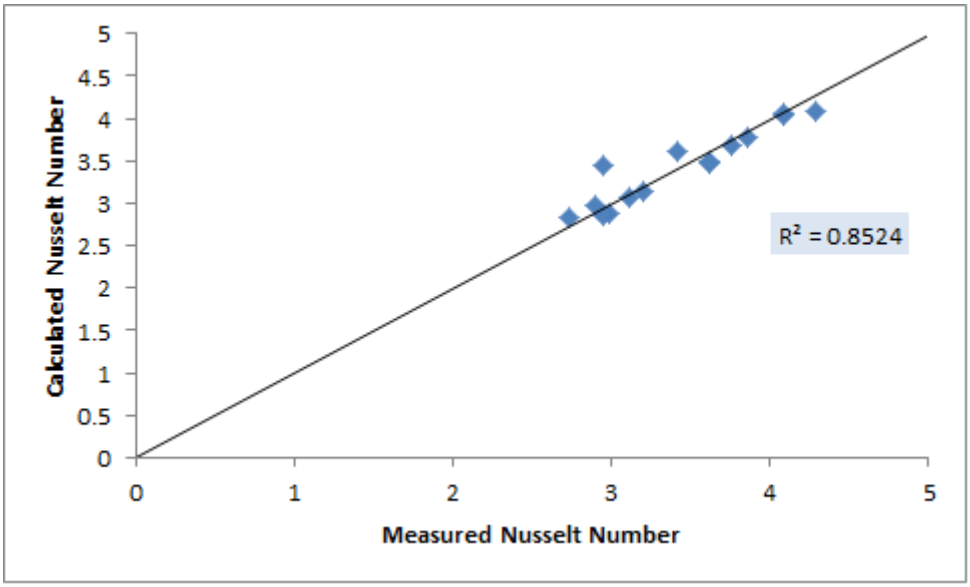

Figure 4.60: The correlation between numerically obtained and calculated using Equation (4.9) Nusselt numbers - the pure PCM.

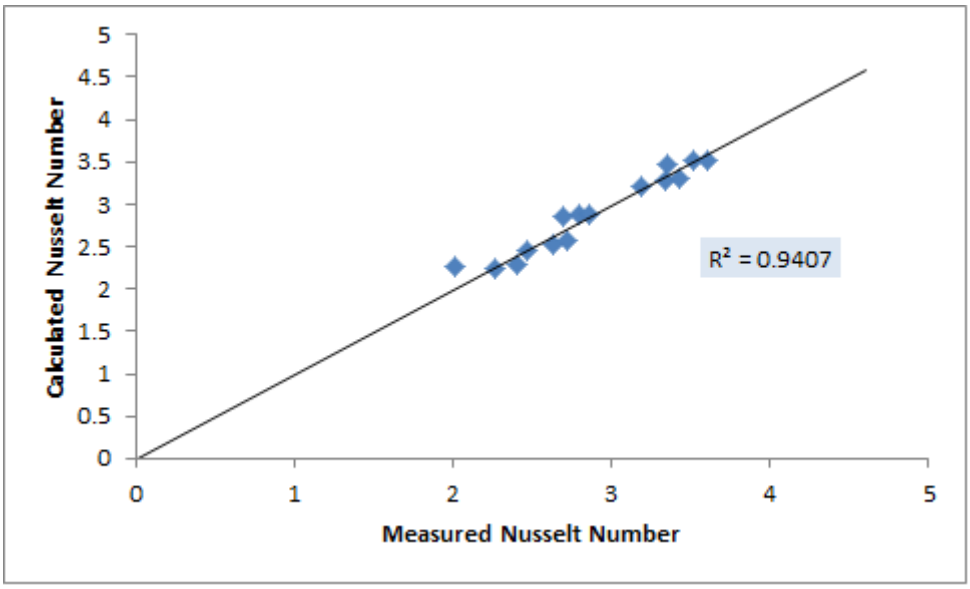

Figure 4.61: The correlation between numerically obtained and calculated using Equation (4.10) Nusselt numbers – the PCM with 6% volumetric concentration of CuO nano-particles.

Chapter 5 Experimental Study of the PCM Thermal Storage System

5.1 Introduction

The main objective of this experimental study is to examine the performance of a heat storage system filled with paraffin wax as a PCM. The heat to the storage system was supplied by evacuated tube solar collectors using water as an HTF. The system was tested during three different seasons in the North East region of the UK. Additionally, the system was tested under the steady state conditions in order to validate the CFD model. This chapter describes the experimental setup, the test procedures and the thermal characteristics of the system during the charging and discharging processes. Finally, a comparison of the experimental data and numerical results from FLUENT ANSYS simulations were carried out for validation purposes.

5.2 Experimental setup

The experimental set-up is to establish the thermal characteristics of the PCM heat storage system as shown in Figures 5.1 and 5.2. It consists of four main components including the storage system (1), solar radiation simulator (2), evacuated tube solar collectors (3), and a circulating pump (4). The heat exchanger was connected to the evacuated tube solar collector using flexible plastic piping insulated by Styrofoam. The HTF was circulated through the system using a small pump powered by the main power supply. The flow rates were regulated by a manually operated valve and measured by a flow meter.

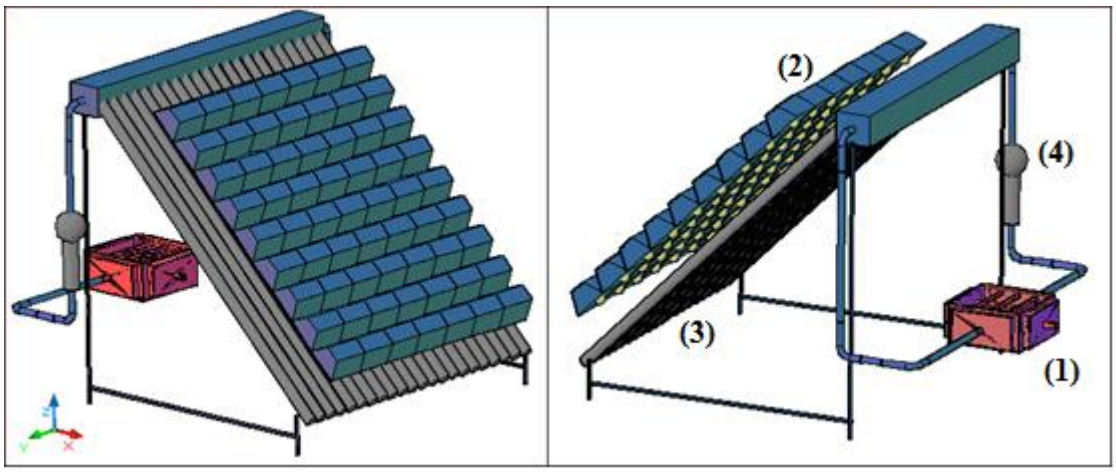

Figure 5.1: Experimental set-up.

Figure 5.2: Experimental prototype of the heat storage system heated by evacuated tube solar collectors.

5.2.1 Solar radiation simulator

The solar radiation simulator was used to provide an artificial source of solar radiation with different levels regardless of the outdoor weather conditions. It consists of 110 tungsten halogen floodlights installed within approximately 1.8 m^2. The maximum electrical power for each floodlight is 150 W. The array of the floodlight was installed parallel to the evacuated tube solar collector. In order to produce an artificial solar radiation with different levels, the floodlight was divided into three groups and connected to a 3-phase variable transformer. Figure 5.3 shows the solar radiation simulator with 3-phase transformer.

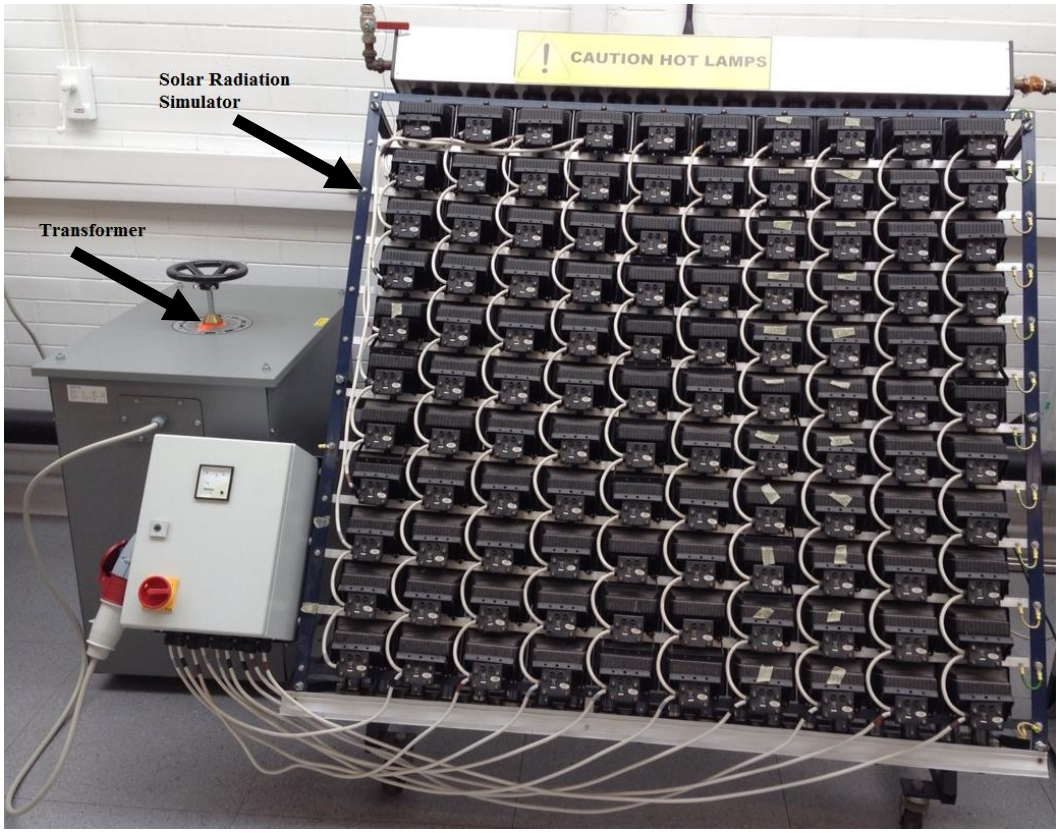

Figure 5.3: Solar radiation simulator.

5.2.2 Evacuated tube solar collectors

The 20 evacuated tube solar collectors are made of heat pipes installed in transparent glass tubes (see Figure 5.4). The solar radiation heats the heat pipes which then transfer the produced heat to the HTF in the manifold. The manifold is made of a copper pipe that is 1.5 m in length and has a diameter of 0.06 m. The condensing zone of the heat pipes is inserted into the manifold and is put in contact with the HTF at the top of the solar collector. In order to minimize the heat loss, the manifold is insulated by glass wool and placed into a steel casing. Table 5.1 shows the main specification of the solar collector.

Table 5.1: Specification of the evacuated tube solar collector.

Parameter	Description
Collector Type	Evacuated-tube with heat pipe
Number of tubes	20 tubes
Tube Length	1.74 m
Outer Tube Diameter	0.047 m
Collector Area	2.250 m^2
Absorber Area	1.80 m^2
Dimensions L×W×H	1760×1500×130 (mm)
Weight	55 kg
Maximum Operating Temperature	190 ℃
Stagnation Temperature	247 ℃

Figure 5.4: Evacuated tube solar collector.

5.2.3 Heat storage system

The heat storage system is made of a rectangular copper container with the following dimensions; 0.3 m length, 0.3 m width, and 0.1 5m height. The heat storage system was filled with Paraffin wax to serve as a PCM with melting temperature of 331 K. The container holds a total of 15 pipes; each pipe is 1 mm thick with a diameter of 10 mm (see Figure 5.5). The pipes were arranged in sets of three; three sets for hot HTF (9 pipes), and two sets for cold HTF (6 pipes). The horizontal distance between centre-to-centre pipes is 75 mm. The first set of hot pipes is placed at a height of 25 mm from the bottom of the container, the second and third sets are placed at heights of 75 mm and 125 mm, respectively (see Figure 5.6). The first set of cold pipes is placed at a height of 50 mm, and the second set is placed at a height of 100 mm as shown in Figure 5.7. The flow enters the mixing chambers before it enters the

pipes in order to allow a single flow to be distributed among the various pipes. Moreover, the heat storage system is insulated with thick polystyrene in order to minimize the amount of heat loss.

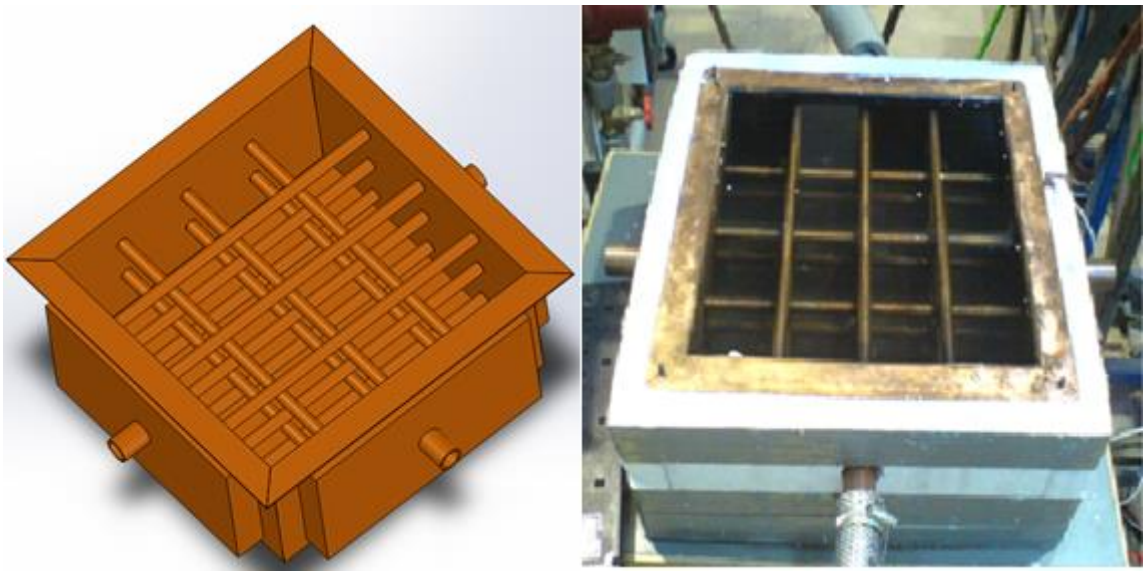

Figure 5.5: Heat storage system design

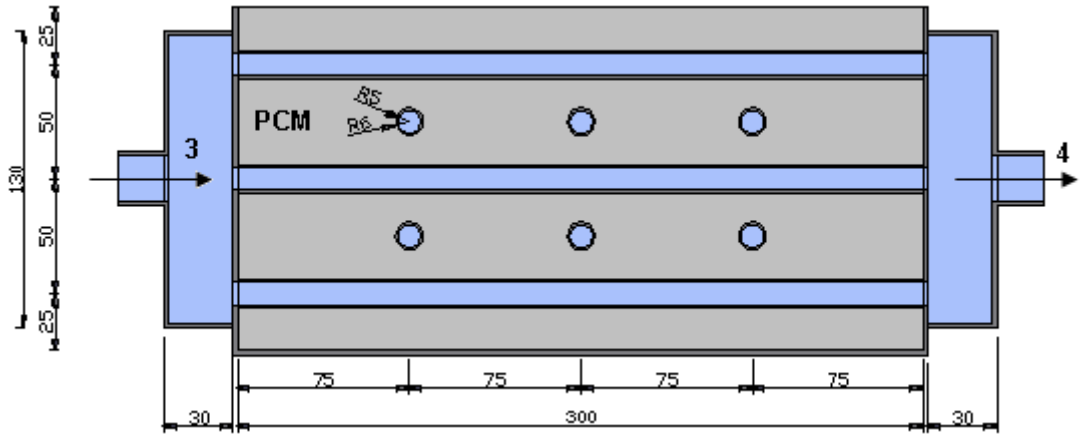

Figure 5.6: A cross section of the hot pipes. The inlet of the hot HTF is 3 and the outlet is 4.

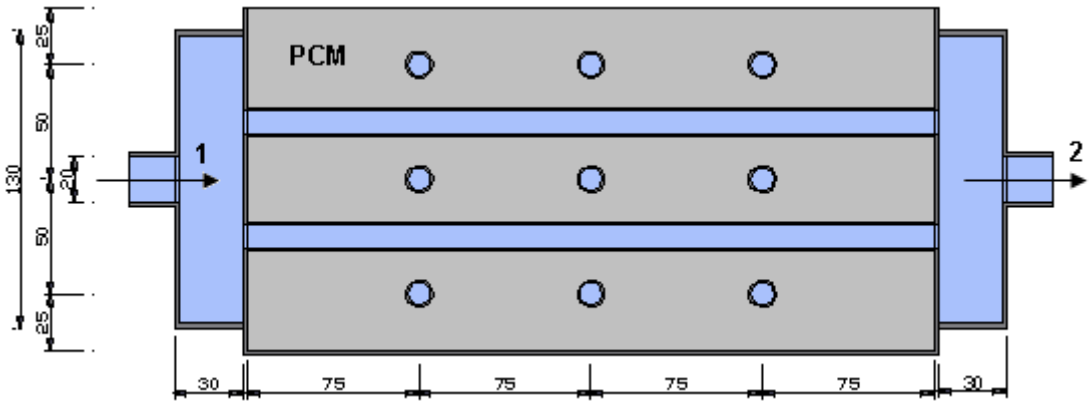

Figure 5.7: A cross section of the cold pipes. The inlet of the cold HTF is 1 and the outlet is 2.

In these experiments set of cold pipes was not engaged during tests, since the heat discharging process was not investigated in this PhD study.

5.3 Measurements

5.3.1 Temperature measurements

The temperature was measured and recorded at several locations inside the PCM during the charging processes to determine the temperature profile. Sixteen thermocouples were placed inside the PCM at different distances and distributed in four columns, as shown in Figure 5.8. Type K thermocouples were chosen as they have appropriate temperature range. The upper area of the heat storage system was split into 16 sections, and each thermocouple was placed at the centre of each section at the central depth of the unit as shown in (Figure 5.8). In order to ensure the accuracy of the temperature profile of the PCM, the position of each thermocouple was chosen carefully. Additionally, some measures were taken to hold the thermocouples in place in order to endure the forces generated inside the PCM such as the melting and solidification processes as well as the volume change during the phase change. Hence, each thermocouple was fixed on a thin wooden rod to help keep it in place. The lid of

the system was pierced in order to allow the thermocouples to be inserted. The attached wooden rods secured the thermocouples into the PCM as shown in (Figure 5.9). The temperature of the HTF inlet and outlet were measured using two thermocouples; T_i and T_o.

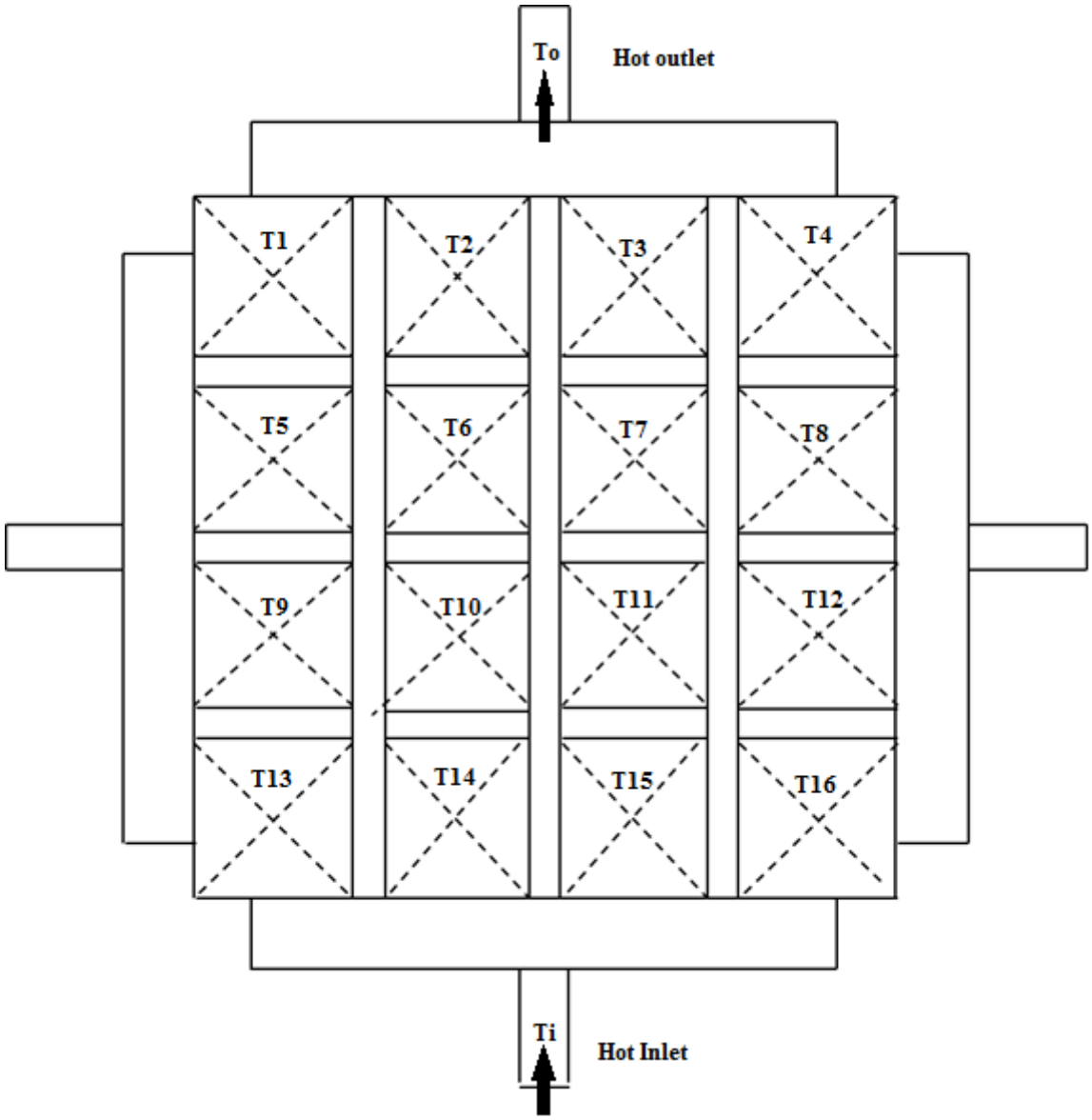

Figure 5.8: Thermocouples positions in the heat storage system.

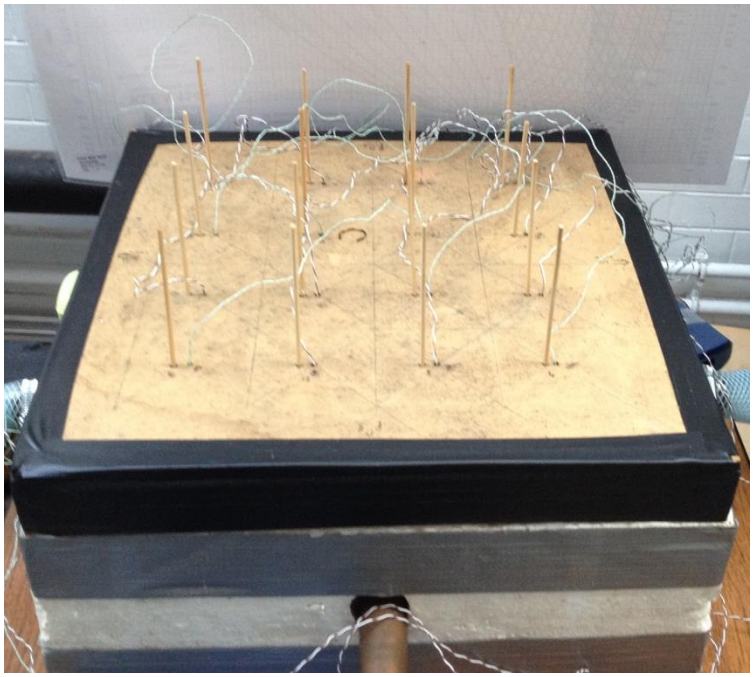

Figure 5.9: Wooden rods with thermocouples at the tip.

5.3.2 Flow measurements

A GRUNDFOS –USP 15-50 Selectric domestic heating circulator pump was used to circulate the water through the system. This pump was selected to withstand the high temperature of the circulated water up to 100 ℃ and a maximum pressure of 10 bars. Figure 5.10 shows the pump performance curves.

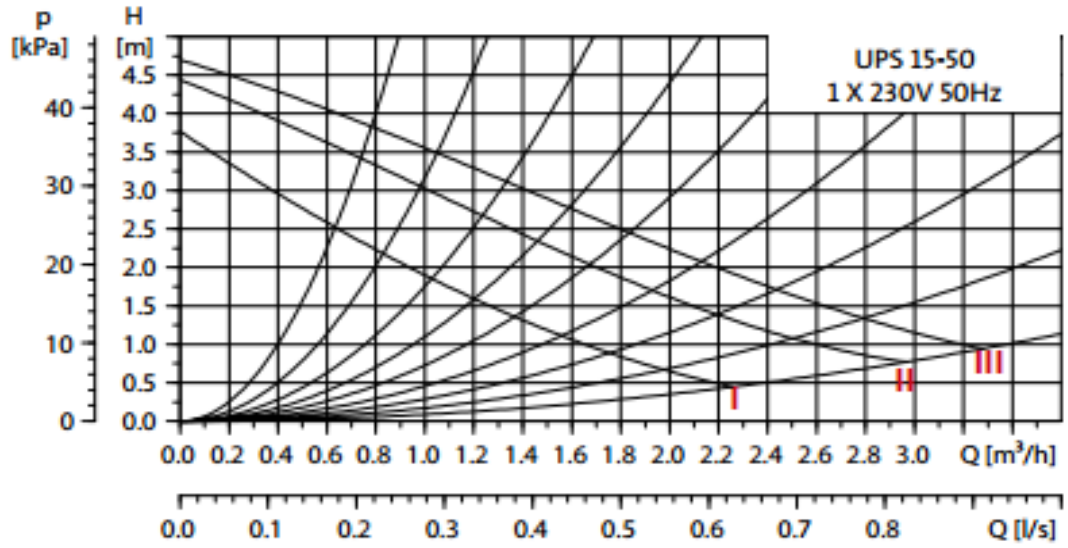

Figure 5.10: Pump curves for flow rate versus head pressure- GRUNDFOS –USP 15-50 Selectric domestic heating circulator pump.

To measure the flow rate of the HTF a Platon flow meter with a capacity of measuring flows on a scale from 1 to 10 LPM is used. Figure 5.11 depicts the pump and flow meter.

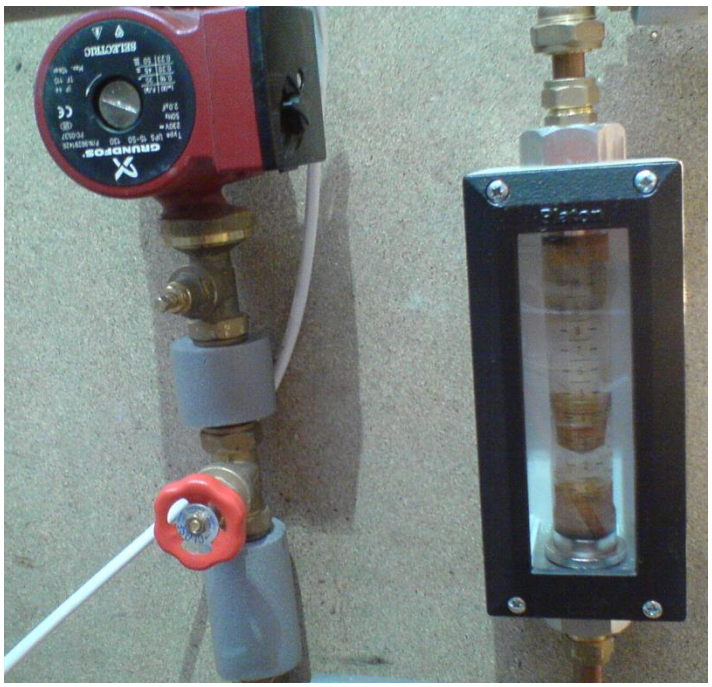

Figure 5.11: Flow meter and Pump.

5.3.3 Solar insolation measurements

The Personal Measurement Assistant model PMA2200 shown in Figure 5.12 was used to measure the radiation produced from the solar radiation simulator. The sensor is designed to detect a full spectrum of radiation including ultraviolet, visible and infrared waves.

Figure 5.12: Photometer PMA 2200.

5.3.4 Data acquisition

A Data Acquisition System (DAQ) was used to record all output values collected from the thermocouples. The data was recorded once every second in order to observe how the values change over time. Several channels used to record sixteen K-type thermocouples inside the PCM, two K-type thermocouples for the inlet and outlet of the HTF. All values collected from the thermocouples were recorded onto a computer where the PICO data logger software stored the data on a spreadsheet.

5.4 Experiment uncertainty

In order to validate the experimental results with the numerical, care was given to the uncertainty in measurements. According to Kline and McClintock [299], the experimental uncertainty of a measured value consists of a fixed (bias) error and random (precision) error. The total uncertainty is defined as the root sum square of the fixed error and random error. Bias errors can be obtained through calibration curve for most instruments. The experimental data recorded in this study were temperature, flow rate, and solar insolation measurements.

The fluid flow rate is measured by means of a calibrated rotameter with an accuracy ratio of ±4%. The rotameter was calibrated by collecting and weighing the water that passed through the meter during a certain period of time. The water was collected in a tank, and then weighed to determine the total mass accumulated during the period of experiment. The flow rate was calculated by dividing mass over time. The temperature of the PCM and HTF were measured by means of K-Type thermocouples with an accuracy ratio of ±0.5 ^{o}C and they are calibrated by the manufacturer. The level of solar radiation was measured by means of PMA 2200 photometer with an accuracy ratio of 0.5% of full scale and it is calibrated by the supplier. Positional uncertainty may occur if the thermocouple readings are used to estimate the position of the melt front or to determine the temperature gradient. The margin of uncertainty was set to ±2mm. All of these sources of uncertainty will be taken into account when comparing the experimental data to the numerical CFD results.

5.5 Experimental procedure

For the purposes of the experiment, the solar simulator was controlled by a three phase power supply transformer to adjust the voltage every 20 minutes in order to produce a daily solar irradiance profile. This was conducted on several occasions during various seasons in the

north-east region at UK. Figure 5.13 illustrates the variation of solar insolation rates during a typical summer day in the northeast region.

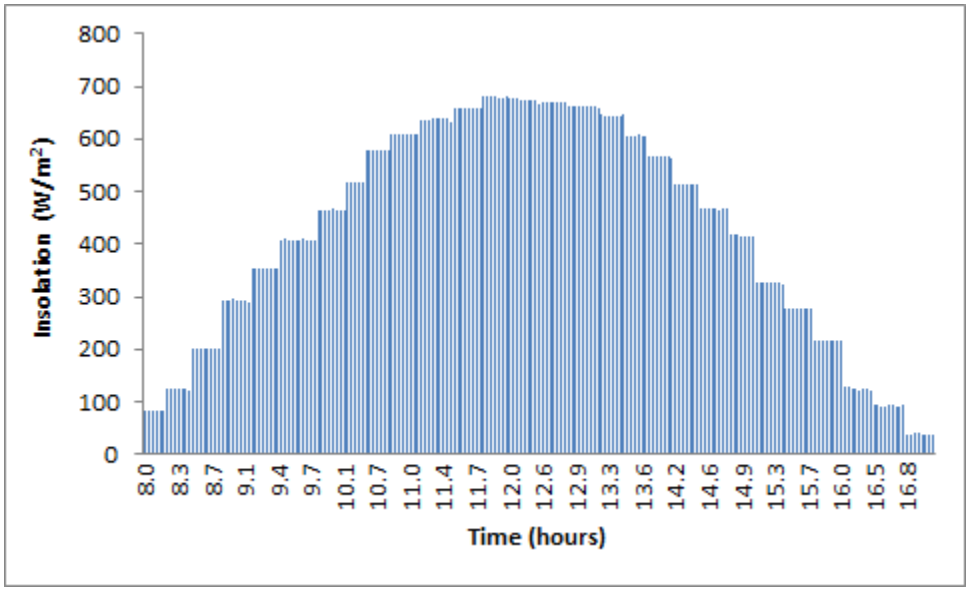

Figure 5.13: The variation of solar insolation rates during a typical summer day in the northeast region.

The objective of the calibration process is to measure the average radiation rate produced by the solar simulator of halogen floodlights at different levels of voltage regulated by the 3-phase transformer. A light stand was used to arrange the halogen floodlights for the purposes of this experiment. The light stand was designed to hold 110 halogen floodlights. The floodlights were arranged in eleven rows and ten columns equally spaced as shown in (Figure 5.14). The total amount of radiation produced by the light stand was measured using a Photometer. The total amount of radiation includes the average rate of radiation from the halogen floodlights as well as the radiation in the spaces between the rows and columns. First, the average amount of radiation produced at the centre of a halogen lamp was calculated and then multiplied it by the total area lamps. Second, the average amount of

radiation for the spaces between the rows and the columns of lamps was calculated using a similar process. The average amount of radiation produced from the whole stand was calculated by first combining the amount of radiation from the lamps and the amount of radiation calculated from the spaces between the rows and columns then dividing it over the total area of the light stand. Then, the calculated data was further analysed to generate the insolation voltage diagram shown in Figure 5.15.

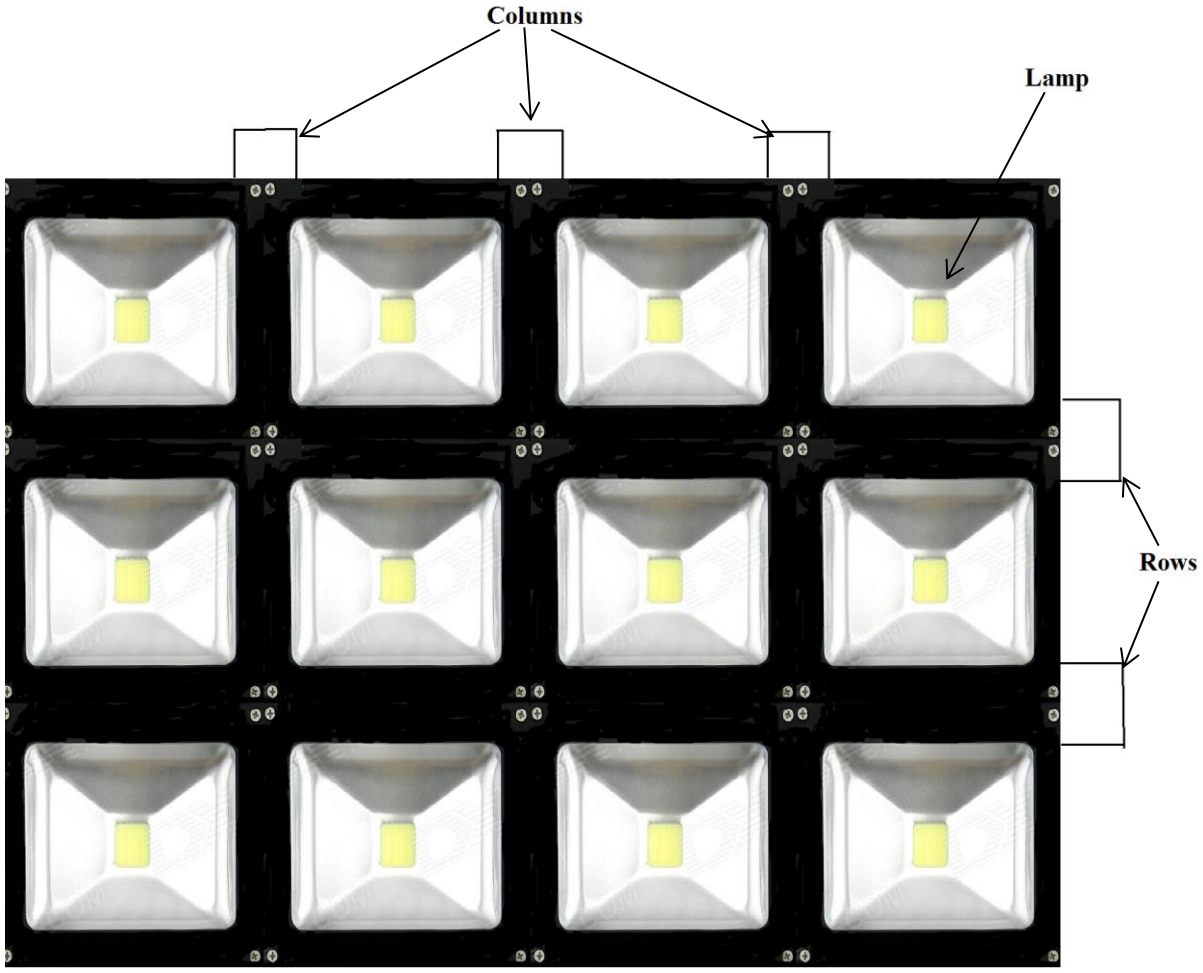

Figure 5.14: Lights stand.

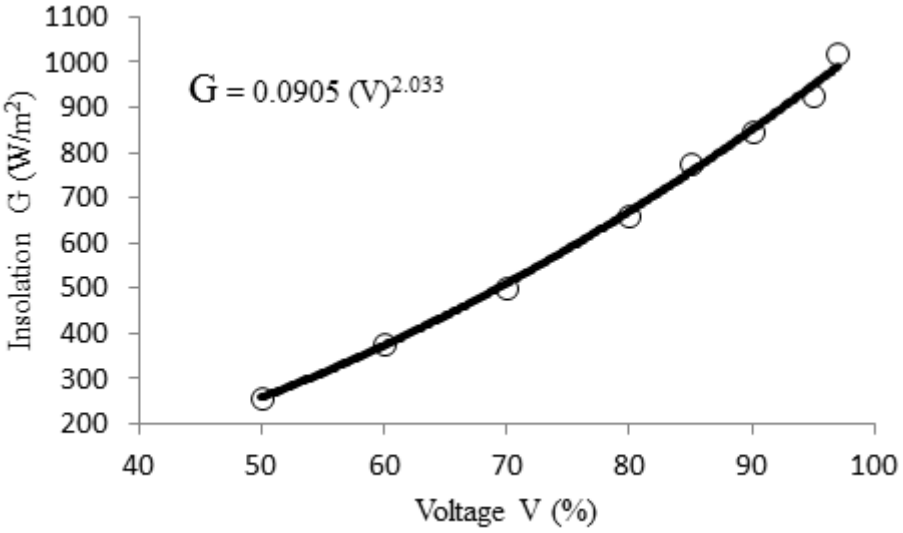

Figure 5.15: Solar Radiation levels verses transformer voltage.

Meanwhile, the solid powder of the paraffin wax was placed into the annular space in the heat exchanger unit. In order to obtain a homogeneous mixture, it was heated at a high temperature of 353K. Additional amounts of paraffin solid powder were added since the level of the paraffin molten receded.

Initially, the pump was switched on and the solar collector started to heat the HTF. The mass flow rate of the HTF passing through the collector was kept at constant rate of 0.126 Kg/s during the charging process. The charging process was finished after the insolation cycle was completed, and then, the experiment was left overnight with the recorded software still running, recording the data from the thermocouples and storing this data automatically. All temperature data were recorded by PICO data logger during charging process of the PCM at every second.

5.6 Results and analysis

To examine the performance of the heat storage system, it was tested under three different weather conditions in the northeast regions namely during typical summer, winter, and spring days. The results of the experiment which include the temperature distribution profiles for the charging cycle, the cumulative heat storage, and the total heat capacity are presented and analysed in this section.

5.6.1 Summer conditions

The experiment was conducted to simulate the solar heating of a typical summer day in the northeast region as shown in Figure 5.13. The temperature profiles inside the heat exchanger during the melting process were recorded on a typical summer day as shown in Figure 5.16. Initially the temperature of the PCM increased gradually however during the phase change process it increased significantly. Once, the PCM completely melted into its liquid state, the temperatures began to rapidly increase again. The PCM begins to melt after 7000 seconds after the start of the experiment and finish phase change at approximately 8200 seconds after the start of the experiment. The PCM fully melts at 9800 seconds after the start of the experiment.

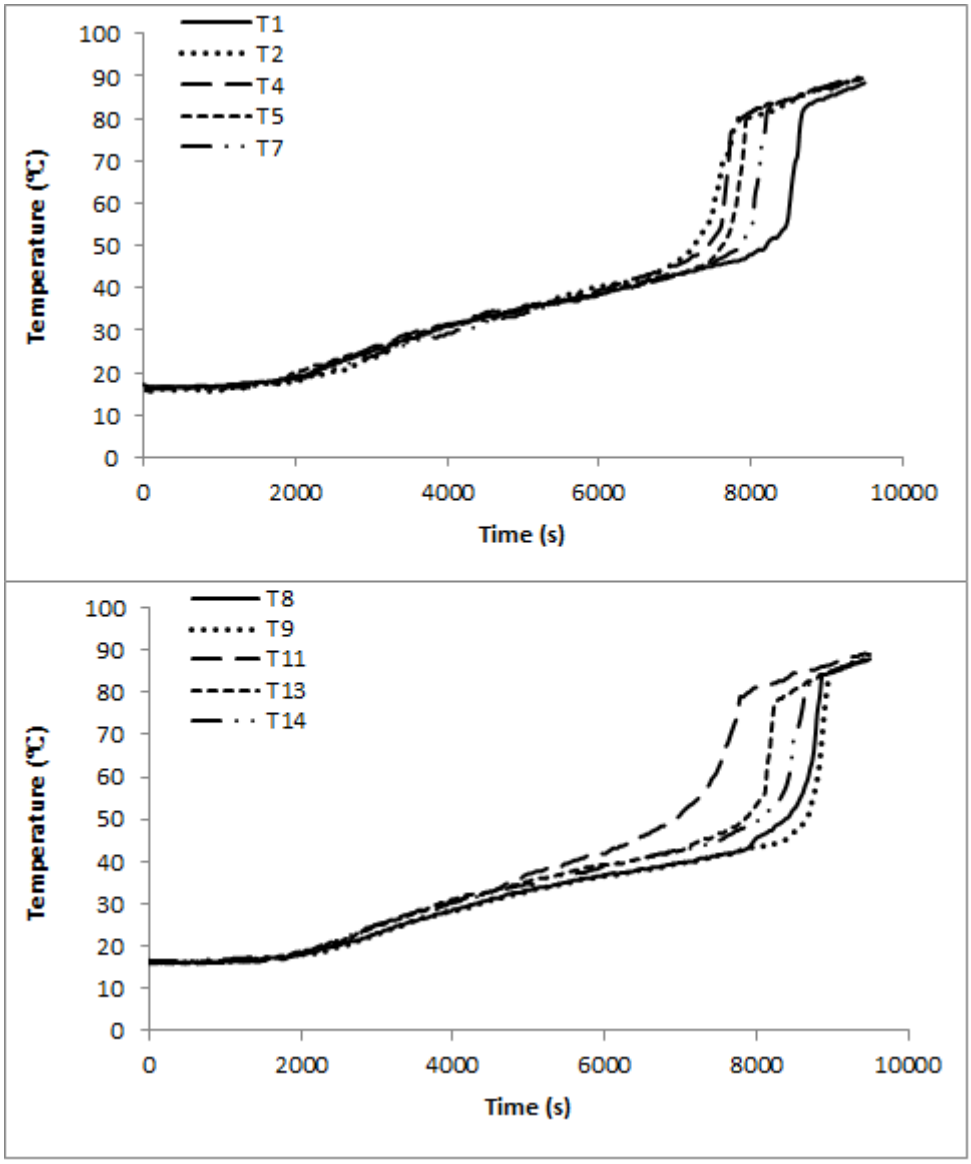

Figure 5.16: Variation of the PCM temperatures during the melting process on a typical summer day.

5.6.2 Winter conditions

In order to simulate winter conditions, a different insolation graph was used see (Figure 5.17). The figure illustrates the variation in solar insolation of a typical winter day in the northeast region.

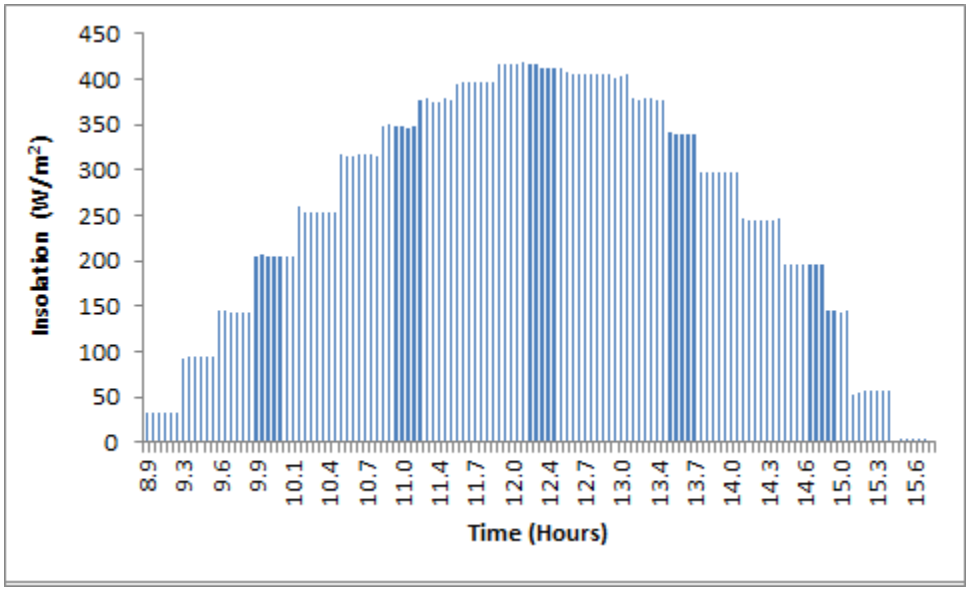

Figure 5.17: Daily insolation variation in mid-winter.

Figure 5.18 below shows the temperature variation at different points inside the PCM. A portion of the PCM remains solid. This indicates that the amount of heat gradient produced by the solar collector in the winter condition is insufficient to melt all the PCM in the heat storage system.

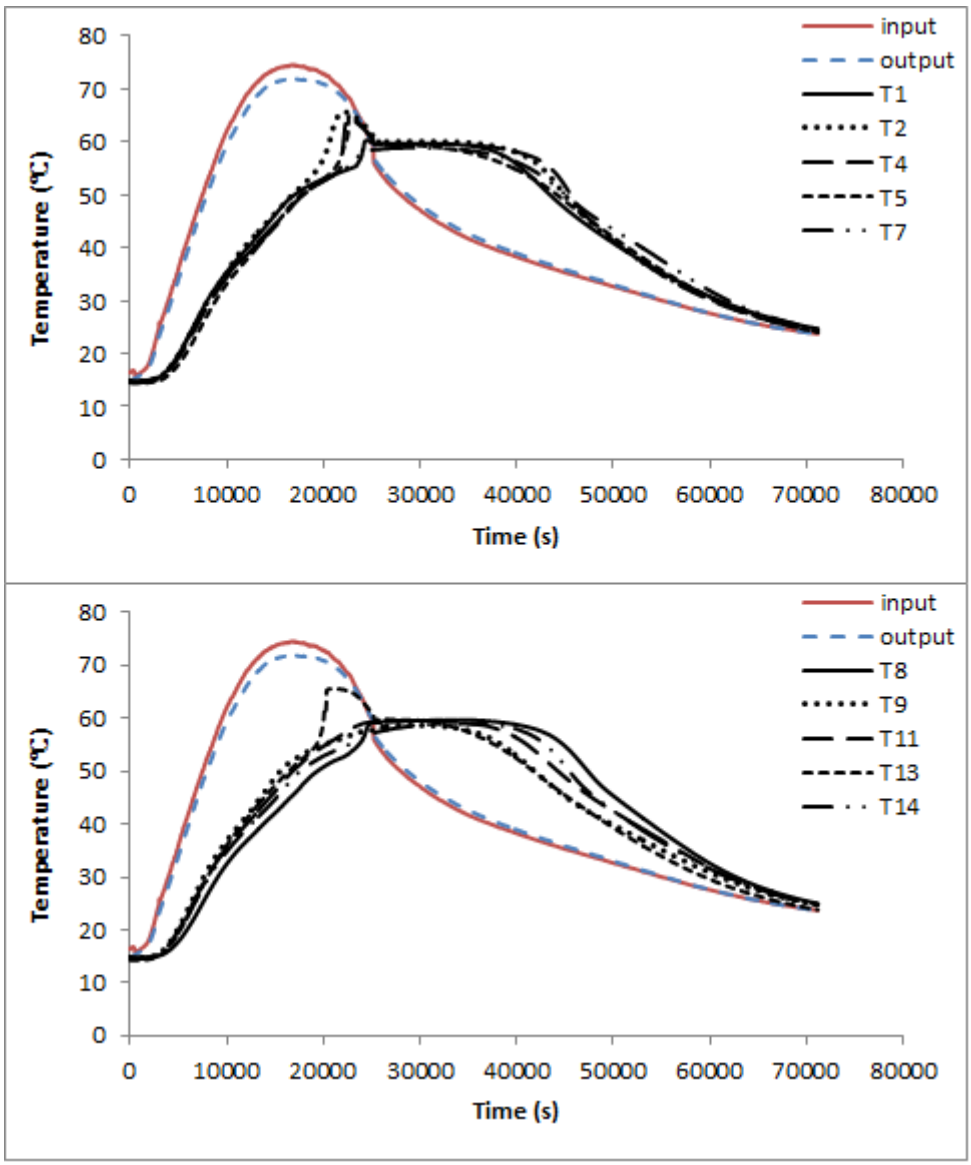

Figure 5.18: The temperature profile during the full melting and solidification cycle in winter time condition (solidification due to heat losses over night period).

5.6.3 Spring conditions

Figure 5.19 below shows the daily variation in solar insolation during the spring equinox in the northeast region.

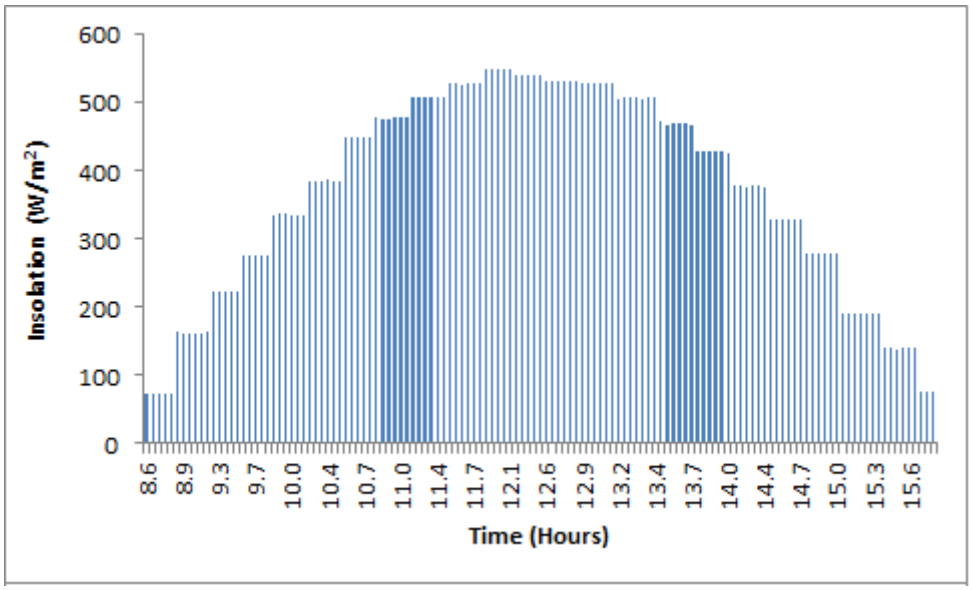

Figure 5.19: Daily variation in insolation variation during the spring equinox.

As shown in Figure 5.20 below, the spring condition provides enough solar radiation to fully melt all the PCM in the heat exchanger unit in 295 minutes. Thus the total melting time has increased up to 63.8 %.

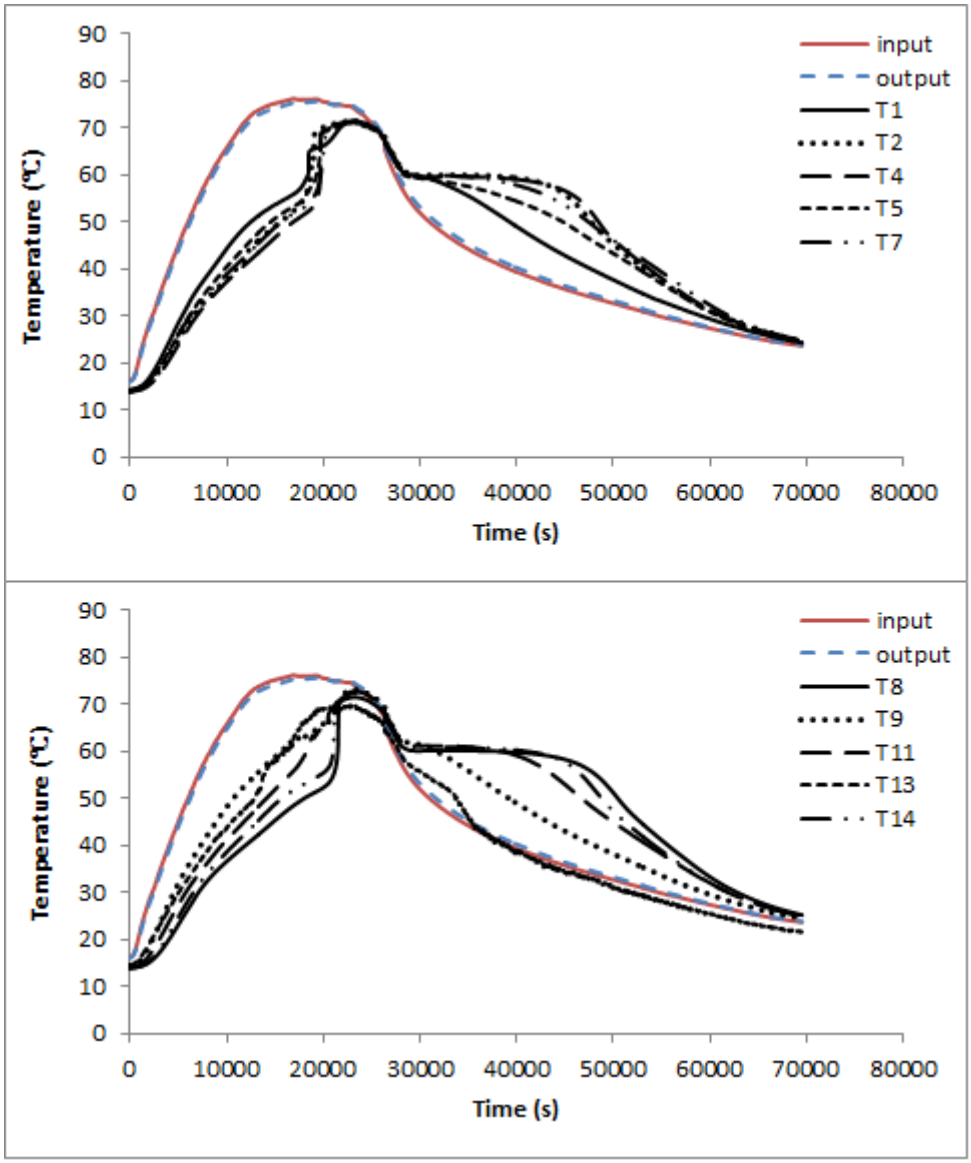

Figure 5.20: The temperature profile during the full melting and solidification cycle in spring (solidification due to heat losses over night period).

5.6.4 Observation analysis

Figure 5.21 below shows photographs taken progressively through the melting cycle during the summer condition. These pictures explain the nature of the melting process within the heat storage system. (A) shows that the melting starts peripherally near the hot HTF tubes as a result of conduction, forming a thin layer of liquid paraffin around the tube walls (B). Diagram (C), shows that the solid-liquid interface has expanded gradually over the axial and radial directions with respect to time. Thereafter, the molten paraffin ascends to the top parts of the heat exchanger as a result of natural convection. In consequence, a layer of liquid paraffin is formed over the solid paraffin (D). In diagram (E), the melting process continues gradually; the melting fronts are subject to the natural convection heat transfer, and so, a few randomly shaped chunks of solid wax are seen in the bottom of the heat storage unit. Diagram (F) shows the heat storage unit full of liquid paraffin wax by the end of the melting cycle.

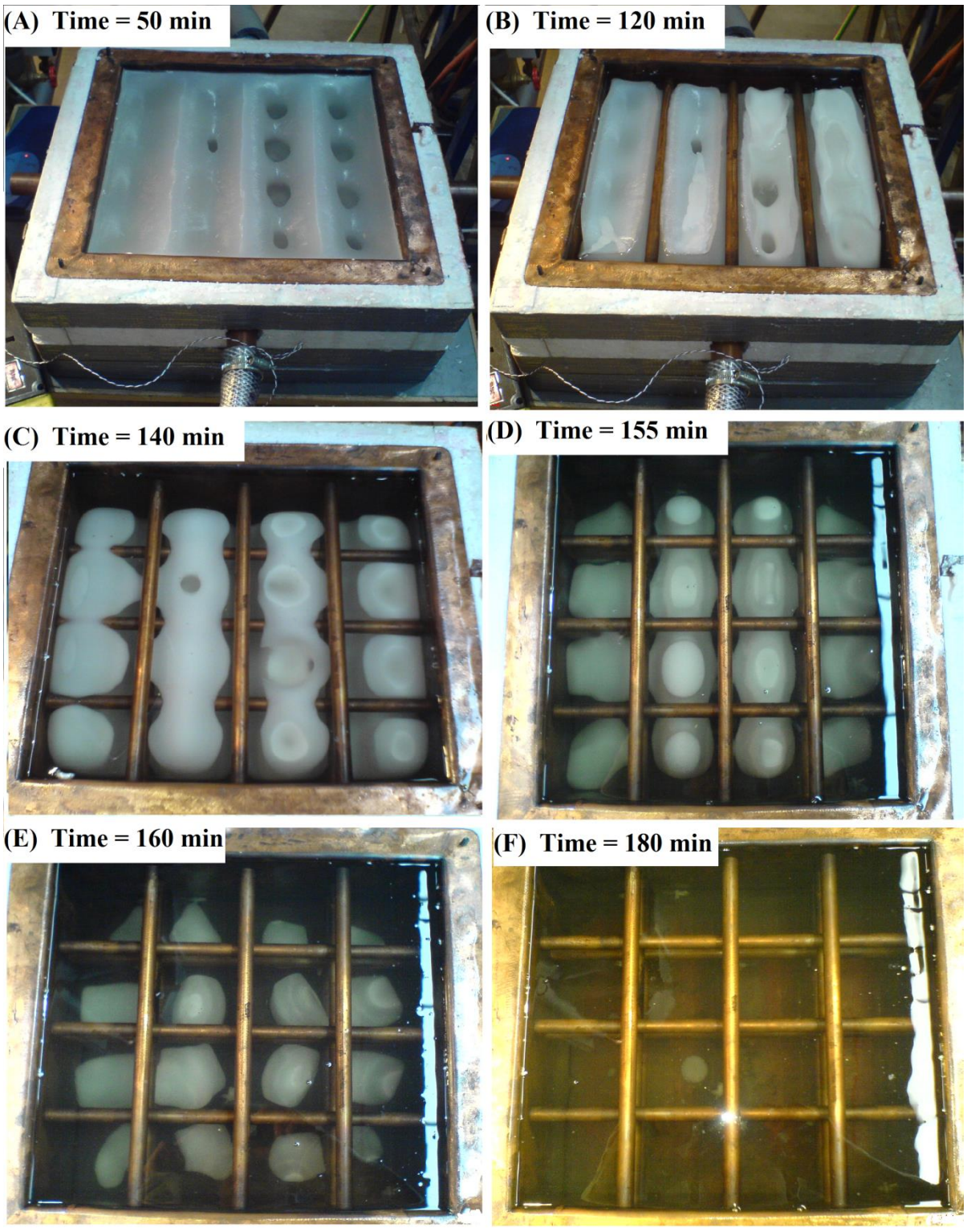

Figure 5.21: Illustrates the progression of the melting cycle during the summer condition.

5.6.5 Steady state operation

The main goal in this section is to obtain experimental data on the performance of the heat storage system to be used for examining numerical data obtained by CFD simulation in order to validate the CFD model. The mass flow rate of the HTF through the collector was kept at a constant 0.126 Kg/s and the flux from the artificial solar simulator was adjusted so that the temperature of the HTF inlet remains equal to 353 K. The experimental measurements; include data collected from various parts of the heat storage unit, as well as the inlet and outlet are compared to numerical results from the CFD model.

5.6.6 Description of the 3D CFD model

5.6.6.1 Computational grid

The computational grid (mesh) of the heat storage system was built using ICEM CFD 13.0 software by ANSYS. Figure 5.22A illustrates the computational grid for the heat storage unit with both the hot and the cold HTF pipes. Figure 5.22B shows the computational grid of the heat storage in which cold pipes were treated as void space (not shown). Concerning the 3D CFD model, only the second computational grid (Fig. 5.23B) was used for the numerical simulations. The computational grid was built using hexahedral elements and boundary layers were created around the pipes. Upon several trials it was found that the hexahedral computational grid with 1029875 elements would be sufficient for accurate 3D modelling of the heat transfer in the PCM heat storage system. The grid is finer in the area close to the pipes than near the walls in order to obtain a good approximation of the free convection phenomena, which is a very important factor for this study.

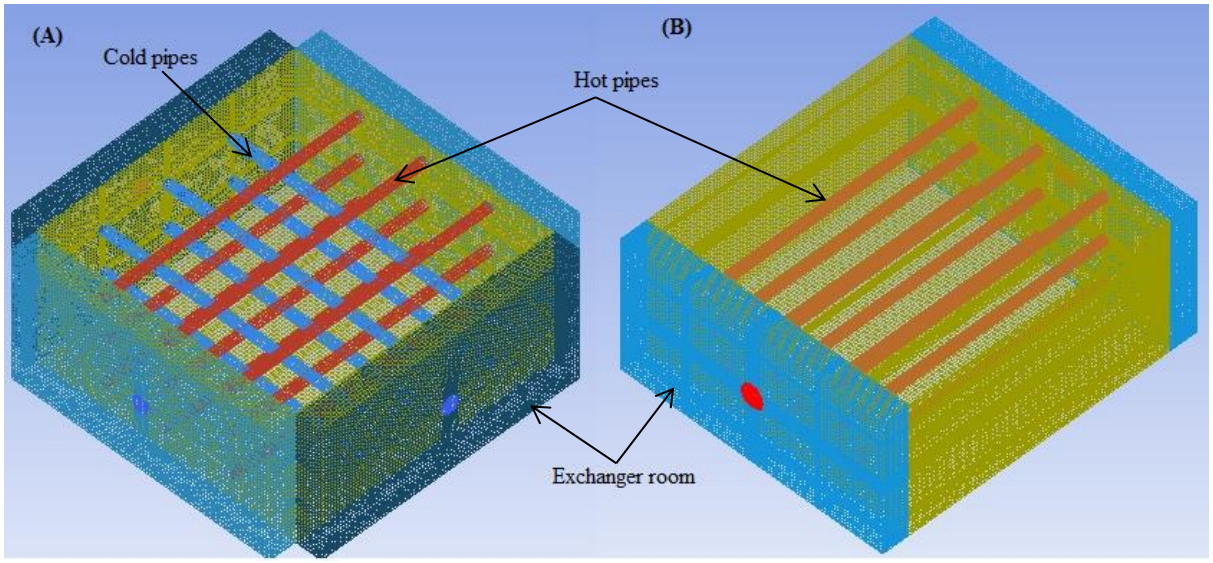

Figure 5.22: Heat storage system's computational grid (A) with both cold and hot HTF pipes (B) without cold HTF pipes.

5.6.6.2 Model settings

The HTF flow inside heat storage system was analysed using transient simulations with *k-epsilon* turbulence model deployed. The solidification/melting model was used in order to examine the phase change phenomena in paraffin wax. The time step used in calculations was set to 0.1 s. To obtain numerical results the first-order upwind spatial discretization and the pressure solver with PRESTO algorithm for pressure-velocity coupling were used. Convergence criteria were defined by setting the absolute residual values at 10^{-6} for energy and at 10^{-3} for all other variables. Zero heat flux boundary conditions were set on all sides of the rectangular box; the mass flow rate and temperature of the HTF were specified at the entry of the heat exchanger room. The thermo-physical properties of the paraffin wax are summarized in Table 5.2.

Table 5.2: Thermo-physical properties of the paraffin wax.

Properties	**Value**
Density, ρ	800 kg/m^3
Thermal conductivity, k	0.25 W/(m^{o}C)
Specific heat, Cp	2050 J/Kg ^{o}C
Latent heat, L	200 KJ/Kg
Viscosity, μ	0.035 Kg/ms
Thermal expansion coefficient, β	0.0001 1/K
Liquid Temperature, T_L	331 K
Solid Temperature, T_s	333 K

5.6.6.3 Validation of the 3D CFD model

The predicted temperature inside the PCM was compared against the results obtained by the experimental study. Figure 5.23 shows an example of comparison between the results obtained from the 3D CFD model and the experiment at points T5, T6, T11 and T14 inside the PCM. As illustrated, a very good agreement between predictions of the 3D CFD model and the experimental data is observed. The maximum deviation between CFD and experimental results in other points does not exceed 12%.

Figures 5.24 and 5.25 show the temperature contours in the middle plane of the heat storage system and velocity vector. As expected, the natural convection flows are present in the liquid PCM. Therefore, the molten PCM ascends upwards from the bottom to the upper regions of the heat storage unit and after cooling flows downwards. Such predicted behaviour of the molten PCM was also observed during experimental tests.

Therefore, the proposed numerical model can be used with full confidence for modelling and designing similar PCM heat storage system.

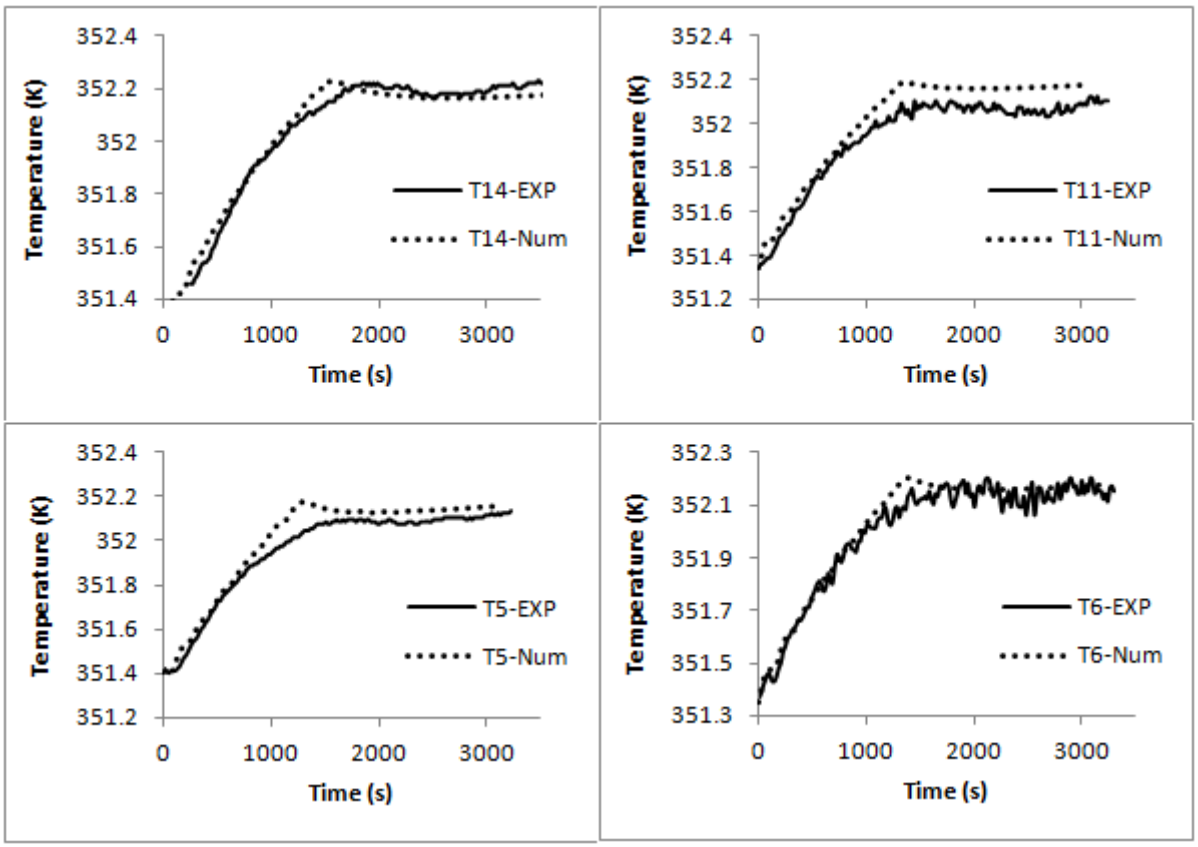

Figure 5.23: Comparison between the experiment and 3D CFD results.

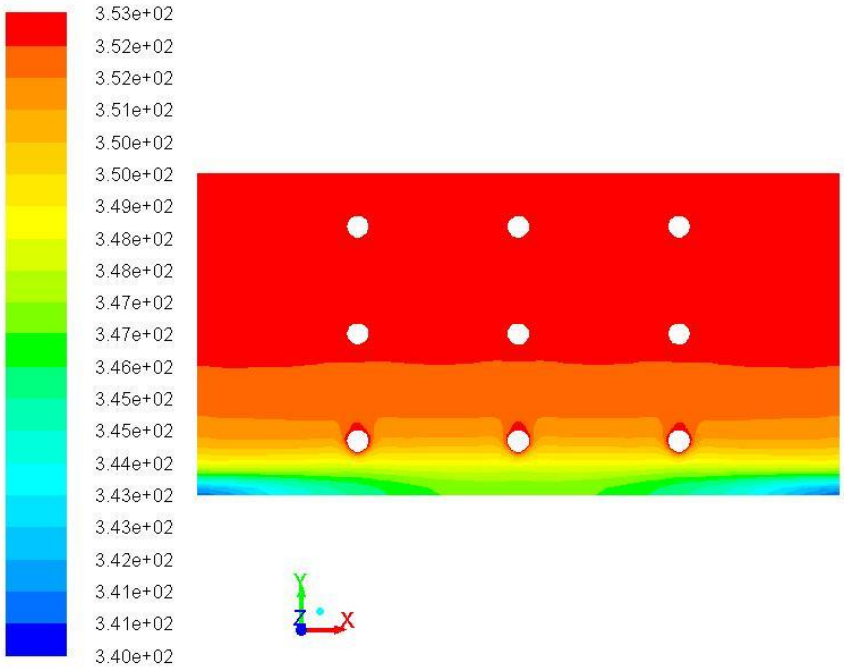

Figure 5.24: Temperature contours in the middle plane.

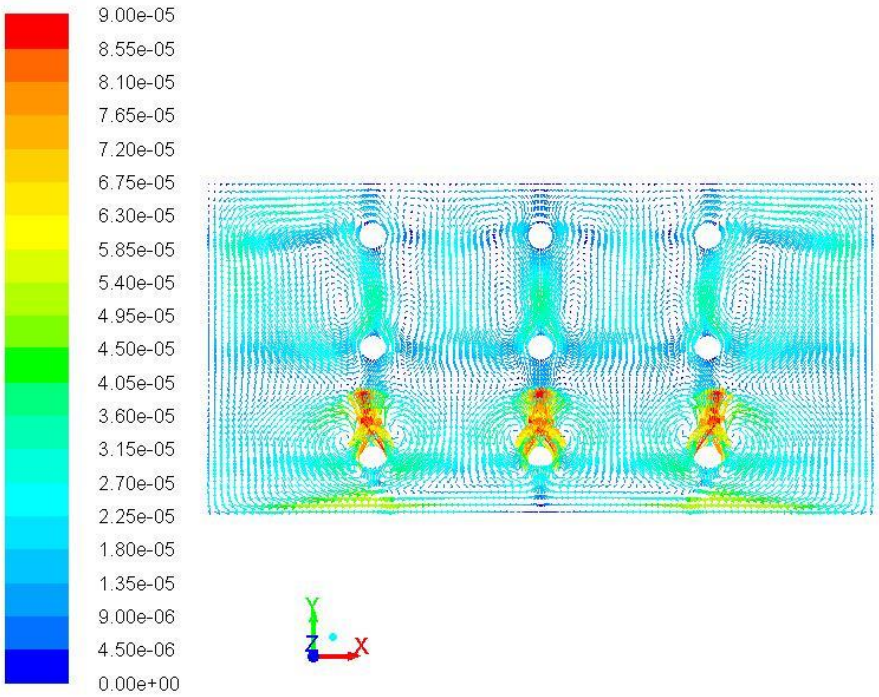

Figure 5.25: The velocity vectors in the middle plane.

Chapter 6 Numerical Study of Performance of a Rectangular PCM Storage Unit

6.1 Introduction

The present study explores numerically the intensification methods of heat transfer in Thermal Storage Systems (TSS). A rectangular container with a pipe fixed horizontally at its centre surrounded by a phase change material (PCM) is used as a TSS. Paraffin wax with melting temperature of 60^{o}C was used as a PCM whilst water was used as a heat transfer fluid (HTF). The thermo-physical properties of paraffin wax were assumed to be constant in the process modelling, whereas the density variation was handled using the Boussinesq approximation. Numerical simulations of transient heat transfer were carried out using ANSYS/FLUENT 13.0 software. Simulations performed provide information on the instantaneous temperature distribution, solidification/melting dynamics and the velocities field in the storage unit during the melting process. The effects of the inlet temperature and mass flow rate of the HTF on the charging (melting) process were also investigated. Further, the influence of the number of longitudinal fins and porosity on the temperature distribution, dynamics of melting, total melting time and natural convection phenomena were also investigated.

6.2 Physical model

A schematic view of the physical model of the TSS is shown in Figure 6.1. The TSS consisted of a rectangular PCM storage unit with a pipe fixed horizontally at its centre. The test unit had the following dimensions: 75 mm width, 50 mm height, and 500 mm length. The

rectangular container was filled with paraffin wax with a melting point of 60℃ (see Table 5.2 for it properties). The inner and outer diameters of the pipe (D) were 10 and 12 mm, respectively. The flow of the heated HTF inside the pipe was used as a heat source to charge the PCM thermal storage system.

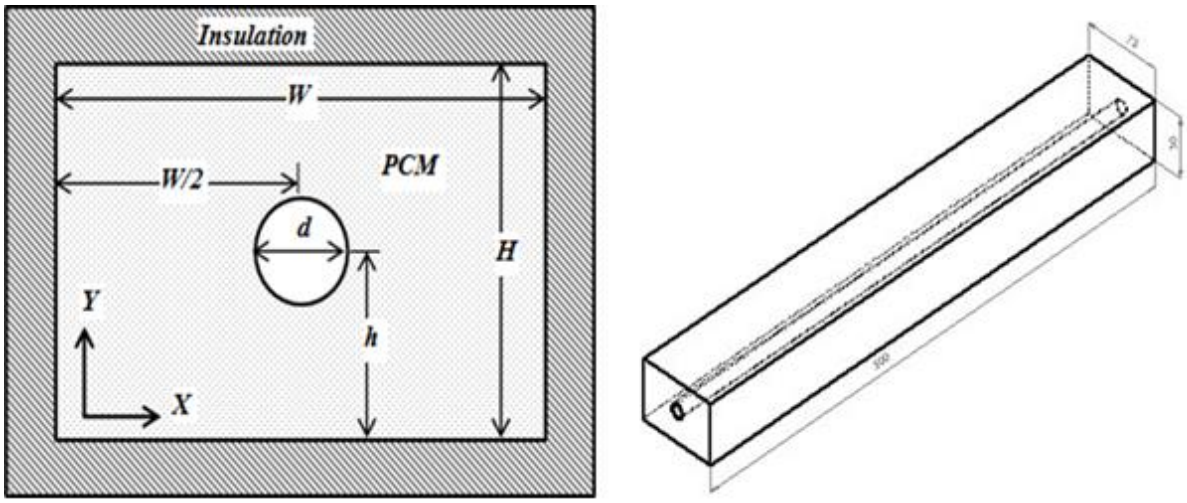

Figure 6.1**:** Physical model.

The computational grid of the system was built using ICEM CFD 13.0 software by ANSYS. Figure 6.2 shows the computational grid of the system. The computational grid was built using hexahedral elements and boundary layers were created around the pipe. Upon several trials it was found that the hexahedral computational grid with 636768 elements would be sufficient for accurate 3D modelling of the heat transfer in the PCM system.

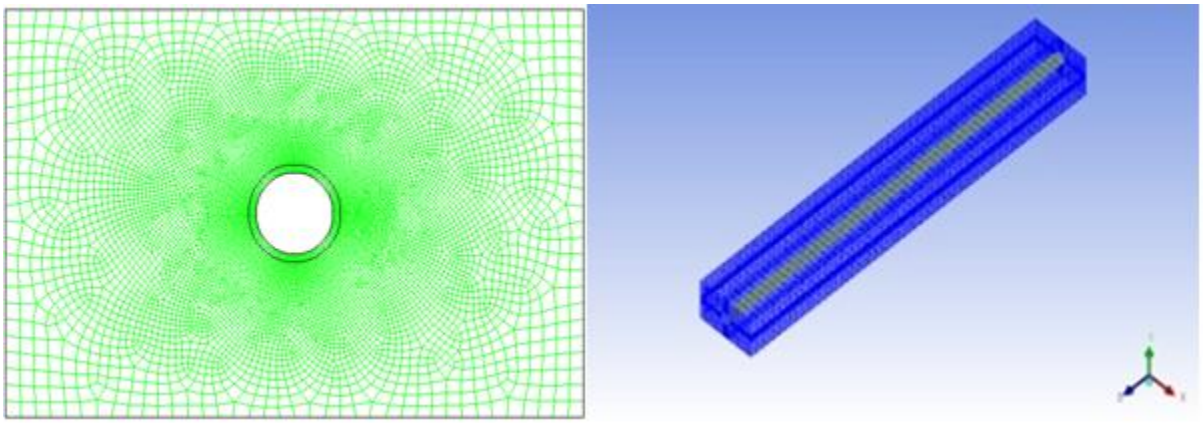

Figure 6.2: A schematic view of the storage system computational grid.

6.3 Boundary and initial conditions

The following boundary conditions were used in the modelling process:

1. The mass flow rate and temperature of the HTF values are specified at the entry of the copper pipe

$$u = U^{in}, \quad T = T^{max}$$

2. Outlet zone is defined as outflow boundary (for the pipe);
3. Rectangular box walls were treated as adiabatic walls;

6.4 Solution parameters

The flow inside the pipe was described using transient simulations with *k-epsilon* turbulence model deployed. The solidification/melting model was used in order to examine the phase change phenomena in paraffin wax. The time step used in calculations was set to 0.1 second. To obtain numerical results the first-order upwind spatial discretization and the pressure

solver with PRESTO algorithm for pressure-velocity coupling were used. Convergence criteria were defined by setting the absolute residual value at 10^{-6} for energy and at 10^{-3} for all other variables.

6.5 Results and discussion

Figure 6.3 shows results on the temperature distribution and melting process in the computational domain for the case in which the HTF inlet temperature is 353 K and the mass flow rate is 0.0037 Kg/s after for instances when 5000, 8000, 13000 and 22000 seconds elapsed from the start of the charging process**.** It can be seen that the temperature first starts to increase in the vicinity of the pipe in the entry region and then the temperature rise occurs downstream the pipe and upwards when some of wax turns into the liquid and free convection flows are formed. Later on, the melting process expands to the bottom regions of the computational domain.

In order to evaluate the performance of the thermal storage unit 132 monitoring points were set inside the domain with PCM to record the variation of the temperature as a function of time. These points are located in 11 measurement planes perpendicular to the axis of the domain, see Figure 6.4. Each plane contains 12 monitoring points, as shown in Figure 6.5A and Figure 6.5B. All monitoring points are divided into three groups. The first group of 44 points were set in the upper part of the computational domain (u1-u44). The second group of 44 points are located in the bottom part of the domain (b1-b44), and the last group of 44 points are located at the side of the domain (e1-e44). In addition, 33 monitoring points were set to measure the surface temperature along the pipe. Finally, two monitoring points were set on the inlet and outlet of the pipe to evaluate the cumulative energy charge.

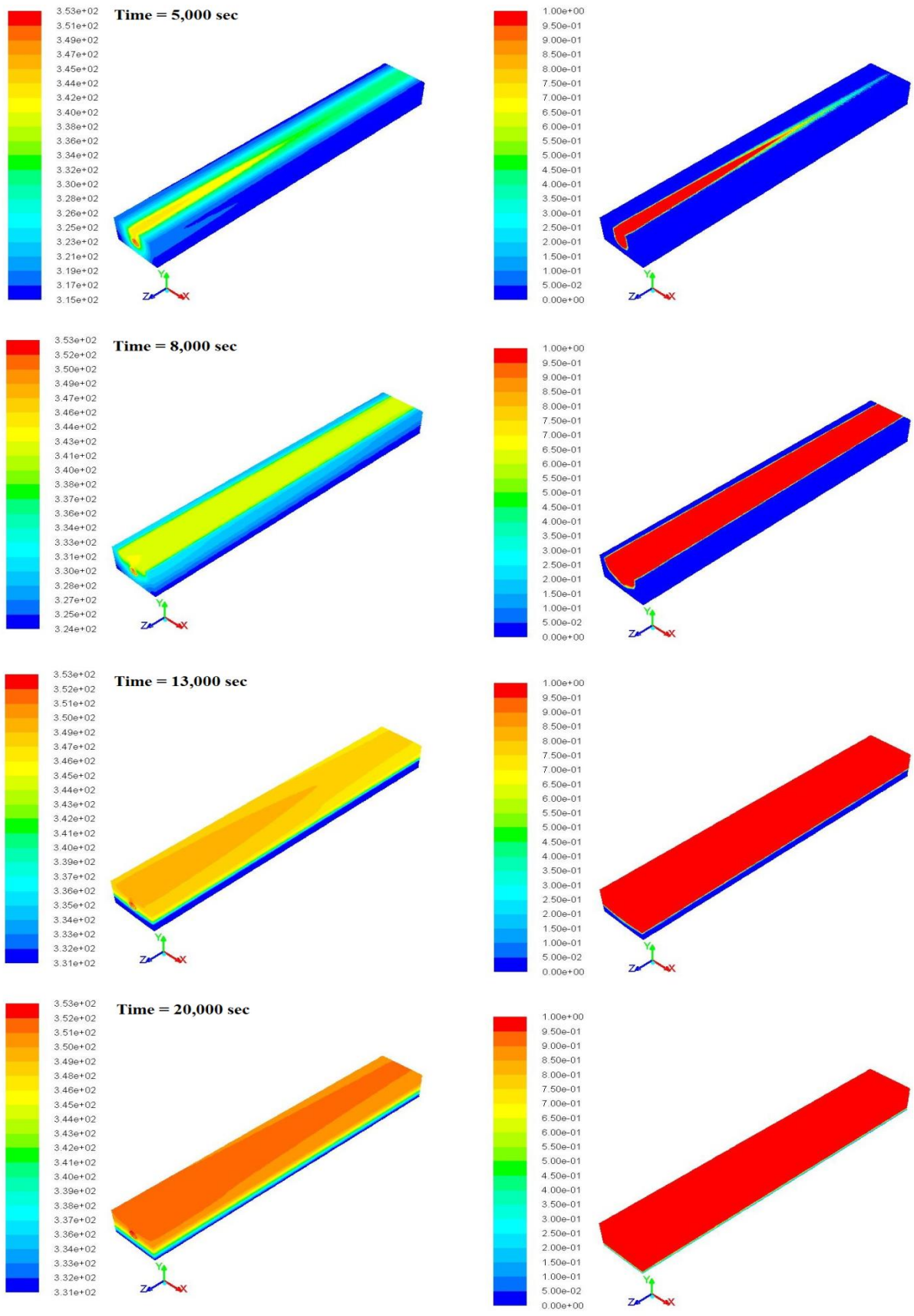

Figure 6.3: Temperature distribution and Melting/Solidification process in the computational domain.

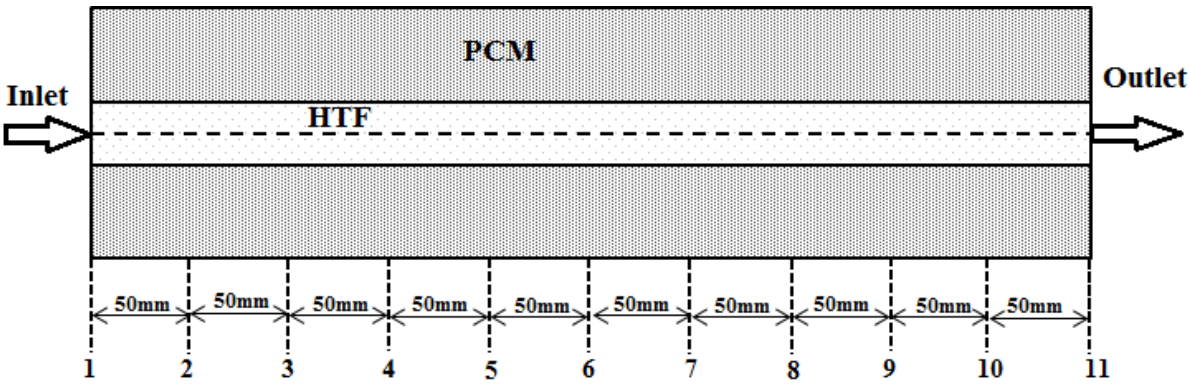

Figure 6.4: Measurement planes along the tube.

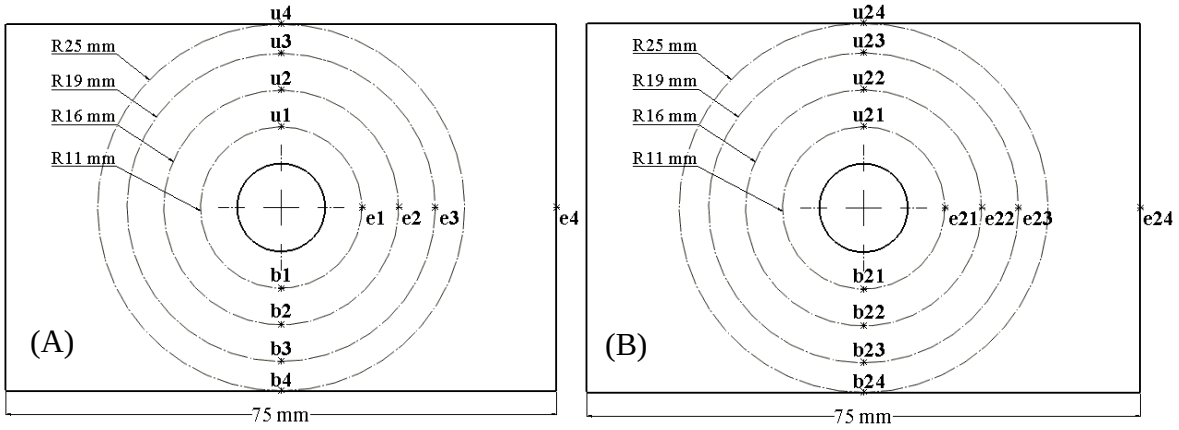

Figure 6.5: (A) The location of 12 monitoring points in the measurement plane 1. (B) The location of 12 monitoring points in the measurement plane 6.

Figure 6.6 shows the temperature variations monitoring points in the middle section of the computational domain (the measurement plane 6). In the first stage, the temperatures increase almost linearly from 300 to 331 K the heat transfer from the pipe walls to the solid PCM occurs by conduction. The temperatures at points u21, b21 and e21 are the highest at this stage due to proximity to the pipe walls. The lowest temperatures are recorded in point e24, which is located on the edge of the storage container. During the melting process, in which the temperatures range between 331 to 333 K, temperature curves level out. During initial melting a thin liquid layer is formed between the pipe and the solid PCM. The solid-liquid

interface gradually expands in the axial and radial directions. Thereafter, the melting is dominated by natural convection in the liquid regions of PCM. The melting process is relatively intensive in the upper regions of the container. Consequently, the temperature at points u21 and u24 are the highest during the melting stage. Two main factors affecting the natural convection intensity in the melted PCM is the temperature difference and the distance to the pipe walls. Similar results were reported in [63, 66, 124].

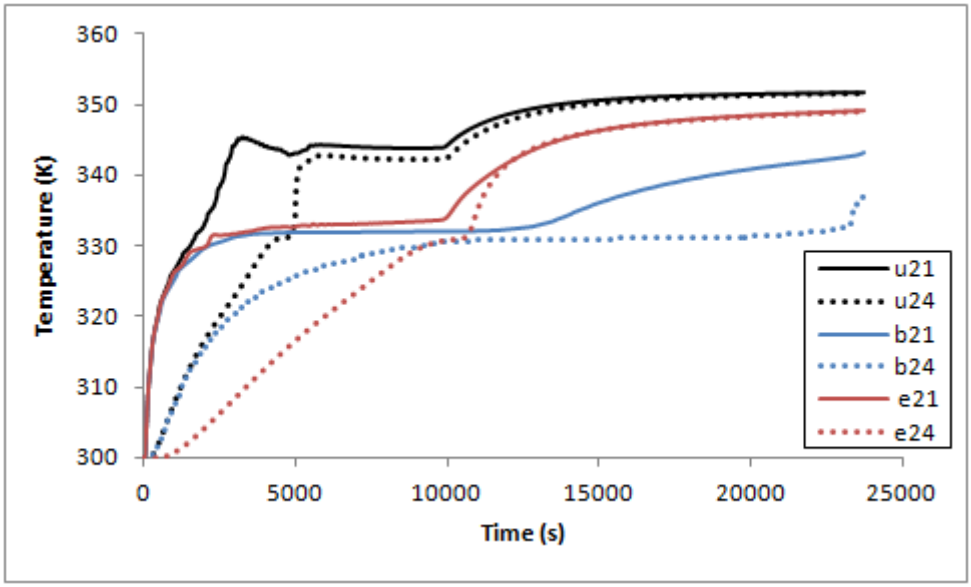

Figure 6.6: Variation of the PCM temperature as a function of time.

Figure 6.7 presents the comparison of the temperature gradients along X (the monitoring plane 1), Y (the monitoring plane 1), and Z (the top of the domain) directions in the domain. It can be seen that the temperature difference in the PCM along the length of pipe (Z direction) is very small (less than $1^{o}C$) which indicates fast transition thermal response and intensive heat transfer due to free convection at the top of the domain. Similar dynamics was observed near the HTF pipe. Similar results were found in [98, 300]. The highest temperature gradients are observed at the bottom and the side regions of the domain in which heat is transferred mainly through conduction mechanism.

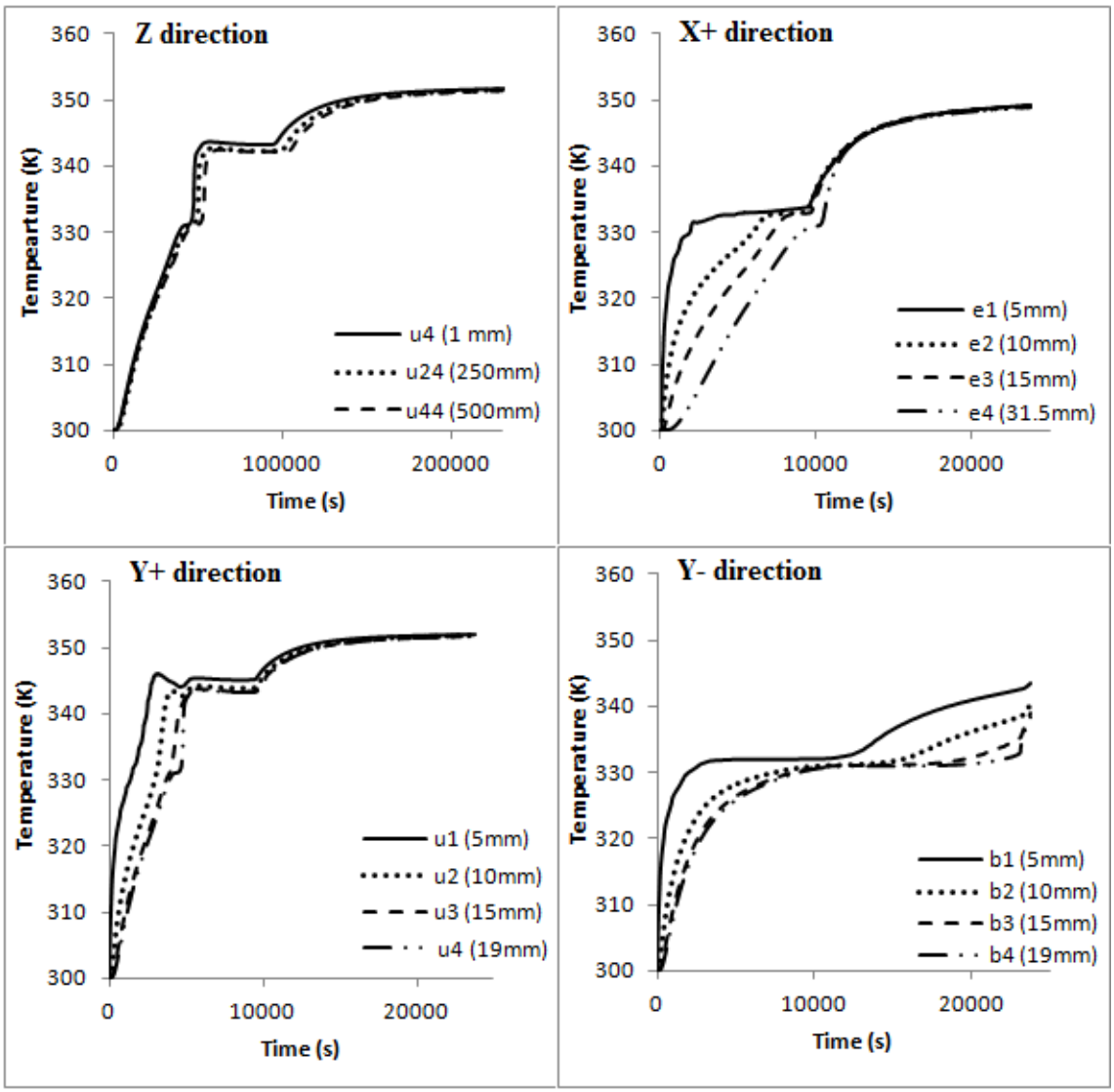

Figure 6.7: The temperature as a function of time along X (the monitoring plane 1), Y (the monitoring plane 1), and Z (the top of the domain) directions in the domain.

Figures 6.8-6.10 present temperature distribution, liquid fraction, and the velocities field in the middle section of the computational domain for 5000, 8000 and 20000 seconds from the start of the charging process. It can be seen that the molten PCM ascends upwards from around the pipe at the centre of the container due to the effect of the natural convection. The convection intensifies when the liquid fraction volume increases.

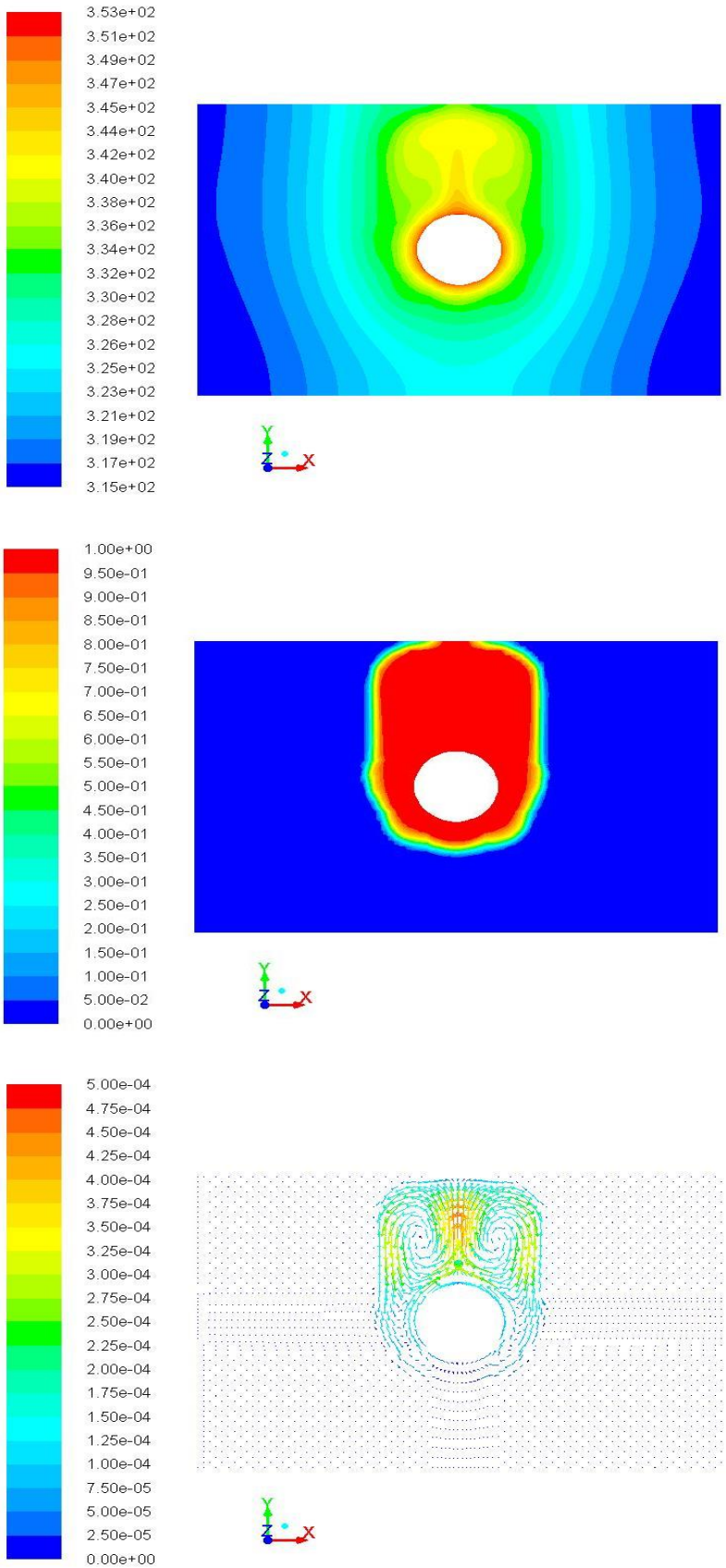

Figure 6.8: Temperature distribution, melting process and velocities field in the middle section of the computational domain. Elapsed time is 5000 s.

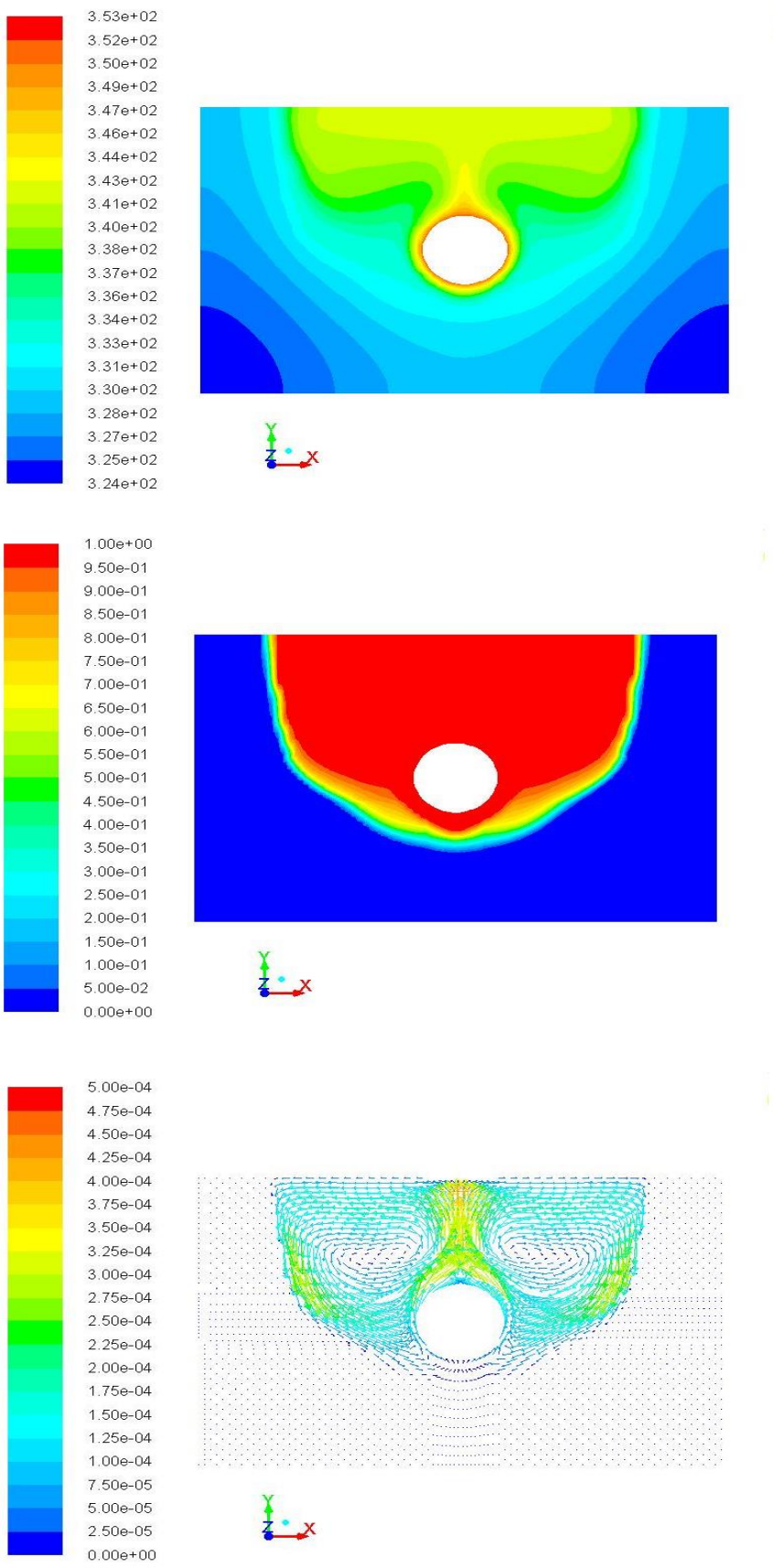

Figure 6.9: Temperature distribution, melting process and velocities field in the middle section of the computational domain. Elapsed time is 8000 s.

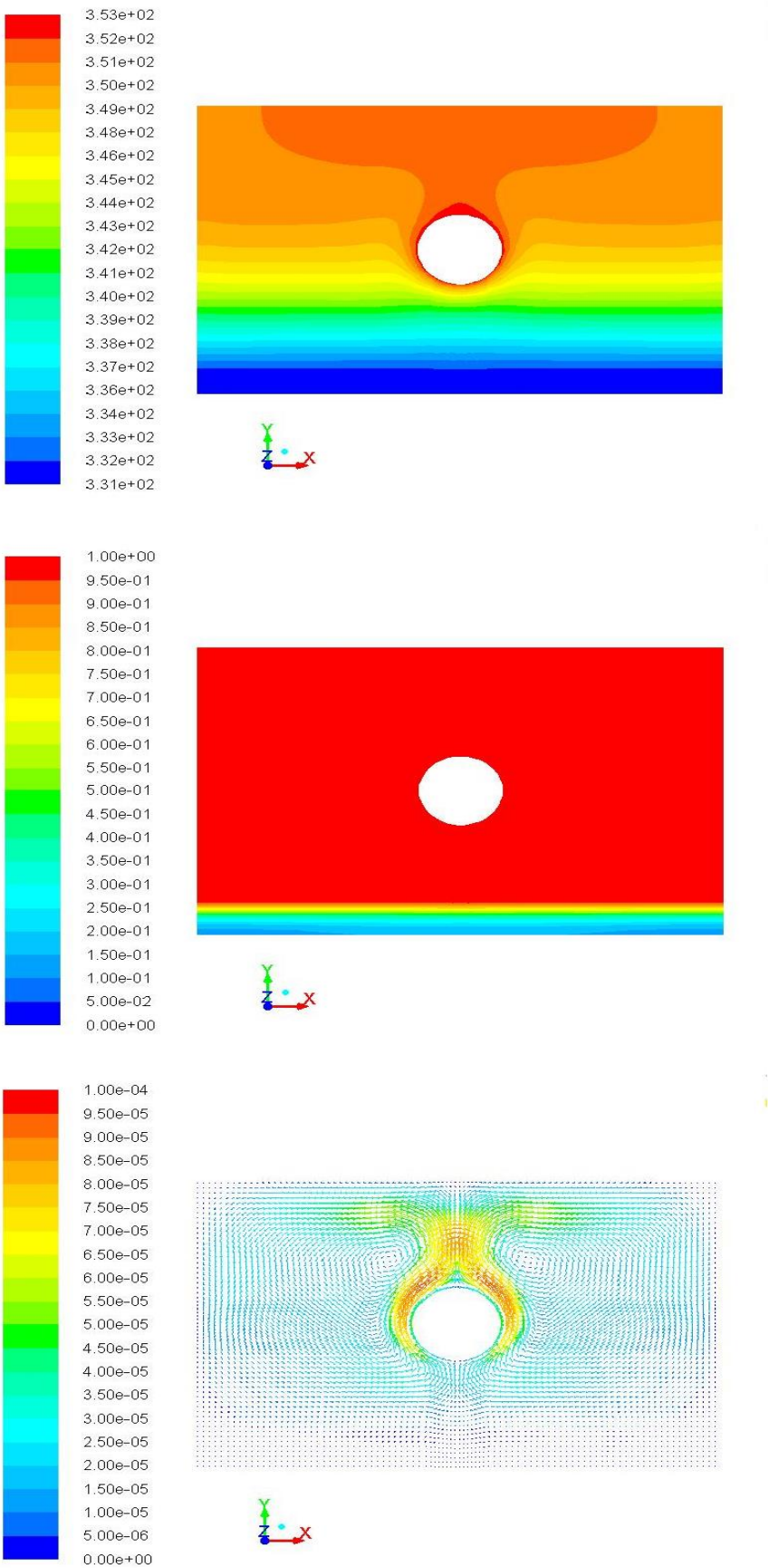

Figure 6.10: Temperature distribution, melting process and velocities field in the middle section of the computational domain. Elapsed time is 20000 s.

Figure 6.11 shows the change in the liquid fraction of the PCM in the storage container as function of time. It can be seen that there is a rapid increase of the liquid fraction up to the instance when elapsed time is 10,000 s and then the rate of melting is slightly reduced. This is determined by the change in the intensity of the free convectional flows in the given geometry of the storage system.

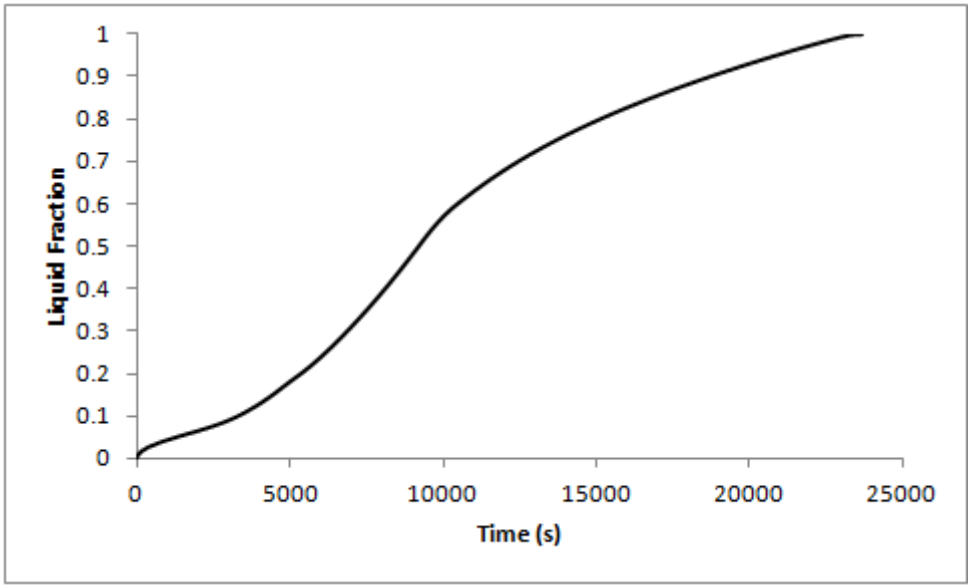

Figure 6.11: Formation of the liquid fraction as a function of time.

The effect of the HTF inlet temperature on the temperature distribution in both radial and axial directions in the PCM storage is shown in Figures 6.12-6.14. The diagrams show that increasing the inlet temperature of HTF by 10^{o}C significantly increases the temperature variation in the radial and axial directions of the PCM storage. The increase of the inlet temperature of the HTF leads to the rise in the temperature difference of the pipe walls and the bulk of PCM, which increase the heat transfer rate.

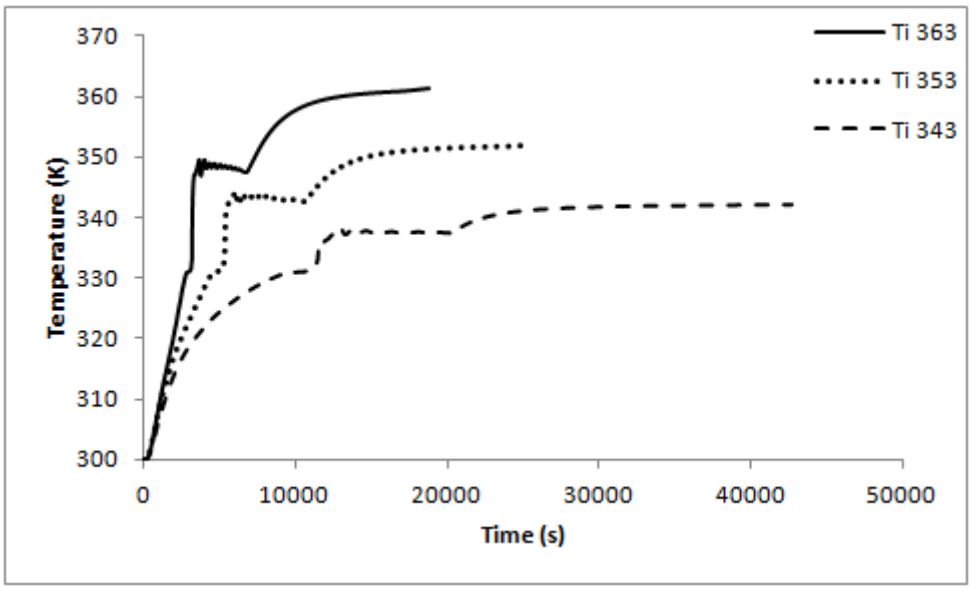

Figure 6.12: The effect of the HTF inlet temperature on the temperature variation at point u4 (the top of the domain, first measurement plane).

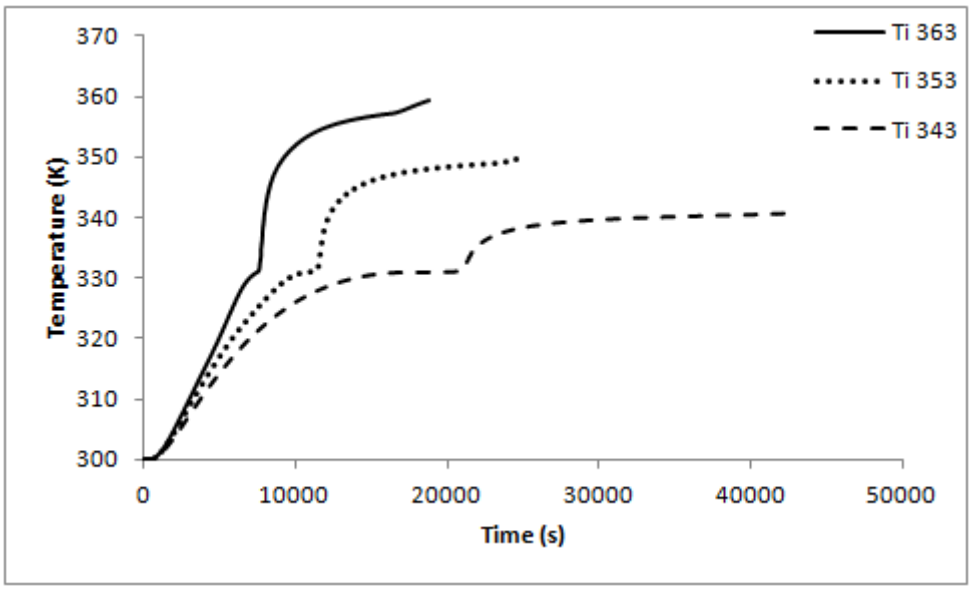

Figure 6.13: The effect of the HTF inlet temperature on the temperature variation at point e4 (the side of the domain, first measurement plane).

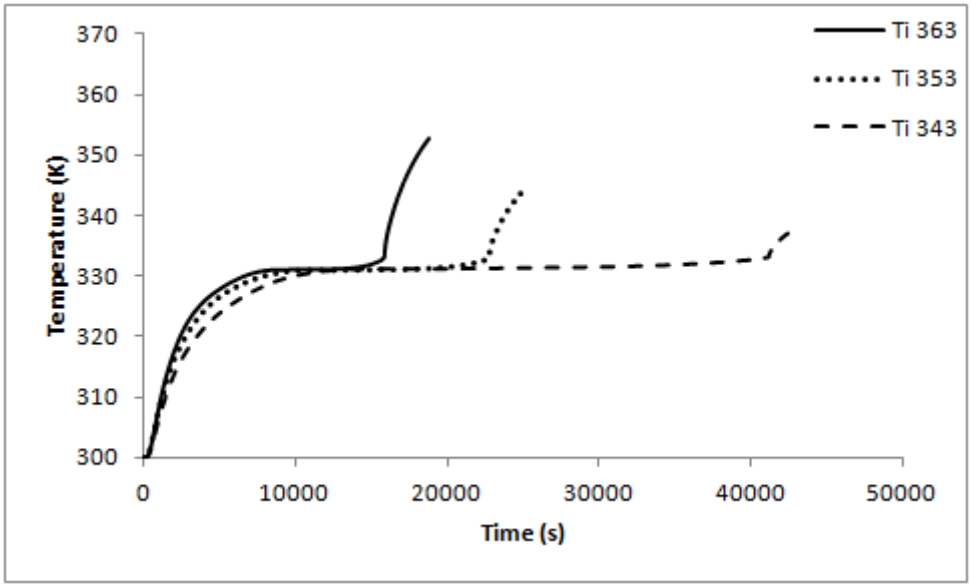

Figure 6.14: The effect of the HTF inlet temperature on the temperature variation at point b4 (the bottom of the domain, first measurement plane).

The effects of the inlet temperature on the formation of the liquid fraction of the PCM and on the total melting time are shown in Figures 6.15 and 6.16. It can be seen that the total melting time reduced approximately by 61.5% when the inlet temperature is increased from 343 to 363 ^{o}C and by 54.5% when the inlet temperature is increased from 343 to 353 ^{o}C.

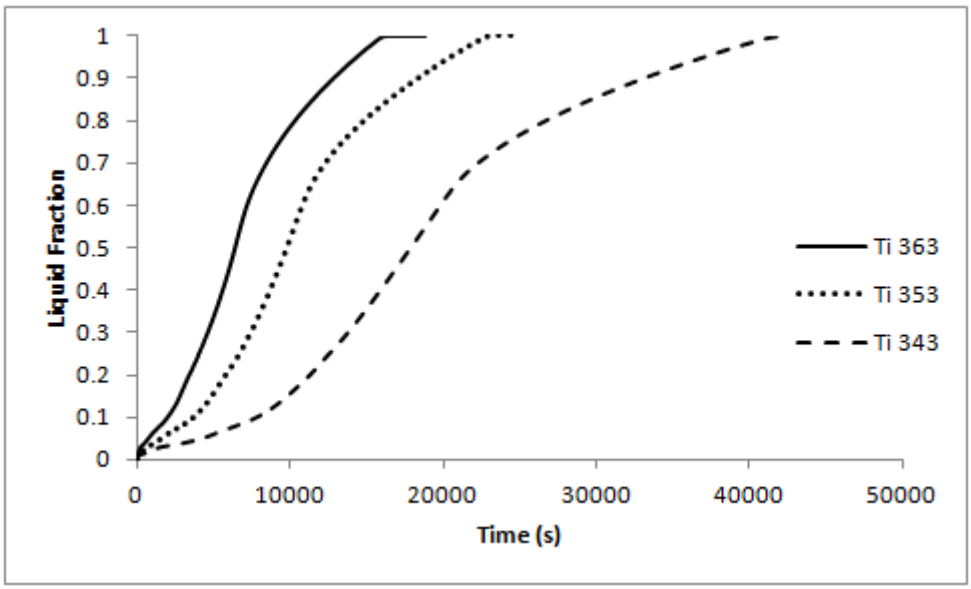

Figure 6.15: The effect of the HTF inlet temperature value on the dynamics of melting.

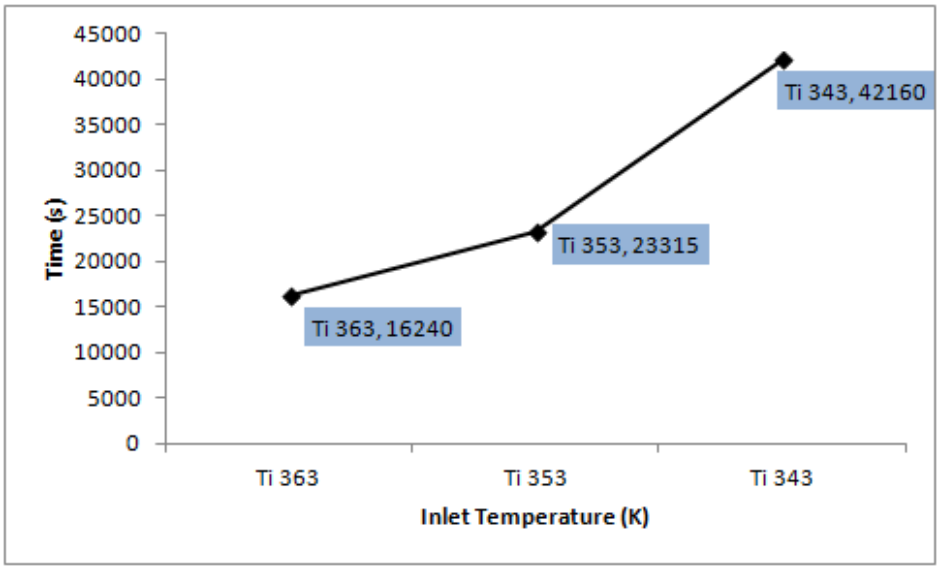

Figure 6.16: The effect of the HTF inlet temperature value on the PCM melting time.

The effect of the change in the mass flow rate of the HTF on the temperature variation in both radial and axial directions in the PCM system is illustrated in Figures 6.17-6.19. It can be seen from diagrams that the mass flow rate of the HTF has a negligible effect on the temperature variation inside the PCM storage system.

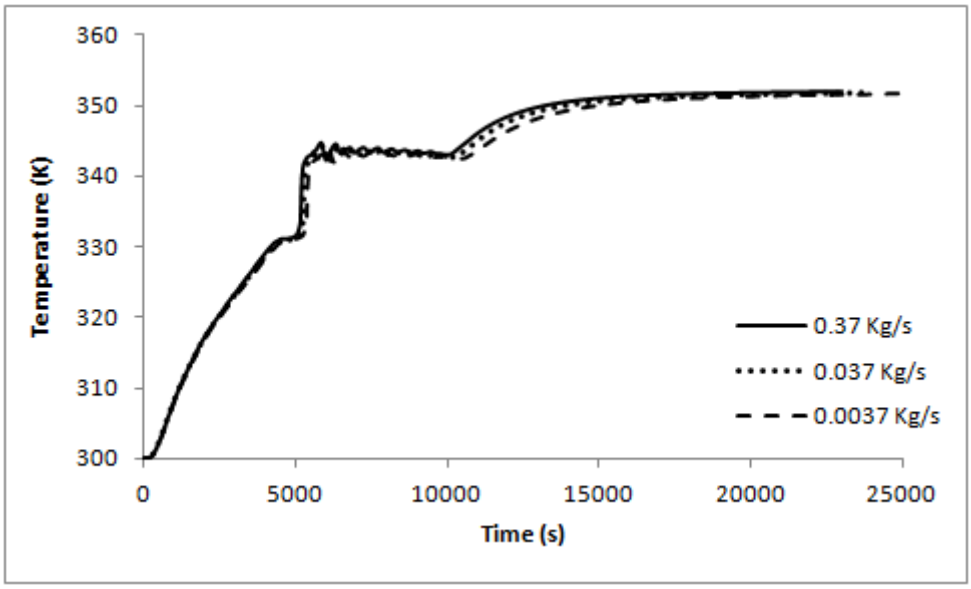

Figure 6.17: The effect of the HTF mass flow rate on the temperature variation at point u4 (the top of the domain, first measurement plane).

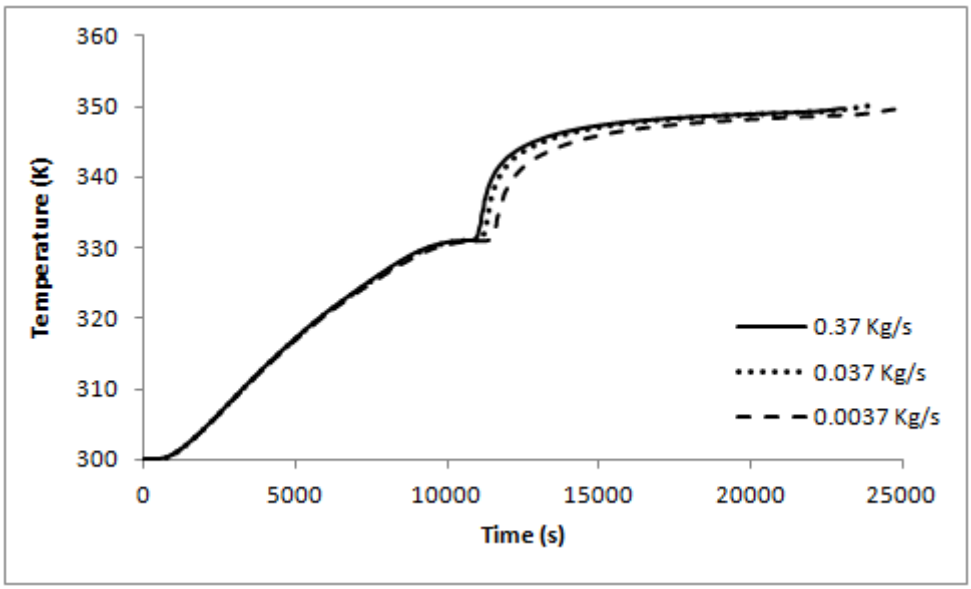

Figure 6.18: The effect of the HTF mass flow rate on the temperature variation at point e4 (the side of the domain, first measurement plane).

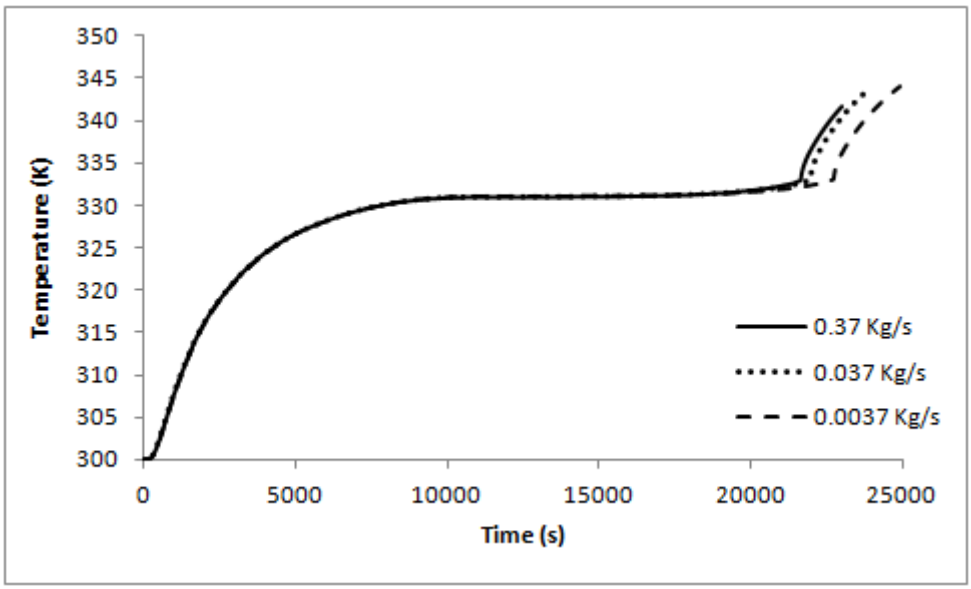

Figure 6.19: The effect of the HTF mass flow rate on the temperature variation at point b4 (the bottom of the domain, first measurement plane).

Figures 6.20 and 6.21 show the influence of the mass flow rate on the formation of the liquid fraction in the PCM bulk and on the melting time, respectively. It can be observed that the mass flow rate of the HTF has a very small effect on the melting time and formation of the liquid fraction in the PCM bulk. The melting time reduced by approximately 4.8% when the flow rate is increased from 0.0037 to 0.037 kg/s and by 6.2% when the mass flow rate is increased from 0.0037 to 0.37 kg/s.

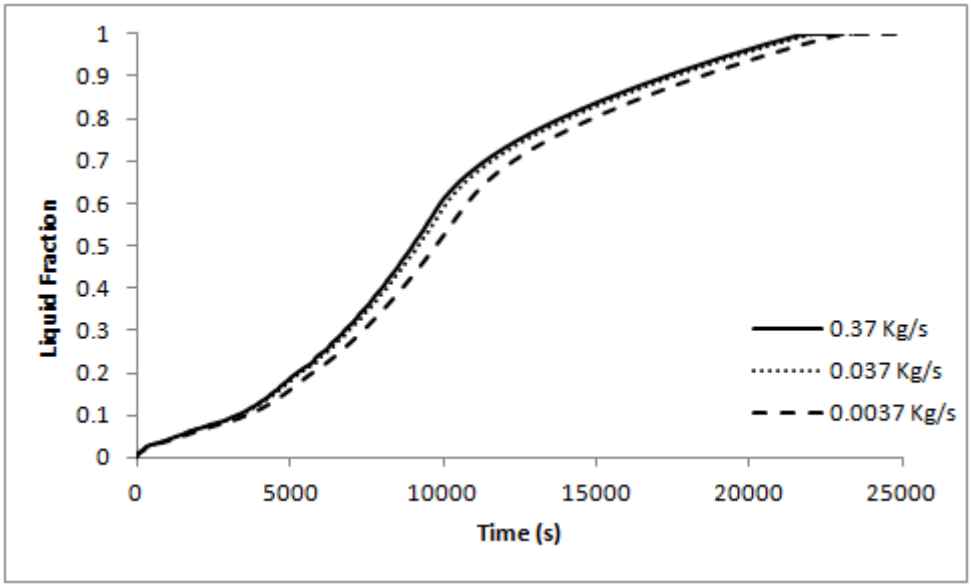

Figure 6.20: The effect of the mass flow rate value on the dynamics of the melting.

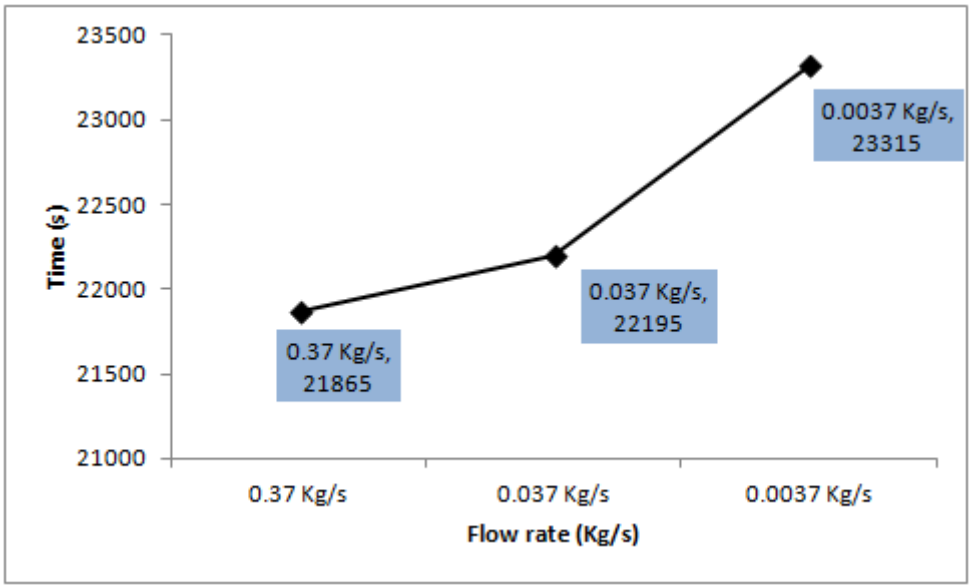

Figure 6.21: The effect of the mass flow rate the PCM melting time.

Figure 6.22 shows variation of the heat accumulation rate as a function of time. Initially, this parameter has a very high value due to the large temperature difference between the inlet temperature of the HTF and that of the solid PCM. Over the time the temperature difference for the HTS in the pipe's inlet and outlet decreases (see Figure 6.23) which results in the drop in the value of the heat accumulation rate. The rise in the value of this parameter between instances when elapsed time is 2500 and 10000 s can be explained by the effect of the heat transfer due to intensifying e natural conviction in the fluid PCM.

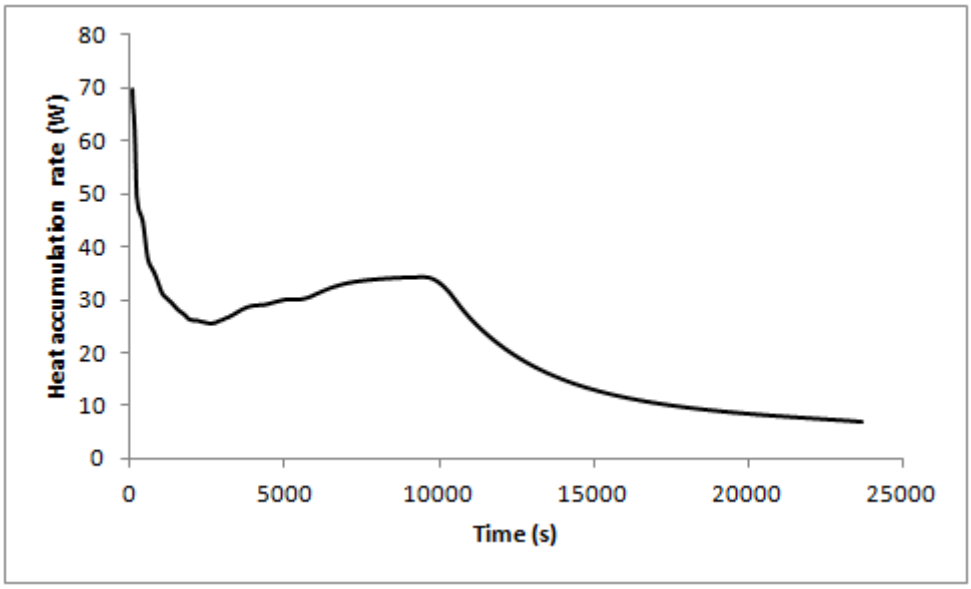

Figure 6.22: Heat accumulation rate as a function of time.

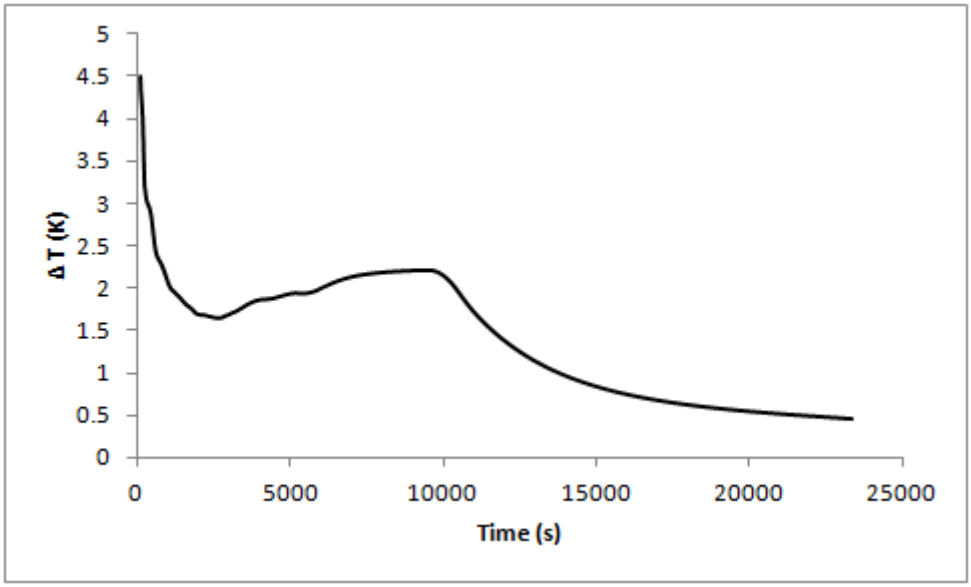

Figure 6.23: The temperature difference for the HTF in the pipe's inlet and outlet $(\Delta T = T_i - T_o)$.

For designing process of the similar thermal storage systems in the future at Northumbria University the average heat transfer coefficient between the HTF pipe and the PCM was evaluated.

The heat transfer coefficient varies along the axis of the unit, due to the temperature variation inside the PCM. Therefore, the heat transfer coefficients were calculated for the upper, bottom and side regions of the computational domain. In each region the heat transfer coefficient was calculated along the axis and in radial directions.

For example, the coefficient of heat transfer between the outer wall of the HTF pipe and the PCM was calculated using temperature difference at the radial distance of 5 mm at the upper region for the full length of the system, i.e. using temperatures at monitoring points u1 and u41. The logarithmic mean temperature difference, ΔT (LMTD) for these points was obtained as

$$\Delta T\left(LMTD\right)=\frac{\left(T_{w11}-T_{u41}\right)-\left(T_{w1}-T_{u1}\right)}{\left[\ln\left(T_{w11}-T_{u41}\right)/\left(T_{w1}-T_{u1}\right)\right]} \tag{6.1}$$

where T_{u1} and T_{u41} are the PCM temperature at points u1 (first measurement plane) and u41 (last measurement plane); T_{w1} and T_{w11} are the pipe wall temperatures at the same corresponding measurement planes.

Figure 6.24 shows the temperature variations at points u1 and u41 as a function of time. Figure 6.25 presents variation of LMTD between the outer wall of the HTF pipe and the PCM calculated using temperatures at points u1 and u41. Figure 6.26 shows variation of the heat transfer coefficient between the outer wall of the HTF pipe and the PCM calculated using temperatures at points u1 and u41.

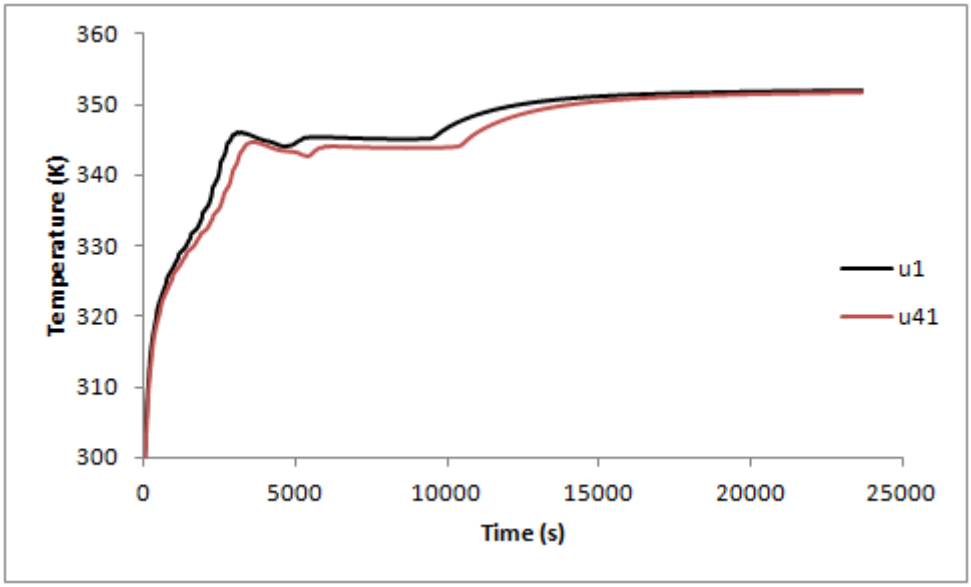

Figure 6.24: Temperature at points u1 and u41 as a function of time.

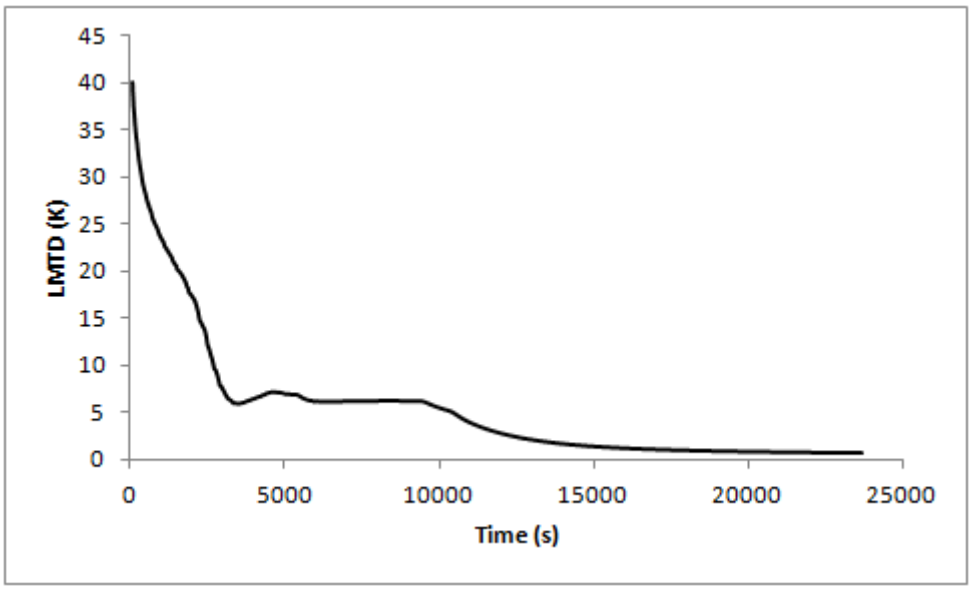

Figure 6.25: LMTD between the outer wall of the HTF pipe and the PCM calculated using temperatures at points u1 and u41.

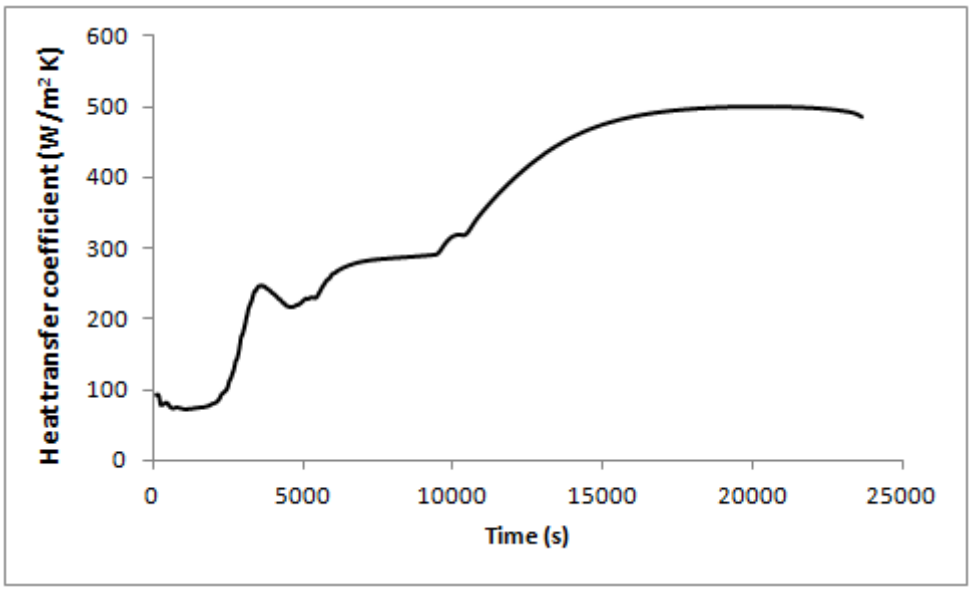

Figure 6.26: Heat transfer coefficient between the outer wall of the HTF pipe and the PCM using temperatures at points u1 and u41.

It can be seen that LMTD continuously decreases over time in the process of PCM melting and the dynamics of variation of heat transfer coefficient mirrors the dynamics of LMTD curve, see Figure 6.24. Fluctuations in the variation of LMTD and heat transfer coefficient

can be explained by the effect of intensification of natural convection in the liquid PCM at certain phase of the melting process. Once the PCM is completely melted, the temperatures rapidly increase which leads to decrease in the LMTD and rise in the heat transfer coefficient. The heat transfer coefficient varies in the range between 90 and 500 W/(m^{2}K) during the melting process.

Similar calculations were performed for the coefficient of heat transfer between the PCM and the HTF pipe at the bottom region of the domain. As an example, the heat transfer coefficients between the outer wall of the HTF pipe and the PCM was calculated using temperature difference at the radial distance of 5 mm at the bottom region for the full length of the system, i.e. using temperatures at monitoring points b1 and b41. The logarithmic mean temperature difference, ΔT (LMTD) for these points was obtained as

$$\Delta T\left(LMTD\right)=\frac{\left(T_{w22}-T_{b41}\right)-\left(T_{w12}-T_{b1}\right)}{\left[\ln\left(T_{w22}-T_{b41}\right)/\left(T_{w12}-T_{b1}\right)\right]} \tag{6.2}$$

where T_{b1} and T_{b41} are the PCM temperature at points b1 (first measurement plane) and b41 (last measurement plane); T_{w12} and T_{w22} are the pipe wall temperatures at the same corresponding measurement planes.

Figures 6.27 and 6.28 show variations of the LMTD and coefficient of heat transfer between the outer wall of the HTF pipe and the PCM calculated using temperatures at points b1 and b41. It can be seen that the magnitude of the heat transfer coefficient is significantly less compared to the top region and varies between 40 and 100 during the melting process. This is mainly due to the conduction heat transfer being dominant in the bottom region of the system. During the phase change process, the LMTD is nearly constant and the heat accumulation rate gradually increases. The heat transfer coefficient also rises reaching the maximum value.

Once the PCM is completely melted the heat transfer coefficient value remains nearly constant.

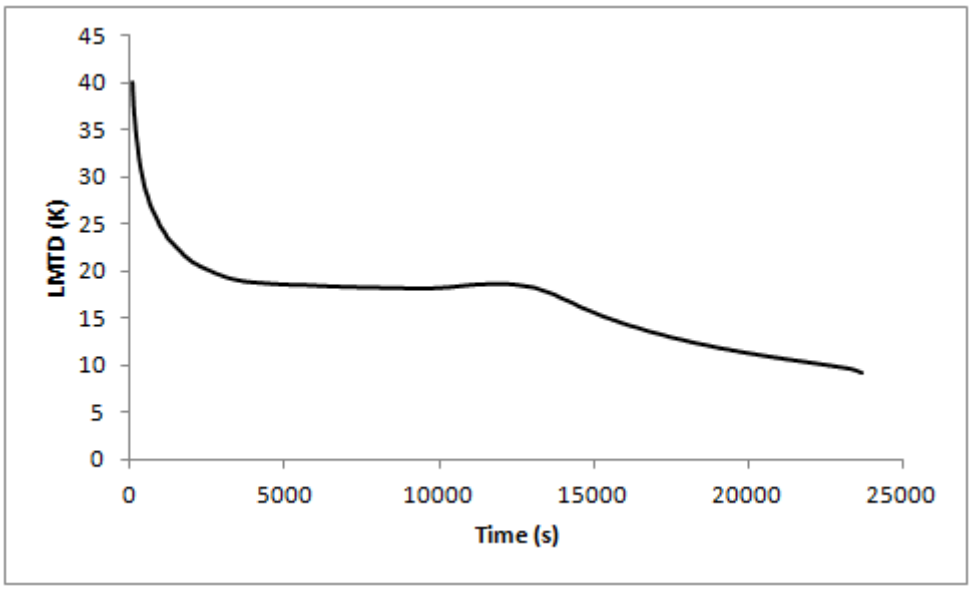

Figure 6.27: LMTD between the outer wall of the HTF pipe and the PCM calculated using temperatures at points b1 and b41.

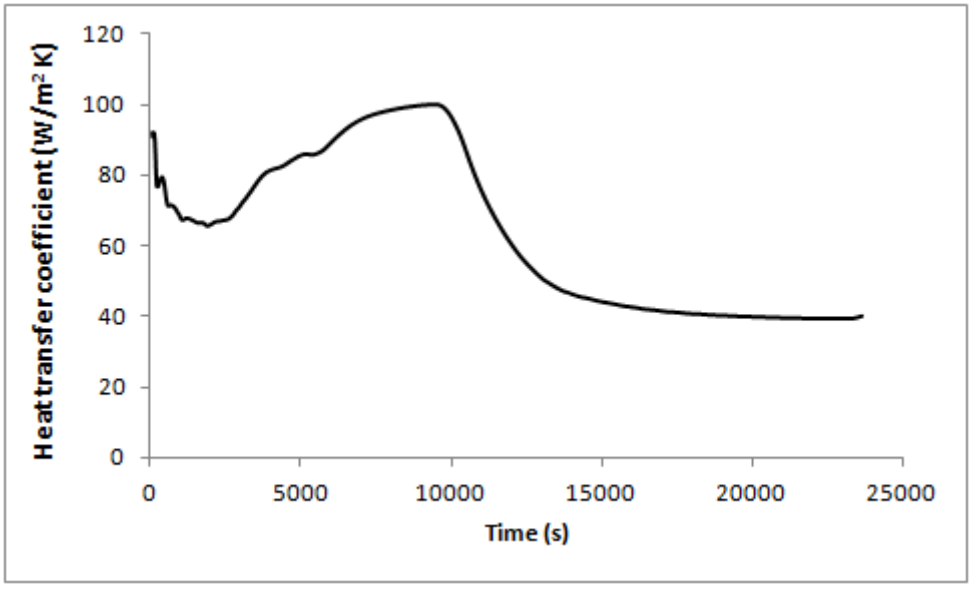

Figure 6.28: Heat transfer coefficient between the outer wall of the HTF pipe and the PCM using temperatures at points b1 and b41.

The heat transfer coefficient values were also obtained in similar way at the side regions. For example, the coefficient of heat transfer between the outer wall of the HTF pipe and the PCM was calculated using temperature difference at the radial distance of 5 mm at the side region for the full length of the system, i.e. using temperatures at monitoring points e1 and e41.The logarithmic mean temperature difference, ΔT (LMTD) for these points was obtained as

$$\Delta T\left(LMTD\right)=\frac{\left(T_{w33}-T_{e41}\right)-\left(T_{w23}-T_{e1}\right)}{\left[\ln\left(T_{w33}-T_{e41}\right)/\left(T_{w23}-T_{e1}\right)\right]} \tag{6.3}$$

where T_{e1} and T_{e41} are the PCM temperature at points e1 (first measurement plane) and e41 (last measurement plane); T_{w23} and T_{w33} are the pipe wall temperatures at the same corresponding measurement planes.

Figures 6.29 and 6.30 show variations of the LMTD and coefficient of heat transfer between the outer wall of the HTF pipe and the PCM calculated using temperatures at points e1 and e41.

Similar to the upper and bottom regions, the LMTD decreases with time and consequently, the heat transfer coefficient rises over the melting period. The magnitude of the heat transfer coefficient in this region is higher than that at the bottom region of the domain because of the influence of the natural convection.

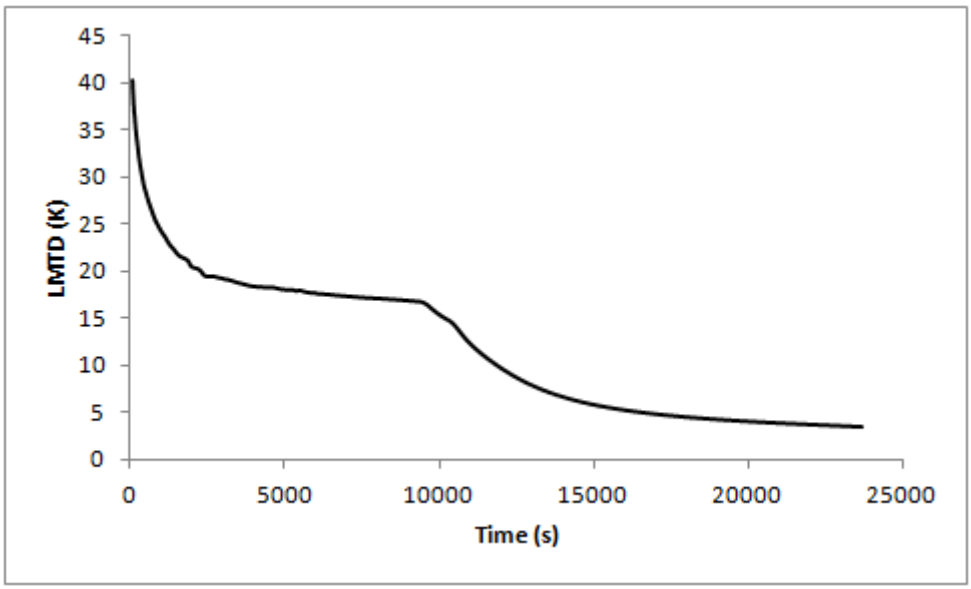

Figure 6.29: LMTD between the outer wall of the HTF pipe and the PCM at intervals e1 and e41as a function of time.

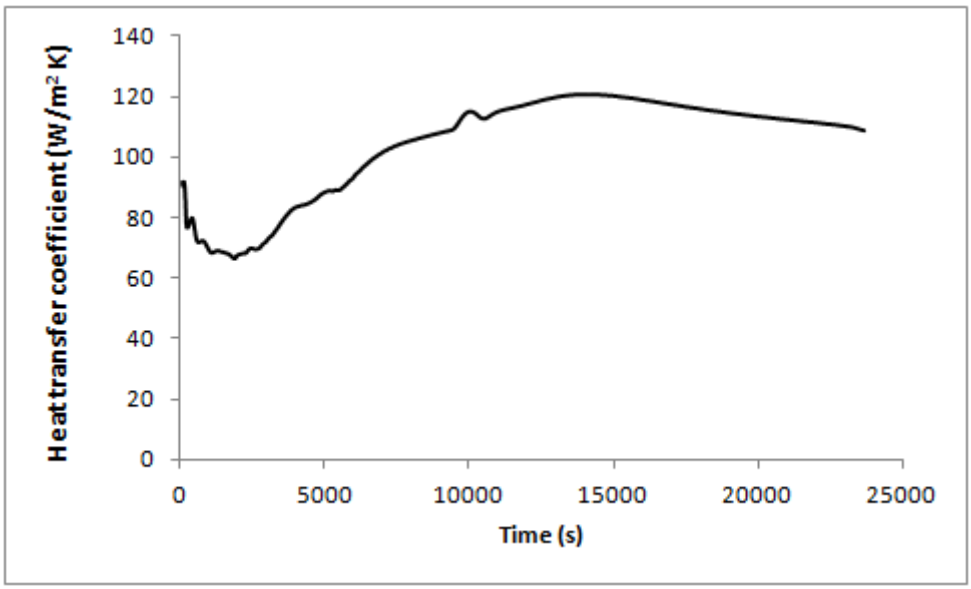

Figure 6.30: Heat transfer coefficient between the outer wall of the HTF pipe and the PCM at intervals e1 and e41in the side parts of the domain.

The variations in the heat transfer coefficient, as a function of time, were calculated at the upper, bottom, and side regions of the computational domain. It was found that the heat transfer coefficient in the upper region has a maximum value of 501 $W/m^2 K$. On the other hand, the maximum heat transfer coefficients for the bottom and side regions are 100.1 $W/m^2 K$ and 120.3 $W/m^2 K$, respectively. The higher value of heat transfer coefficient for the upper region is a result of natural convection in the liquid PCM and heat conduction. The natural convection heat transfer coefficient at the upper region can be calculated by subtracting the heat transfer coefficient at the bottom region from the total heat transfer coefficient at the upper region. Figure 6.31 shows variation of the natural convection heat transfer coefficient as a function of time.

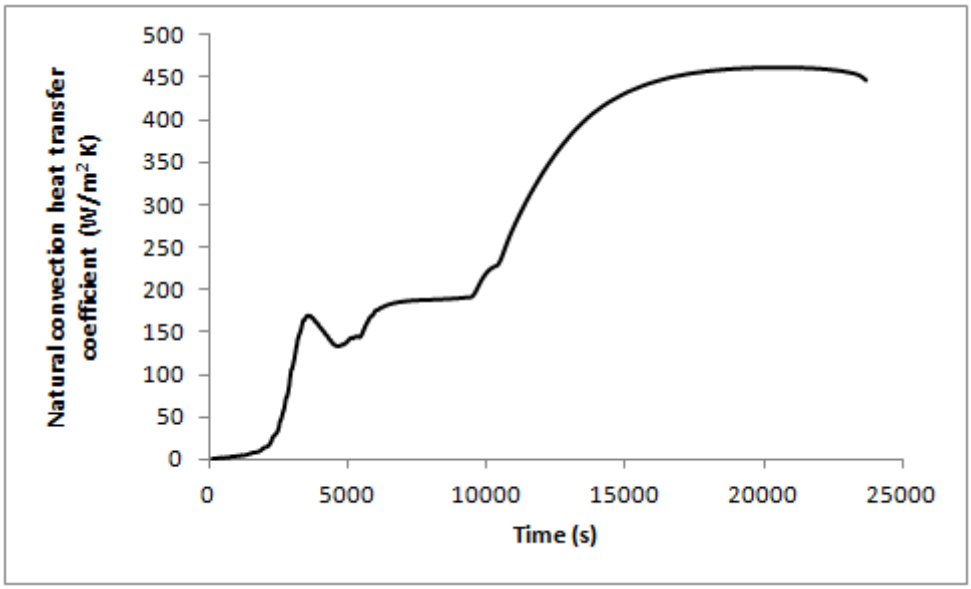

Figure 6.31: The natural convection heat transfer coefficient as a function of time.

Figure 6.32 shows variation of the coefficient of heat transfer between the outer wall of the HTF pipe and the PCM in the upper region of domain calculated at different axial distances, namely 100, 300 and 500 (full length) mm using temperatures at monitoring points located at 5 mm radial distance from the pipe walls (u17 & u25: fifth & seventh measurement planes;

u9 & 33: third & ninth measurement planes and u1 & u41: first and eleventh measurement planes). The figure shows that the heat transfer coefficient calculated for the full length of the system is slightly greater and this because the LMTD for the PCM temperatures is slightly decreased, see Figure 6.33.

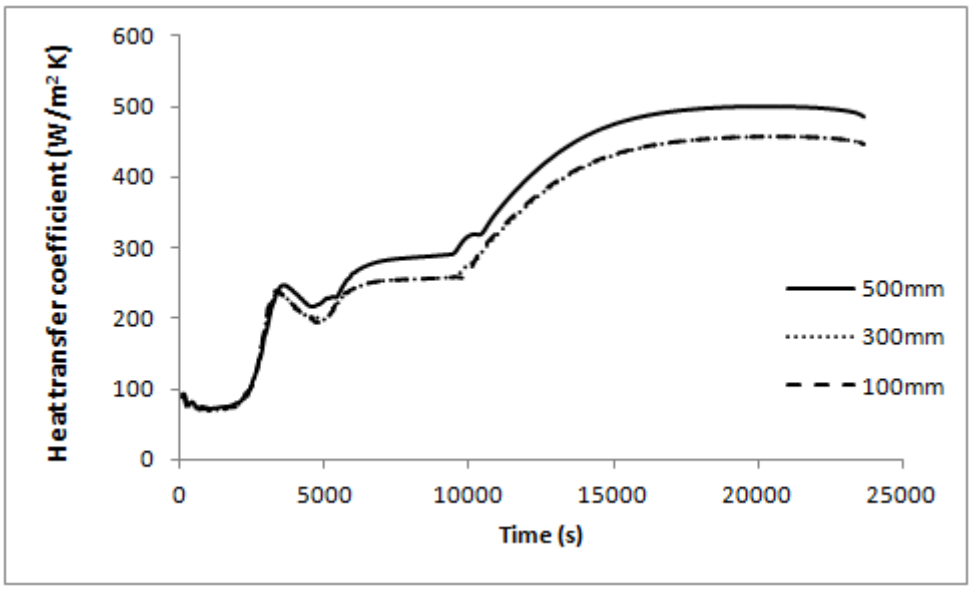

Figure 6.32: Variations in the heat transfer coefficient in the upper region of domain calculated at different axial distances.

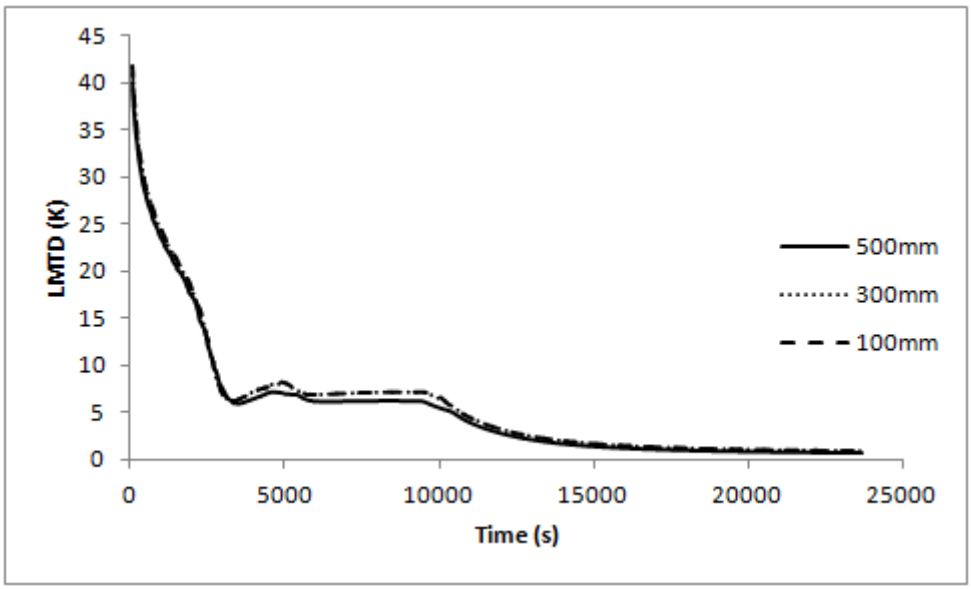

Figure 6.33: LMTD in the upper region of domain calculated at different axial distances.

Similar tendency was obtained for the both bottom and side regions of the computational domain. Figures 6.34 and 6.35 show the variations in the heat transfer coefficient and LMTD calculated at different axial distances for the bottom region of the domain. Figures 6.36 and 6.37 present these information for the side region of the domain.

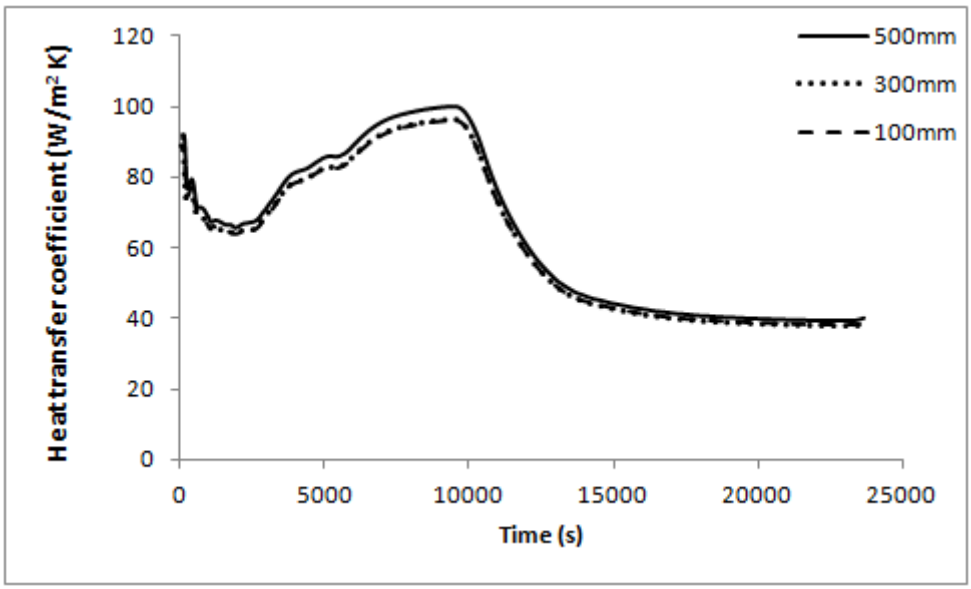

Figure 6.34: Variations in the heat transfer coefficient in the bottom region of domain calculated at different axial distances.

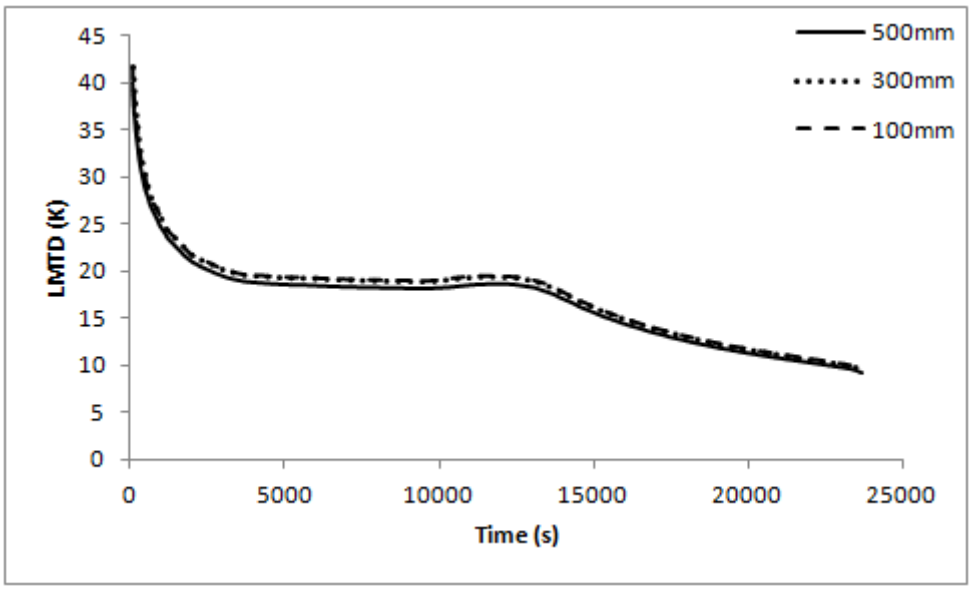

Figure 6.35: LMTD in the bottom region of domain calculated at different axial distances.

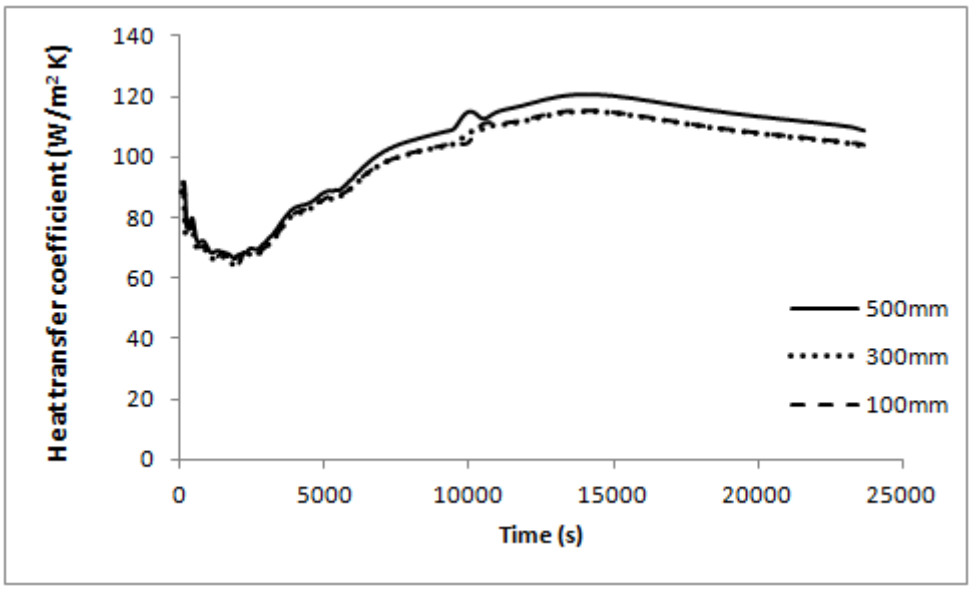

Figure 6.36: Variations in the heat transfer coefficient in the side region of domain calculated at different axial distances.

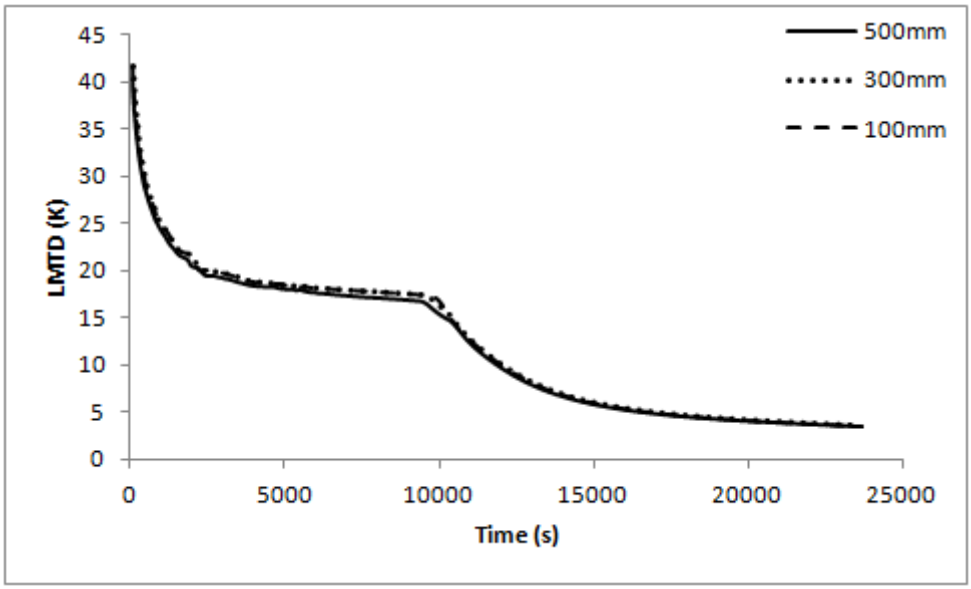

Figure 6.37: LMTD in the side region of domain calculated at different axial distances.

Figure 6.38 shows the variation of the coefficient of heat transfer between the outer wall of the HTF pipe and the PCM calculated using temperatures at points located at different radial distances from the pipe wall in the upper region of the domain. Calculations were performed

for the full length of the domain i.e. using temperature values in the first and eleventh measurement planes. It can be seen from Figure 6.38 that the heat transfer coefficient is greater at the location closer to the HTF pipe and it decreases as the distance from the location and the HTF pipe is increased. It can be explained by higher value of the LMTD for points located at the maximum distance from the pipe, see Figure 6.39. Similar tendencies for variations of the coefficient of heat transfer and LMTD were found in the bottom (Figures 6.40 and 6.41) and side (Figures 6.42 and 6.43) regions of the domain.

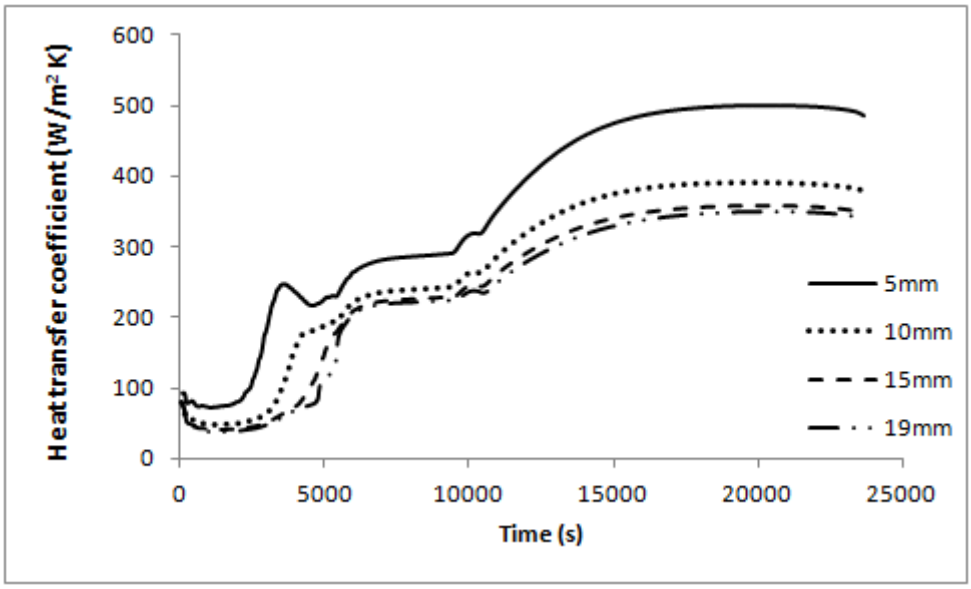

Figure 6.38: The coefficient of heat transfer calculated using temperatures at points located at different radial distances from the pipe wall in the upper region of the domain.

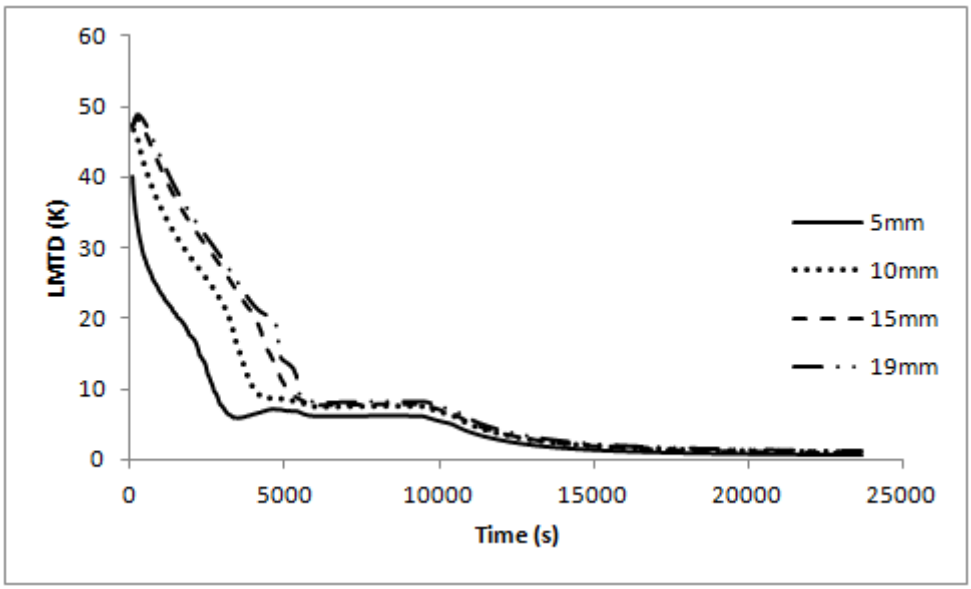

Figure 6.39: LMTD calculated using temperatures at points located at different radial distances from the pipe wall in the upper region of the domain.

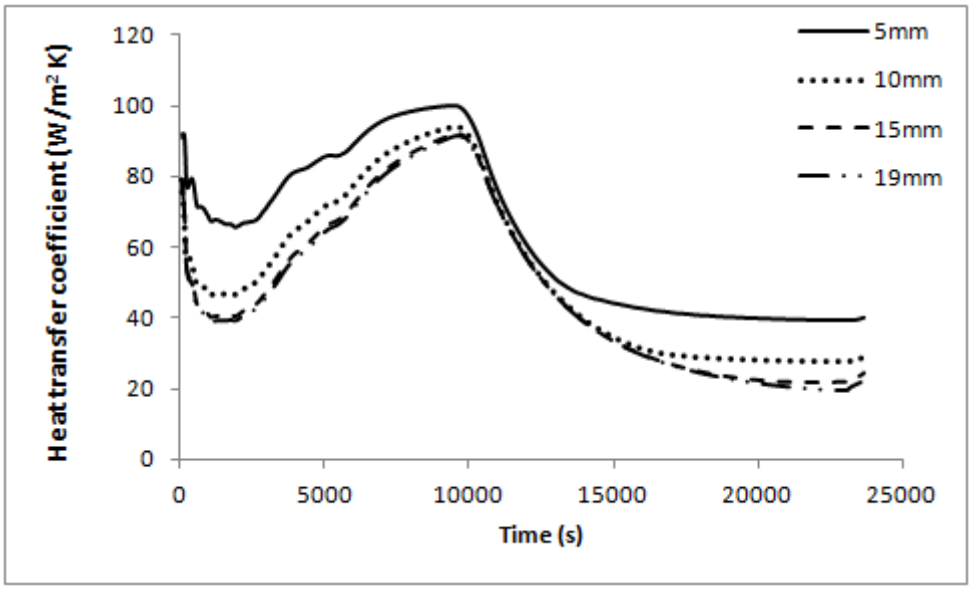

Figure 6.40: The coefficient of heat transfer calculated using temperatures at points located at different radial distances from the pipe wall in the bottom region of the domain.

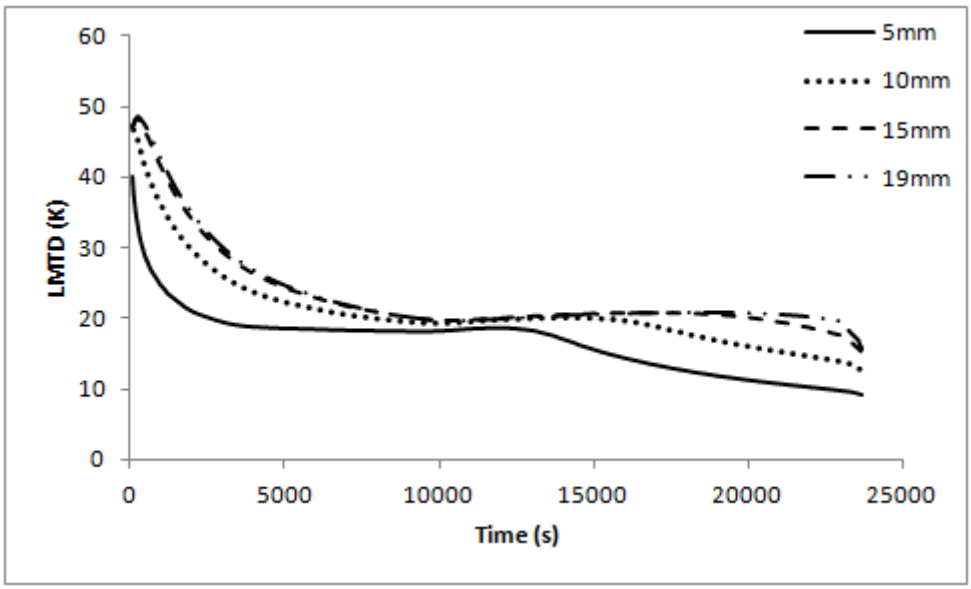

Figure 6.41: LMTD calculated using temperatures at points located at different radial distances from the pipe wall in the bottom region of the domain.

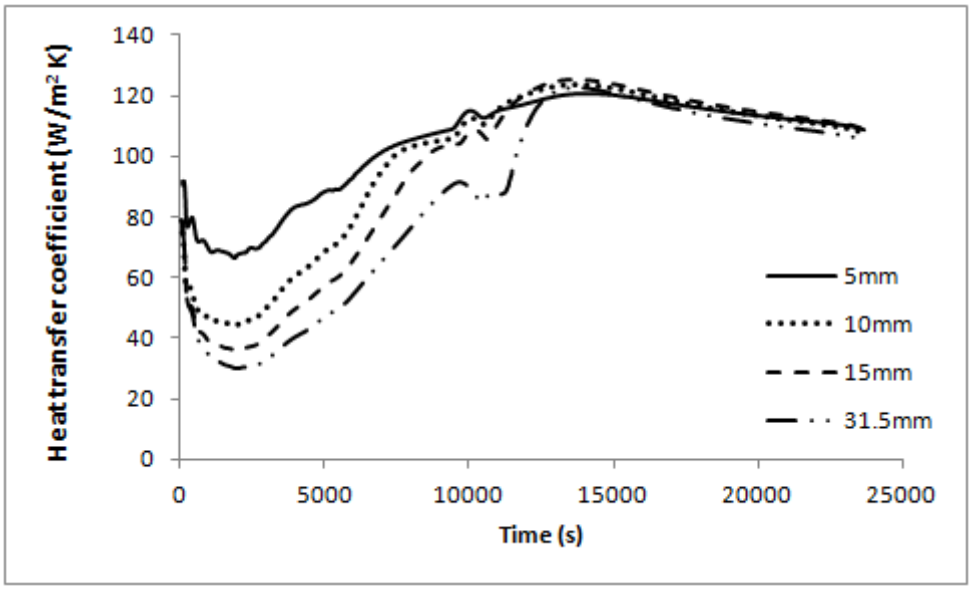

Figure 6.42: The coefficient of heat transfer calculated using temperatures at points located at different radial distances from the pipe wall in the side region of the domain.

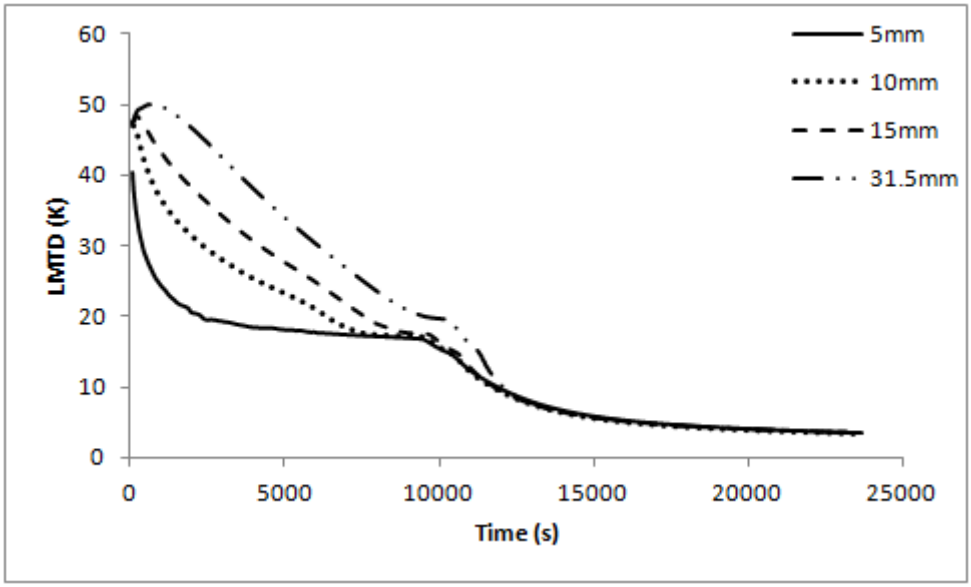

Figure 6.43: LMTD calculated using temperatures at points located at different radial distances from the pipe wall in the side region of the domain.

Using the array of results obtained on values of heat transfer coefficients the average coefficients of the heat transfer between the HTF pipe and the PCM were calculated for the upper, bottom and side regions of the computational domain, see Figure 6.44. The average heat transfer coefficient in the upper, bottom and side regions is 236.71, 55.74 and 91.51 $W/m^2\ K$, respectively for the specified inlet temperature of the HTF and its mass flow rate.

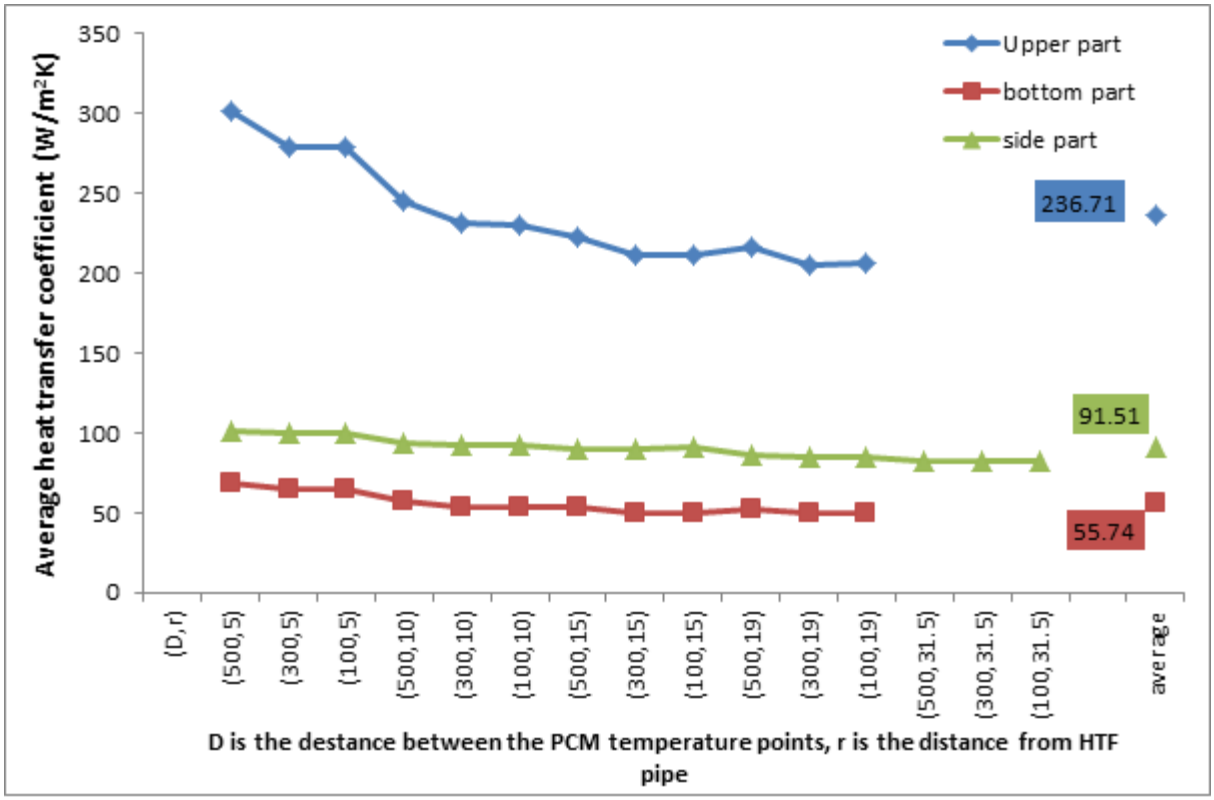

Figure 6.44: The average heat transfer coefficients in the upper, bottom and side regions of the domain.

The above calculations of the average heat transfer coefficient in the different regions of the domain were repeated for various values of the HTF inlet temperature and flow rates to derive dimensionless Nusselt number correlations. The flow rates of the HTF used in CFD simulations were 0.0037, 0.037, and 0.37 Kg/s. The HTF inlet temperatures were set to 343, 348, 353 and 363 K. The Nusselt number values were calculated at the top, side, and bottom regions of the PCM domain. Then, the average Nusselt number for all regions was calculated and evaluated. The Nusselt number correlations were expressed in terms of Stefan (*Ste*), Fourier (*Fo*), and Rayleigh (*Ra*) numbers.

Variations of Nusselt number as a function of Stefan number are shown in figures 6.45-6.47 for upper, side, and bottom regions, respectively. It can be seen that the Nusselt number is increased with rise in the Stefan number. This is because the Stefan number is proportional to

the difference between the inlet temperature of the HTF and the melting temperature of the PCM, and therefore an increase in the inlet temperature of HTF leads to an increase in the Stefan number. The results further indicate a significant difference between the Nusselt number in the upper region and those in the lower regions. The Nusselt number in the upper regions is higher as a result of natural convection. Figure 6.48 shows the variation of the average Nusselt number for all regions as a function of Stefan number.

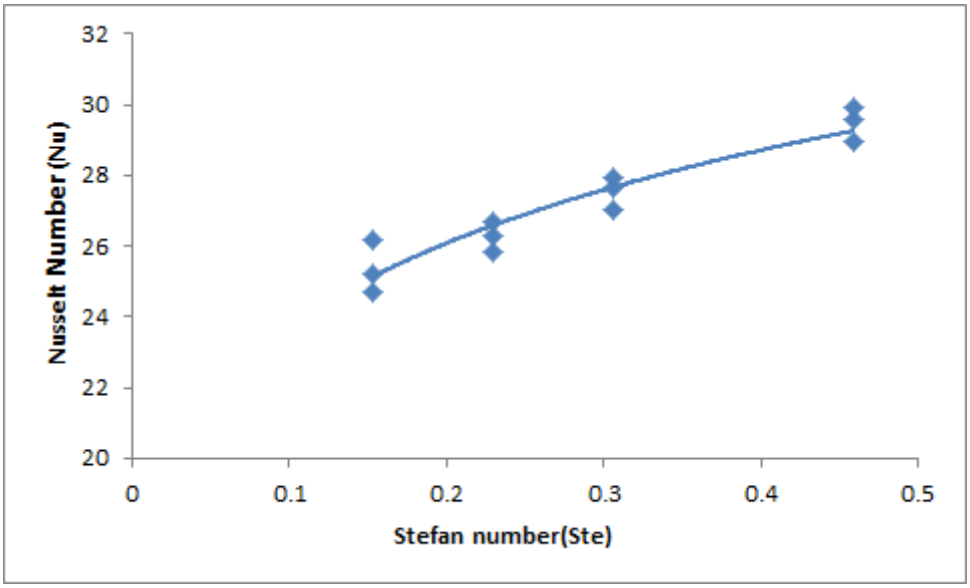

Figure 6.45: Variation in the Nusselt number as a function of Stefan number in the upper region.

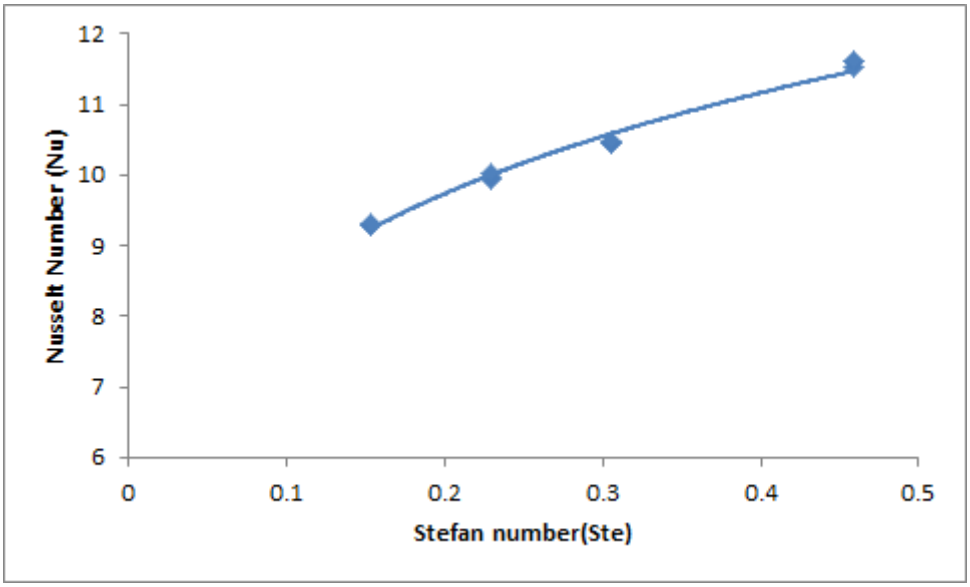

Figure 6.46: Variation in the Nusselt number as a function of Stefan number in the side region.

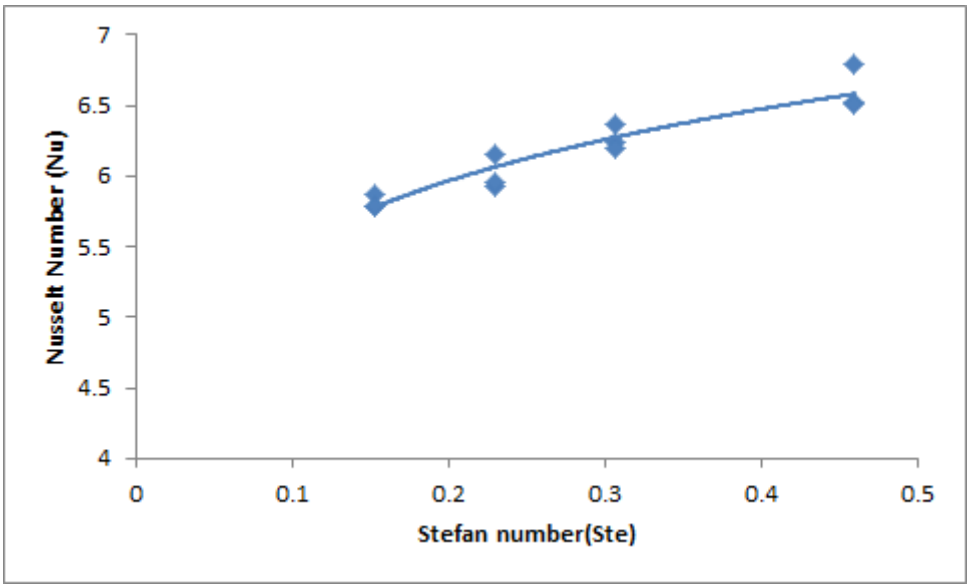

Figure 6.47: Variation in the Nusselt number as a function of Stefan number in the bottom region.

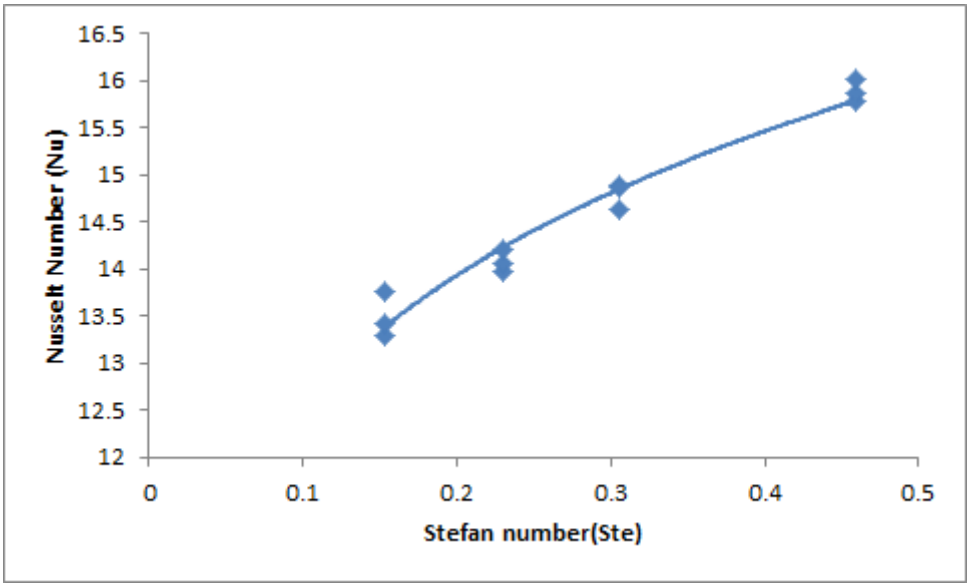

Figure 6.48: Variation in average Nusselt number as a function of Stefan number.

Variations of Nusselt number as a function of Rayleigh number are shown in Figures 6.49-6.52. It can be seen that the Nusselt number increases with the increase in the Rayleigh number. This is because the Rayleigh number is also proportionate to the difference between the inlet temperature of the HTF and the melting temperature of the PCM. This temperature difference is increased at high HTF temperatures, which consequently raises both the Rayleigh and Nusselt numbers.

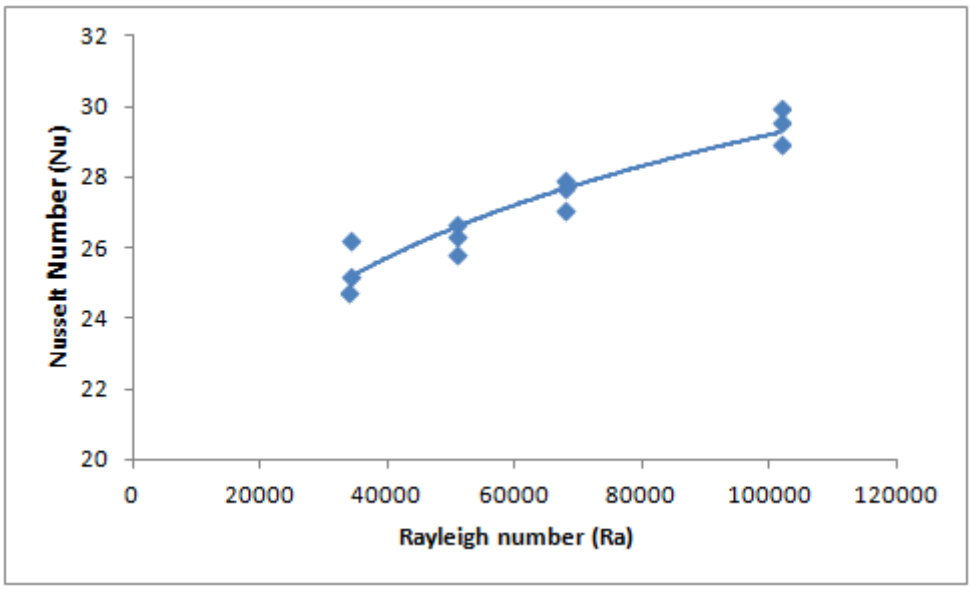

Figure 6.49: Variation of the Nusselt number as a function of Rayleigh number in the upper region.

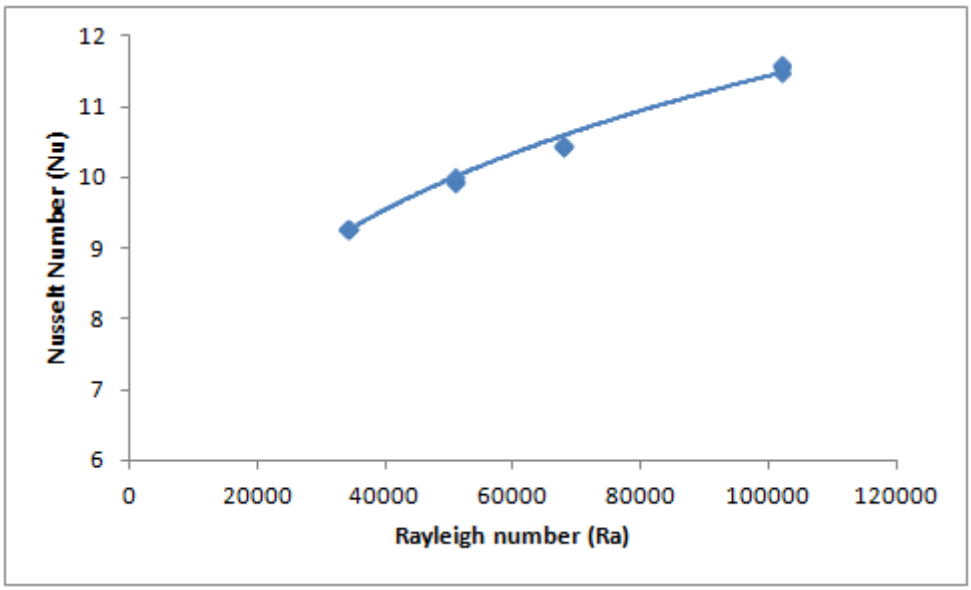

Figure 6.50: Variation of the Nusselt number as a function of Rayleigh number in the side region.

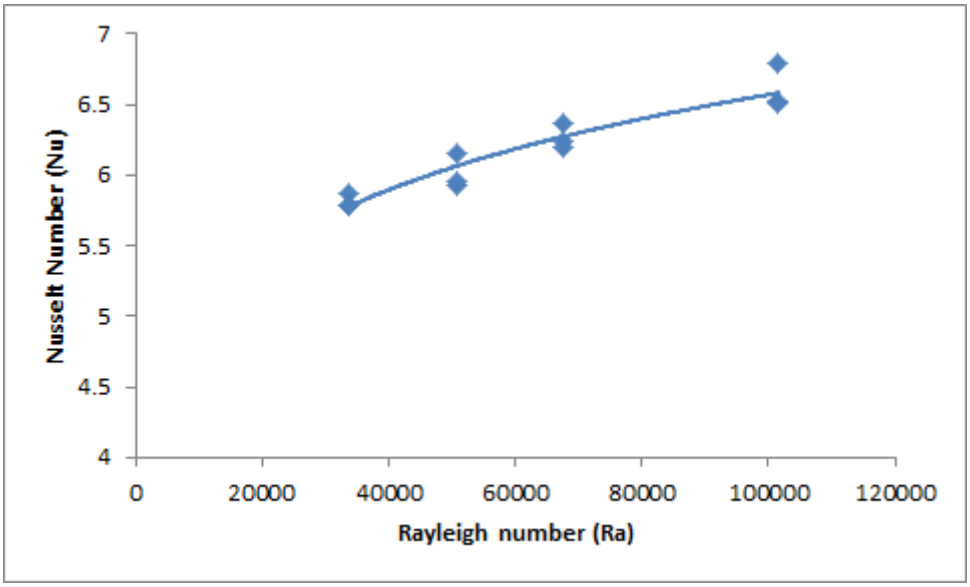

Figure 6.51: Variation of the Nusselt number as a function of Rayleigh number in the bottom region.

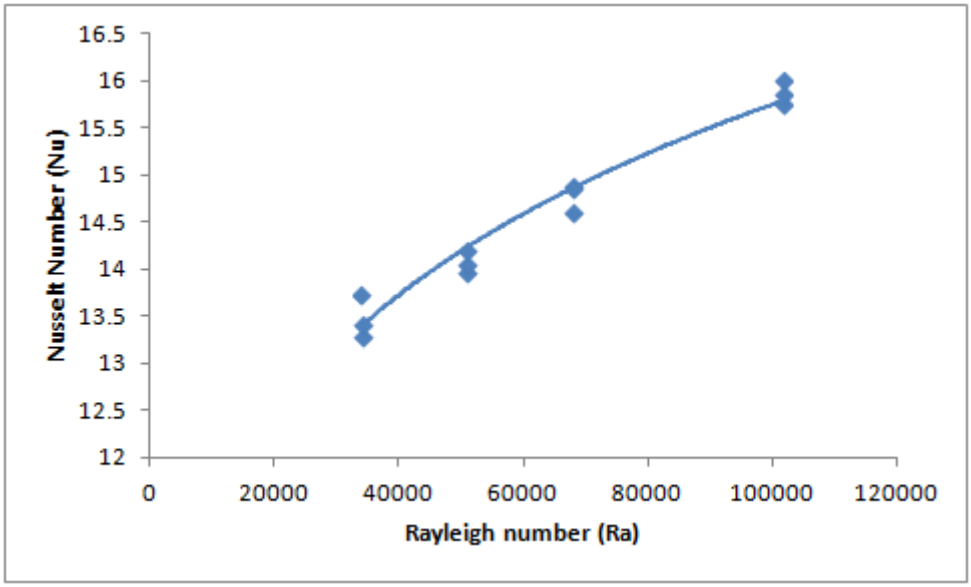

Figure 6.52: The variation of average Nusselt number as a function of Rayleigh.

Variations of Nusselt number as a function of Fourier number are shown in Figures 6.53-6.56. The Nusselt number decreases with the increase of Fourier number. This is because the Fourier number is proportional to the melting time. The increase of the HTF inlet temperature

and of the flow rate leads to the reduction in the melting time, thus resulting in lower Fourier number and higher values of the Nusselt number.

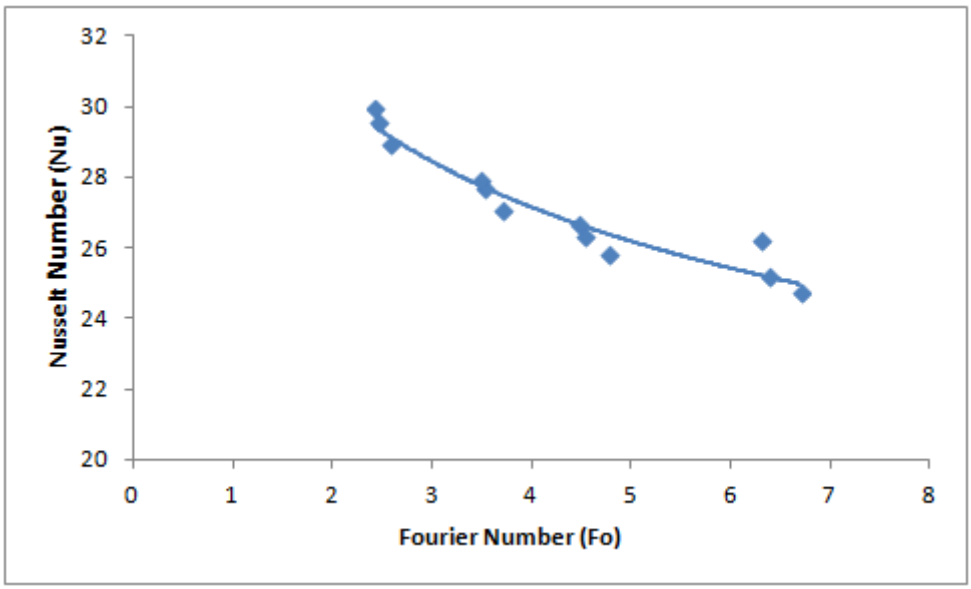

Figure 6.53: Variation of the Nusselt number as a function of Fourier number in the upper region.

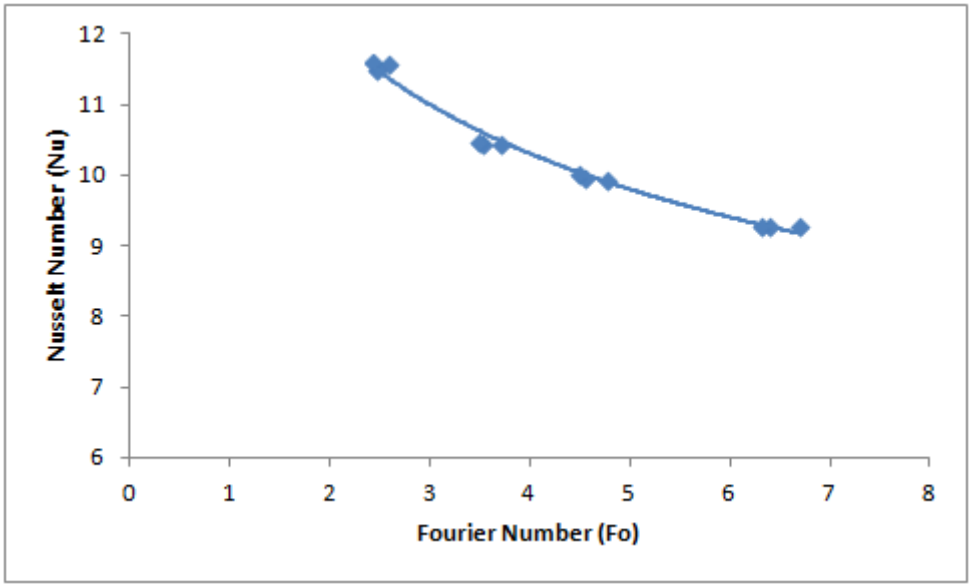

Figure 6.54: Variation of the Nusselt number as a function of Fourier number in the side region.

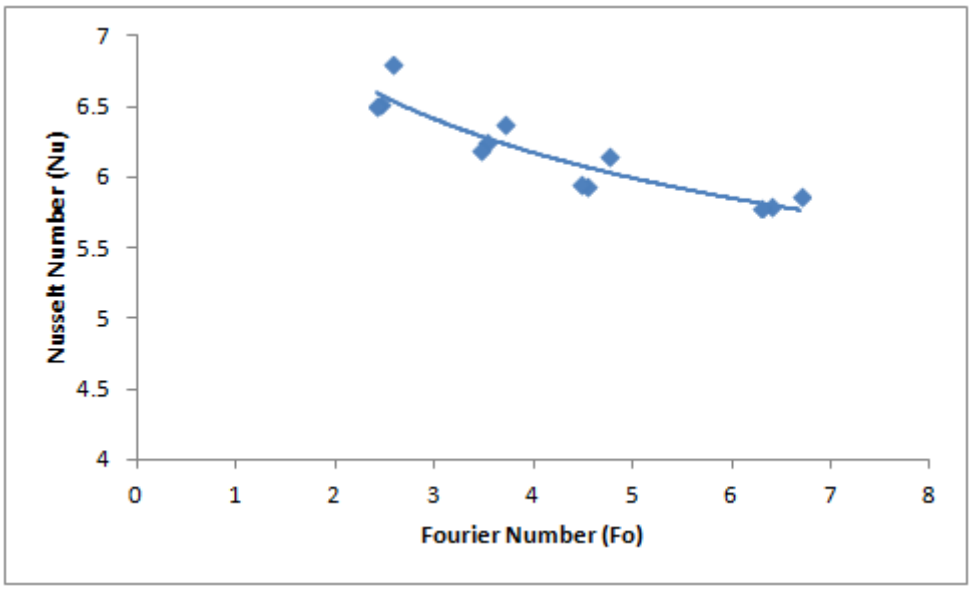

Figure 6.55: Variation of the Nusselt number as a function of Fourier number in the bottom region.

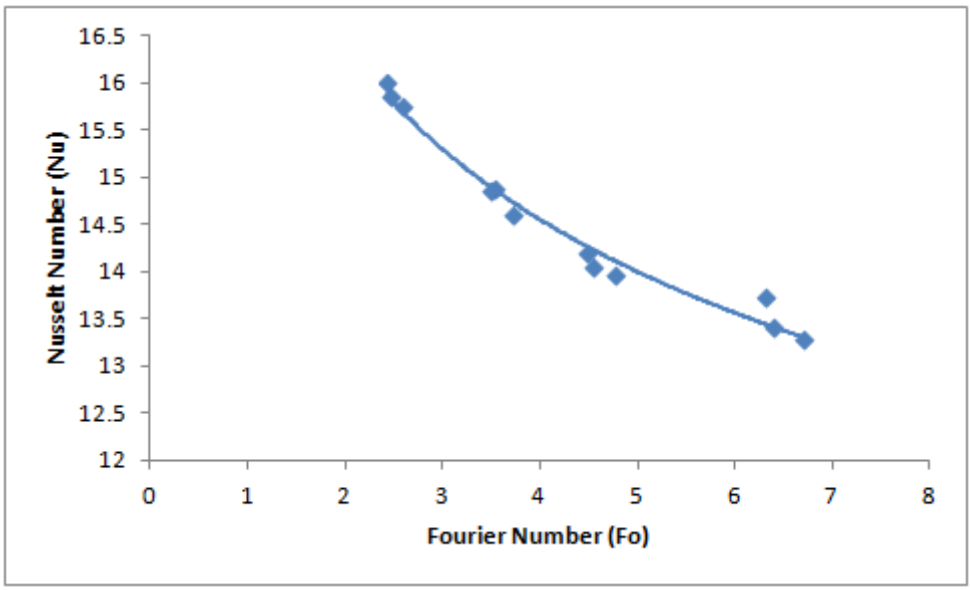

Figure 6.56: Variation of the average Nusselt number as a function of Fourier number.

The above data was used to derive Nusselt number correlations as a function of Stefan, Rayleigh and Fourier numbers in order to take into account the effect of all design and operational conditions:

The Nusselt number correlation for the upper regions of the PCM storage system (coefficient of correlation $R^2 = 0.9044$) -

$$Nu = 18.74(Ste)^{0.04617}(Fo)^{-0.054}(Ra)^{0.0461} \quad (6.4)$$

The Nusselt number correlation for the side regions of the PCM storage system (coefficient of correlation $R^2 = 0.9877$) -

$$Nu = 6.0642(Ste)^{0.0658}(Fo)^{-0.0753}(Ra)^{0.0657} \quad (6.5)$$

The Nusselt number correlation for the bottom region of the PCM storage system (coefficient of correlation $R^2 = 0.8681$) -

$$Nu = 4.4877(Ste)^{0.0393}(Fo)^{-0.044}(Ra)^{0.0393} \quad (6.6)$$

The average Nusselt number correlation in the system (coefficient of correlation $R^2 = 0.9695$) -

$$Nu = 9.7299(Ste)^{0.05}(Fo)^{-0.058}(Ra)^{0.0501} \quad (6.7)$$

The correlations between numerically obtained and calculated using Equations (6.4) - (6.7) are shown in Figures 6.57-6.60. It can be seen that the Nusselt number varies between 12 and 18 for the system investigated in this Chapter. The lower Nusselt numbers are for the low HTF inlet temperature, and the high Nusselt numbers values are obtained at the high HTF inlet temperatures.

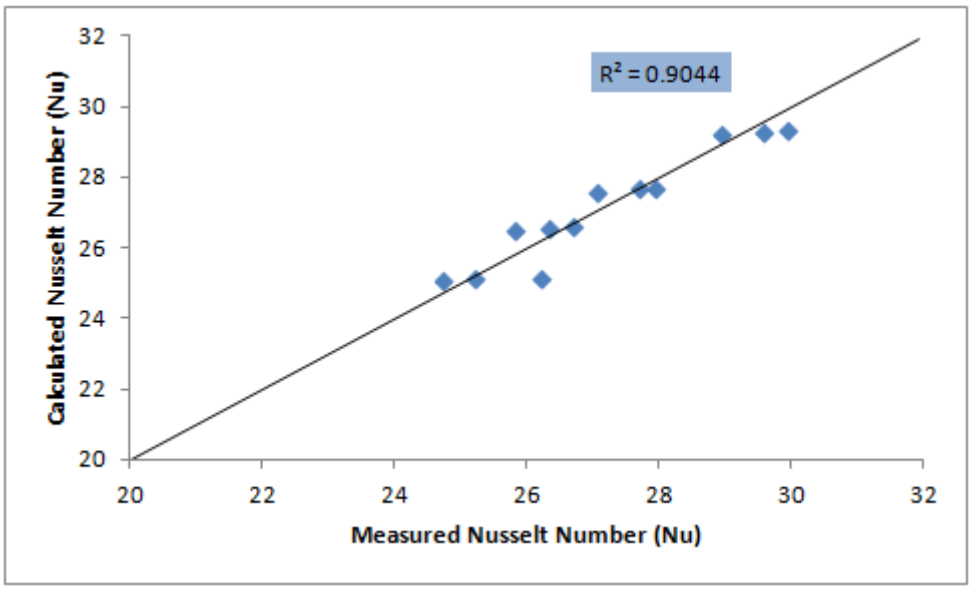

Figure 6.57: The correlation between numerically obtained and calculated using Equation (6.4) Nusselt numbers - for the upper region of the domain.

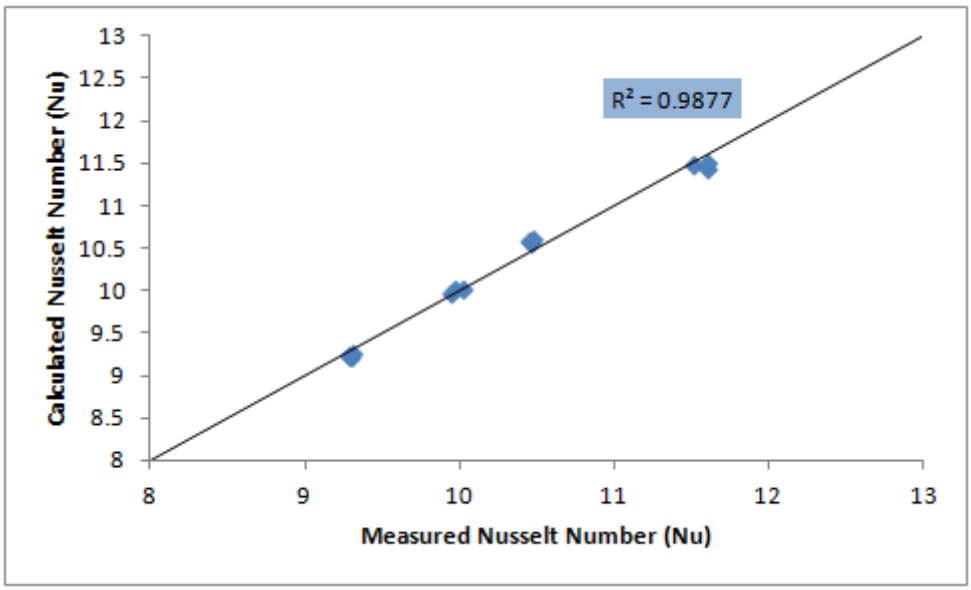

Figure 6.58: The correlation between numerically obtained and calculated using Equation (6.5) Nusselt numbers - for the side region of the domain.

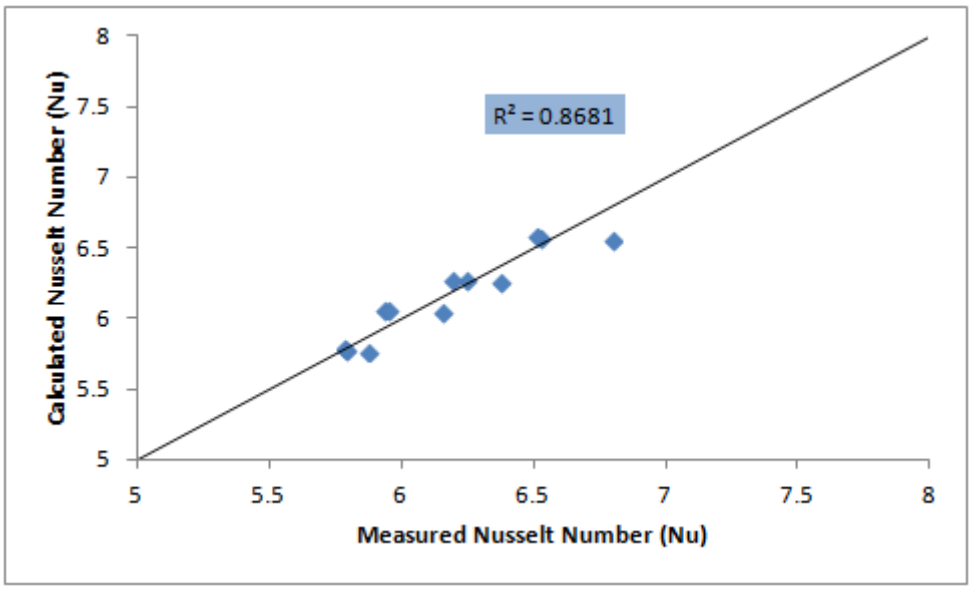

Figure 6.59: The correlation between numerically obtained and calculated using Equation (6.6) Nusselt numbers - for the bottom region of the domain.

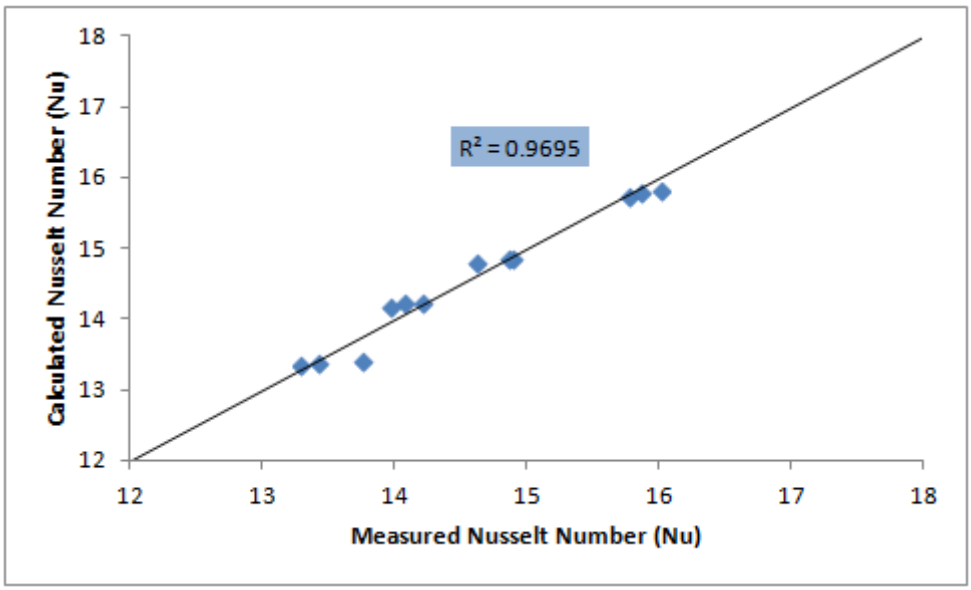

Figure 6.60: The correlation between numerically obtained and calculated using Equation (6.7) Nusselt numbers - average for the whole domain.

Subtracting the Nusselt numbers obtained for the bottom region from the Nusselt numbers for the upper regions results in the Nusselt numbers for heat transfer caused by natural

convection. These were presented as the Nusselt number correlation for natural convection (coefficient of correlation $R^2 = 0.8796$):

$$Nu = 13.6964(Ste)^{0.0523}(Fo)^{-0.0613}(Ra)^{0.0522} \tag{6.8}$$

Natural convection effect is increased by 9.7 % and 17.4 % when the HTF inlet temperatures rises to 353 and 363K, respectively, from 343 K, see Figure 6.61.

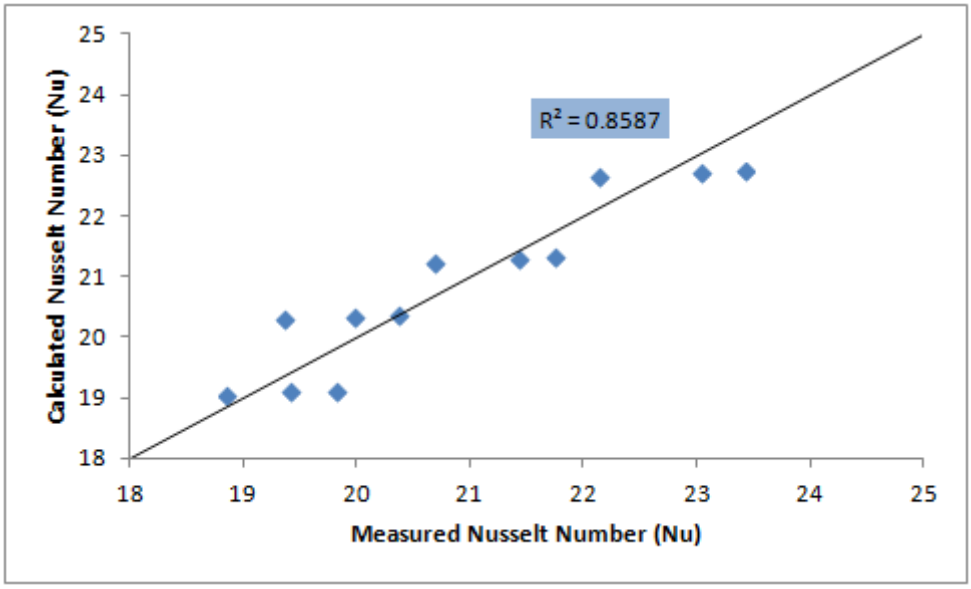

Figure 6.61: The correlation between numerically obtained and calculated using Equation (6.8) natural convection Nusselt numbers.

6.6 Heat transfer intensification using longitudinal fins

The use of fins embedded in PCM is one of the important methods of intensification of heat transfer in PCM thermal storage systems. Various fin geometries were used, namely circular, spiral and longitudinal.

In the current study, the heat transfer intensification using longitudinal horizontal fins was investigated. Three different longitudinal fin configurations were studied for melting PCM in a rectangular storage unit. The first system was equipped with a single horizontal pipe with 3 external longitudinal fins, see Figure 6.62. The second system had a single horizontal pipe with 4 external longitudinal fins, see Figure 6.63 and in the final storage system a single horizontal pipe with 6 external longitudinal fins was installed, see Figure 6.64. In all cases the fin thickness and width were 1 and 10 mm, respectively.

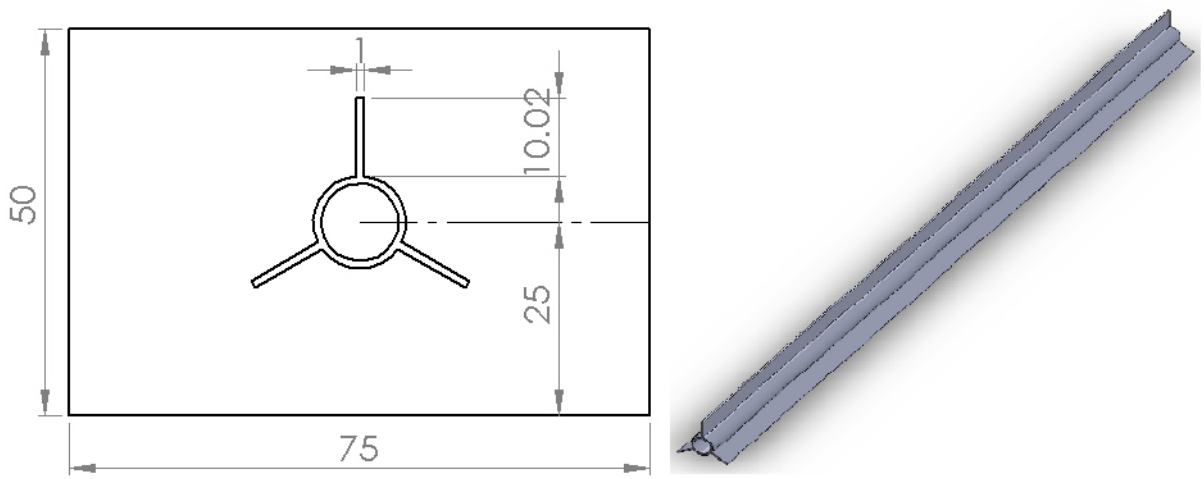

Figure 6.62: A schematic of the storage system with 3 external longitudinal fins.

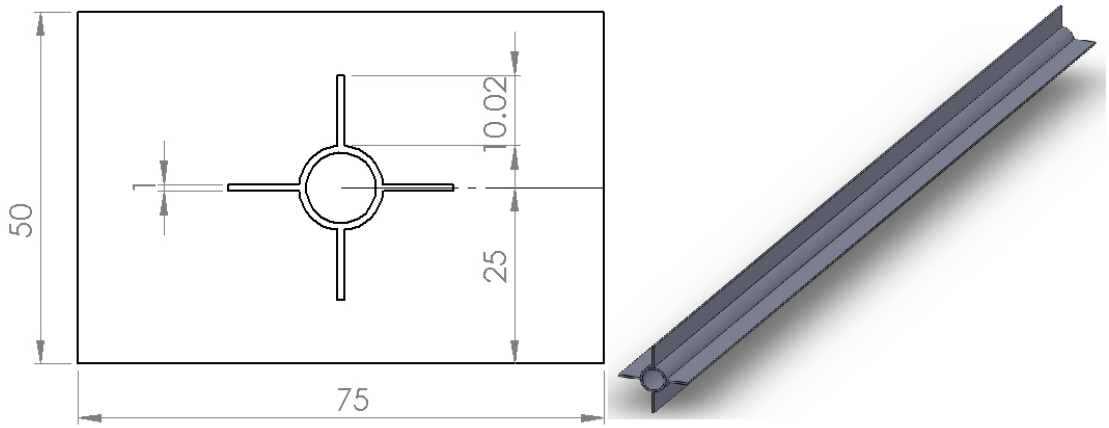

Figure 6.63: A schematic of the storage system with 4 external longitudinal fins.

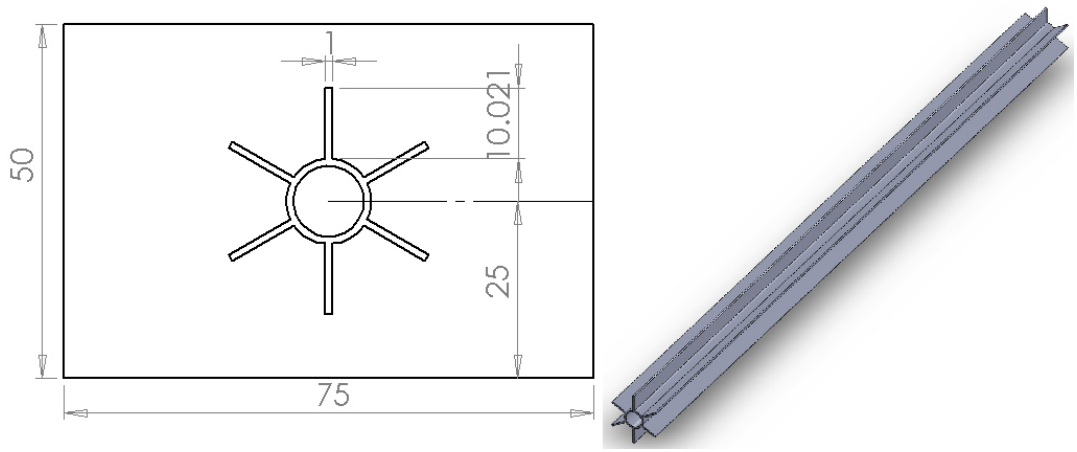

Figure 6.64: A schematic of the storage system with 6 external longitudinal fins.

A series of numerical CFD simulations were performed to test the effect of fins on the heat transfer in the storage unit during the transient melting process. Figures 6.65 and 6.66 show results of the temperature distribution and melting process in the middle section of the computational domain for the case of the rectangular storage with single smooth horizontal pipe and cases of single horizontal pipe with 3, 4 and 6 external longitudinal fins. The inlet temperature of the HTF was set to 353 K and the mass flow rate was 0.0037 kg/s. Results are shown for instances when elapsed time from the start of the charging process is 5000 and 10000 s.

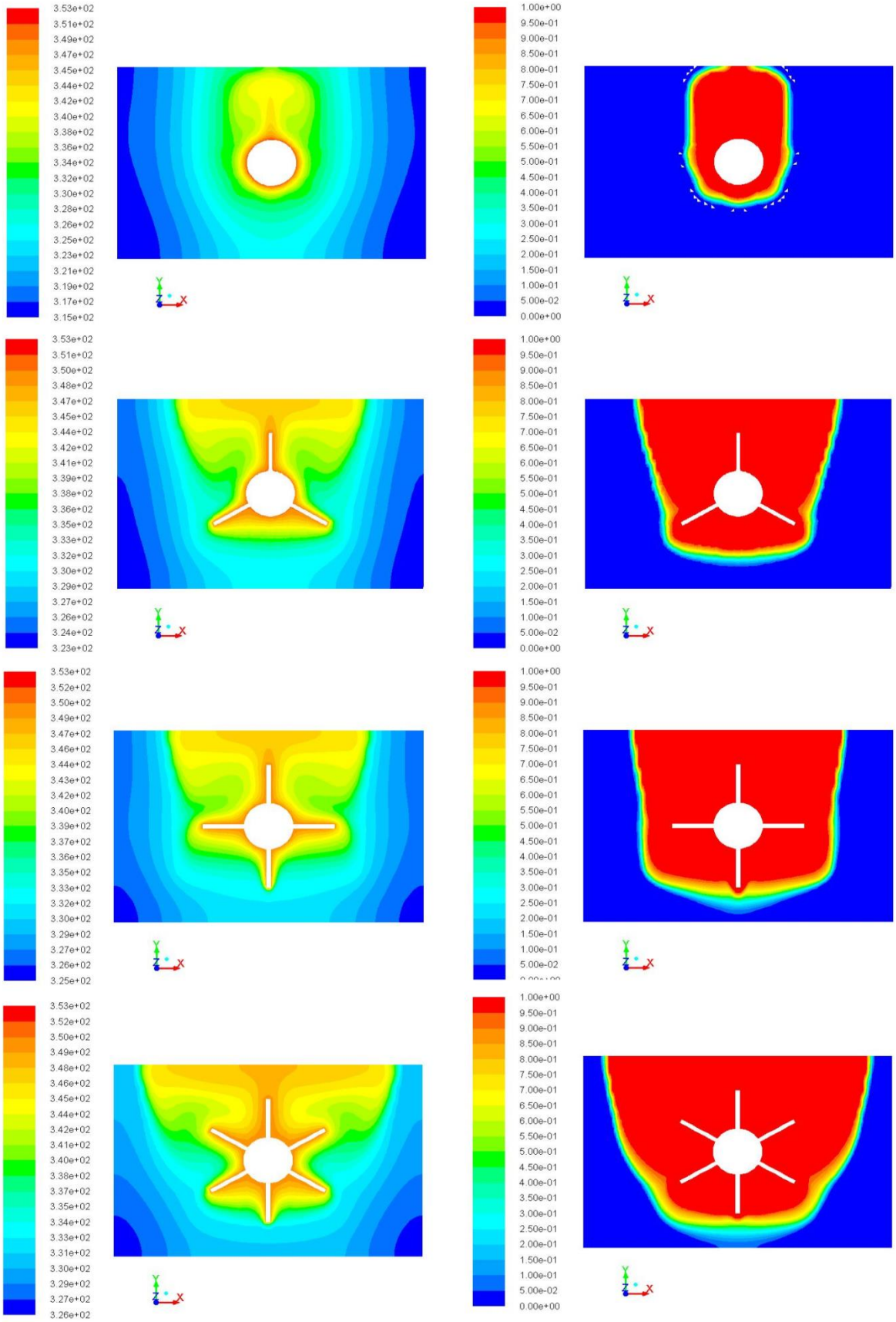

Figure 6.65: Temperature distribution and melting processes in the middle section of the domain. Elapsed time= 5000 s.

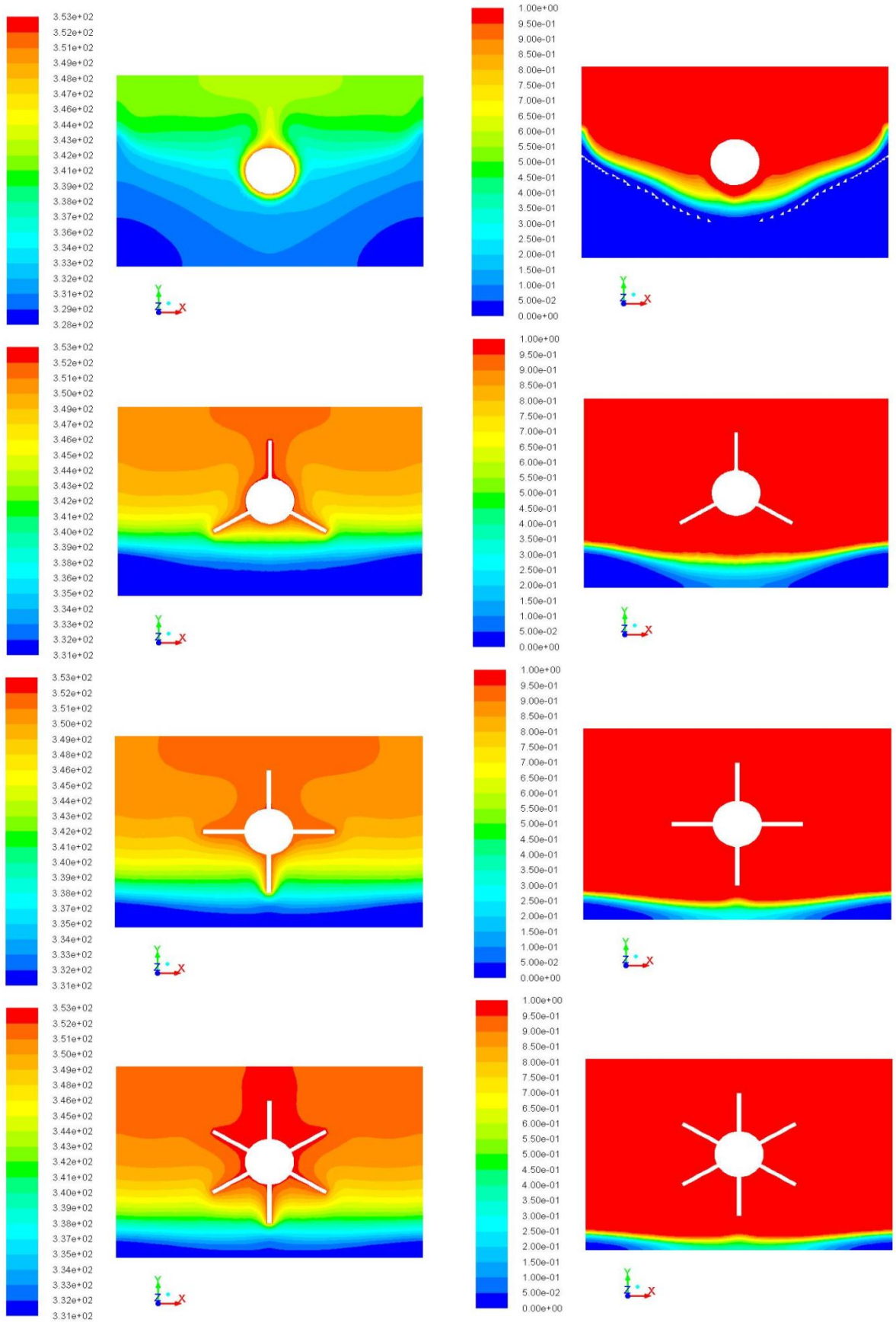

Figure 6.66: Temperature distribution and melting processes in the middle section of the domain. Elapsed time = 10000 s.

It is evident in the above figures that the temperature most rapidly rises in areas close to the pipe and its fins. The upper part of the domain turns into the liquid due to the effect of natural convection. Over the time, the melting process expands to the lower regions of the PCM system. The longitudinal fins increase the surface area and hence the transferred heat which is intensification of the heat transfer to the PCM.

Figures 6.67-6.69 compare the temperature distribution in the PCM in both radial and axial directions for cases of smooth pipe and the pipe with longitudinal fins. It can be seen that application of fins significantly accelerates the melting of the PCM but the number of fins in this particular design does not strongly affect dynamics of melting, particularly at the upper region of the domain.

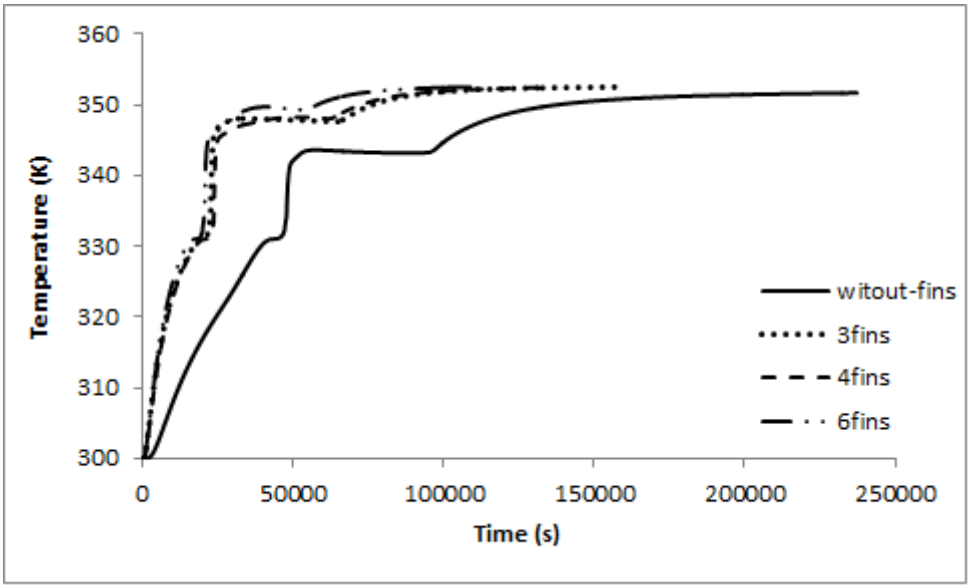

Figure 6.67: The effect of fins on the temperature variation at the point u4 (upper region of the domain, first measurement plane).

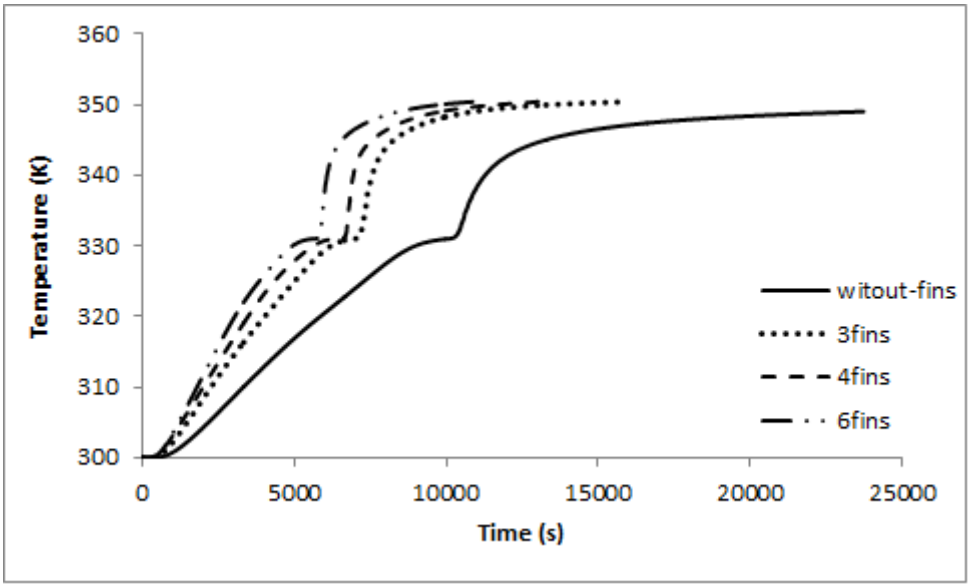

Figure 6.68: The effect of fins on the temperature variation at the point e4 (side region of the domain, first measurement plane).

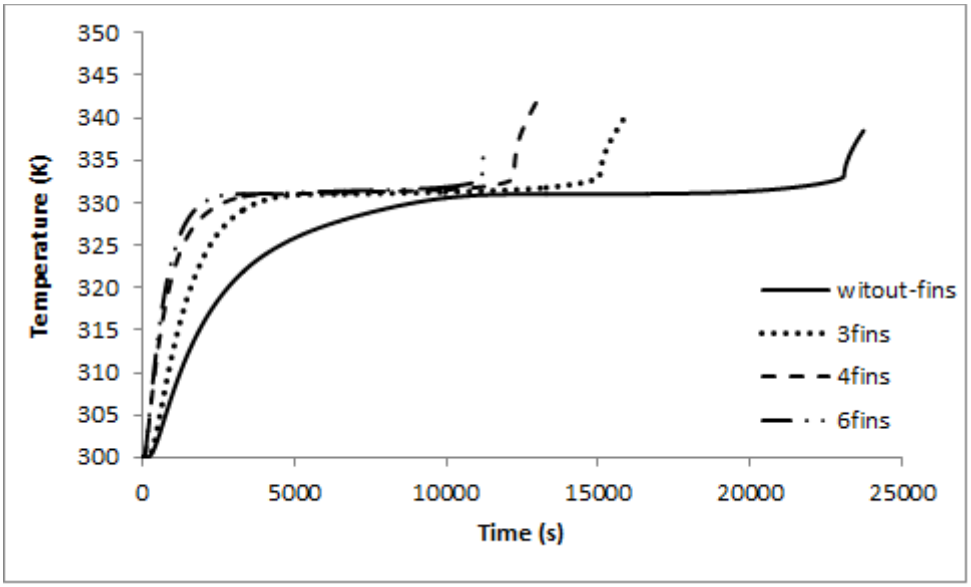

Figure 6.69: The effect of fins on the temperature variation at the point b4 (bottom region of the domain, first measurement plane).

Figures 6.70 and 6.71 present the velocity field in middle section of the system for instances when the time elapsed from the beginning of the charging are 5000 and 10000 s. It can be

seen that, in general, with the rise in the number of fins the bulk volume in which natural convection takes place is enlarged, especially at the side and bottom regions of the domain. This effect is advantageous for accelerating the melting process and achieving uniform temperature distribution. The optimal orientation of fins should be separately studied for 3 and 4 fin configurations to take fuller advantage from intensification of the heat transfer between PCM and fins.

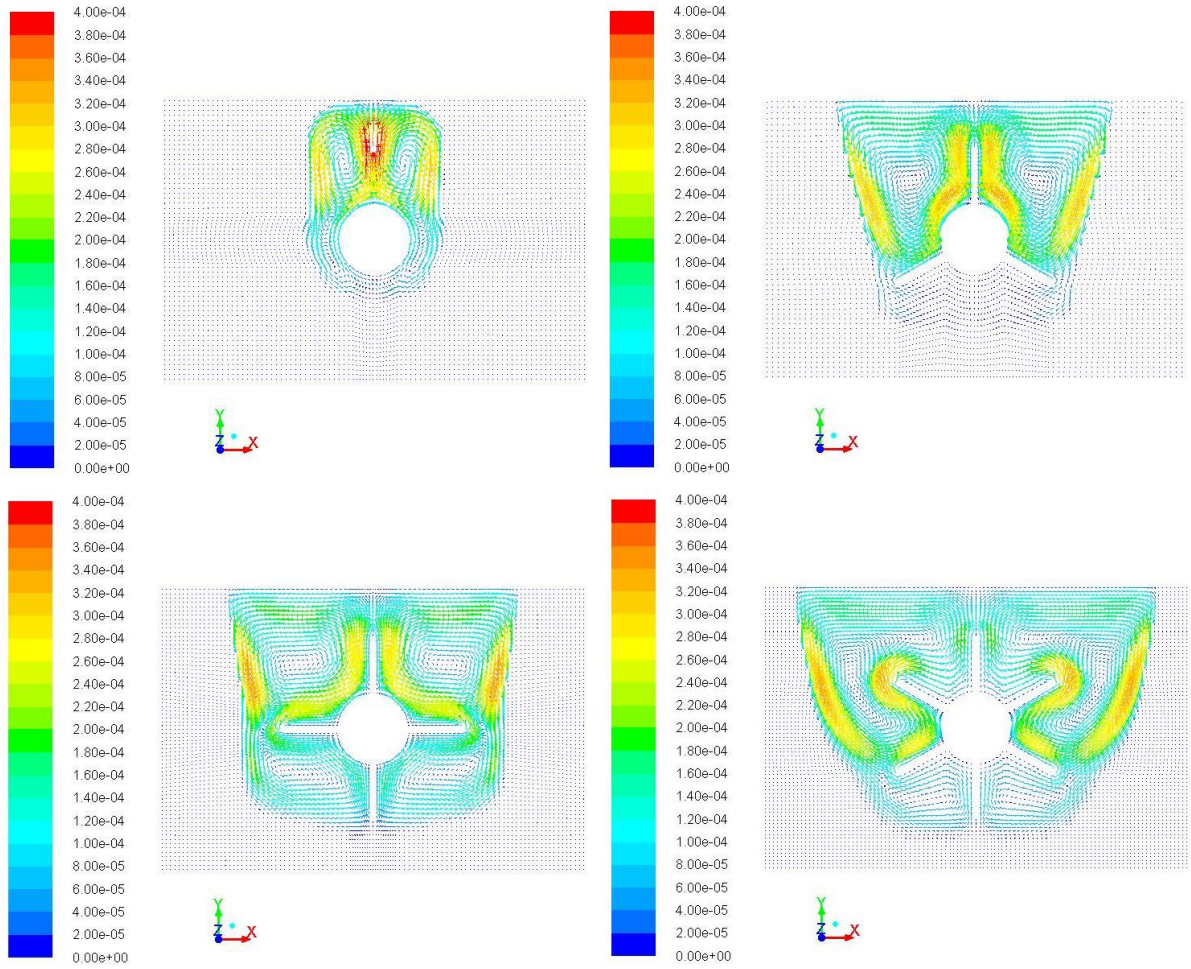

Figure 6.70: The velocity fields in the middle section of the domain. Elapsed time = 5000 s.

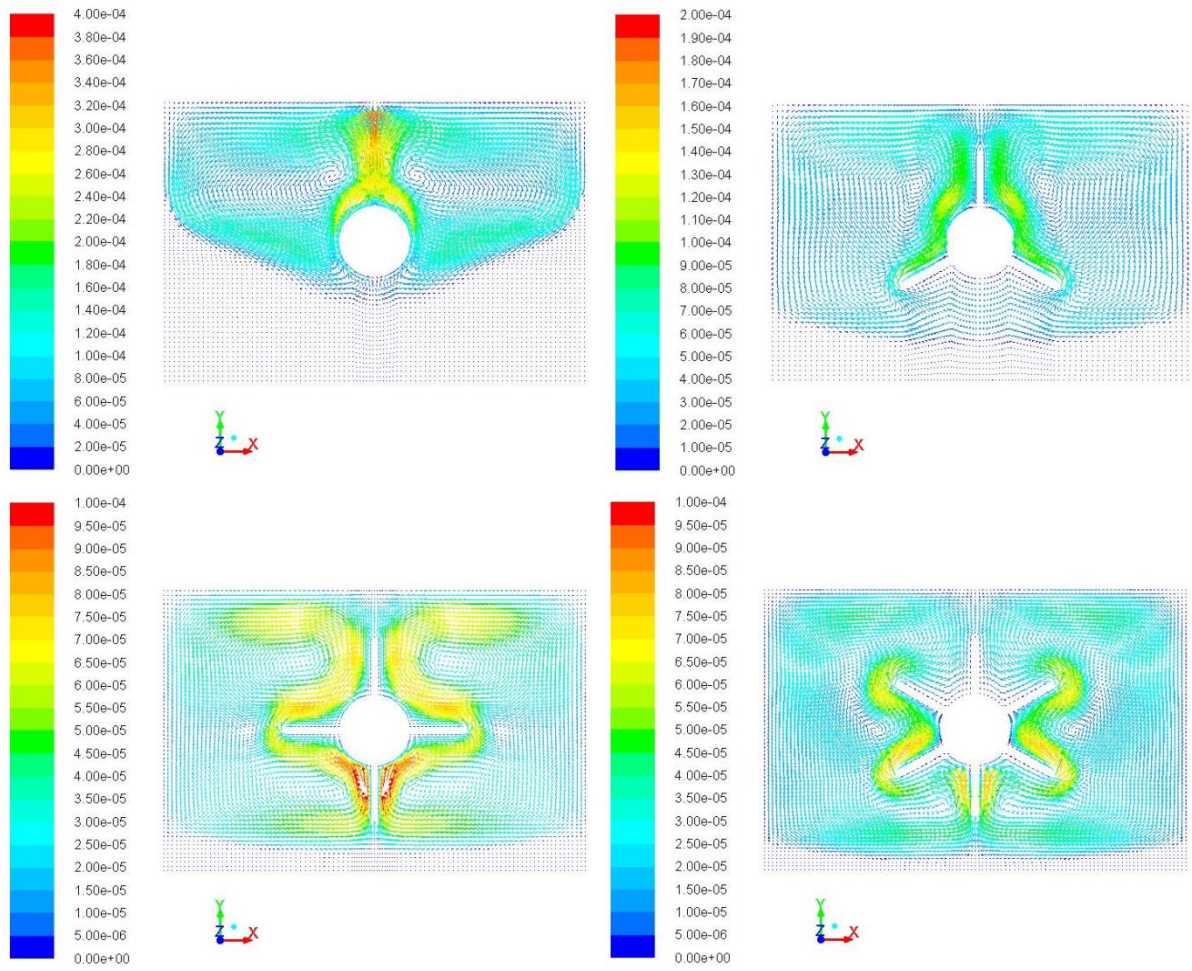

Figure 6.71: The velocity fields in the middle section of the domain. Elapsed time = 10000 s.

The effect of fins on the formation of the liquid fraction of the PCM and the total melting time are shown in Figures 6.72 and 6.73, respectively. The increase in the number of fins reduces the mass of the PCM but the melting time is reduced mainly due to the increase in area of heat transfer between the pipe and PCM. The melting time is reduced by approximately 32.2% for the case of pipe with 3 fins compared to the case of pipe without fins. The melting time is reduced by 44.6% and 52.4% for the cases of pipes with 4 and 6 fins, respectively.

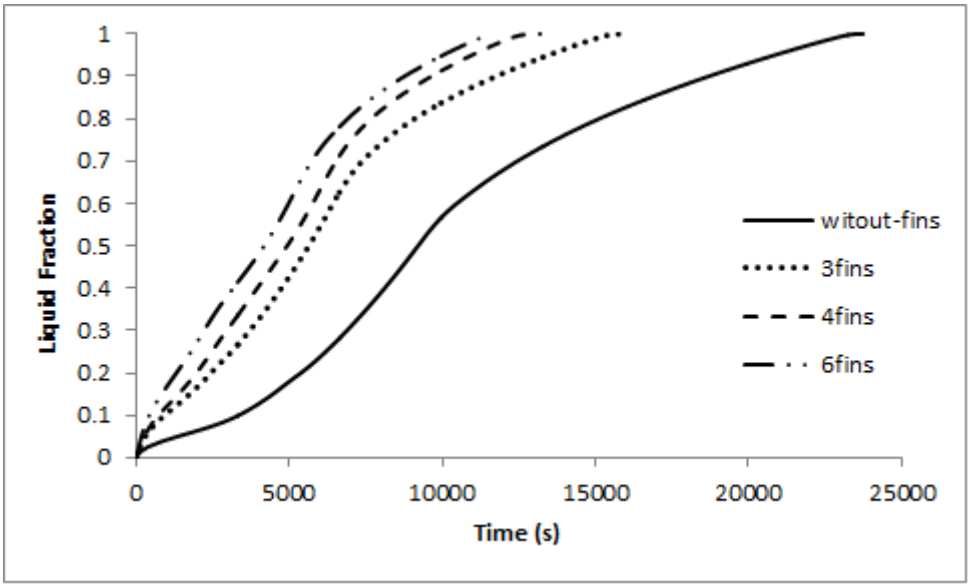

Figure 6.72: The effect of fins on the dynamics of the melting.

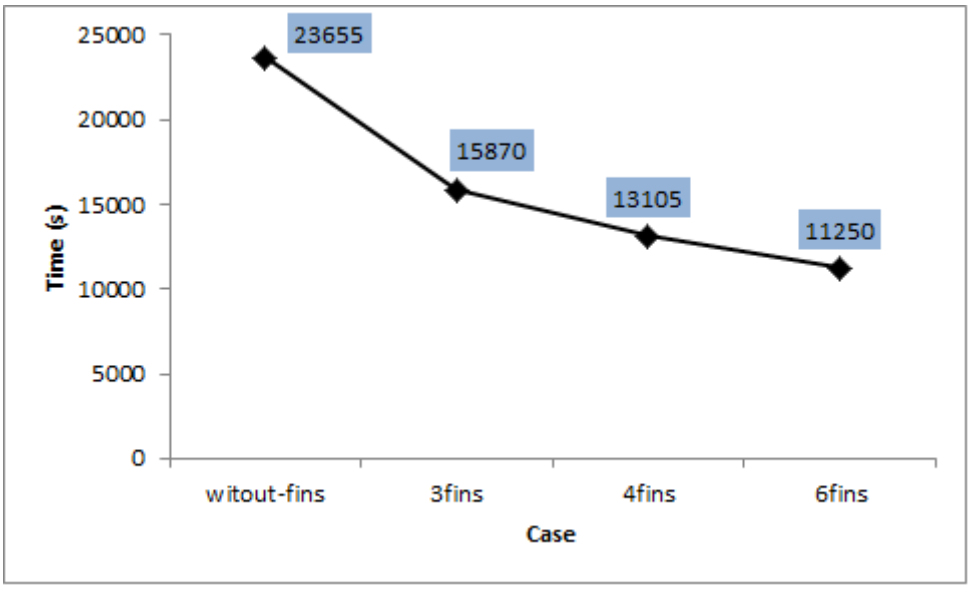

Figure 6.73: The effect of fins on the PCM melting time.

Figure 6.74 shows the rate of heat storage as a function of time for the system with various fins configurations. It can be seen that the maximum amount of energy that can be stored is insignificantly decreased with rise in the number of fins and this is because of a small

reduction in the volume occupied by the PCM. However, the system with finned pipes exhibits better melting performance and higher energy storage capacity for a given storage size.

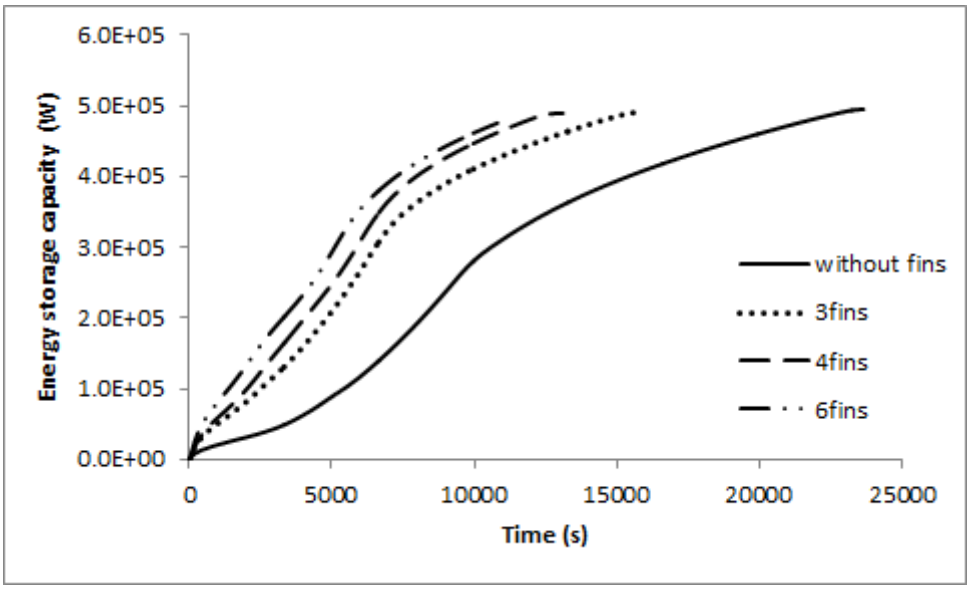

Figure 6.74: The energy storage capacity as a function of time.

The heat transfer coefficients were calculated for the upper, side and bottom regions of the computational domain for the case when the inlet temperature of the HTF was set to 353 K and the HTF mass flow rate was 0.0037 kg/s. Figure 6.75-6.77 show the variation of the coefficients heat transfer between PCM and HTF smooth and finned pipes a function of time. It can be observed in the figures that the greater values of heat transfer coefficient are at the upper regions and these are continuously rising which is a result of natural convection in the liquid zone. The heat transfer coefficients are greater for the systems with fins. The effect of application of fins on the value of heat transfer coefficient is much complex in the side and bottom regions and this depends on the phase in the melting process. It can be seen in Figure 6.76 that in the side region the positive effect on the value of heat transfer coefficient from

increasing number of fins becomes more profound with the advancement in the formation of the liquid fraction. In the bottom region increasing the number of fins does not result in the rise of the heat transfer coefficient when the PCM is melted. However, the overall amount of heat transferred to the PCM is increased due to fins providing larger heat transfer areas.

The average heat transfer coefficient at the upper, side, and bottom regions in the case of the pipe without fins is 359.78, 107.5, and 66.7 W/ m^2K , respectively. For the case of the pipe with 3 fins the average heat transfer coefficient at the upper, side and bottom regions is 638.8, 124.7, and 82 W/ m^2K , respectively. The average heat transfer coefficient in the upper, side and bottom regions is increased by 77.55 %, 16%, and 22.45%, when using the pipe with 3 longitudinal fins. The average heat transfer coefficient in cases of the pipe with 4 and 6 fins is increased by 77.78% and 102%, respectively, in the upper region and by 9.45% and 59.4% in the side region. The average heat transfer coefficient is reduced by 7.5 % and 9.2% in cases of pipes with 4 fins and 6 fins, respectively, in the bottom region.

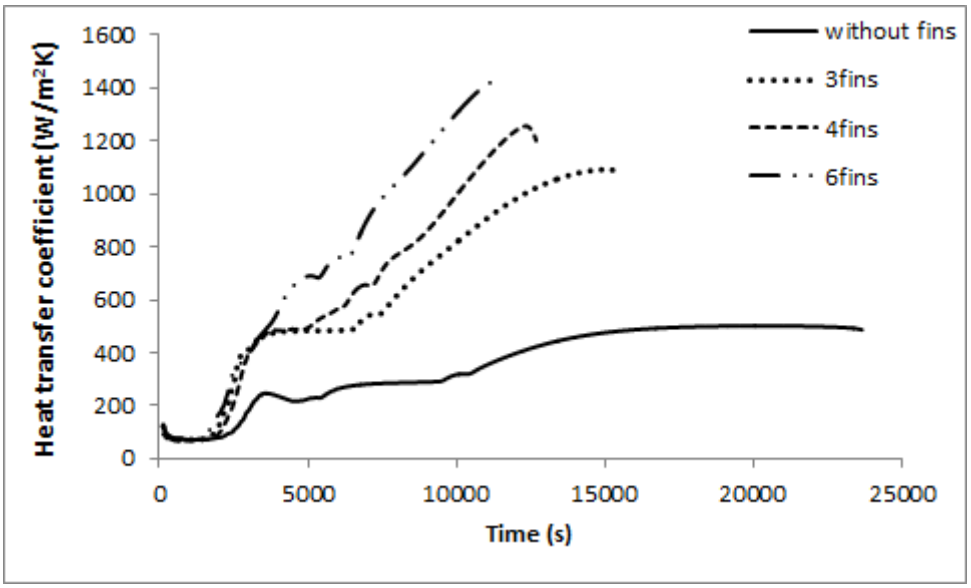

Figure 6.75: Variations in the heat transfer coefficient in the upper region.

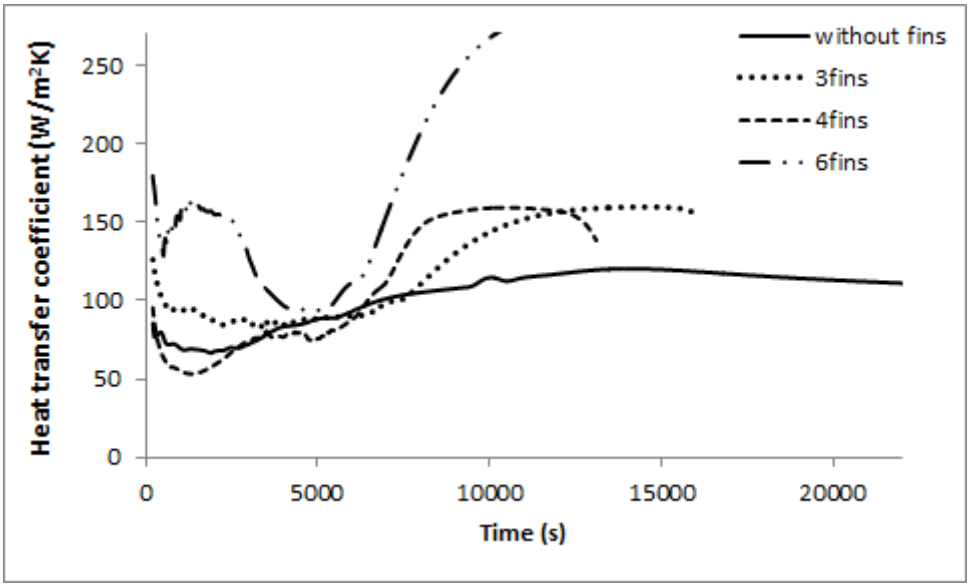

Figure 6.76: Variations in the heat transfer coefficient in the side region.

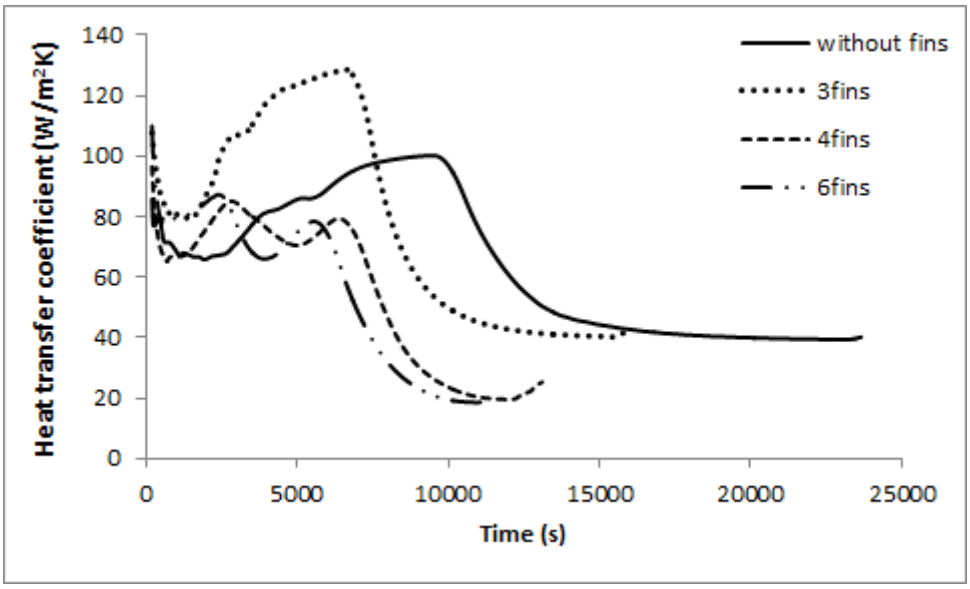

Figure 6.77: Variations in the heat transfer coefficient in the bottom region.

Variations of Nusselt number for the cases of pipe with 3 and 4 fins as a function of Stefan, Raleigh and Fourier numbers are shown in Figures 6.78-6.89 for the upper, side, and bottom regions, respectively. As expected, the highest Nusselt numbers are in the upper regions and the values are higher for the 4 fin pipe. In general, the Nusselt numbers for the finned pipes

are greater than that for the pipe without fins. For the HTF inlet temperature of 353K and 0.0037 Kg/s mass flow rate, the Nusselt number in the upper, side and bottom regions for the pipe without fins was 27.052, 10.458, and 6.37, respectively. For the pipe with 3 fins the Nusselt number in the upper, side and bottom regions are 64.848, 12.569, and 7.47, respectively. This is 139.7%, 20.18% and 17.27% increase, respectively. The Nusselt numbers in the upper, side and bottom regions is increased by 150%, 16.63%, and 1.8% respectively, for the case in which the pipe with 4 longitudinal fins is used. Overall, the dependence of the Nusselt number from Stefan, Raleigh and Fourier numbers have the same trend as results in the case of the smooth pipe, which were presented in the previous section.

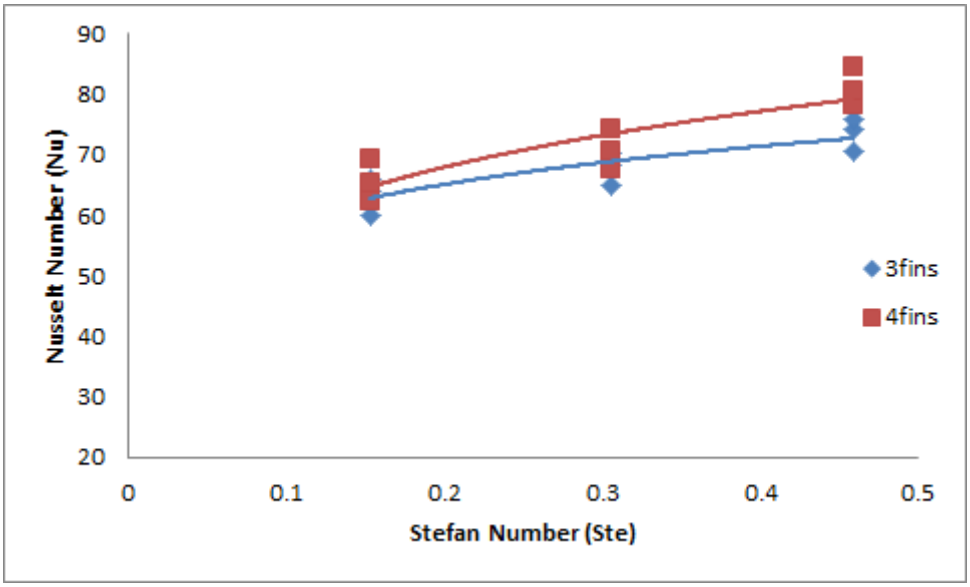

Figure 6.78: Variation in the Nusselt number as a function of Stefan number in the upper region.

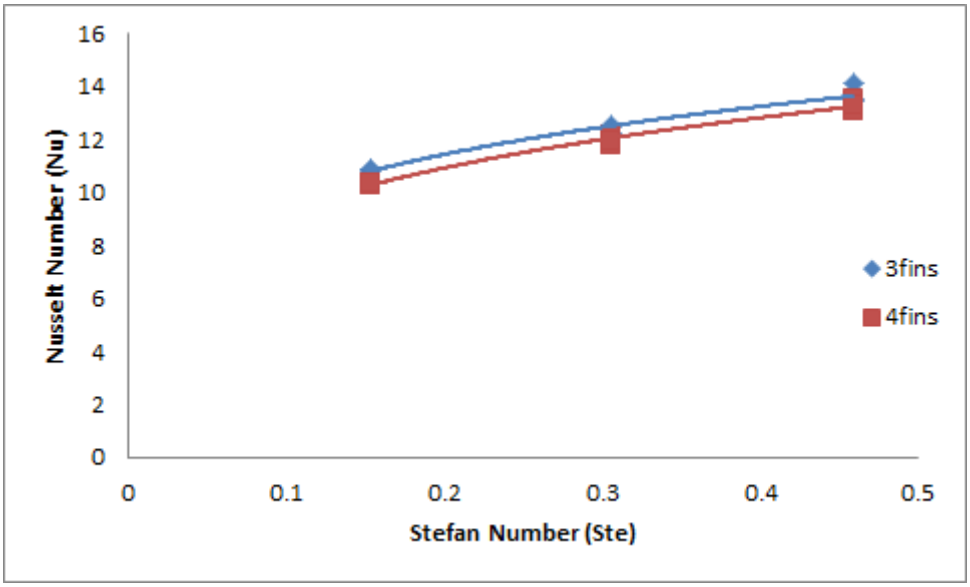

Figure 6.79: Variation in the Nusselt number as a function of Stefan number in the side region.

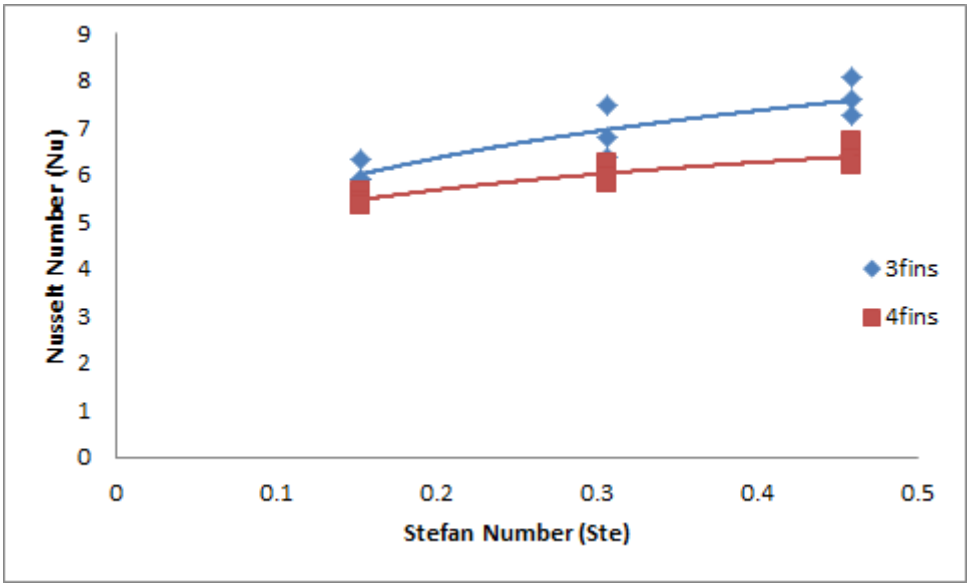

Figure 6.80: Variation in the Nusselt number as a function of Stefan number in the bottom region.

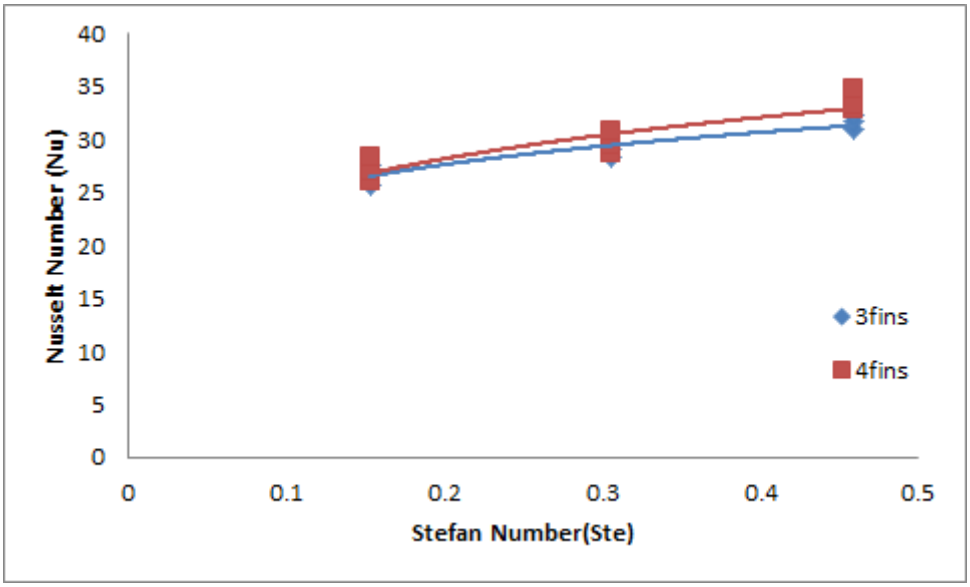

Figure 6.81: The variation of the average Nusselt number as a function of Stefan number.

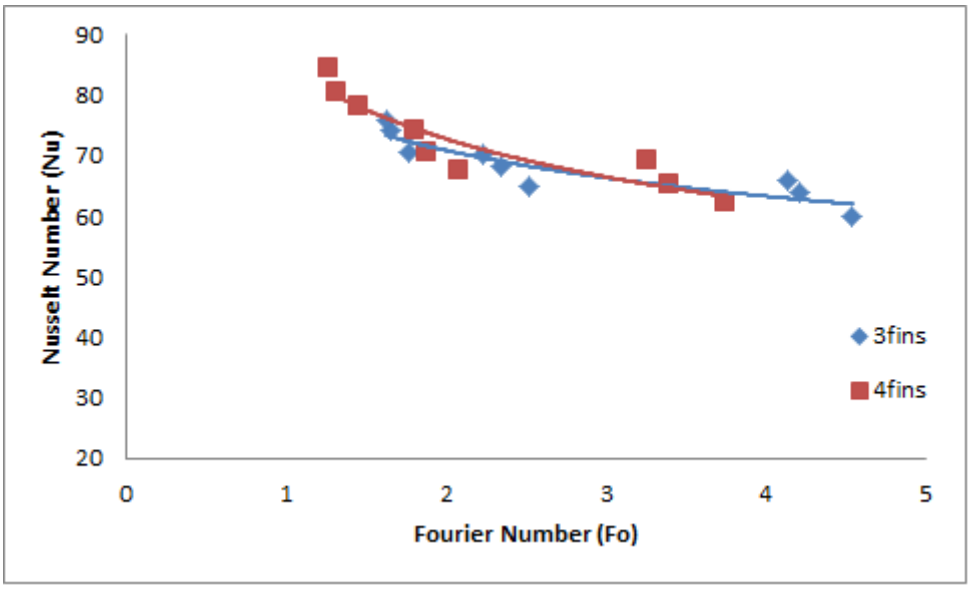

Figure 6.82: Variation in the Nusselt number as a function of Fourier number for the upper region.

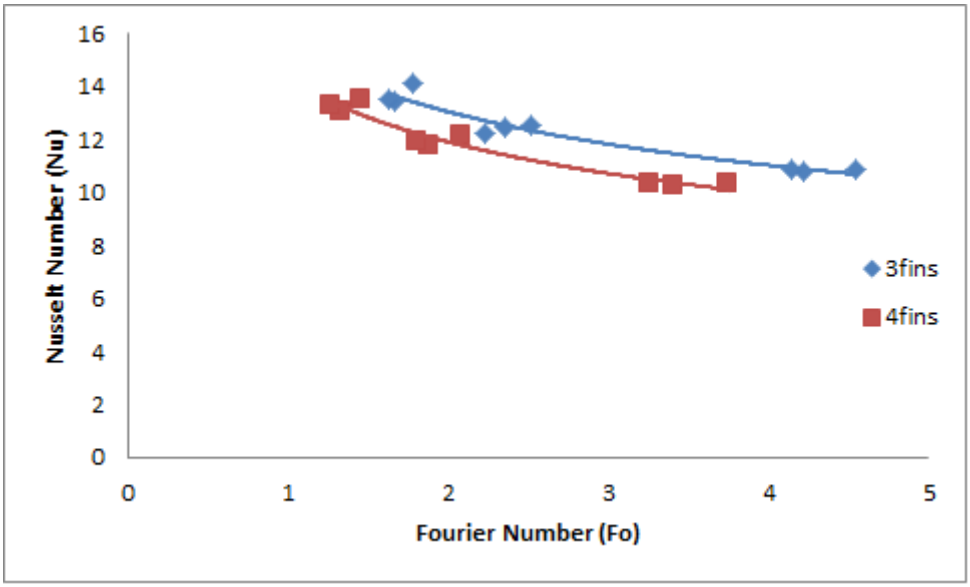

Figure 6.83: Variation in the Nusselt number as a function of Fourier number for the side region.

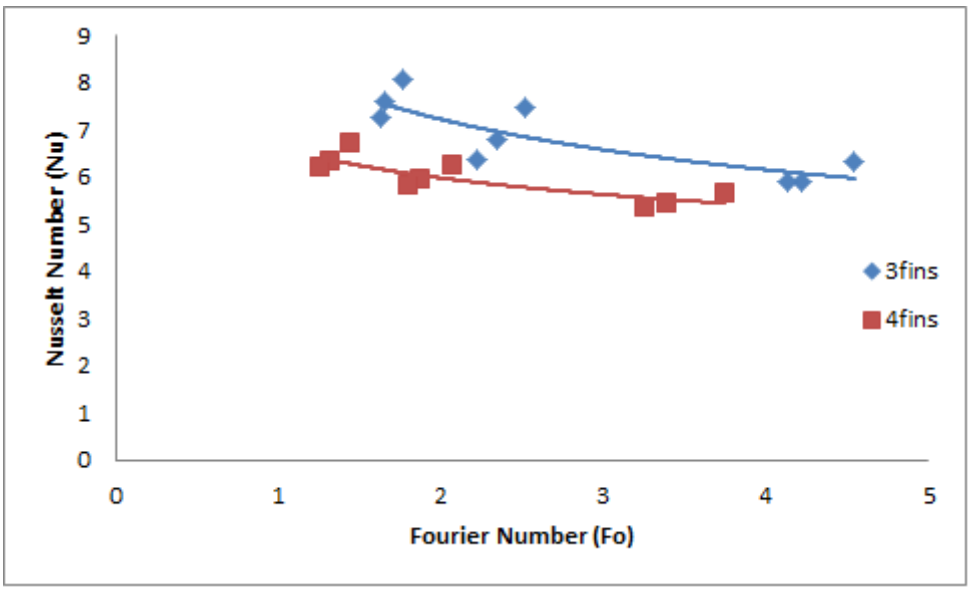

Figure 6.84: Variation in the Nusselt number as a function of Fourier number for the bottom region.

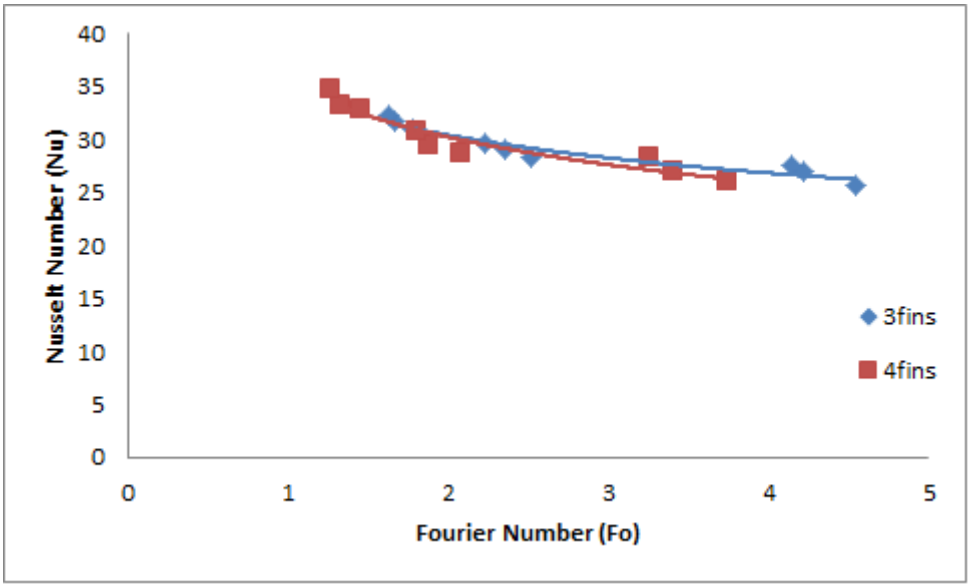

Figure 6.85: The variation in average Nusselt number as a function of Fourier number.

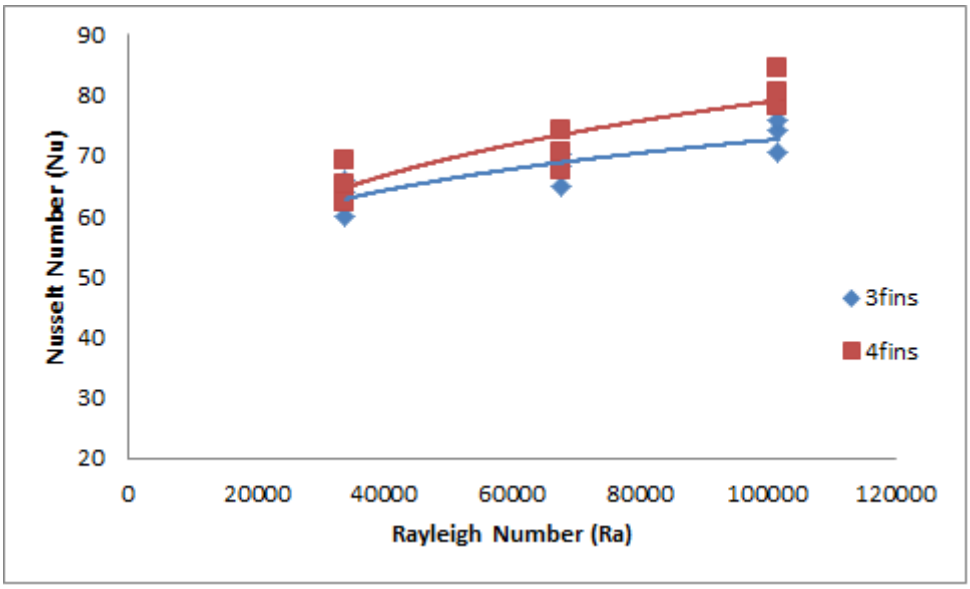

Figure 6.86: Variation in the Nusselt number as a function of Rayleigh number in the upper region.

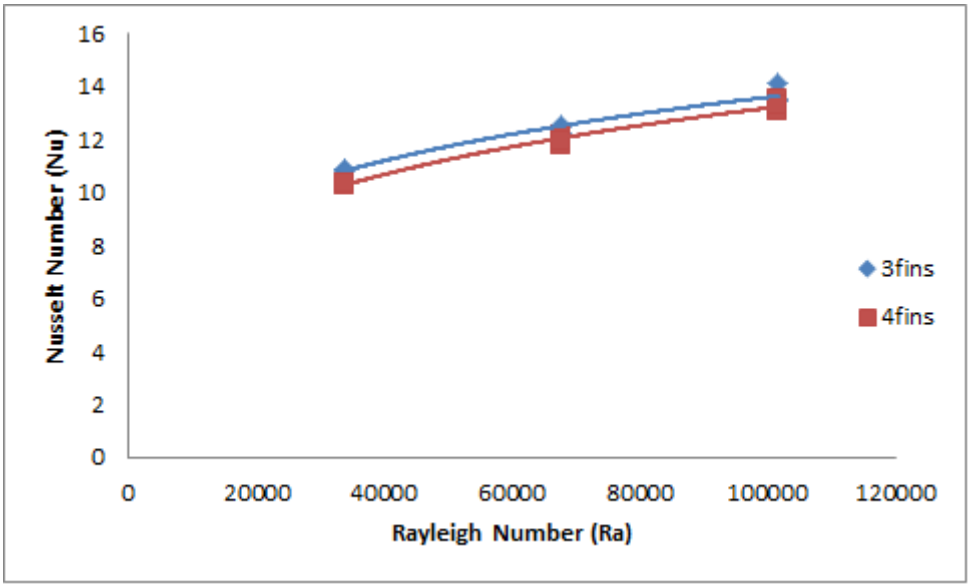

Figure 6.87: Variation in the Nusselt number as a function of Rayleigh number in the side region.

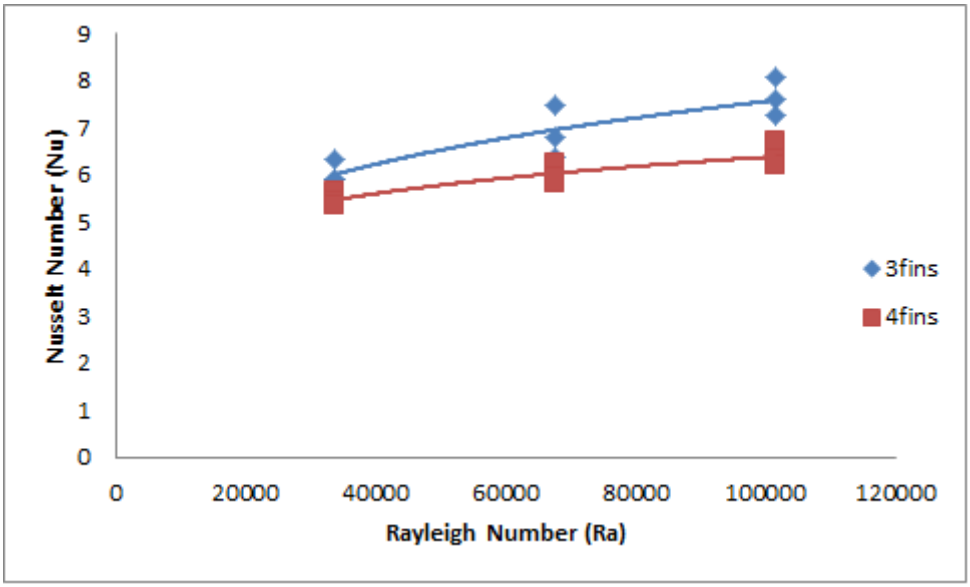

Figure 6.88: Variation in the Nusselt number as a function of Rayleigh number in the bottom region.

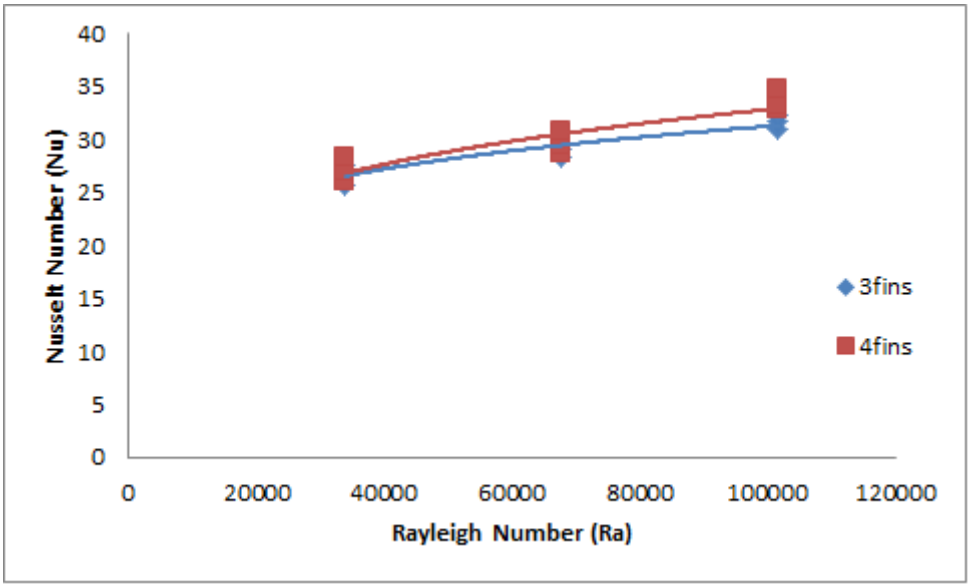

Figure 6.89: The variation in the average Nusselt number as a function of Rayleigh number.

The above data was used to derive dimensionless correlations to calculate the Nusselt number as a function of Stefan, Raleigh and Fourier numbers. The derived correlations are as follows:

The Nusselt number correlation for the upper region in case of the pipe with 3 fins (correlation factor $R^2 = 0.6853$) -

$$Nu = 46.5316(Ste)^{0.0443}(Fo)^{-0.0543}(Ra)^{0.0443} \tag{6.9}$$

The Nusselt number correlation for the upper region in case of the pipe with 4 fins (correlation factor $R^2 = 0.732$) -

$$Nu = 42.049(Ste)^{0.0611}(Fo)^{-0.074}(Ra)^{0.061} \tag{6.10}$$

The Nusselt number correlation for the side region in case of the pipe with 3 fins (correlation factor $R^2 = 0.959$) -

$$Nu = 6.6629\left(Ste\right)^{0.0706}\left(Fo\right)^{-0.0807}\left(Ra\right)^{0.0705} \tag{6.11}$$

The Nusselt number correlation for the side region in case of the pipe with 4 fins (correlation factor $R^2 = 0.9698$) -

$$Nu = 5.9524\left(Ste\right)^{0.0768}\left(Fo\right)^{-0.0863}\left(Ra\right)^{0.0767} \tag{6.12}$$

The Nusselt number correlation for the bottom region in case of the pipe with 3 fins (correlation factor $R^2 = 0.7477$) -

$$Nu = 3.6881\left(Ste\right)^{0.0706}\left(Fo\right)^{-0.0773}\left(Ra\right)^{0.0706} \tag{6.13}$$

The Nusselt number correlation for the bottom region in case of the pipe with 4 fins (correlation factor $R^2 = 0.7007$) -

$$Nu = 3.9004\left(Ste\right)^{0.0471}\left(Fo\right)^{-0.05}\left(Ra\right)^{0.0471} \tag{6.14}$$

The Nusselt number correlation in the system with 3 fins (correlation factor $R^2 = 0.9046$) -

$$Nu = 18.8861\left(Ste\right)^{0.0501}\left(Fo\right)^{-0.06}\left(Ra\right)^{0.05} \tag{6.15}$$

The Nusselt number correlation in the system with 4 fins (correlation factor $R^2 = 0.8455$) -

$$Nu = 17.2736\left(Ste\right)^{0.0622}\left(Fo\right)^{-0.074}\left(Ra\right)^{0.06} \tag{6.16}$$

6.7 Heat transfer intensification using porous metallic matrix

This section presents results of study of using porous matrix to enhance the heat transfer in PCM thermal storage systems. The numerical CFD results were obtained on the melting process in the rectangular storage unit with a smooth pipe with and without porous matrix. The geometry of the storage unit is the same as shown in Figure 6.1. Aluminium porous

matrix with porosities in the range between 75 and 95% were considered in this study. In the modelling process the inlet temperature of the HTF was set to 353 K and the mass flow rate was 0.0037 kg/s. Figure 6.90 shows results obtained on the temperature distribution and melting process in the computational domain for the instance when 1000 seconds elapsed from the beginning of the charging process. It can be observed that the melting process is considerable accelerated in both axial and radial directions by application of less porous aluminium matrices which is due to enhancement of the conduction heat transfer mode. The lower porosity value increases the mass of the metal per unit volume of the system which results in enhancement of heat conduction in the system. However, it should be highlighted that using matrices with low porosities will reduce the volume filled with a PCM which results in the reduction of heat storage capacity.

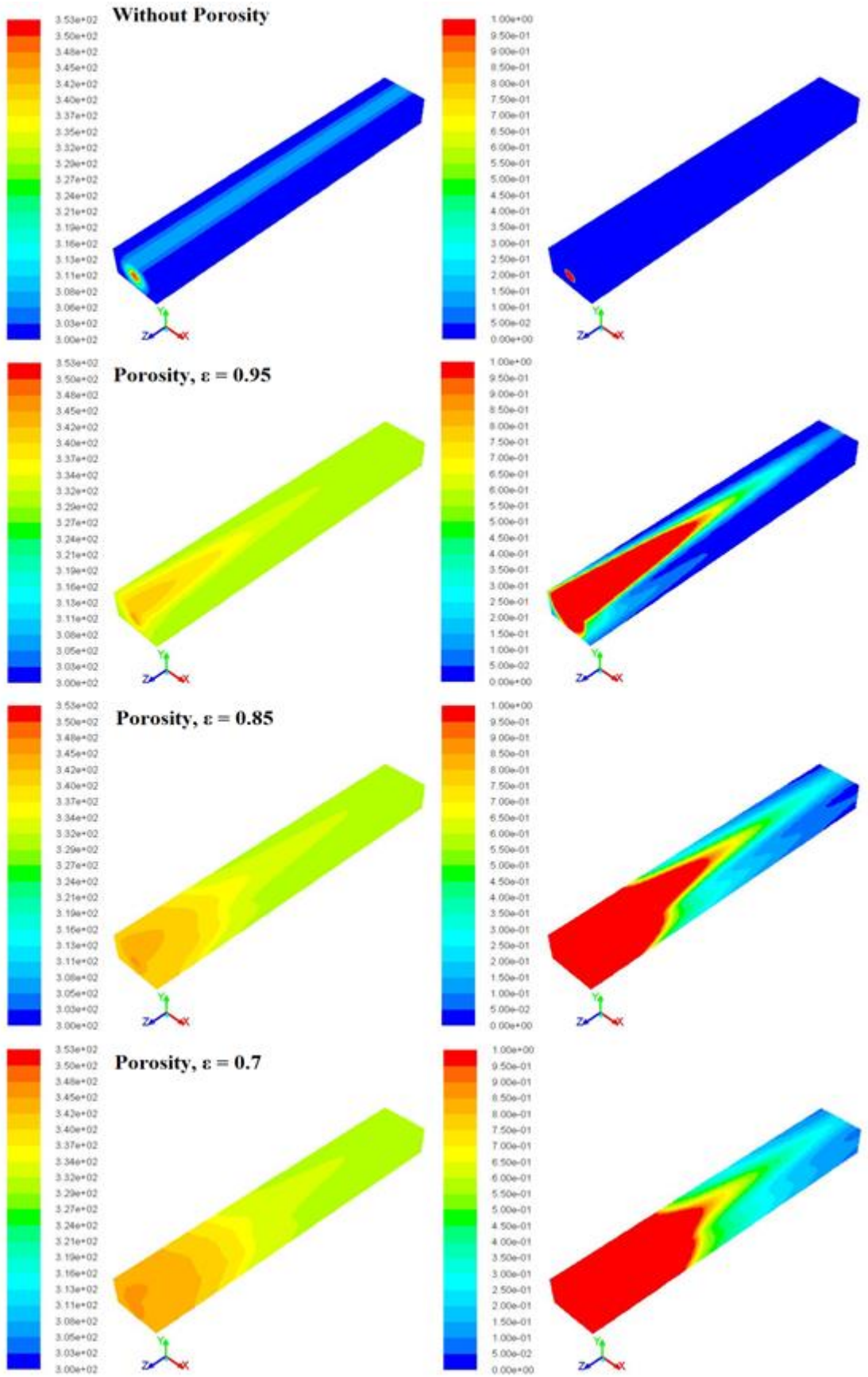

Figure 6.90: Temperature distribution and melting process in the computational domain. Elapsed time = 1000sec.

Figures 6.91-6.93 present results on the temperature variation in the upper, side and bottom regions in the first measurement plane for the cases of the system without matrix and in which the system has a matrix of 95% porosity. It can be seen in these figures that the period for reaching the melting temperature and for melting process is substantially shortened, especially in the side and bottom regions of the system. Figure 6.91 demonstrates that the melting temperature at location u4 (the monitoring point furthest from the pipe walls in the upper region) is reached in about 4300 s for the pure PCM. In case of 95% porosity matrix this time is only 340 s. This acceleration effect is more profound at monitoring points e4 (the monitoring point furthest from the pipe walls in the side region) and b4 (the monitoring point furthest from the pipe walls in the bottom region), see Figures 6.92 and 6.93. Additionally, the porous matrix provides the uniform distribution of the temperature in the measurement plane. Figure 6.94 shows that values of temperatures in all these three points remain close through the whole period of heating.

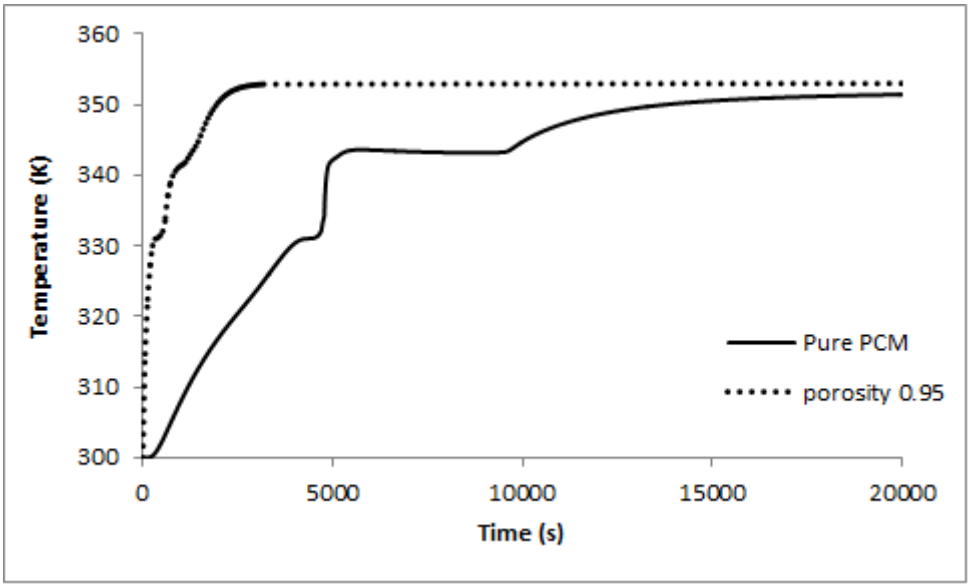

Figure 6.91: The effect of the 95% porosity matrix on the temperature variation at point u4 (the monitoring point furthest from the pipe walls in the upper region).

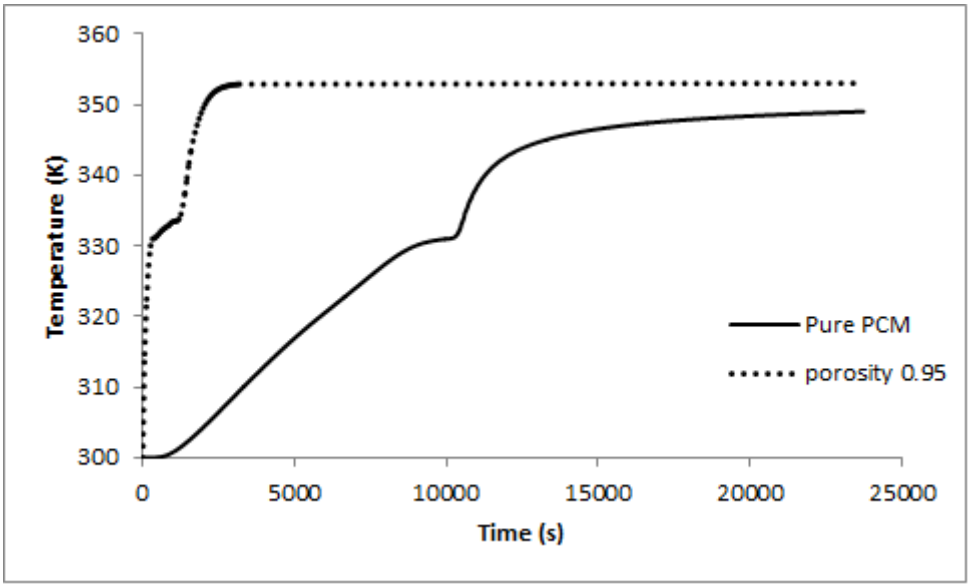

Figure 6.92: The effect of the 95% porosity matrix on the temperature variation at point e4 (the monitoring point furthest from the pipe walls in the side region).

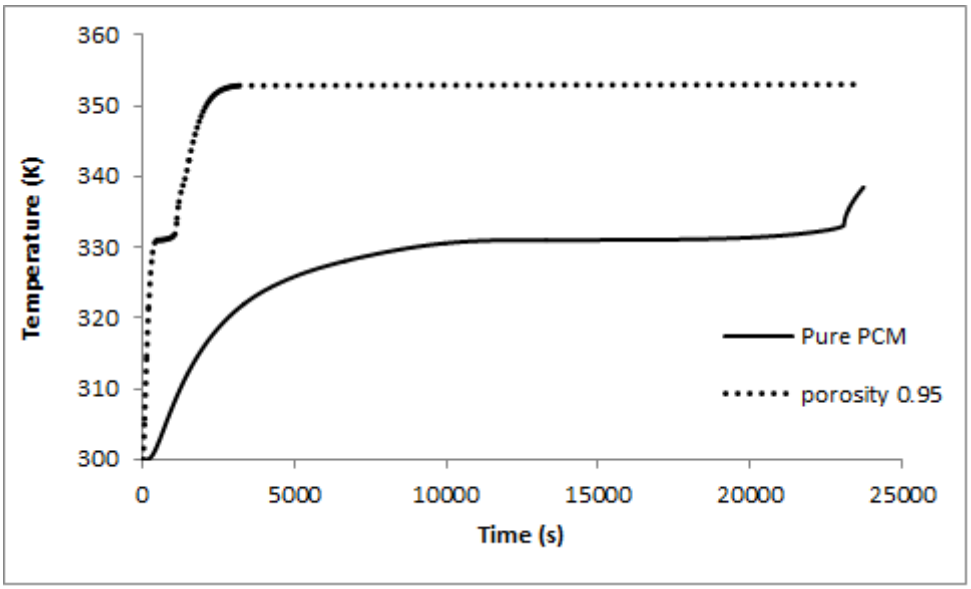

Figure 6.93: The effect of the 95% porosity matrix on the temperature variation at point b4 (the monitoring point furthest from the pipe walls in the bottom region).

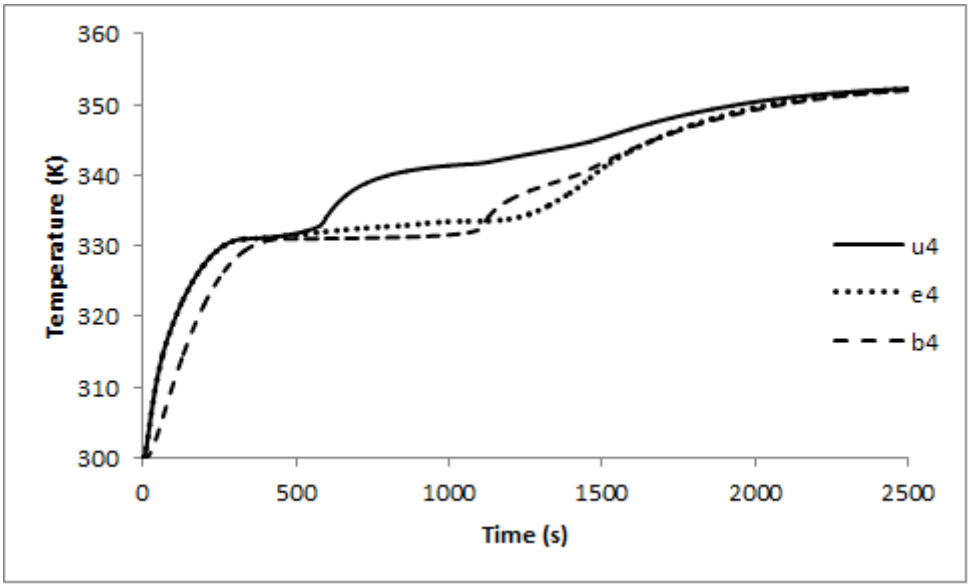

Figure 6.94: Variation of the temperatures in the PCM with 95% porosity matrix.

The effect of the metal matrix porosity on the temperature at u4 (the monitoring point furthest from the pipe walls in the upper region) is presented in Figure 6.95. It can be seen that the temperature is to some extent higher when the matrix with lower porosity is used.

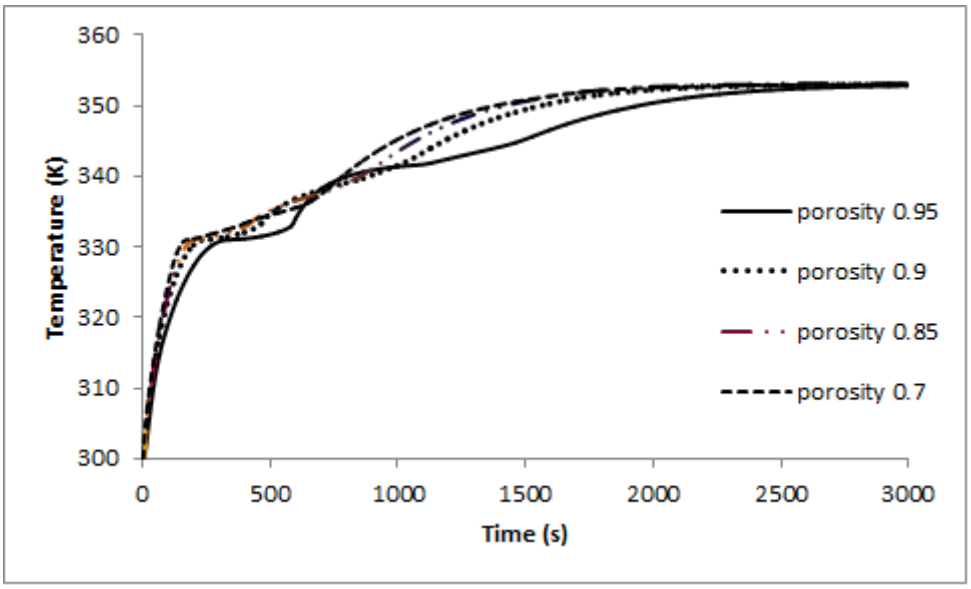

Figure 6.95: The effect of the matrix porosity on the temperature variation at point u4 (the monitoring point furthest from the pipe walls in the bottom region).

Figure 6.96 presents diagrams with velocity field in the first measurement plane of the computational domain for the instance when 1000 sec elapsed from the beginning of the charging process. It can be seen that the matrix with low porosity actually suppresses the development of the natural convection in the PCM due to increasing hydraulic resistance to the flow and that the heat is transferred mainly through the conduction mode.

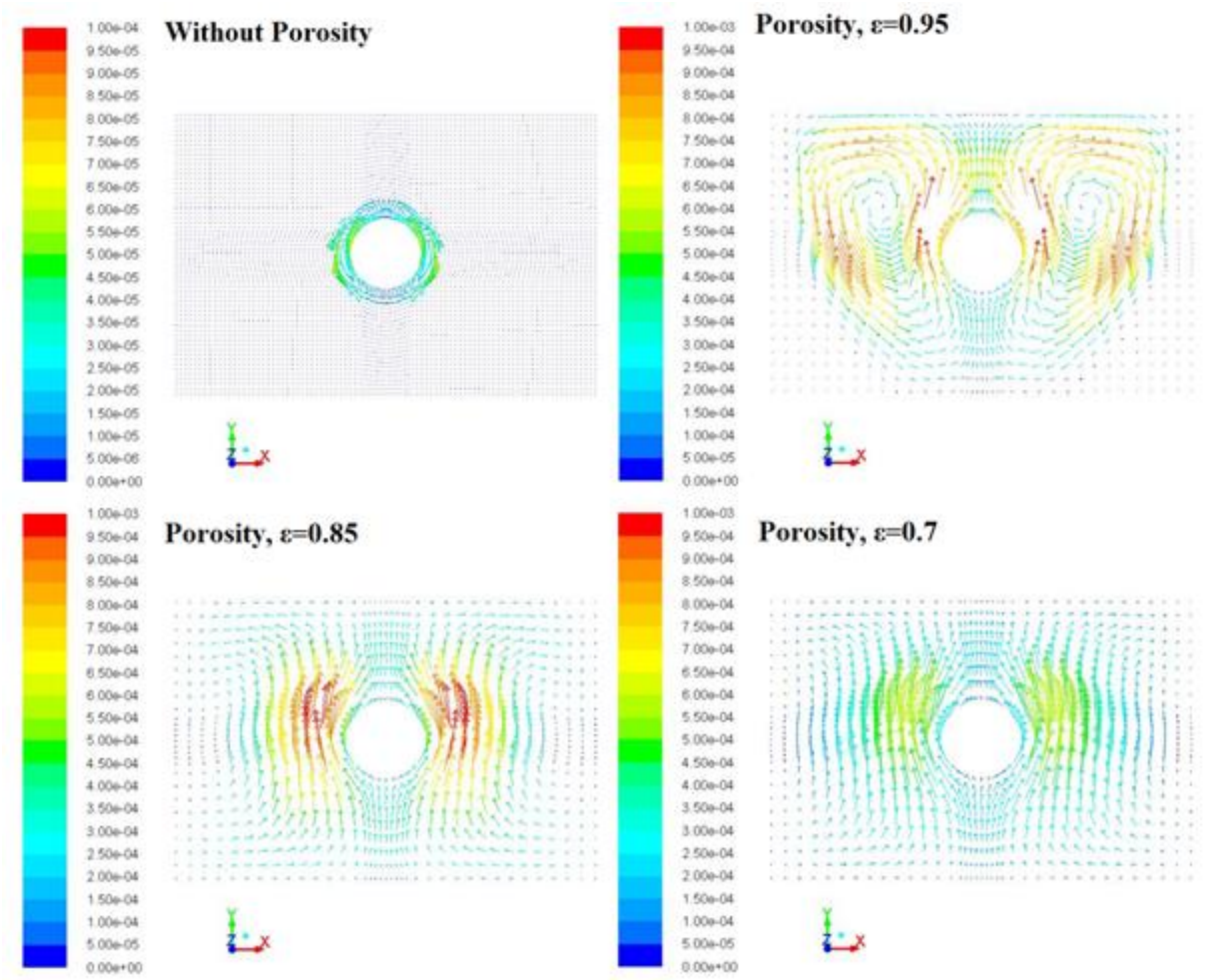

Figure 6.96: The velocity fields in the first measurement plane of the domain.

Elapsed time = 1000 seconds.

The effect of porosity on the evolution of the liquid fraction of the PCM and on the melting time are shown in Figures 6.97 - 6.99, respectively and this information re-iterates the

conclusion that the porous metallic matrix substantially accelerates process of PCM heating and reduces the melting time by factor of 10 depending on the porosity value.

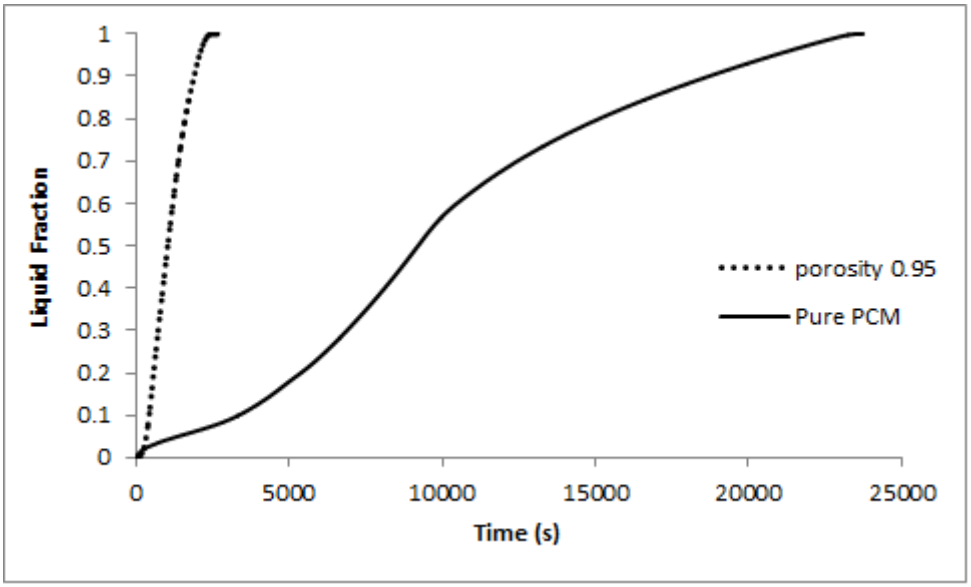

Figure 6.97: The effect of the 95% porosity matrix on the formation of the PCM liquid fraction.

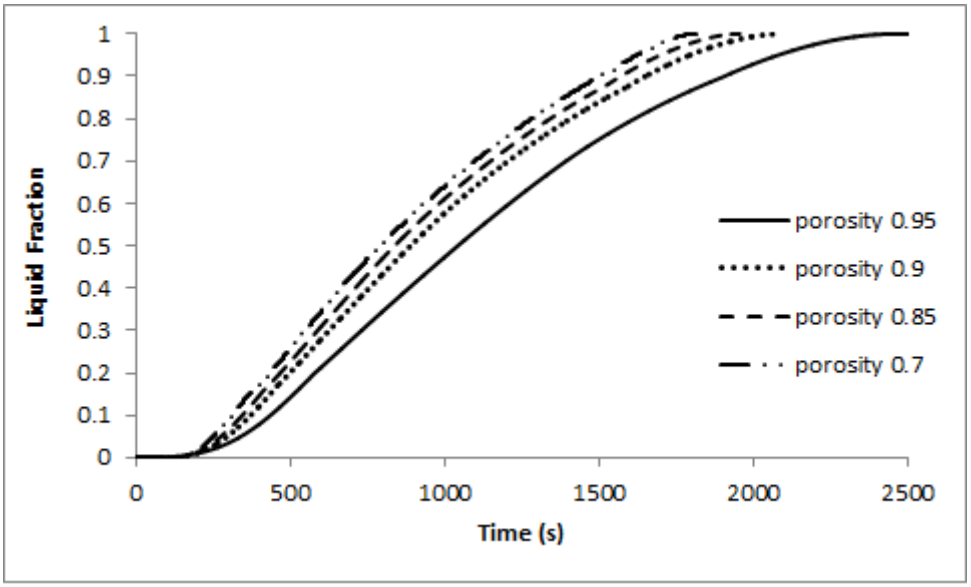

Figure 6.98: The effect of the matrix porosity on the dynamics of the melting.

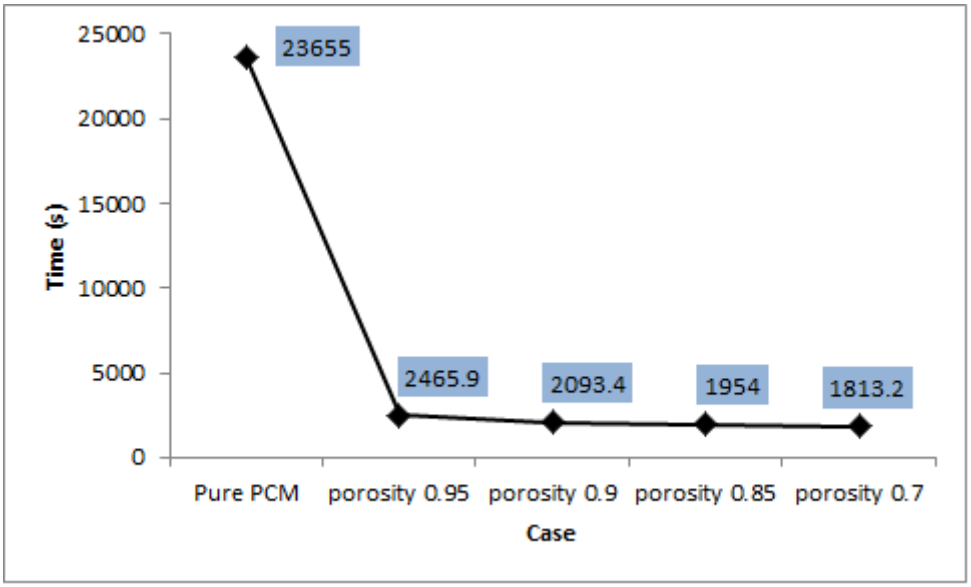

Figure 6.99: The effect of the matrix porosity on the PCM melting time.

6.8 Summary

In this chapter, CFD numerical investigations were carried out on the melting process in the PCM thermal storage unit, namely the rectangular container. Three design groups were considered, namely with a smooth central horizontal pipe; with a central horizontal pipe with longitudinal fins; and with a smooth central horizontal pipe and metallic porous matrix.

The effects of the inlet temperature and mass flow rate of the HTF on the charging (melting) process were investigated for the PCM thermal storage unit with a smooth central horizontal pipe and the PCM thermal storage unit with a central horizontal pipe with 3 and 4 longitudinal fins. For these cases dimensionless correlations for calculation of Nusselt number as function of Stefan, Fourier and Rayleigh numbers were derived separately for upper, side and bottom regions of the storage system and also averaged for whole system. The HTF inlet temperatures considered were 10, 20, and 30℃ above the melting temperature of the PCM, while the HTF mass flow rates used were 0.0037, 0.037, and 0.37 Kg/s.

Both considered methods of intensification of heat transfer in the PCM thermal storage systems, namely using longitudinal fins and metallic porous matrix accelerate melting process in the system with the metallic porous matrix being the most efficient in the improvement of the performance of the PCM storage system.

Chapter 7 Conclusions and Recommendations for Future Work

7.1 Conclusions

1. The literature review carried out on the state of art in PCM thermal storage systems shown relevance of the development accurate and feasible CFD models for numerical simulations of heat transfer processes taking place during charging and discharging processes. Review also shown importance of derivation of heat transfer correlations which accurately define values of coefficient of heat transfer in the system for a wide range of design configurations and exploitation conditions. Such correlations are necessary for designing the high performance PCM thermal storage systems.

2. 3D CFD model of the shell-and-tube storage unit with the PCM on the shell side, and the HTF flowing inside the tube was developed. The PCM used in the system was *n-Octadecane* and water was used as the heat transfer fluid. Transient simulations were run using the *k-epsilon* turbulence with the time step set to 0.1s. The solidification/melting model was enabled to describe the phase change phenomena in *n-Octadecane*. The first-order upwind spatial discretization and the pressure solver with the PRESTO algorithm for pressure-velocity coupling were selected to obtain converged solution. Convergence criteria were established by setting the absolute residual values to 10^{-6} for energy and 10^{-3} for all other variables. The obtained results were compared to experimental results by Lacroix [9]. Calibration of results demonstrated that the developed CFD model provides an accurate prediction of the behaviour of the thermal storage system. 3D CFD simulations were performed for a range of the HTF inlet temperature values and its mass flow rate. The

obtained numerical data was used to derive Nusselt number correlations as a function of Stefan, Rayleigh and Fourier numbers in order to take into account the effect of all design and operational conditions. The Nusselt number for the system with the pure PCM was found to be ($R^2 = 0.8524$)

$$Nu = 2.9883(Ste)^{0.0758}(Fo)^{-0.095}(Ra)^{0.0759}$$

3. The performance of the laboratory thermal heat storage system filled with paraffin was experimentally investigated. The thermal storage unit was coupled with the evacuated tube solar collectors and water was used as the HTF. The system was tested at variable and constant heat source conditions. Temperatures inside the PCM were recorded in 16 points to determine temperature distribution and dynamics of the melting process. The system was numerically simulated using its 3D CFD model for constant heat source conditions. Numerical and experimental results were compared which demonstrated that the proposed CFD model provides accurate results with maximum error of 12% and can be used with confidence for simulations of specific PCM thermal storage systems with intensification of heat transfer which is the subject of R & D activities at Northumbria University.

4. The developed method of numerical simulations, which was tested against the case study by Lacroix [9] and experimentally using test rig at Northumbria University, was deployed to numerically simulate the melting process in the rectangular thermal storage system with a horizontal central pipe. Paraffin was used as a PCM and water was used as the heat transfer fluid. An array of monitoring points was set in the 3D computational domain to record data on temperature variations in the PCM during the melting process. 3D CFD simulations were performed for a range of the HTF inlet temperature values and its mass flow rate. The obtained numerical data was used to derive Nusselt number correlations as a function of Stefan, Rayleigh and Fourier numbers in order to take into account the effect of all design

and operational conditions. Correlations were obtained separately for three characteristic regions (the upper, side and bottom regions of the storage system) and for the whole system. These are as follows:

The Nusselt number correlation for the upper regions of the PCM storage system (coefficient of correlation $R^2 = 0.9044$) -

$$Nu = 18.74(Ste)^{0.04617}(Fo)^{-0.054}(Ra)^{0.0461}$$

The Nusselt number correlation for the side regions of the PCM storage system (coefficient of correlation $R^2 = 0.9877$) -

$$Nu = 6.0642(Ste)^{0.0658}(Fo)^{-0.0753}(Ra)^{0.0657}$$

The Nusselt number correlation for the bottom region of the PCM storage system (coefficient of correlation $R^2 = 0.8681$) -

$$Nu = 4.4877(Ste)^{0.0393}(Fo)^{-0.044}(Ra)^{0.0393}$$

The average Nusselt number correlation in the system (coefficient of correlation $R^2 = 0.9695$) -

$$Nu = 9.7299(Ste)^{0.05}(Fo)^{-0.058}(Ra)^{0.0501}$$

5. Heat transfer intensification with the use of metal oxides nano-particles was investigated using the developed 3D CFD model of the shell-and-tube storage unit with *n-Octadecane* on the shell side, and water flowing inside the tube was developed. Special User Defined Functions were created for ANSYS FLUENT software to take into account temperature dependence of thermo-physical properties of nano-particles made of Al_2O_3, ZnO and CuO were written in C++ programming language. User Defined functions also were written to

calculate thermo-physical properties of *n-Octadecane* with various volumetric concentration of nano-particles. Two volumetric concentrations of nano-particles were considered, namely 3 and 6%. It was numerically obtained that the total melting time was reduced as the nano-particles volumetric concentration was increased. However, there was a reduction in the fusion's latent heat which in its turn reduced the thermal energy accumulated per mass unit of the nano PCM. For the 3% and 6% volumetric concentration of CuO the time of melting was reduced by 19.4% and 31.7%. A similar conclusion could be drawn for the PCM with Al_2O_3 and ZnO nano-particles. The total melting time was reduced by 18.5% and 28.6% when the volumetric concentration of Al_2O_3 was 3% and a 6%. The reduction in the time of melting was 17.2% and 27.2% when the volumetric concentration of ZnO was 3% and a 6%, respectively. Results indicated the higher heat transfer rates in PCMs with nano-particles were due to the PCM's increased thermal conductivity. 3D CFD simulations were performed for a range of the HTF inlet temperature values and its mass flow rate. The obtained numerical data was used to derive Nusselt number correlations as a function of Stefan, Rayleigh and Fourier numbers for 6% volumetric concentration of CuO nano-particles is ($R^2 = 0.9407$):

$$Nu = 2.7597\left(Ste\right)^{0.0968}\left(Fo\right)^{-0.121}\left(Ra\right)^{0.0873}$$

6. Heat transfer intensification was investigated using 3D CFD modelling for the rectangularly shaped thermal storage system with horizontal heating pipe by using 3, 4 and 6 longitudinal finned pipes. 3D CFD simulations were performed for a range of the HTF inlet temperature values and its mass flow rate. Results of numerical investigations demonstrate that overall the melting time is reduced by approximately 32.2% for the case of pipe with 3 fins compared to the case of pipe without fins. The melting time is reduced by 44.6% and 52.4% for the cases of pipes with 4 and 6 fins, respectively.

The obtained numerical data was used to derive Nusselt number correlations as a function of Stefan, Rayleigh and Fourier numbers in order to take into account the effect of all design and operational conditions. Correlations were derived for 3 and 4 fin configurations. Correlations were obtained separately for three characteristic regions (the upper, side and bottom regions of the storage system) and for the whole system. These are as follows:

The Nusselt number correlation for the upper region in case of the pipe with 3 fins (correlation factor $R^2 = 0.6853$) -

$$Nu = 46.5316\left(Ste\right)^{0.0443}\left(Fo\right)^{-0.0543}\left(Ra\right)^{0.0443}$$

The Nusselt number correlation for the upper region in case of the pipe with 4 fins (correlation factor $R^2 = 0.732$) -

$$Nu = 42.049\left(Ste\right)^{0.0611}\left(Fo\right)^{-0.074}\left(Ra\right)^{0.061}$$

The Nusselt number correlation for the side region in case of the pipe with 3 fins (correlation factor $R^2 = 0.959$) -

$$Nu = 6.6629\left(Ste\right)^{0.0706}\left(Fo\right)^{-0.0807}\left(Ra\right)^{0.0705}$$

The Nusselt number correlation for the side region in case of the pipe with 4 fins (correlation factor $R^2 = 0.9698$) -

$$Nu = 5.9524\left(Ste\right)^{0.0768}\left(Fo\right)^{-0.0863}\left(Ra\right)^{0.0767}$$

The Nusselt number correlation for the bottom region in case of the pipe with 3 fins (correlation factor $R^2 = 0.7477$) -

$$Nu = 3.6881\left(Ste\right)^{0.0706}\left(Fo\right)^{-0.0773}\left(Ra\right)^{0.0706}$$

The Nusselt number correlation for the bottom region in case of the pipe with 4 fins (correlation factor $R^2 = 0.7007$) -

$$Nu = 3.9004\left(Ste\right)^{0.0471}\left(Fo\right)^{-0.05}\left(Ra\right)^{0.0471}$$

The Nusselt number correlation in the system with 3 fins (correlation factor $R^2 = 0.9046$) -

$$Nu = 18.8861\left(Ste\right)^{0.0501}\left(Fo\right)^{-0.06}\left(Ra\right)^{0.05}$$

The Nusselt number correlation in the system with 4 fins (correlation factor $R^2 = 0.8455$) -

$$Nu = 17.2736\left(Ste\right)^{0.0622}\left(Fo\right)^{-0.074}\left(Ra\right)^{0.06}$$

7.2 Recommendations for Future Work

The following are recommendations for further research:

1. The application of metal based nano-particles, namely Al_2O_3, ZnO and CuO in concentric thermal storage system with paraffin as a PCM was numerically simulated and dimensionless correlations were obtained for calculation of Nusselt number as a function of Stefan, Fourier and Rayleigh numbers for the system in which the pure PCM and 6% volumetric concentration of CuO nano-particles were used for intensification of heat transfer.

It is highly recommended that similar correlations were derived which takes into account the type of nano-particles and their volumetric concentration. Furthermore, the proposed correlations should be validated experimentally.

2. Nano-particles based on carbon (carbon fibres, nano-tubes etc) should be further tested for feasible intensification of heat transfer in the system.

3. Dimensionless correlations were obtained for calculation of Nusselt number as a function of Stefan, Fourier and Rayleigh numbers for the rectangularly shaped thermal storage system with horizontal heating smooth and longitudinally finned pipes. It is highly recommended that the proposed correlations should be validated experimentally. Additionally, it would be useful for designing process to have similar dimensionless correlations derived for other types of fins (circular, spiral and rectangular).

4. Intensification of heat transfer in the PCM thermal storage system was numerically investigated using aluminium based porous matrix. Further numerical and experimental investigations are required on this method, including the use of other materials. Additionally, dimensionless heat transfer correlations should be derived for application in the designing process.

5. Further work can also be extended to study the process of solidification of the PCM in the latent heat storage system. It is highly recommended to study the effects of the flow parameters and various methods of enhancement heat transfer in PCMs (using nano-particles, metallic fins and porous medium) on the discharging process in the thermal storage with PCMs.

References

[1] T. A. Boden, G. Marland, and R. J. Andres, "Global, Regional, and National Fossil Fuel CO2 Emissions," *Carbon Dioxide Information Analysis Center, Environmental Sciences Division , Oak Ridge National Laboratory,* 2011.

[2] IEA, *Technology Roadmaps Solar Photovoltaic Energy*, 2011.

[3] D. Y. Goswami, F. Kreith, and J. F. Kreider, *Principles of Solar Engineering, Second Edition*: Taylor & Francis, 2000.

[4] A. Abhat, "Low temperature latent heat thermal energy storage: Heat storage materials," *Solar Energy,* vol. 30, pp. 313-332, 1983.

[5] M. Kenisarin and K. Mahkamov, "Solar energy storage using phase change materials," *Renewable and Sustainable Energy Reviews,* vol. 11, pp. 1913-1965, 2007.

[6] M. M. Farid, A. M. Khudhair, S. A. K. Razack, and S. Al-Hallaj, "A review on phase change energy storage: materials and applications," *Energy Conversion and Management,* vol. 45, pp. 1597-1615, 2004.

[7] F. Agyenim, N. Hewitt, P. Eames, and M. Smyth, "A review of materials, heat transfer and phase change problem formulation for latent heat thermal energy storage systems (LHTESS)," *Renewable and Sustainable Energy Reviews,* vol. 14, pp. 615-628, 2010.

[8] B. Zalba, J. M. Marín, L. F. Cabeza, and H. Mehling, "Review on thermal energy storage with phase change: materials, heat transfer analysis and applications," *Applied Thermal Engineering,* vol. 23, pp. 251-283, 2003.

[9] M. Lacroix, "Numerical simulation of a shell-and-tube latent heat thermal energy storage unit," *Solar Energy,* vol. 50, pp. 357-367, 1993.

[10] A. F. Regin, S. C. Solanki, and J. S. Saini, "Heat transfer characteristics of thermal energy storage system using PCM capsules: A review," *Renewable and Sustainable Energy Reviews,* vol. 12, pp. 2438-2458, 2008.

[11] H. Singh, R. P. Saini, and J. S. Saini, "A review on packed bed solar energy storage systems," *Renewable and Sustainable Energy Reviews,* vol. 14, pp. 1059-1069, 2010.

[12] A. Felix Regin, S. C. Solanki, and J. S. Saini, "An analysis of a packed bed latent heat thermal energy storage system using PCM capsules: Numerical investigation," *Renewable Energy,* vol. 34, pp. 1765-1773, 2009.

[13] Zeinab S. Abdel-Rehim and A. Lashine, "Packed bed-PCM material latent heat thermal energy storage system," *ESRJ– Faculty of Engineering at Shoubra,* vol. 14, p. 23, 2011.

[14] K. Cho and S. H. Choi, "Thermal characteristics of paraffin in a spherical capsule during freezing and melting processes," *International Journal of Heat and Mass Transfer,* vol. 43, pp. 3183-3196, 2000.

[15] J. P. Bédécarrats, F. Strub, B. Falcon, and J. P. Dumas, "Phase-change thermal energy storage using spherical capsules: performance of a test plant," *International Journal of Refrigeration,* vol. 19, pp. 187-196, 1996.

[16] J. P. Dumas, J. P. Bedecarrats, F. Strub, and B. Falcon, "Modelization of a tank filled with spherical nodules containing a phase change material," presented at the 10th Int Heat Transfer Conf, Brighton, 1994.

[17] K. A. R. Ismail and J. R. Henríquez, "Numerical and experimental study of spherical capsules packed bed latent heat storage system," *Applied Thermal Engineering,* vol. 22, pp. 1705-1716, 2002.

[18] R. Singh, R. P. Saini, and J. S. Saini, "Simulated Performance of Packed Bed Solar Energy Storage System having Storage Material Elements of Large Size - Part I," *The Open Fuels & Energy Science Journal,* pp. 91-96, 2008.

[19] R. Singh, R. P. Saini, and J. S. Saini, "Simulated Performance of Packed Bed Solar Energy Storage System having Storage Material Elements of Large Size - Part II," *The Open Fuels & Energy Science Journal,* pp. 97-101, 2008.

[20] R. Singh, R. P. Saini, and J. S. Saini, "Simulated Performance of Packed Bed Solar Energy Storage System having Storage Material Elements of Large Size - Part III," *The Open Fuels & Energy Science Journal,* pp. 102-106, 2008.

[21] R. Singh, R. P. Saini, and J. S. Saini, "Models for predicting thermal performance of packed bed energy storage for solar air heaters- A Review " *The Open Fuels & Energy Science Journal,* vol. 2, pp. 47-53, 2009.

[22] J. Wang, Y. Ouyang, and G. Chen, "Experimental study on charging processes of a cylindrical heat storage capsule employing multiple-phase-change materials," *International Journal of Energy Research,* vol. 25, pp. 439-447, 2001.

[23] B. Zivkovic and I. Fujii, "An analysis of isothermal phase change of phase change material within rectangular and cylindrical containers," *Solar Energy,* vol. 70, pp. 51-61, 2001.

[24] F. L. Tan, S. F. Hosseinizadeh, J. M. Khodadadi, and L. Fan, "Experimental and computational study of constrained melting of phase change materials (PCM) inside a spherical capsule," *International Journal of Heat and Mass Transfer,* vol. 52, pp. 3464-3472, 2009.

[25] F. L. Tan and C. W. Chan, "Solidification inside a sphere—an experimental study," *International Communications in Heat and Mass Transfer,* vol. 33, pp. 335-341, 2006.

[26] F. L. Tan., "Constrained and unconstrained melting inside a sphere," *International Communications in Heat and Mass Transfer,* vol. 35, pp. 466–475, 2008.

[27] H. Koizumi, "Time and spatial heat transfer performance around an isothermally heated sphere placed in a uniform, downwardly directed flow (in relation to the enhancement of latent heat storage rate in a spherical capsule)," *Applied Thermal Engineering,* vol. 24, pp. 2583-2600, 2004.

[28] T. Yuge, "Experiments on heat transfer from spheres including combined natural and forced convection," *Journal of Heat Transfer (U.S.)* vol. 82, pp. 214-20, 1960.

[29] H. Jia and G. Gogos, "Laminar natural convection heat transfer from isothermal spheres," *International Journal of Heat and Mass Transfer,* vol. 39, pp. 1603-1615, 1996.

[30] D. E. Beasley. and C. Ramanarayanan, "Thermal response of a packed bed of spheres containing a phase-change material," *International journal of energy research,* vol. 13, pp. 253-265, 1989.

[31] A. Khalil, M. A. e. w. Kassem, and M. Salama., "Experimental Evaluation of Packed Bed Heat Transfer Relations," *Journal of engineering and computer sciences* vol. 1, pp. 43-55, 2008.

[32] E. C. Nsofor and G. A. Adebiyi, "Measurements of the gas-particle convective heat transfer coefficient in a packed bed for high-temperature energy storage," *Experimental Thermal and Fluid Science,* vol. 24, pp. 1-9, 2001.

[33] Varun., F. Singh, S. K. Tyagi, and H. Nautiyal, "Experimental Investigation of packed bed solar thermal energy system with cylindrical elements," *International journal of science and technology* vol. 1, pp. 43-50, 2010.

[34] Y. Shiina and T. Inagaki, "Study on the efficiency of effective thermal conductivities on melting characteristics of latent heat storage capsules," *International Journal of Heat and Mass Transfer,* vol. 48, pp. 373-383, 2005.

[35] M. N. A. Hawlader, M. S. Uddin, and H. J. Zhu, "Encapsulated phase change materials for thermal energy storage: Experiments and simulation," *International Journal of Energy Research,* vol. 26, pp. 159-171, 2002.

[36] S. L. Chen, "One-dimensional analysis of energy storage in packed capsules," *Journal Name: Transactions of the ASAE; (United States); Journal Volume: 114*, pp. Medium: X; Size: Pages: 127-130, 1992.

[37] S. L. Chen and J. S. Yue, "A simplified analysis for cold storage in porous capsules with solidification," *Journal Name: Journal of Energy Resources Technology; (United States); Journal Volume: 113:2*, pp. Medium: X; Size: Pages: 108-116, 1991.

[38] P. D. Silva, L. C. Gonçalves, and L. Pires, "Transient behaviour of a latent-heat thermal-energy store: numerical and experimental studies," *Applied Energy,* vol. 73, pp. 83-98, 2002.

[39] L. Bilir and Z. İlken, "Total solidification time of a liquid phase change material enclosed in cylindrical/spherical containers," *Applied Thermal Engineering,* vol. 25, pp. 1488-1502, 2005.

[40] K. A. R. Ismail and J. R. Henríquez, "Solidification of pcm inside a spherical capsule," *Energy Conversion and Management,* vol. 41, pp. 173-187, 2000.

[41] K. A. R. Ismail and R. Stuginsky Jr, "A parametric study on possible fixed bed models for pcm and sensible heat storage," *Applied Thermal Engineering,* vol. 19, pp. 757-788, 1999.

[42] M. M. Farid and R. M. Husian, "An electrical storage heater using the phase-change method of heat storage," *Energy Conversion and Management,* vol. 30, pp. 219-230, 1990.

[43] T. Kousksou, J. P. Bédécarrats, J. P. Dumas, and A. Mimet, "Dynamic modelling of the storage of an encapsulated ice tank," *Applied Thermal Engineering,* vol. 25, pp. 1534-1548, 2005.

[44] I. W. Eames and K. T. Adref, "Freezing and melting of water in spherical enclosures of the type used in thermal (ice) storage systems," *Applied Thermal Engineering*, vol. 22, pp. 733-745, 2002.

[45] T. Hirata, Y. Makino, and Y. Kaneko, "Analysis of close-contact melting for octadecane and ice inside isothermally heated horizontal rectangular capsule," *International Journal of Heat and Mass Transfer*, vol. 34, pp. 3097-3106, 1991.

[46] J. M. Khodadadi and Y. Zhang, "Effects of buoyancy-driven convection on melting within spherical containers," *International Journal of Heat and Mass Transfer*, vol. 44, pp. 1605-1618, 2001.

[47] S. A. Fomin and T. S. Saitoh, "Melting of unfixed material in spherical capsule with non-isothermal wall," *International Journal of Heat and Mass Transfer*, vol. 42, pp. 4197-4205, 1999.

[48] A. Saito, S. Okawa, T. Shintani, and R. Iwamoto, "On the heat removal characteristics and the analytical model of a thermal energy storage capsule using gelled Glauber's salt as the PCM," *International Journal of Heat and Mass Transfer*, vol. 44, pp. 4693-4701, 2001.

[49] J. Yagi and T. Akiyama, "Storage of thermal energy for effective use of waste heat from industries," *Journal of Materials Processing Technology*, vol. 48, pp. 793-804, 1995.

[50] A. Benmansour, M. A. Hamdan, and A. Bengeuddach, "Experimental and numerical investigation of solid particles thermal energy storage unit," *Applied Thermal Engineering*, vol. 26, pp. 513-518, 2006.

[51] K. Katayama, A. Saito, Y. Utaka, A. Saito, H. Matsui, H. Maekawa, and A. Z. A. Saifullah, "Heat transfer characteristics of the latent heat thermal energy storage capsule," *Solar Energy*, vol. 27, pp. 91-97, 1981.

[52] J. Wei, Y. Kawaguchi, S. Hirano, and H. Takeuchi, "Study on a PCM heat storage system for rapid heat supply," *Applied Thermal Engineering,* vol. 25, pp. 2903-2920, 2005.

[53] C. Arkar and S. Medved, "Influence of accuracy of thermal property data of a phase change material on the result of a numerical model of a packed bed latent heat storage with spheres," *Thermochimica Acta,* vol. 438, pp. 192-201, 2005.

[54] M. Lacroix, "Contact melting of a phase change material inside a heated parallelepedic capsule," *Energy Conversion and Management,* vol. 42, pp. 35-47, 2001.

[55] E. Assis, L. Katsman, G. Ziskind, and R. Letan, "Numerical and experimental study of melting in a spherical shell," *International Journal of Heat and Mass Transfer,* vol. 50, pp. 1790-1804, 2007.

[56] L. Jian-you, "Numerical and experimental investigation for heat transfer in triplex concentric tube with phase change material for thermal energy storage," *Solar Energy,* vol. 82, pp. 977-985, 2008.

[57] C. J. Ho and S. Chen, "Numerical simulation of melting of ice around a horizontal cylinder," *International Journal of Heat and Mass Transfer,* vol. 29, pp. 1359-1369, 1986.

[58] D. A. White, "Melting of ice and freezing of water around a horizontal cylinder," M.S Purdue University, Indiana, 1984.

[59] H. Rieger, U. Projahn, and H. Beer, "Analysis of the heat transport mechanisms during melting around a horizontal circular cylinder," *International Journal of Heat and Mass Transfer,* vol. 25, pp. 137-147, 1982.

[60] M. N. R. Dimaano and T. Watanabe, "Performance investigation of the capric and lauric acid mixture as latent heat energy storage for a cooling system," *Solar Energy,* vol. 72, pp. 205-215, 2002.

[61] M. Bareiss and H. Beer, "An analytical solution of the heat transfer process during melting of an unfixed solid phase change material inside a horizontal tube," *International Journal of Heat and Mass Transfer*, vol. 27, pp. 739-746, 1984.

[62] K. A. R. Ismail and M. M. Abugderah, "Performance of a thermal storage system of the vertical tube type," *Energy Conversion and Management*, vol. 41, pp. 1165-1190, 2000.

[63] A. Sari and K. Kaygusuz, "Thermal performance of a eutectic mixture of lauric and stearic acids as PCM encapsulated in the annulus of two concentric pipes," *Solar Energy*, vol. 72, pp. 493-504, 2002.

[64] A. Sari and K. Kaygusuz, "Thermal energy storage system using stearic acid as a phase change material," *Solar Energy*, vol. 71, pp. 365-376, 2001.

[65] A. Sari and K. Kaygusuz, "Thermal performance of palmitic acid as a phase change energy storage material," *Energy Conversion and Management*, vol. 43, pp. 863-876, 2002.

[66] A. Sarı and K. Kaygusuz, "Thermal and heat transfer characteristics in a latent heat storage system using lauric acid," *Energy Conversion and Management*, vol. 43, pp. 2493-2507, 2002.

[67] A. S. K. Kaygusuz, "Thermal Energy Storage System Using Some Fatty Acids as Latent Heat Energy Storage Materials," *Energy Sources*, vol. 23, pp. 275-285, 2001.

[68] A. Sarı and K. Kaygusuz, "Thermal performance of myristic acid as a phase change material for energy storage application," *Renewable Energy*, vol. 24, pp. 303-317, 2001.

[69] D. B. Khillarkar, Z. X. Gong, and A. S. Mujumdar, "Melting of a phase change material in concentric horizontal annuli of arbitrary cross-section," *Applied Thermal Engineering*, vol. 20, pp. 893-912, 2000.

[70] H. Shmueli, G. Ziskind, and R. Letan, "Melting in a vertical cylindrical tube: Numerical investigation and comparison with experiments," *International Journal of Heat and Mass Transfer,* vol. 53, pp. 4082-4091, 2010.

[71] B. J. Jones, D. Sun, S. Krishnan, and S. V. Garimella, "Experimental and numerical study of melting in a cylinder," *International Journal of Heat and Mass Transfer,* vol. 49, pp. 2724-2738, 2006.

[72] A. F. Regin, S. C. Solanki, and J. S. Saini, "Latent heat thermal energy storage using cylindrical capsule: Numerical and experimental investigations," *Renewable Energy,* vol. 31, pp. 2025-2041, 2006.

[73] D. Sun, S. R. Annapragada, and S. V. Garimella, "Experimental and numerical study of melting of particle-laden materials in a cylinder," *International Journal of Heat and Mass Transfer,* vol. 52, pp. 2966-2978, 2009.

[74] Y. Zhang and A. Faghri, "Semi-analytical solution of thermal energy storage system with conjugate laminar forced convection," *International Journal of Heat and Mass Transfer,* vol. 39, pp. 717-724, 1996.

[75] Y. Zhang and A. Faghri, "Heat transfer enhancement in latent heat thermal energy storage system by using an external radial finned tube," *Journal of Enhanced Heat Transfer,* vol. 3, pp. 119-127, 1996.

[76] L. F. Cabeza, M. Ibáñez, C. Solé, J. Roca, and M. Nogués, "Experimentation with a water tank including a PCM module," *Solar Energy Materials and Solar Cells,* vol. 90, pp. 1273-1282, 2006.

[77] Y. K. Wu and M. Lacroix, "Melting of a PCM inside a vertical cylindrical capsule," *International Journal for Numerical Methods in Fluids,* vol. 20, pp. 559-572, 1995.

[78] Y. K. Wu, "Numerical Studies of Melting Process in a Cylindrical Enclosure," Ph.D., École Polytechnique de Montréal, 1990.

[79] M. Prud'homme, T. H. Nguyen, and Y. K. Wu, "Simulation numérique de la fusion à l'intérieur d'un cylindre adiabatique chauffé par le bas," *International Journal of Heat and Mass Transfer,* vol. 34, pp. 2275-2286, 1991.

[80] Y. K. Wu, M. Prud'homme, and T. H. Nguyen, "Étude numérique de la fusion autour d'un cylindre vertical soumis à deux types de conditions limites," *International Journal of Heat and Mass Transfer,* vol. 32, pp. 1927-1938, 1989.

[81] H. Rieger and H. Beer, "The Melting Process of Ice Inside a Horizontal Cylinder: Effects of Density Anomaly," *Journal of Heat Transfer,* vol. 108, pp. 166-173, 1986.

[82] H. Rieger, U. Projahn, M. Bareiss, and H. Beer, "Heat Transfer During Melting Inside a Horizontal Tube," *Journal of Heat Transfer,* vol. 105, pp. 226-234, 1983.

[83] N. H. S. Tay, M. Belusko, and F. Bruno, "Experimental investigation of tubes in a phase change thermal energy storage system," *Applied Energy,* vol. 90, pp. 288-297, 2012.

[84] N. H. S. Tay, F. Bruno, and M. Belusko, "Experimental validation of a CFD model for tubes in a phase change thermal energy storage system," *International Journal of Heat and Mass Transfer,* vol. 55, pp. 574-585, 2012.

[85] T. Saitoh and K. Hirose, "High Rayleigh Number Solutions to Problems of Latent Heat Thermal Energy Storage in a Horizontal Cylinder Capsule," *Journal of Heat Transfer,* vol. 104, pp. 545-553, 1982.

[86] J. Pannu, G. Joglekar, and P. A. Rice, "Natural convection heat transfer to cylinders of phase change material used for thermal storage," *American Institute of Chemical Engineers,* vol. 76, pp. 47-55, 1980.

[87] E. M. Sparrow and J. A. Broadbent, "Inward Melting in a Vertical Tube Which Allows Free Expansion of the Phase-Change Medium," *Journal of Heat Transfer,* vol. 104, pp. 309-315, 1982.

[88] J. Fukai, M. Kanou, Y. Kodama, and O. Miyatake, "Thermal conductivity enhancement of energy storage media using carbon fibers," *Energy Conversion and Management,* vol. 41, pp. 1543-1556, 2000.

[89] J. Fukai, Y. Hamada, Y. Morozumi, and O. Miyatake, "Effect of carbon-fiber brushes on conductive heat transfer in phase change materials," *International Journal of Heat and Mass Transfer,* vol. 45, pp. 4781-4792, 2002.

[90] J. Fukai, Y. Hamada, Y. Morozumi, and O. Miyatake, "Improvement of thermal characteristics of latent heat thermal energy storage units using carbon-fiber brushes: experiments and modeling," *International Journal of Heat and Mass Transfer,* vol. 46, pp. 4513-4525, 2003.

[91] Y. Hamada, W. Ohtsu, and J. Fukai, "Thermal response in thermal energy storage material around heat transfer tubes: effect of additives on heat transfer rates," *Solar Energy,* vol. 75, pp. 317-328, 2003.

[92] A. Trp, "A numerical and experimental study of transient heat transfer in a shell-and-tube latent heat storage unit with paraffin as a phase change material," presented at the Energy and the Environment, 2002.

[93] A. Trp, "An experimental and numerical investigation of heat transfer during technical grade paraffin melting and solidification in a shell-and-tube latent thermal energy storage unit," *Solar Energy,* vol. 79, pp. 648-660, 2005.

[94] A. Trp, K. Lenic, and B. Frankovic, "Analysis of the influence of operating conditions and geometric parameters on heat transfer in water-paraffin shell-and-tube latent thermal energy storage unit," *Applied Thermal Engineering,* vol. 26, pp. 1830-1839, 2006.

[95] V. H. Morcos, "Investigation of a latent heat thermal energy storage system," *Solar & Wind Technology,* vol. 7, pp. 197-202, 1990.

[96] M. A. Ezan, M. Ozdogan, and A. Erek, "Experimental study on charging and discharging periods of water in a latent heat storage unit," *International Journal of Thermal Sciences,* vol. 50, pp. 2205-2219, 2011.

[97] M. Akgün, O. Aydın, and K. Kaygusuz, "Experimental study on melting/solidification characteristics of a paraffin as PCM," *Energy Conversion and Management,* vol. 48, pp. 669-678, 2007.

[98] M. Akgün, O. Aydın, and K. Kaygusuz, "Thermal energy storage performance of paraffin in a novel tube-in-shell system," *Applied Thermal Engineering,* vol. 28, pp. 405-413, 2008.

[99] J. Lu, J. Ding, and J. Yang, "Solidification and melting behaviors and characteristics of molten salt in cold filling pipe," *International Journal of Heat and Mass Transfer,* vol. 53, pp. 1628-1635, 2010.

[100] A. Hasan, "Phase change material energy storage system employing palmitic acid," *Solar Energy*, vol. 52, pp. 143-154, 1994.

[101] M. Yang and W. Q. Tao, "Numerical study of natural convection heat transfer in a cylindrical envelope with internal concentric slotted hollow cylinder," *Numerical Heat Transfer, Part A: Applications,* vol. 22, pp. 289-305, 1992.

[102] R. Hendra, Hamdani, T. M. I. Mahlia, and H. H. Masjuki, "Thermal and melting heat transfer characteristics in a latent heat storage system using mikro," *Applied Thermal Engineering*, vol. 25, pp. 1503-1515, 2005.

[103] K. A. R. Ismail and M. M. Gonçalves, "Thermal performance of a pcm storage unit," *Energy Conversion and Management*, vol. 40, pp. 115-138, 1999.

[104] A. Castell, M. Belusko, F. Bruno, and L. F. Cabeza, "Maximisation of heat transfer in a coil in tank PCM cold storage system," *Applied Energy*, vol. 88, pp. 4120-4127, 2011.

[105] Z. Liu, X. Sun, and C. Ma, "Experimental investigations on the characteristics of melting processes of stearic acid in an annulus and its thermal conductivity enhancement by fins," *Energy Conversion and Management,* vol. 46, pp. 959-969, 2005.

[106] U. Stritih, "An experimental study of enhanced heat transfer in rectangular PCM thermal storage," *International Journal of Heat and Mass Transfer,* vol. 47, pp. 2841-2847, 2004.

[107] R. Velraj, R. V. Seeniraj, B. Hafner, C. Faber, and K. Schwarzer, "Experimental analysis and numerical modelling of inward solidification on a finned vertical tube for a latent heat storage unit," *Solar Energy,* vol. 60, pp. 281-290, 1997.

[108] R. Velraj, R. V. Seeniraj, B. Hafner, C. Faber, and K. Schwarzer, "Heat transfer enhancement in a latent heat storage system," *Solar Energy,* vol. 65, pp. 171-180, 1999.

[109] N. Kayansayan and M. Ali Acar, "Ice formation around a finned-tube heat exchanger for cold thermal energy storage," *International Journal of Thermal Sciences,* vol. 45, pp. 405-418, 2006.

[110] M. Lacroix, "Study of the heat transfer behavior of a latent heat thermal energy storage unit with a finned tube," *International Journal of Heat and Mass Transfer,* vol. 36, pp. 2083-2092, 1993.

[111] K. A. R. Ismail, C. L. F. Alves, and M. S. Modesto, "Numerical and experimental study on the solidification of PCM around a vertical axially finned isothermal cylinder," *Applied Thermal Engineering,* vol. 21, pp. 53-77, 2001.

[112] Y. Zhang and A. Faghri, "Heat transfer enhancement in latent heat thermal energy storage system by using the internally finned tube," *International Journal of Heat and Mass Transfer,* vol. 39, pp. 3165-3173, 1996.

[113] A. Castell, C. Solé, M. Medrano, J. Roca, L. F. Cabeza, and D. García, "Natural convection heat transfer coefficients in phase change material (PCM) modules with external vertical fins," *Applied Thermal Engineering,* vol. 28, pp. 1676-1686, 2008.

[114] F. Agyenim, P. Eames, and M. Smyth, "A comparison of heat transfer enhancement in a medium temperature thermal energy storage heat exchanger using fins," *Solar Energy,* vol. 83, pp. 1509-1520, 2009.

[115] V. Shatikian, G. Ziskind, and R. Letan, "Numerical investigation of a PCM-based heat sink with internal fins: Constant heat flux," *International Journal of Heat and Mass Transfer,* vol. 51, pp. 1488-1493, 2008.

[116] V. Shatikian, G. Ziskind, and R. Letan, "Numerical investigation of a PCM-based heat sink with internal fins," *International Journal of Heat and Mass Transfer,* vol. 48, pp. 3689-3706, 2005.

[117] E. M. Sparrow, E. D. Larson, and J. W. Ramsey, "Freezing on a finned tube for either conduction-controlled or natural-convection-controlled heat transfer," *International Journal of Heat and Mass Transfer,* vol. 24, pp. 273-284, 1981.

[118] K. Ermis, A. Erek, and I. Dincer, "Heat transfer analysis of phase change process in a finned-tube thermal energy storage system using artificial neural network," *International Journal of Heat and Mass Transfer,* vol. 50, pp. 3163-3175, 2007.

[119] J. Eftekhar, A. Haji-Sheikh, and D. Y. S. Lou, "Heat Transfer Enhancement in a Paraffin Wax Thermal Storage System," *Journal of Solar Energy Engineering,* vol. 106, pp. 299-306, 1984.

[120] A. G. Bathelt and R. Viskanta, "Heat transfer at the solid-liquid interface during melting from a horizontal cylinder," *International Journal of Heat and Mass Transfer,* vol. 23, pp. 1493-1503, 1980.

[121] P. V. Padmanabhan and M. V. Krishna Murthy, "Outward phase change in a cylindrical annulus with axial fins on the inner tube," *International Journal of Heat and Mass Transfer*, vol. 29, pp. 1855-1868, 1986.

[122] L. Tan, Y. Kwok, A. Date, and A. Akbarzadeh, "Numerical study of natural convection effects in latent heat storage using aluminum fins and spiral fillers," *International Journal of Mechanical and Aerospace Engineering* vol. 6, pp. 238-245, 2012.

[123] F. Agyenim, P. Eames, and M. Smyth, "Experimental study on the melting and solidification behaviour of a medium temperature phase change storage material (Erythritol) system augmented with fins to power a LiBr/H2O absorption cooling system," *Renewable Energy*, vol. 36, pp. 108-117, 2011.

[124] J. C. Choi and S. D. Kim, "Heat transfer in a latent heat-storage system using MgCl2·6H2O at the melting point," *Energy*, vol. 20, pp. 13-25, 1995.

[125] K. A. R. Ismail and F. A. M. Lino, "Fins and turbulence promoters for heat transfer enhancement in latent heat storage systems," *Experimental Thermal and Fluid Science*, vol. 35, pp. 1010-1018, 2011.

[126] S. K. Saha and P. Dutta, "Heat transfer correlations for PCM-based heat sinks with plate fins," *Applied Thermal Engineering*, vol. 30, pp. 2485-2491, 2010.

[127] S. Pincemin, R. Olives, X. Py, and M. Christ, "Highly conductive composites made of phase change materials and graphite for thermal storage," *Solar Energy Materials and Solar Cells*, vol. 92, pp. 603-613, 2008.

[128] C. Y. Zhao and Z. G. Wu, "Heat transfer enhancement of high temperature thermal energy storage using metal foams and expanded graphite," *Solar Energy Materials and Solar Cells*, vol. 95, pp. 636-643, 2011.

[129] X. Py, R. Olives, and S. Mauran, "Paraffin/porous-graphite-matrix composite as a high and constant power thermal storage material," *International Journal of Heat and Mass Transfer,* vol. 44, pp. 2727-2737, 2001.

[130] Z. Zhang and X. Fang, "Study on paraffin/expanded graphite composite phase change thermal energy storage material," *Energy Conversion and Management,* vol. 47, pp. 303-310, 2006.

[131] M. Xiao, B. Feng, and K. Gong, "Preparation and performance of shape stabilized phase change thermal storage materials with high thermal conductivity," *Energy Conversion and Management,* vol. 43, pp. 103-108, 2002.

[132] A. Sarı and A. Karaipekli, "Thermal conductivity and latent heat thermal energy storage characteristics of paraffin/expanded graphite composite as phase change material," *Applied Thermal Engineering,* vol. 27, pp. 1271-1277, 2007.

[133] A. Karaipekli, A. Sarı, and K. Kaygusuz, "Thermal conductivity improvement of stearic acid using expanded graphite and carbon fiber for energy storage applications," *Renewable Energy,* vol. 32, pp. 2201-2210, 2007.

[134] F. Frusteri, V. Leonardi, S. Vasta, and G. Restuccia, "Thermal conductivity measurement of a PCM based storage system containing carbon fibers," *Applied Thermal Engineering,* vol. 25, pp. 1623-1633, 2005.

[135] J. M. Marín, B. Zalba, L. F. Cabeza, and H. Mehling, "Improvement of a thermal energy storage using plates with paraffin–graphite composite," *International Journal of Heat and Mass Transfer,* vol. 48, pp. 2561-2570, 2005.

[136] A. Sarı, "Form-stable paraffin/high density polyethylene composites as solid–liquid phase change material for thermal energy storage: preparation and thermal properties," *Energy Conversion and Management,* vol. 45, pp. 2033-2042, 2004.

[137] N. K. Bansal and D. Buddhi, "An analytical study of a latent heat storage system in a cylinder," *Energy Conversion and Management,* vol. 33, pp. 235-242, 1992.

[138] Y. Zhang, J. Ding, X. Wang, R. Yang, and K. Lin, "Influence of additives on thermal conductivity of shape-stabilized phase change material," *Solar Energy Materials and Solar Cells*, vol. 90, pp. 1692-1702, 2006.

[139] A. Mills, M. Farid, J. R. Selman, and S. Al-Hallaj, "Thermal conductivity enhancement of phase change materials using a graphite matrix," *Applied Thermal Engineering*, vol. 26, pp. 1652-1661, 2006.

[140] J. H. Han, K. W. Cho, K. H. Lee, and H. Kim, "Porous graphite matrix for chemical heat pumps," *Carbon*, vol. 36, pp. 1801-1810, 1998.

[141] M. Bonnissel, L. Luo, and D. Tondeur, "Compacted exfoliated natural graphite as heat conduction medium," *Carbon*, vol. 39, pp. 2151-2161, 2001.

[142] O. Mesalhy, K. Lafdi, A. Elgafy, and K. Bowman, "Numerical study for enhancing the thermal conductivity of phase change material (PCM) storage using high thermal conductivity porous matrix," *Energy Conversion and Management*, vol. 46, pp. 847-867, 2005.

[143] C. J. Hoogendoorn and G. C. J. Bart, "Performance and modelling of latent heat stores," *Solar Energy*, vol. 48, pp. 53-58, 1992.

[144] M. S. Phanikumar and R. L. Mahajan, "Non-Darcy natural convection in high porosity metal foams," *International Journal of Heat and Mass Transfer*, vol. 45, pp. 3781-3793, 2002.

[145] C. Beckermann, S. Ramadhyani, and R. Viskanta, "Natural Convection Flow and Heat Transfer Between a Fluid Layer and a Porous Layer Inside a Rectangular Enclosure," *Journal of Heat Transfer*, vol. 109, pp. 363-370, 1987.

[146] K. Sasaguchi, K. Kusano, and R. Viskanta, "A numerical analysis of solid-liquid phase change heat transfer around a single and two horizontal, vertically spaced cylinders in a rectangular cavity," *International Journal of Heat and Mass Transfer*, vol. 40, pp. 1343-1354, 1997.

[147] K. Sasaguchi, K. Kuwabara, K. Kusano, and H. Kitagawa, "Transient cooling of water around a cylinder in a rectangular cavity—a numerical analysis of the effect of the position of the cylinder," *International Journal of Heat and Mass Transfer,* vol. 41, pp. 3149-3156, 1998.

[148] A. Bhattacharya, V. V. Calmidi, and R. L. Mahajan, "Thermophysical properties of high porosity metal foams," *International Journal of Heat and Mass Transfer,* vol. 45, pp. 1017-1031, 2002.

[149] K. Boomsma and D. Poulikakos, "On the effective thermal conductivity of a three-dimensionally structured fluid-saturated metal foam," *International Journal of Heat and Mass Transfer,* vol. 44, pp. 827-836, 2001.

[150] V. V. Calmidi and R. L. Mahajan, "The Effective Thermal Conductivity of High Porosity Fibrous Metal Foams," *Journal of Heat Transfer,* vol. 121, pp. 466-471, 1999.

[151] V. V. Calmidi and R. L. Mahajan, "Forced Convection in High Porosity Metal Foams," *Journal of Heat Transfer,* vol. 122, pp. 557-565, 2000.

[152] M. L. Hunt and C. L. Tien, "Effects of thermal dispersion on forced convection in fibrous media," *International Journal of Heat and Mass Transfer,* vol. 31, pp. 301-309, 1988.

[153] H. F. Erk and M. P. Duduković, "Phase-change heat regenerators: Modeling and experimental studies," *AIChE Journal,* vol. 42, pp. 791-808, 1996.

[154] J. A. Weaver and R. Viskanta, "Freezing of water saturated porous media in a rectangular cavity," *Journal Name: Int. Commun. Heat Mass Transfer; (United States); Journal Volume: 13:3,* pp. Medium: X; Size: Pages: 245-252, 1986.

[155] C. Beckermann and R. Viskanta, "Natural convection solid/liquid phase change in porous media," *International Journal of Heat and Mass Transfer,* vol. 31, pp. 35-46, 1988.

[156] W. Lu, C. Y. Zhao, and S. A. Tassou, "Thermal analysis on metal-foam filled heat exchangers. Part I: Metal-foam filled pipes," *International Journal of Heat and Mass Transfer,* vol. 49, pp. 2751-2761, 2006.

[157] C. Y. Zhao, W. Lu, and S. A. Tassou, "Thermal analysis on metal-foam filled heat exchangers. Part II: Tube heat exchangers," *International Journal of Heat and Mass Transfer,* vol. 49, pp. 2762-2770, 2006.

[158] C. Y. Zhao, W. Lu, and Y. Tian, "Heat transfer enhancement for thermal energy storage using metal foams embedded within phase change materials (PCMs)," *Solar Energy,* vol. 84, pp. 1402-1412, 2010.

[159] Z. G. Wu and C. Y. Zhao, "Experimental investigations of porous materials in high temperature thermal energy storage systems," *Solar Energy,* vol. 85, pp. 1371-1380, 2011.

[160] Y. Y. Tian and C.-Y. Zhao, "Heat transfer analysis for phase change materials (PCMs)," presented at the The 11th International Conference on Energy Storage (Effstock 2009), Stockholm, Sweden, 2009.

[161] Y. Y. Tian and C.-Y. Zhao, "Numerical Investigation of heat transfer in Phase change Materials Using Non-equilibrium Model," presented at the proceeding of 11th UK National Heat Transfer Conference, London, UK, 2009.

[162] C. M. Kramer and C. J. Wilson, "The phase diagram of NaNO3—KNO3," *Thermochimica Acta,* vol. 42, pp. 253-264, 1980.

[163] D. J. Rogers and G. J. Janz, "Melting-crystallization and premelting properties of sodium nitrate-potassium nitrate. Enthalpies and heat capacities," *Journal of Chemical & Engineering Data,* vol. 27, pp. 424-428, 1982.

[164] D. Haillot, X. Py, V. Goetz, and M. Benabdelkarim, "Storage composites for the optimisation of solar water heating systems," *Chemical Engineering Research and Design,* vol. 86, pp. 612-617, 2008.

[165] H. Yin, X. Gao, J. Ding, and Z. Zhang, "Experimental research on heat transfer mechanism of heat sink with composite phase change materials," *Energy Conversion and Management,* vol. 49, pp. 1740-1746, 2008.

[166] A. Siahpush, J. O'Brien, and J. Crepeau, "Phase Change Heat Transfer Enhancement Using Copper Porous Foam," *Journal of Heat Transfer,* vol. 130, pp. 082301-11, 2008.

[167] C. Y. Zhao, T. Kim, T. J. Lu, and H. P. Hodson, "Thermal Transport in High Porosity Cellular Metal Foams," *Journal of Thermophysics and Heat Transfer,* vol. 18, pp. 309-317, 2004.

[168] S. Krishnan, J. Y. Murthy, and S. V. Garimella, "A Two-Temperature Model for Solid-Liquid Phase Change in Metal Foams," *Journal of Heat Transfer,* vol. 127, pp. 995-1004, 2005.

[169] S. Krishnan, J. Y. Murthy, and S. V. Garimella, "A Two-Temperature Model for Solid/Liquid Phase Change in Metal Foams," *ASME Conference Proceedings,* vol. 2004, pp. 609-619, 2004.

[170] X. Tong, J. A. Khan, and M. RuhulAmin, "Enhancement of heat transfer by inserting a metal matrix into a phase change material," *Numerical Heat Transfer, Part A: Applications,* vol. 30, pp. 125-141, 1996.

[171] E. M. Sparrow, S. V. Patankar, and S. Ramadhyani, "Analysis of Melting in the Presence of Natural Convection in the Melt Region," *Journal of Heat Transfer,* vol. 99, pp. 520-526, 1977.

[172] D. S. Lin and M. W. Nansteel, "Natural Convection in a Vertical Annulus Containing Water Near the Density Maximum," *Journal of Heat Transfer,* vol. 109, pp. 899-905, 1987.

[173] K. Charn-Jung, R. Sung Tack, and L. Joon Sik, "An efficient computational technique to solve the moving boundary problems in the axisymmetric geometries," *International Journal of Heat and Mass Transfer*, vol. 36, pp. 3759-3764, 1993.

[174] H. M. Ettouney, I. Alatiqi, M. Al-Sahali, and S. Ahmad Al-Ali, "Heat transfer enhancement by metal screens and metal spheres in phase change energy storage systems," *Renewable Energy*, vol. 29, pp. 841-860, 2004.

[175] C. J. Ho and J. Y. Gao, "Preparation and thermophysical properties of nanoparticle-in-paraffin emulsion as phase change material," *International Communications in Heat and Mass Transfer*, vol. 36, pp. 467-470, 2009.

[176] W. R. Humphries and E. I. Griggs, *A design for phase change thermal control and energy storage devices*. USA: National Aeronautics and Space Administration (NASA), 1977.

[177] S. Wu, D. Zhu, X. Zhang, and J. Huang, "Preparation and Melting/Freezing Characteristics of Cu/Paraffin Nanofluid as Phase-Change Material (PCM)," *Energy & Fuels*, vol. 24, pp. 1894-1898, 2010.

[178] J. Zeng, L. Sun, F. Xu, Z. Tan, Z. Zhang, J. Zhang, and T. Zhang, "Study of a PCM based energy storage system containing Ag nanoparticles," *Journal of Thermal Analysis and Calorimetry*, vol. 87, pp. 371-375, 2007.

[179] A. V. Arasu, A. P. Sasmito, and A. S. Mujumdar, "Numerical performance study of paraffin wax dispersed with alumina in a concentric pipe latent heat storage system," *Thermal Science 2012 OnLine*, pp. 4-4, 2012.

[180] A. V. Arasu and A. S. Mujumdar, "Numerical study on melting of paraffin wax with Al2O3 in a square enclosure," *International Communications in Heat and Mass Transfer*, vol. 39, pp. 8-16, 2012.

[181] A. V. Arasu, A. P. Sasmito, and A. S. Mujumdar, "Thermal performance enhancement of paraffin wax with AL2O3 and CuO nanoparticles – a numerical study," *Frontiers in Heat and Mass Transfer (FHMT),* 2011.

[182] J. M. Khodadadi and L. Fan, "Expedited Freezing of Nanoparticle-Enhanced Phase Change Materials (NEPCM) Exhibited Through a Simple 1-D Stefan Problem Formulation," *ASME Conference Proceedings,* vol. 2009, pp. 345-351, 2009.

[183] L. Fan and J. M. Khodadadi, "Experimental Verification of Expedited Freezing of Nanoparticle-Enhanced Phase Change Materials (NEPCM)," *ASME Conference Proceedings,* vol. 2011, pp. T10221-T10221-7, 2011.

[184] J. M. Khodadadi and S. F. Hosseinizadeh, "Nanoparticle-enhanced phase change materials (NEPCM) with great potential for improved thermal energy storage," *International Communications in Heat and Mass Transfer,* vol. 34, pp. 534-543, 2007.

[185] K. Khanafer, K. Vafai, and M. Lightstone, "Buoyancy-driven heat transfer enhancement in a two-dimensional enclosure utilizing nanofluids," *International Journal of Heat and Mass Transfer,* vol. 46, pp. 3639-3653, 2003.

[186] A. D. Brent, V. R. Voller, and K. J. Reid, "Enthalpy-porosity technique for modeling convection-diffusion phase change: application to the melting of a pure metal," *Numerical Heat Transfer,* vol. 13, pp. 297-318, 1988.

[187] C. Gau and R. Viskanta, "Melting and Solidification of a Pure Metal on a Vertical Wall," *Journal of Heat Transfer,* vol. 108, pp. 174-181, 1986.

[188] Y. J. T. A. K. M. R. J. Banaszek, "Semi-implicit FEM analysis of natural convection in freezing water," *Numerical Heat Transfer, Part A: Applications,* vol. 36, pp. 449-472, 1999.

[189] A. A. Ranjbar, S. Kashani, S. F. Hosseinizadeh, and M. Ghanbarpour, "Numerical heat transfer studies of a latent heat storage system containing nano-enhanced phase change material," *Thermal Science* vol. 15, pp. 169-181, 2011.

[190] S. Kim and L. T. Drzal, "High latent heat storage and high thermal conductive phase change materials using exfoliated graphite nanoplatelets," *Solar Energy Materials and Solar Cells*, vol. 93, pp. 136-142, 2009.

[191] Y.-D. Liu, Y.-G. Zhou, M.-W. Tong, and X.-S. Zhou, "Experimental study of thermal conductivity and phase change performance of nanofluids PCMs," *Microfluidics and Nanofluidics*, vol. 7, pp. 579-584, 2009/10/01 2009.

[192] B.-X. Wang, L.-P. Zhou, and X.-F. Peng, "A fractal model for predicting the effective thermal conductivity of liquid with suspension of nanoparticles," *International Journal of Heat and Mass Transfer*, vol. 46, pp. 2665-2672, 2003.

[193] L. P. Zhou and B. X. Wang, "Experimental research on the thermophysical properties of nanoparticle suspensions using the quasi-steady state method," *Ann. Proc. Chinese Eng. Thermophys*, pp. 889–892 (in Chinese), 2002.

[194] R. V. Seeniraj, R. Velraj, and N. L. Narasimhan, "Heat Transfer Enhancement Study of a LHTS Unit Containing Dispersed High Conductivity Particles," *Journal of Solar Energy Engineering*, vol. 124, pp. 243-249, 2002.

[195] R. Siegel, "Solidification of low conductivity material containing dispersed high conductivity particles," *International Journal of Heat and Mass Transfer*, vol. 20, pp. 1087-1089, 1977.

[196] X. Wang, X. Xu, and S. U. S. Choi, "Thermal Conductivity of Nanoparticle - Fluid Mixture," *Journal of Thermophysics and Heat Transfer*, vol. 13, pp. 474-480, 1999.

[197] J. C. Maxwell, *Electricity and magnetism, Part II*, 3 ed. Clarendon: Oxford, 1904.

[198] D. J. Jeffrey, "Conduction Through a Random Suspension of Spheres," *Proceedings of the Royal Society of London*, vol. 335, pp. 355-367, 1973.

[199] R. H. Davis, "The effective thermal conductivity of a composite material with spherical inclusions," *International Journal of Thermophysics,* vol. 7, pp. 609-620, 1986.

[200] S. Lu, x, Yuan, H. Lin, and Chi, "Effective conductivity of composites containing aligned spheroidal inclusions of finite conductivity," *Journal of Applied Physics,* vol. 79, pp. 6761-6769, 1996.

[201] R. T. Bonnecaze and J. F. Brady, "A Method for Determining the Effective Conductivity of Dispersions of Particles," *Proceedings of the Royal Society of London,* vol. 430 pp. 285-313, 1990.

[202] R. T. Bonnecaze and J. F. Brady, "The Effective Conductivity of Random Suspensions of Spherical Particles," *Proceedings of the Royal Society of London,* vol. 432, pp. 445– 465, 1991.

[203] S. Shaikh, K. Lafdi, and K. Hallinan, "Carbon nanoadditives to enhance latent energy storage of phase change materials," *Journal of Applied Physics,* vol. 103, pp. 094302-094302-6, 2008.

[204] Y. Ding, H. Chen, L. Wang, C. Yang, Y. He, W. Yang, W. Lee, L. Zhang, and R. Huo, "Heat Transfer Intensification Using Nanofluids," *Kona-Powder and Particle,* vol. 25, pp. 23-38, 2007.

[205] L. Godson, B. Raja, D. Mohan Lal, and S. Wongwises, "Enhancement of heat transfer using nanofluids—An overview," *Renewable and Sustainable Energy Reviews,* vol. 14, pp. 629-641, 2010.

[206] V. Trisaksri and S. Wongwises, "Critical review of heat transfer characteristics of nanofluids," *Renewable and Sustainable Energy Reviews,* vol. 11, pp. 512-523, 2007.

[207] C. J. Ho, M. W. Chen, and Z. W. Li, "Numerical simulation of natural convection of nanofluid in a square enclosure: Effects due to uncertainties of viscosity and thermal

conductivity," *International Journal of Heat and Mass Transfer,* vol. 51, pp. 4506-4516, 2008.

[208] R. S. Vajjha, D. K. Das, and B. M. Mahagaonkar, "Density Measurement of Different Nanofluids and Their Comparison With Theory," *Petroleum Science and Technology,* vol. 27, pp. 612-624, 2009.

[209] B. C. Pak and Y. I. Cho, "Hydrodynamic and heat transfer study of dispersed fluids with submicron metallic oxide particles," *Experimental Heat Transfer,* vol. 11, pp. 151-170, 1998.

[210] R. S. Vajjha and D. K. Das, "Experimental determination of thermal conductivity of three nanofluids and development of new correlations," *International Journal of Heat and Mass Transfer,* vol. 52, pp. 4675-4682, 2009.

[211] D. A. G. Bruggeman, "Berechnung verschiedener physikalischer Konstanten von heterogenen Substanzen. I. Dielektrizitätskonstanten und Leitfähigkeiten der Mischkörper aus isotropen Substanzen," *Annalen der Physik,* vol. 416, pp. 636-664, 1935.

[212] W. Yu and S. U. S. Choi, "The Role of Interfacial Layers in the Enhanced Thermal Conductivity of Nanofluids: A Renovated Maxwell Model," *Journal of Nanoparticle Research,* vol. 5, pp. 167-171, 2003.

[213] Y. Xuan, Q. Li, and W. Hu, "Aggregation structure and thermal conductivity of nanofluids," *AIChE Journal,* vol. 49, pp. 1038-1043, 2003.

[214] J. Koo and C. Kleinstreuer, "A new thermal conductivity model for nanofluids," *Journal of Nanoparticle Research,* vol. 6, pp. 577-588, 2004.

[215] J. Koo and C. Kleinstreuer, "Laminar nanofluid flow in microheat-sinks," *International Journal of Heat and Mass Transfer,* vol. 48, pp. 2652-2661, 2005.

[216] Q. Xue and W.-M. Xu, "A model of thermal conductivity of nanofluids with interfacial shells," *Materials Chemistry and Physics,* vol. 90, pp. 298-301, 2005.

[217] C. H. Chon, K. D. Kihm, S. P. Lee, and S. U. S. Choi, "Empirical correlation finding the role of temperature and particle size for nanofluid (Al_2O_3) thermal conductivity enhancement," *Applied Physics Letters,* vol. 87, pp. 153107-3, 2005.

[218] R. Prasher, P. Bhattacharya, and P. E. Phelan, "Brownian-Motion-Based Convective-Conductive Model for the Effective Thermal Conductivity of Nanofluids," *Journal of Heat Transfer,* vol. 128, pp. 588-595, 2006.

[219] S. P. Jang and S. U. S. Choi, "Effects of Various Parameters on Nanofluid Thermal Conductivity," *Journal of Heat Transfer,* vol. 129, pp. 617-623, 2007.

[220] R. S. Vajjha, D. K. Das, and P. K. Namburu, "Numerical study of fluid dynamic and heat transfer performance of Al2O3 and CuO nanofluids in the flat tubes of a radiator," *International Journal of Heat and Fluid Flow,* vol. 31, pp. 613-621, 2010.

[221] G. Barakos, E. Mitsoulis, and D. Assimacopoulos, "Natural convection flow in a square cavity revisited: Laminar and turbulent models with wall functions," *International Journal for Numerical Methods in Fluids,* vol. 18, pp. 695-719, 1994.

[222] N. C. Markatos and K. A. Pericleous, "Laminar and turbulent natural convection in an enclosed cavity," *International Journal of Heat and Mass Transfer,* vol. 27, pp. 755-772, 1984.

[223] G. De Vahl Davis, "Natural convection of air in a square cavity: A bench mark numerical solution," *International Journal for Numerical Methods in Fluids,* vol. 3, pp. 249-264, 1983.

[224] T. Fusegi, J. M. Hyun, K. Kuwahara, and B. Farouk, "A numerical study of three-dimensional natural convection in a differentially heated cubical enclosure," *International Journal of Heat and Mass Transfer,* vol. 34, pp. 1543-1557, 1991.

[225] Q. Li and Y. Xuan, "Convective heat transfer and flow characteristics of Cu-water nanofluid," *Science in China Series E: Technolgical Science,* vol. 45, pp. 408-416, 2002.

[226] Abdulhassan Abd. K, Sattar Al-Jabair, and K. Sultan, "Experimental investigation of heat transfer and flow of nano fluids in horizontal circular tube," *International Journal of Mechanical and Aerospace Engineering*, vol. 6, 2012.

[227] G. K. Batchelor, "The effect of Brownian motion on the bulk stress in a suspension of spherical particles," *Journal of Fluid Mechanics*, vol. 83, pp. 97-117, 1977.

[228] R. L. Hamilton and O. K. Crosser, "Thermal Conductivity of Heterogeneous Two-Component Systems," *Industrial & Engineering Chemistry Fundamentals*, vol. 1, pp. 187-191, 1962/08/01 1962.

[229] E. V. Timofeeva, A. N. Gavrilov, J. M. McCloskey, Y. V. Tolmachev, S. Sprunt, L. M. Lopatina, and J. V. Selinger, "Thermal conductivity and particle agglomeration in alumina nanofluids: Experiment and theory," *Physical Review E*, vol. 76, p. 061203, 2007.

[230] Y. Xuan and W. Roetzel, "Conceptions for heat transfer correlation of nanofluids," *International Journal of Heat and Mass Transfer*, vol. 43, pp. 3701-3707, 2000.

[231] B. Gavtash, K. Hussain, M. Layeghi, and S. S. Lafmejani, "Numerical simulation of the effects of nanofluid on a heat pipe thermal performance," *International Journal of Mechanical and Aerospace Engineering* vol. 6, pp. 480-486, 2012.

[232] S. E. B. Maïga, C. T. Nguyen, N. Galanis, and G. Roy, "Heat transfer enhancement in forced convection laminar tube flow by using nanofluids," *Proceedings of International Symposium on Advances in Computational Heat Transfer III*, Paper CHT-040101, p. 24, 2004.

[233] L. Syam Sundar, K. V. Sharma, S. Parveen, and M. A. Gaffar, "Laminar convective heat transfer of nanofluids in a circular tube under constant heat flux," *International Journal of Nanoparticles*, vol. 2, pp. 314-320, 2009.

[234] A. P. Sasmito, J. C. Kurnia, and A. S. Mujumdar, "Numerical evaluation of laminar heat transfer enhancement in nanofluid flow in coiled square tubes," *Nanoscale research letters,* vol. 6, p. 376, 2011.

[235] D. Wen and Y. Ding, "Experimental investigation into convective heat transfer of nanofluids at the entrance region under laminar flow conditions," *International Journal of Heat and Mass Transfer,* vol. 47, pp. 5181-5188, 2004.

[236] P. K. Namburu, D. K. Das, K. M. Tanguturi, and R. S. Vajjha, "Numerical study of turbulent flow and heat transfer characteristics of nanofluids considering variable properties," *International Journal of Thermal Sciences,* vol. 48, pp. 290-302, 2009.

[237] V. Gnielinski, "New equations for heat and mass transfer in turbulent pipe and channel flow," *International Chemical Engineering,* vol. 16, pp. 359--368, 1976.

[238] H. C. Brinkman, "The Viscosity of Concentrated Suspensions and Solutions," *The Journal of Chemical Physics,* vol. 20, pp. 571-571, 1952.

[239] "2009 ASHRAE Handbook - Fundamentals (I-P Edition)," ed: American Society of Heating, Refrigerating and Air-Conditioning Engineers, Inc.

[240] P. K. Namburu, D. P. Kulkarni, D. Misra, and D. K. Das, "Viscosity of copper oxide nanoparticles dispersed in ethylene glycol and water mixture," *Experimental Thermal and Fluid Science,* vol. 32, pp. 397-402, 2007.

[241] B. C. Sahoo, R. S. Vajjha, R. Ganguli, G. A. Chukwu, and D. K. Das, "Determination of Rheological Behavior of Aluminum Oxide Nanofluid and Development of New Viscosity Correlations," *Petroleum Science and Technology,* vol. 27, pp. 1757-1770, 2009.

[242] P. Charunyakorn, S. Sengupta, and S. K. Roy, "Forced convection heat transfer in microencapsulated phase change material slurries: flow in circular ducts," *International Journal of Heat and Mass Transfer,* vol. 34, pp. 819-833, 1991.

[243] P. Keblinski, S. R. Phillpot, S. U. S. Choi, and J. A. Eastman, "Mechanisms of heat flow in suspensions of nano-sized particles (nanofluids)," *International Journal of Heat and Mass Transfer*, vol. 45, pp. 855-863, 2002.

[244] S. Jegadheeswaran and S. D. Pohekar, "Performance enhancement in latent heat thermal storage system: A review," *Renewable and Sustainable Energy Reviews*, vol. 13, pp. 2225-2244, 2009.

[245] M. N. A. Hawlader, M. S. Uddin, and M. M. Khin, "Microencapsulated PCM thermal-energy storage system," *Applied Energy*, vol. 74, pp. 195-202, 2003.

[246] B. Chen, X. Wang, R. Zeng, Y. Zhang, X. Wang, J. Niu, Y. Li, and H. Di, "An experimental study of convective heat transfer with microencapsulated phase change material suspension: Laminar flow in a circular tube under constant heat flux," *Experimental Thermal and Fluid Science*, vol. 32, pp. 1638-1646, 2008.

[247] C. Alkan, A. Sarı, A. Karaipekli, and O. Uzun, "Preparation, characterization, and thermal properties of microencapsulated phase change material for thermal energy storage," *Solar Energy Materials and Solar Cells*, vol. 93, pp. 143-147, 2009.

[248] J.-S. Cho, A. Kwon, and C.-G. Cho, "Microencapsulation of octadecane as a phase-change material by interfacial polymerization in an emulsion system," *Colloid and Polymer Science*, vol. 280, pp. 260-266, 2002.

[249] L. Bayés-García, L. Ventolà, R. Cordobilla, R. Benages, T. Calvet, and M. A. Cuevas-Diarte, "Phase Change Materials (PCM) microcapsules with different shell compositions: Preparation, characterization and thermal stability," *Solar Energy Materials and Solar Cells*, vol. 94, pp. 1235-1240, 2010.

[250] Y. Xuan, Y. Huang, and Q. Li, "Experimental investigation on thermal conductivity and specific heat capacity of magnetic microencapsulated phase change material suspension," *Chemical Physics Letters*, vol. 479, pp. 264-269, 2009.

[251] F. Salaün, E. Devaux, S. Bourbigot, P. Rumeau, P.-O. Chapuis, S. K. Saha, and S. Volz, "Polymer nanoparticles to decrease thermal conductivity of phase change materials," *Thermochimica Acta,* vol. 477, pp. 25-31, 2008.

[252] X. Hu and Y. Zhang, "Novel insight and numerical analysis of convective heat transfer enhancement with microencapsulated phase change material slurries: laminar flow in a circular tube with constant heat flux," *International Journal of Heat and Mass Transfer,* vol. 45, pp. 3163-3172, 2002.

[253] M. Goel, S. K. Roy, and S. Sengupta, "Laminar forced convection heat transfer in microcapsulated phase change material suspensions," *International Journal of Heat and Mass Transfer,* vol. 37, pp. 593-604, 1994.

[254] Y. Zhang, X. Hu, and X. Wang, "Theoretical analysis of convective heat transfer enhancement of microencapsulated phase change material slurries," *Heat and Mass Transfer,* vol. 40, pp. 59-66, 2003/12/01 2003.

[255] E. L. Alisetti and S. K. Roy, "Forced Convection Heat Transfer to Phase Change Material Slurries in Circular Ducts," *Journal of Thermophysics and Heat Transfer,* vol. 14, pp. 115-118, 2000.

[256] J. L. Alvarado, C. Marsh, C. Sohn, G. Phetteplace, and T. Newell, "Thermal performance of microencapsulated phase change material slurry in turbulent flow under constant heat flux," *International Journal of Heat and Mass Transfer,* vol. 50, pp. 1938-1952, 2007.

[257] J.-F. Su, X.-Y. Wang, Z. Huang, Y.-H. Zhao, and X.-Y. Yuan, "Thermal conductivity of microPCMs-filled epoxy matrix composites," *Colloid and Polymer Science,* vol. 289, pp. 1535-1542, 2011.

[258] Y. Özonur, M. Mazman, H. Ö. Paksoy, and H. Evliya, "Microencapsulation of coco fatty acid mixture for thermal energy storage with phase change material," *International Journal of Energy Research,* vol. 30, pp. 741-749, 2006.

[259] Y. Rao, F. Dammel, P. Stephan, and G. Lin, "Convective heat transfer characteristics of microencapsulated phase change material suspensions in minichannels," *Heat and Mass Transfer,* vol. 44, pp. 175-186, 2007.

[260] R. C. Brown, J. D. Rasberry, and S. P. Overmann, "Microencapsulated phase-change materials as heat transfer media in gas-fluidized beds," *Powder Technology,* vol. 98, pp. 217-222, 1998.

[261] A. Sarı and A. Karaipekli, "Preparation, thermal properties and thermal reliability of capric acid/expanded perlite composite for thermal energy storage," *Materials Chemistry and Physics,* vol. 109, pp. 459-464, 2008.

[262] A. Karaipekli and A. Sarı, "Capric–myristic acid/expanded perlite composite as form-stable phase change material for latent heat thermal energy storage," *Renewable Energy,* vol. 33, pp. 2599-2605, 2008.

[263] A. Sarı, A. Karaipekli, and C. Alkan, "Preparation, characterization and thermal properties of lauric acid/expanded perlite as novel form-stable composite phase change material," *Chemical Engineering Journal,* vol. 155, pp. 899-904, 2009.

[264] J. Wang, H. Xie, and Z. Xin, "Thermal properties of paraffin based composites containing multi-walled carbon nanotubes," *Thermochimica Acta,* vol. 488, pp. 39-42, 2009.

[265] A. Karaipekli and A. Sarı, "Capric–myristic acid/vermiculite composite as form-stable phase change material for thermal energy storage," *Solar Energy,* vol. 83, pp. 323-332, 2009.

[266] S. A. Putnam, D. G. Cahill, B. J. Ash, and L. S. Schadler, "High-precision thermal conductivity measurements as a probe of polymer/nanoparticle interfaces," *Journal of Applied Physics,* vol. 94, pp. 6785-6788, 2003.

[267] V. Halte, J.-Y. Bigot, B. Palpant, M. Broyer, B. Prevel, and A. Perez, "Size dependence of the energy relaxation in silver nanoparticles embedded in dielectric matrices," *Applied Physics Letters*, vol. 75, pp. 3799-3801, 1999.

[268] A. Elgafy and K. Lafdi, "Effect of carbon nanofiber additives on thermal behavior of phase change materials," *Carbon*, vol. 43, pp. 3067-3074, 2005.

[269] J. L. Zeng, Z. Cao, D. W. Yang, F. Xu, L. X. Sun, X. F. Zhang, and L. Zhang, "Effects of MWNTs on phase change enthalpy and thermal conductivity of a solid-liquid organic PCM," *Journal of Thermal Analysis and Calorimetry*, vol. 95, pp. 507-512, 2009.

[270] J. L. Zeng, Z. Cao, D. W. Yang, L. X. Sun, and L. Zhang, "Thermal conductivity enhancement of Ag nanowires on an organic phase change material," *Journal of Thermal Analysis and Calorimetry*, vol. 101, pp. 385-389, 2010/07/01 2010.

[271] S. Wu, D. Zhu, X. Li, H. Li, and J. Lei, "Thermal energy storage behavior of Al2O3–H2O nanofluids," *Thermochimica Acta*, vol. 483, pp. 73-77, 2009.

[272] Y. D. Liu, "Study On Preparation And Thermal Properties Of Phase Change Nanocomposites For Cool Storage," PhD, Engineering & Technology, Chongqing University, China, 2005.

[273] J. L. Alvarado, C. Marsh, C. Sohn, M. Vilceus, V. Hock, G. Phetteplace, and T. Newell, "Characterization of supercooling suppression of microencapsulated phase change material by using DSC," *Journal of Thermal Analysis and Calorimetry*, vol. 86, pp. 505-509, 2006.

[274] E. R. G. Eckert and R. M. Drake Jr, *Analysis of Heat and Mass Transfer*. New York, USA Hemisphere Publishing,New York, NY, 1972.

[275] R. K. Shah, "thermal entry lrnght solution for the circular tube and parallel plates," in *Proceedings of 3rd National Heat and Mass Transfer Conference III*, Bombay, 1975, pp. 314-320.

[276] K. B. Anoop, T. Sundararajan, and S. K. Das, "Effect of particle size on the convective heat transfer in nanofluid in the developing region," *International Journal of Heat and Mass Transfer,* vol. 52, pp. 2189-2195, 2009.

[277] X.-j. Wang, X. Li, and S. Yang, "Influence of pH and SDBS on the Stability and Thermal Conductivity of Nanofluids," *Energy & Fuels,* vol. 23, pp. 2684-2689, 2009.

[278] H. Bönnemann, S. S. Botha, B. Bladergroen, and V. M. Linkov, "Monodisperse copper- and silver-nanocolloids suitable for heat-conductive fluids," *Applied Organometallic Chemistry,* vol. 19, pp. 768-773, 2005.

[279] J. W. Gao, R. T. Zheng, H. Ohtani, D. S. Zhu, and G. Chen, "Experimental Investigation of Heat Conduction Mechanisms in Nanofluids. Clue on Clustering," *Nano Letters,* vol. 9, pp. 4128-4132, 2009.

[280] R. Chein and G. Huang, "Analysis of microchannel heat sink performance using nanofluids," *Applied Thermal Engineering,* vol. 25, pp. 3104-3114, 2005.

[281] S. Lee and S. U. S. Choi, "Application of metallic nanoparticle suspensions in advanced cooling systems," presented at the Proceedings of Recent Advances in Solids/Structures and Application of Metallic Materials, 1996.

[282] Versteeg. H and Malalasekera. W, *An Introduction to Computational Fluid Dynamics: The Finite Volume Method,* : Prentice Hall, 2007.

[283] J. D. Anderson, G. Degrez, E. Dick, and R. Grundmann, *Computational Fluid Dynamics* 2nd Edition ed.: A Von Karman Institute Book, 1995.

[284] *ANSYS FLUENT 14.0 Theory Guide,* : ANSYS, Inc, 2011.

[285] N. Özişik, *Finite Difference Methods in Heat Transfer,*: Taylor & Francis, 1994.

[286] A. A. Al-abidi, S. Bin Mat, K. Sopian, M. Y. Sulaiman, and A. T. Mohammed, "CFD applications for latent heat thermal energy storage: a review," *Renewable and Sustainable Energy Reviews,* vol. 20, pp. 353-363, 2013.

[287] A. Joulin, Z. Younsi, L. Zalewski, D. R. Rousse, and S. Lassue, "A numerical study of the melting of phase change material heated from a vertical wall of a rectangular enclosure," *International Journal of Computational Fluid Dynamics,* vol. 23, pp. 553-566, 2009.

[288] V. R. Voller and C. Prakash, "A fixed grid numerical modelling methodology for convection-diffusion mushy region phase-change problems," *International Journal of Heat and Mass Transfer,* vol. 30, pp. 1709-1719, 1987.

[289] L. C. Chow, J. K. Zhong, and J. E. Beam, "Thermal conductivity enhancement for phase change storage media," *International Communications in Heat and Mass Transfer,* vol. 23, pp. 91-100, 1996.

[290] R. Kandasamy, X.-Q. Wang, and A. S. Mujumdar, "Transient cooling of electronics using phase change material (PCM)-based heat sinks," *Applied Thermal Engineering,* vol. 28, pp. 1047-1057, 2008.

[291] R. C. Reid, J. M. Prausnitz, and T. K. Sherwood, *The properties of gases and liquids,* : McGraw-Hill, 1977.

[292] J. P. Holman, *Heat Transfer*: McGraw Hill Higher Education, 2010.

[293] A. Shukla, D. Buddhi, and R. L. Sawhney, "Solar water heaters with phase change material thermal energy storage medium: A review," *Renewable and Sustainable Energy Reviews,* vol. 13, pp. 2119-2125, 2009.

[294] M. Pinelli and S. Piva, "Solid/Liquid Phase Change in Presence of Natural Convection: A Thermal Energy Storage Case Study," *Journal of Energy Resources Technology,* vol. 125, pp. 190-198, 2003.

[295] J. D. Chung, J. S. Lee, and H. Yoo, "Thermal instability during the melting process in an isothermally heated horizontal cylinder," *International Journal of Heat and Mass Transfer,* vol. 40, pp. 3899-3907, 1997.

[296] V. R. Voller, "FAST IMPLICIT FINITE-DIFFERENCE METHOD FOR THE ANALYSIS OF PHASE CHANGE PROBLEMS," *Numerical Heat Transfer, Part B: Fundamentals,* vol. 17, pp. 155-169, 1990.

[297] J. Crank, *Free and Moving Boundary Problems*. Oxford, UK: Clarendon Press, 1987.

[298] S. Wu, H. Wang, S. Xiao, and D. Zhu, "Numerical Simulation on Thermal Energy Storage Behavior of Cu/paraffin nanofluids PCMs," *Procedia Engineering,* vol. 31, pp. 240-244, 2012.

[299] S. J. Kline and F. A. McClintock, "Describing uncertainties in single sample experiments," *Mechanical Engineering,* vol. 75, No. 1, pp. 3-8, 1953.

[300] Z. Liu, Z. Wang, and C. Ma, "An experimental study on heat transfer characteristics of heat pipe heat exchanger with latent heat storage. Part I: Charging only and discharging only modes," *Energy Conversion and Management,* vol. 47, pp. 944-966, 2006.

Appendix A. UDF for PCM physical Properties with Al_2O_3 nano-particles

```
#include "udf.h"
#define npvf 0.03                /* volum fraction of nanoparticles */
#define d_np 29e-9               /* nanoparticles diameter (m)*/
#define npd 3600                 /* density of Al2O3 nano-particles*/
#define cp_np 765                /* specific heat of Al2O3 nano-particles*/
#define T0 273                   /* reference temperature*/
#define Knp 36                   /* thermal conductivity of Al2O3 nano-particles*/
#define B 1.381e-23              /* Boltzman constant   */
#define K1 5e4                   /* Brownian motion constant */
#define Z1 8.4407                /*Brownian motion parameter1 for AL2O3*/
#define Z2 -1.07304              /*Brownian motion parameter2 for AL2O3*/
#define C1 0.9830                /*Viscosity parameter constant1 for AL2O3*/
#define C2 12.959                /*Viscosity parameter constant2 for AL2O3*/
#define c1 28.217e-3             /*Constant C1*/
#define c2 3.917e-3              /*Constant C2*/
#define c3 -3.0669e-2            /*Constant C3*/
#define c4 -3.91123e-3           /*Constant C4*/
#define Ts 299                   /* PCM solid temperature */
#define Tl 300.7                 /* PCM liquid temperature */
#define Bt 0.00091               /* PCM thermal expantion coefficent*/
#define Kpcm 0.253               /* PCM thermal conductivity */
#define cp_pcm 2050              /* PCM specific heat*/
```

```
DEFINE_PROPERTY(cell_density, cell, thread)
{
real npcm_den;                    /*density of nanoPCM*/
real pcmd;                        /* density of PCM*/
real temp = C_T(cell, thread);          /* cell temperature*/
if (temp <= Ts)
{pcmd = 814;}
else
{pcmd = (814)/((Bt*(temp-Tl))+1);}
npcm_den = (npvf*npd)+((1-npvf)*pcmd);
return npcm_den;
}

DEFINE_SPECIFIC_HEAT(cell_specific_heat, T, Tref, h, yi)
{
real cp;                          /*cp is specific heat capacity of nanoPCM*/
real pcmd;                          /*density of PCM*/
real npcm_den;                        /* density of nanoPCM*/
if (T <= Ts)
{pcmd = 814;}
else
{pcmd = (814)/((Bt*(T-Tl))+1);}
npcm_den = (npvf*npd)+((1-npvf)*pcmd);       /* density of nanoPCM*/
cp = ((npvf*npd*cp_np)+((1-npvf)*pcmd*cp_pcm))/npcm_den;    /* specific heat of
nanoPCM */
*h = cp*(T-Tref);
return cp;
}
```

```
DEFINE_PROPERTY(thermal_conductivity, cell, thread)
{

real Bk;                    /* Brownian motion term*/
real Ft;
real pcmd;                  /* density of PCM*/
real temp= C_T(cell,thread);    /* cell temperature */
real Knpcm;                 /* thermal conductivity of nanoPCM */
real L;                 /* liquid fraction of PCM*/

if (temp <= Ts)
{L = 0;
pcmd = 814;}
else if (temp >= Tl)
{L = 1;
pcmd = (814)/((Bt*(temp-Tl))+1);}
else
{L = (temp - Ts)/(Tl - Ts);
pcmd = (814)/((Bt*(temp-Tl))+1);}
Bk = Z1*(pow((100*npvf) ,Z2));              /* Brownian motion term*/
Ft = (((c1*npvf)+c2)*(temp/T0))+((c3*npvf)+c4);
Knpcm =(((Knp+(2*Kpcm)-(2*(Kpcm-Knp)*npvf))/(Knp+(2*Kpcm)+((Kpcm-
Knp)*npvf)))*Kpcm)+((L*K1*Bk*npvf*pcmd*cp_pcm)*(sqrt((B*temp)/(npd*d_np)))*Ft);
return Knpcm;
}
```

```
DEFINE_PROPERTY(viscosity, cell, thread)
{
real vs_npcm;                    /* dynamic viscosity of nanoPCM*/
real vs_pcm;
real temp= C_T(cell,thread);
vs_pcm = Bt*(exp(-4.5+(1790/temp)));
vs_npcm = C1*(exp(C2*npvf))*vs_pcm;        /* dynamic viscosity of nanoPCM*/
return vs_npcm;
}
```

Appendix B. UDF for PCM physical Properties with CuO nano-particles

```
#include "udf.h"
#define npvf 0.03                /* volum fraction of nanoparticles (Cu)*/
#define d_np 29e-9               /* nanoparticles diameter (m)*/
#define npd 6510                 /* density of CuO nano-particles*/
#define cp_np 540                /* specific heat of CuO nano-particles*/
#define T0 273                   /* reference temperature*/
#define Knp 18                   /* thermal conductivity of CuO nano-particles*/
#define B 1.381e-23              /* Boltzman constant   */
#define K1 5e4                   /* Brownian motion constant */
#define Z1 9.881                 /*Brownian motion parameter1 for CuO nano-particles*/
#define Z2 -0.9446               /*Brownian motion parameter2 for CuO nano-particles*/
#define C1 0.9197                /*Viscosity parameter constant1 for CuO nano-particles*/
#define C2 22.8539               /*Viscosity parameter constant2 for CuO nano-particles*/
#define c1 28.217e-3             /*Constant C1*/
#define c2 3.917e-3              /*Constant C2*/
#define c3 -3.0669e-2            /*Constant C3*/
#define c4 -3.91123e-3           /*Constant C4*/
#define Ts 299                   /* PCM solid temperature */
#define Tl 300.7                 /* PCM liquid temperature */
#define Bt 0.00091               /* PCM thermal expantion coefficent*/
#define Kpcm 0.253               /* PCM thermal conductivity */
#define cp_pcm 2050              /* PCM specific heat*/
```

```
DEFINE_PROPERTY(cell_density, cell, thread)
{
real npcm_den;                    /*density of nanoPCM*/
real pcmd;                        /* density of PCM*/
real temp = C_T(cell, thread);          /* cell temperature*/
if (temp <= Ts)
{pcmd = 814;}
else
{pcmd = (814)/((Bt*(temp-Tl))+1);}
npcm_den = (npvf*npd)+((1-npvf)*pcmd);
return npcm_den;
}

DEFINE_SPECIFIC_HEAT(cell_specific_heat, T, Tref, h, yi)
{
real cp;                          /*cp is specific heat capacity of nanoPCM*/
real pcmd;                          /*density of PCM*/
real npcm_den;                        /* density of nanoPCM*/
if (T <= Ts)
{pcmd = 814;}
else
{pcmd = (814)/((Bt*(T-Tl))+1);}
npcm_den = (npvf*npd)+((1-npvf)*pcmd);       /* density of nanoPCM*/
cp = ((npvf*npd*cp_np)+((1-npvf)*pcmd*cp_pcm))/npcm_den;    /* specific heat of
nanoPCM */
*h = cp*(T-Tref);
return cp;
}
```

```
DEFINE_PROPERTY(thermal_conductivity, cell, thread)
{

real Bk;                    /* Brownian motion term*/
real Ft;
real pcmd;                  /* density of PCM*/
real temp= C_T(cell,thread);    /* cell temperature */
real Knpcm;                 /* thermal conductivity of nanoPCM */
real L;                 /* liquid fraction of PCM*/


if (temp <= Ts)
{L = 0;
pcmd = 814;}
else if (temp >= Tl)
{L = 1;
pcmd = (814)/((Bt*(temp-Tl))+1);}
else
{L = (temp - Ts)/(Tl - Ts);
pcmd = (814)/((Bt*(temp-Tl))+1);}
Bk = Z1*(pow((100*npvf) ,Z2));              /* Brownian motion term*/
Ft = (((c1*npvf)+c2)*(temp/T0))+((c3*npvf)+c4);
Knpcm =(((Knp+(2*Kpcm)-(2*(Kpcm-Knp)*npvf))/(Knp+(2*Kpcm)+((Kpcm-
Knp)*npvf)))*Kpcm)+((L*K1*Bk*npvf*pcmd*cp_pcm)*(sqrt((B*temp)/(npd*d_np)))*Ft);
return Knpcm;
}
```

```
DEFINE_PROPERTY(viscosity, cell, thread)
{
real vs_npcm;                    /* dynamic viscosity of nanoPCM*/
real vs_pcm;
real temp= C_T(cell,thread);
vs_pcm = Bt*(exp(-4.5+(1790/temp)));
vs_npcm = C1*(exp(C2*npvf))*vs_pcm;        /* dynamic viscosity of nanoPCM*/
return vs_npcm;
}
```

Appendix C. UDF for PCM physical Properties with ZnO nano-particles

```
#include "udf.h"
#define npvf 0.03                /* volum fraction of nanoparticles */
#define d_np 29e-9               /* nanoparticles diameter (m)*/
#define npd 5600                 /* density of ZnO nano-particles*/
#define cp_np 502.4              /* specific heat of ZnO nano-particles*/
#define T0 273                   /* reference temperature*/
#define Knp 13                   /* thermal conductivity of ZnO nano-particles*/
#define B 1.381e-23              /* Boltzman constant   */
#define K1 5e4                   /* Brownian motion constant */
#define Z1 8.4407                /*Brownian motion parameter1 for ZnO nano-particles*/
#define Z2 -1.07304              /*Brownian motion parameter2 for ZnO nano-particles*/
#define C1 0.9830                /*Viscosity parameter constant1 for ZnO nano-particles*/
#define C2 12.959                /*Viscosity parameter constant2 for ZnO nano-particles*/
#define c1 28.217e-3             /*Constant C1*/
#define c2 3.917e-3              /*Constant C2*/
#define c3 -3.0669e-2            /*Constant C3*/
#define c4 -3.91123e-3           /*Constant C4*/
#define Ts 299                   /* PCM solid temperature */
#define Tl 300.7                 /* PCM liquid temperature */
#define Bt 0.00091               /* PCM thermal expantion coefficent*/
#define Kpcm 0.253               /* PCM thermal conductivity */
#define cp_pcm 2050              /* PCM specific heat*/
```

```
DEFINE_PROPERTY(cell_density, cell, thread)
{
real npcm_den;                    /*density of nanoPCM*/
real pcmd;                        /* density of PCM*/
real temp = C_T(cell, thread);          /* cell temperature*/
if (temp <= Ts)
{pcmd = 814;}
else
{pcmd = (814)/((Bt*(temp-Tl))+1);}
npcm_den = (npvf*npd)+((1-npvf)*pcmd);
return npcm_den;
}

DEFINE_SPECIFIC_HEAT(cell_specific_heat, T, Tref, h, yi)
{
real cp;                          /*cp is specific heat capacity of nanoPCM*/
real pcmd;                          /*density of PCM*/
real npcm_den;                        /* density of nanoPCM*/
if (T <= Ts)
{pcmd = 814;}
else
{pcmd = (814)/((Bt*(T-Tl))+1);}
npcm_den = (npvf*npd)+((1-npvf)*pcmd);       /* density of nanoPCM*/
cp = ((npvf*npd*cp_np)+((1-npvf)*pcmd*cp_pcm))/npcm_den;    /* specific heat of
nanoPCM */
*h = cp*(T-Tref);
return cp;
}
```

```
DEFINE_PROPERTY(thermal_conductivity, cell, thread)
{

real Bk;                    /* Brownian motion term*/
real Ft;
real pcmd;                  /* density of PCM*/
real temp= C_T(cell,thread);    /* cell temperature */
real Knpcm;                 /* thermal conductivity of nanoPCM */
real L;                 /* liquid fraction of PCM*/

if (temp <= Ts)
{L = 0;
pcmd = 814;}
else if (temp >= Tl)
{L = 1;
pcmd = (814)/((Bt*(temp-Tl))+1);}
else
{L = (temp - Ts)/(Tl - Ts);
pcmd = (814)/((Bt*(temp-Tl))+1);}
Bk = Z1*(pow((100*npvf) ,Z2));              /* Brownian motion term*/
Ft = (((c1*npvf)+c2)*(temp/T0))+((c3*npvf)+c4);
Knpcm =(((Knp+(2*Kpcm)-(2*(Kpcm-Knp)*npvf))/(Knp+(2*Kpcm)+((Kpcm-
Knp)*npvf)))*Kpcm)+((L*K1*Bk*npvf*pcmd*cp_pcm)*(sqrt((B*temp)/(npd*d_np)))*Ft);
return Knpcm;
}
```

```
DEFINE_PROPERTY(viscosity, cell, thread)
{
real vs_npcm;                    /* dynamic viscosity of nanoPCM*/
real vs_pcm;
real temp= C_T(cell,thread);
vs_pcm = Bt*(exp(-4.5+(1790/temp)));
vs_npcm = C1*(exp(C2*npvf))*vs_pcm;        /* dynamic viscosity of nanoPCM*/
return vs_npcm;
}
```